# Electroluminescent Displays

## Yoshimasa A. Ono

# Electroluminescent Displays

## SERIES ON INFORMATION DISPLAY

Editor-in-Chief: Hiap L. Ong

# Electroluminescent Displays

**Yoshimasa A. Ono**

*Advanced Research Laboratory*
*Hitachi, Ltd., Japan*

**British Library Cataloguing-in-Publication Data**
A catalogue record for this book is available from the British Library.

**ELECTROLUMINESCENT DISPLAYS**

*To my wife, Saiko,*

*and our children, Sayaka, Haruka and Masaki*

This page is intentionally left blank

# Preface

Electroluminescence (EL) is a non-thermal generation of light resulting from the application of an electric field to a substance. EL devices are divided into four types: ac thin film EL, ac powder EL, dc thin-film EL and dc powder EL. Among these, two types are now commercially available: ac thin film EL devices (ZnS:Mn) are used as flat screens of laptop personal computers and word processors, and ac powder EL devices are used as backlights for liquid crystal displays.

This book discusses recent developments of EL display devices, in particular thin film EL devices, because they have the largest possibility to be commercialized widely. They are all-solid, emissive display devices with the following superior characteristics: fast response, wide viewing angles, high resolution, wide operating temperatures, light weight, and good display qualities. These features ensure suitability to high information-content flat panel screens of personal computers and workstations. By employing the double-insulating layer structure, stable and high-luminance thin-film ZnS:Mn EL display panels have been fabricated, and mass production started in 1983. Recently multi-coloring of EL devices has been extensively studied employing CaS and SrS as well as ZnS as phosphor materials and rare-earth elements as luminescent centers. The luminance level of green emitting ZnS:Tb,F is getting close to that of ZnS:Mn, making it almost to the practical level. As for red emission, bright emission has been obtained by using ZnS:Mn with a thin-film red filter made of CdSSe. Blue emission by SrS:Ce is promising; although the emission color is blue-green, using a blue filter gives a bright blue emission. Based on these results, several prototype multicolor EL panels have been fabricated. The first commercial multicolor thin-film EL panel based on an inverted, filtered thin-film EL structure was put into market in 1993. In the same year, new blue phosphor made of rare-earth thiogallates was developed with bright, pure blue emission, and first prototype full-color EL panel was presented. The first commercial full-color EL display monitor was put into the market in 1994. These reports triggered interests once again in color thin-film EL displays. This book discusses these recent developments in color phosphors and EL device structures in detail. Furthermore, present status of multicolor and full-color thin-film EL display panels is presented.

This book has grown out of notes prepared for invited talks and seminars in the last several years, in particular, notes for Encyclopedia of Applied Physics and SID Seminar Lecture. Special thanks are due to Y. Murayama of Hitachi Advanced Research Laboratory for encouraging me to write an article on EL in Encyclopedia and C.N. King of Planar Systems for inviting me to give a seminar at 1993 SID Seminar Lecture.

I would like to thank C.N. King, R.O. Törnqvist of Planar International, J.F. Wager of Oregon State University, E. Bringuier of Université P. et M. Curie and R.H. Mauch of Heinrich-Hertz Institut für Nachrichtentechnik Berlin for informing me of their results prior to publications, communications and discussions. I learned a lot about EL physics from them. Also their comments and suggestions on the early version of the book helped to improve the clarity and contents of the book. I also would like to acknowledge Japanese colleagues with whom I have had the pleasure of studying EL displays together: H. Kobayashi and S. Tanaka of Tottori University, S. Shionoya of Tokyo Engineering University, A. Mikami of Sharp and T. Nire of Komatsu. Discussions with them and their guidance have made my understanding of EL deeper. Special thanks are due to my colleagues at Hitachi, M. Fuyama, K. Onisawa and M. Ando of Hitachi Research Laboratory, and H. Yamamoto (now at Tokyo Engineering University), O. Kanehisa and M. Shiiki of Central Research Laboratory for their support and encouragement.

This page is intentionally left blank

# Contents

# 1. INTRODUCTION

Electroluminescence (EL) is a nonthermal generation of light resulting from the application of an electric field to a substance. This effect was discovered in 1936 by the French physicist Destriau[1] when he observed that light was emitted from a ZnS compound when a large electric field was applied to it. There are two classes of EL devices. In the familiar light-emitting diodes (LED) devices, light is generated by electron-hole pair recombination near a pn junction. This book, however, will focus on the second type of EL device in which light is generated by impact excitation of a light-emitting center, called an activator or a luminescent center, by high-energy electrons. The electrons gain their high energy from a high electric field on the order of $10^8$ V/m, and thus this type of EL is often called high-field electroluminescence. In these devices, the behavior of the majority carriers (the electrons) predominantly determines the device physics. Based on this high-field electroluminescent phenomenon, four types of EL devices have been developed. They are categorized according to the phosphor configuration and the drive voltage wave forms: ac thin-film EL, ac powder EL, dc thin-film EL and dc powder EL.

Initial effort to utilize the phenomenon of EL focused on powder EL devices, but with the development of thin-film process technology in the 1960's, the majority of the more recent development efforts have been directed to thin-film EL devices.

The first commercial thin-film EL products were introduced by Sharp[2] in 1983. In that year Grid announced the first portable computer which uses a 6-inch-diagonal 320x240 pixel EL display panel. In mid 80's three different manufacturers, Sharp, Planar Systems, and Finlux (Planar International since 1991), introduced half-page, 9-inch-diagonal yellow-emitting ZnS:Mn thin-film EL displays on the market and began offering a variety of EL products. Since 1983 the commercial EL display industry has progressed from the technical novelty stage to its present status as one of the three major flat panel technologies with a broad user group in a wide range of applications. Production costs have lowered considerably along with the growing cumulative volume (learning effect) and the price of thin-film EL displays is getting closer to older, more mature, flat panel technologies.

Now ZnS:Mn thin-film EL displays have gained large acceptance in demanding display applications where excellent viewing characteristics are necessity, and are now readily available in different sizes up to full sizes for workstations. The most common displays are the 640x400 and 640x480 pixel (9-inch-diagonal) half-page displays for personal computers and word processors. Thin-film EL displays are also found in applications where good contrast must be maintained in a very high ambient illumination environment such as in industrial instrumentation. The strongest selling point of thin-film EL display is high legibility because light is emitted from a sub-micrometer thick device with crisp pixel edges. Other well-known features are high contrast (>7:1 at 500 lux ambient with filter), wide viewing angle (>160°), fast response time (several microseconds), and the capability for very high resolution. Thin-film EL displays are addressed at video frame rate, and thus there is no smear in mouse and cursor applications. All this is achieved in a simple solid-state device structure that is insensitive to shocks and wide temperature variation.

The biggest challenge today for the thin-film EL technology is producing multicolor displays. Manufacturing of practical multicolor displays was long delayed due to insufficient luminance of the primary colors, red, green and blue. Recently, however, progress in the development of the multicolor display structure and color phosphors made it possible to fabricate the first multicolor thin-film EL displays[3] fulfilling customer's requirements. Commercial production started in 1993. In comparison to competing multicolor flat-panel technologies with similar performance characteristics, thin-film EL

displays can be made with a very simple device structure. This is expected to give thin-film EL advantages for future applications. The first multicolor thin-film EL displays are based on the inverted, patterned-color-filter device structure, where red and green colors are filtered out from yellow-emitting ZnS:Mn.

The color blue is still inadequate for practical display applications, but recent laboratory results are now close to what is required. Using a cerium-activated calcium thiogallate (CaGa$_2$S$_4$:Ce) phosphor, Barrow et al.[4] reported a deep blue luminance of 13 cd/m$^2$ measured at 60-Hz pulse driving with the CIE color coordinates x=0.15 and y=0.19. Mauch et al.[5)-7)] reported a filtered blue luminance of 14 cd/m$^2$ with x=0.10 and y=0.26 at 60-Hz pulse driving using a multilayer ZnS/SrS:Ce/ZnS/SrS:Ce/.../SrS:Ce/ZnS phosphor film structure. Based on the results of the former phosphor, a prototype 10-inch-diagonal 640x480 pixel full-color EL display was developed[4] in 1993 using a dual-substrate EL structure. This structure combines patterned red/green phosphors on one substrate with a new blue phosphor (CaGa$_2$S$_4$:Ce) on a separate substrate in a stacked configuration. The stacked panel structure efficiently couples the unfiltered blue emission with saturated red and green EL emissions to produce a color gamut approaching that of the color CRT. Based on this, the first commercial full-color thin-film EL display monitor[8] with 320x256 pixels was put into market in 1994.

This book discusses EL displays with an emphasis on ac thin-film EL displays. In particular, recent developments in color phosphors for thin-film EL devices and multicolor thin-film EL panels are discussed in detail. Chapter 2 discusses historical developments of EL devices, and Chapter 3 deals with EL device structures and EL emission mechanisms of four types of EL displays. Physics of ac thin-film EL is discussed in Chapter 4, including display characteristics, ideal model, standard measuring and evaluation methods, properties of phosphor materials and luminescent centers and high-field electronic transport. Materials requirements and materials deposition methods are discussed in Chapters 5 and 6, respectively. Chapter 7 deals with recent development in color thin-film phosphors based on ZnS, CaS, SrS and alkaline-earth thiogallates for color thin-film EL devices, where phosphors for red, green and blue emission as well as white emission are discussed in detail. In addition, luminance requirements for three primary colors are discussed. Chapter 8 reports on EL drive methods such as field-refresh, p-n symmetric, p-p symmetric, grayscale and active-matrix drive methods. EL display panels and other EL applications are detailed in Chapter 9, in particular multicolor display panels in a stacked-phosphor structure, a patterned phosphor and a broadband-spectrum or white phosphor with patterned color filters and full-color thin-film EL panels in the dual-substrate structure. Furthermore, multicolor EL panel in the inverted, filtered structure is discussed in detail, because the first commercial multicolor EL panel is based on this structure. Reliability problems, including electrical reliability and long-time reliability, are discussed in Chapter 10 and the conclusions and future prospects are given in the last chapter.

For further study review articles by the following authors are useful: Howard[9], Mach and Müller[10], Kobayashi[11], Alt[12] and Ono[13]. Also workshop proceedings of EL-88[14] (Tottori, Japan), EL-90[15] (Helsinki, Finland) and EL-92[16] (El Paso, Texas, USA) are recommended for reading.

# 2. HISTORY OF EL DEVICES

Table 1 lists milestones in the development of EL displays until the start of volume production of monochrome ac thin-film EL displays.

Table 1   History of monochrome EL displays

| | |
|---|---|
| 1936 | Discovery of high-field electroluminescence (Destriau, Ref. 1) |
| 1950 | Development of transparent conducting films (SnO$_2$) |
| | —> Development of ac powder EL devices |
| 1950 | Basic studies on ac powder EL devices |
| -1960 | (Problems: Low luminance and short lifetime) |
| 1960 | ZnS:Mn thin-film EL structure (Vlasenko and Popkov, Ref. 18) |
| 1964 | Electroluminescent thin-film research (Reported in 1972) |
| -1970 | (Soxman and Ketchpel, Ref. 21) |
| 1967 | Double-insulating-layer type ac thin-film EL device structure (Russ and Kennedy, Ref. 19) |
| 1968 | High-luminance thin-film EL devices with lumocen* (Kahng, Ref. 20) |
| 1974 | High-luminance and long-lifetime ac thin-film EL display (Inoguchi *et al.*, Ref. 22) |
| 1974 | Application of ac thin-film EL display to TV imaging system (Mito *et al.*, Ref. 23) |
| 1974 | Memory effects in ZnS:Mn ac thin-film EL display (Yamauchi *et al.*, Ref. 24) |
| 1981 | Practical ac thin-film display unit (Uede *et al.*, Ref. 32) |
| 1983 | Start of volume production of ac thin-film EL displays (Takeda *et al.*, Ref. 2) |

*Lumocen: Luminescence from Molecular Centers

As shown in Table 1, high-field electroluminescence was discovered by Destriau[1] in 1936. He observed light emission from a ZnS phosphor powder dispersed in an insulator and sandwiched between two electrodes when a high ac voltage was applied. Until 1950, when transparent electrically conductive films made of SnO$_2$ were developed, no effort was made to develop practical devices. The use of these SnO$_2$ transparent conductive films to develop ac powder EL devices triggered worldwide research and development of EL devices.

During the period from late 1950's to early 1960's basic studies on ac powder EL focused on flat light sources for wall illumination, resulting in lighting devices from night lights to wall-sized panels. Display applications, however, were limited to fixed legend displays for instrument clusters. This era came to an end when it was realized[17] that powder EL had multiplexing limitations, and suffered from low luminance, high operating voltage, poor contrast and significant luminance degradation over fairly short time (~500 hours).

First thin-film EL structures were also deposited in the late 1950's and in 1960 Vlasenko and Popkov[18] observed a much steeper rise of luminance with respect to voltage in yellow-emitting ZnS:Mn thin-film EL devices than in powder EL devices. This gave promise for matrix drive thin-film EL displays. In addition, high luminance and superior contrast were achieved in comparison to ac powder EL devices. The reliability of these thin-film EL devices was at that time, however, insufficient for display applications.

In the 1960's development efforts switched to thin film devices with the advent of modern thin film process technology. A significant step forward was taken in 1967 by Russ and Kennedy[19] when they introduced a double-insulating-layer type ac thin-film EL structure, which is still the basic device structure of thin-film EL display. The importance for improved reliability was, however, not immediately appreciated. In 1968 Kahng[20] reported that thin-film EL with high luminance was attained via impact excitation using

molecules of rare-earth fluoride, such as TbF$_3$, as the luminescent centers. He called this phenomenon Lumocen (luminescence from molecular centers) effect. The pioneering work of Soxman and Ketchpel[21] from 1964 to 1970 succeeded in producing bright displays with good multiplexing capability for matrix addressing and good luminance maintenance. However, the reliability of these devices was unsatisfactory. Thus another era came to an unsuccessful conclusion.

It was not until 1974 that there was new reason for expectations. At the 1974 SID International Symposium Inoguchi *et al.*[22] announced that luminance of 1000 fL (~3400 cd/m$^2$) at 5-kHz driving could be maintained for more than 10000 hours in an orange-yellow-emitting ZnS:Mn thin-film EL device with the double-insulating-layer structure. Furthermore, Mito *et al.*[23] showed that these EL panels could be used for a TV imaging system. This once again triggered industrial development efforts that have now brought thin-film EL displays to the commercial market place.

In the late 70's and in the early 80's hysteresis phenomena in the luminance vs. voltage characteristics of a ZnS:Mn ac thin-film EL device were studied[24]-[28] because of a possibility of driving a matrix display at a constant sustained voltage, while turn-on and turn-off of pixels being controlled by a transient voltage. However, stability problems have so far prevented any practical use of it. Other important topics at that time were the choice of dielectrics[29] for insulating layers and optimization of deposition processes in the thin-film EL devices. EL thin films were mostly deposited by evaporation or sputtering. In 1980, atomic layer epitaxy (ALE) method[30] was introduced to grow high-quality ZnS thin films.

Regarding the production of thin-film EL panels, Takeda *et al.*[31] reported on practical application technologies of ZnS:Mn EL displays and Uede *et al.*[32] reported on practical EL display units. Using these technologies, volume production of 6 inch-diagonal matrix monochrome EL display panels started[2] in 1983.

The introduction of half-page 9-inch-diagonal ZnS:Mn yellow-emitting thin-film EL displays on the market in mid 80's showed that thin-film EL technology was mature for applications. During the last few years thin-film EL displays have experienced a rapidly growing market. Most applications have been found in industrial instrumentation, but recently several computer manufacturers have chosen this display technology. Yellow-emitting ZnS:Mn thin-film EL displays are now readily available in different sizes up to 640x400 pixels (9-inch-diagonal). For this size, power consumption is typically 10-15 W and an average luminance is about 100 cd/m$^2$. Higher-resolution A4-sized display devices with 1024x800 dots are being developed.

The main target today is producing multicolor thin-film EL displays. This in turn requires phosphor materials that emit three primary colors, i.e., red, green and blue. Beginning with the pioneering work by Kahng[20] and his co-workers[33], extensive studies have been conducted on materials and processing technologies.

Table 2 lists recent milestones in the development of color thin-film EL displays. Most efforts were concerned with the ZnS host material doped with various rare-earth luminescent centers[34]. By employing sputtering, high-luminance and high-luminous efficiency green-emitting ZnS:Tb,F EL devices[35]-[37] were obtained with luminance close to that of ZnS:Mn. On the other hand, the maximum luminances of blue-emitting ZnS:Tm,F EL devices and red-emitting ZnS:Sm,F EL devices were much lower[38] than those of green-emitting ZnS:Tb,F EL devices. Luminance improvement in red was realized by changing the coactivator from F to Cl and by employing metal-organic chemical vapor deposition (MOCVD) method[39]. Further increase in red EL emission was achieved[40] by using ZnS:Mn phosphor with a thin-film red filter made of CdSSe. And these ZnS-based

phosphors have been used to make prototype multicolor thin-film EL display panels in a patterned-phosphor EL device structure[40)-45)] and in an inverted, patterned-color-filter EL device structure[46)-49)]. Finally 1993 saw the first commercial multicolor EL display panel[3)] based on the inverted, patterned-color-filter EL device structure using ZnS:Mn phosphor.

Table 2  History of color EL displays

| 1981 | Color thin-film EL devices based on rare-earth doped ZnS (Okamoto, Ref. 34) |
|------|------|
| 1984 | Blue emission from SrS:Ce thin-film EL device (Barrow *et al.*, Ref. 50) |
| 1985 | Multicolor emission from CaS and SrS based thin-film EL (Tanaka *et al.*, Ref. 52) |
| 1986 | Luminance improvement of SrS:Ce (Tanaka *et al.*, Ref. 53) |
| 1986 | Prototype multicolor thin-film EL display (Barrow *et al.*, Ref. 41) |
| 1987 | Luminance improvement of ZnS:Tb,F by sputtering (Ohnishi *et al.*, Ref. 36) |
| 1988 | White emission from SrS:Ce,Eu (Tanaka *et al.*, Ref. 63) |
| 1988 | Prototype full-color thin-film EL display (Barrow *et al.*, Ref. 60) |
| 1991 | Multicolor thin-film EL display using an inverted, patterned-color-filter device structure based on ZnS:Mn (Okibayashi *et al.*, Ref. 47) |
| 1992 | Red/Green/Yellow multicolor EL display in the inverted, patterned-color-filter device structure with ZnS:Mn phosphor (Haaranen *et al.*, Ref. 48) |
| 1993 | First commercial multicolor (Red/Green/Yellow) thin-film EL display panel in EGA format (Cramer *et al.*, Ref. 3) |
| 1993 | Bright blue emission from CaGa$_2$S$_4$:Ce and prototype full-color thin-film EL display (Barrow *et al.*, Ref. 4) |
| 1994 | First commercial full-color thin-film EL display monitor (Barrow *et al.*, Ref. 8) |

In order to obtain efficient color EL phosphors, many studies have been directed to finding suitable combination of new host materials and luminescent centers. Cerium (Ce) doped strontium sulfide (SrS) was the first alkaline-earth thin-film EL phosphor to be investigated and report[50)] of a 100 times improvement in the luminance over ZnS:Tm,F as a blue phosphor stimulated much of the recent investigations of alkaline-earth sulfides SrS and CaS as thin-film EL host materials[51)-56)]: CaS:Eu emits deep red and SrS:Ce emits blue-green. Luminance improvement in CaS:Eu was achieved by raising the substrate temperature[53),56),57)] to 400-500°C. To obtain stoichiometric SrS:Ce with high luminance, sandwiching SrS:Ce with ZnS buffer layers[52)] and sulfur coevaporation[53)] have been found to be effective. Further luminance improvement of blue-green emission was achieved[5)-7)] by employing ZnS/SrS:Ce multilayered phosphor thin film. Using these phosphors, prototype multicolor display panels were fabricated in the patterned-phosphor device structure[58)-60)] and in a hybrid device structure[61)].

White-emitting phosphors[57),62)-64)] have been investigated using SrS and CaS, such as SrS:Ce/SrS:Eu, SrS:Ce,Eu and SrS:Ce/CaS:Eu, for multicolor EL displays[65),66)] by filtering white light through color filters. Another candidate is a layered ZnS:Mn/SrS:Ce thin-film phosphor[67)-74)] with yellowish-white emission. Luminance improvement has been achieved[71)] and filtered three primary colors are very close to those of color CRT display.

Recently, a new class of blue-emitting thin-film EL phosphors based on alkaline-earth thiogallates has been developed[4)]. To obtain good crystallinity and proper stoichiometry, sputtering was necessary with post-deposition rapid thermal annealing above 650°C. In particular, CaGa$_2$S$_4$:Ce emits deep blue with a luminance close to the required value for a practical display, and in 1993 a prototype 10-inch-diagonal 640x480 full-color display was developed[4)] using the dual-substrate EL panel structure. Using this

technology, the first commercial full-color thin-film EL display monitor[8] with 320x256 pixels was put into the market in 1994.

As discussed above, progress in new color phosphor and color EL display panels has been realized through a successive interplay of developments of materials, thin-film deposition methods and EL device structures: Development of new materials has led to the developments of new deposition methods and improvement of EL device structure. And development of new thin-film preparation methods has made it possible to properly fabricate thin films of new materials and to create new device structures. Proposals of new device structures have given a chance to develop new deposition methods. This development interplay of materials, deposition methods and device structure is essential to creating new devices.

# 3. EL DEVICE STRUCTURES AND EL EMISSION MECHANISMS

In this chapter we discuss device structures and emission mechanisms of four types of EL devices, whose main characteristics are shown in Fig. 1. The characteristics of organic thin-film EL diode devices are also discussed.
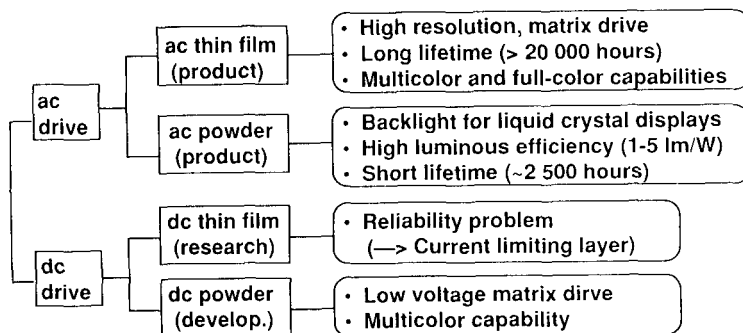


Fig. 1. Characteristics of four types of EL devices

## 3.1. ac Thin-Film EL

Since Inoguchi et al.[22] reported on high-luminance, long-lifetime EL devices, ac thin-film EL with the double-insulating-layer structure has been the center of research and development. A schematic structure of this type of EL device is shown in Fig. 2.
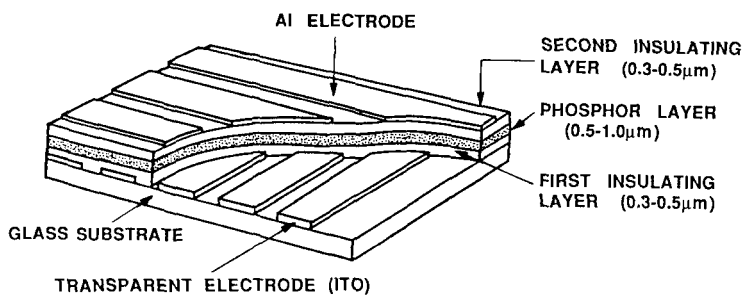


Fig. 2. Structure of a double-insulating-layer-type ac thin-film EL device

The central layer is the thin-film phosphor layer which emits light when a large enough electric field is applied across it. This field level is on the order of $10^8$ V/m. Because of this high applied field level, any imperfection in the thin-film phosphor that produces a short circuit would cause a destructive amount of energy to be dissipated if the phosphor layer were directly connected to the electrodes. Therefore, thin-film insulating layers as current limiting layers are placed on both sides of the phosphor layer to realize a reliable

device. Hence this device is called the double-insulating-layer type thin-film EL device. The insulating layers limit the maximum current to the capacitive charging and discharging displacement current level. Finally, electrodes on the top and bottom of the device complete a basic capacitance structure. At least one set of these electrodes should be transparent to permit viewing of the emitted light. In the conventional double-insulating-layer type thin-film EL device shown in Fig. 2, the lower electrode is usually transparent indium tin oxide (ITO) and the upper (rear) electrode is aluminum (Al). The thicknesses of the phosphor and the insulating layers are 0.5-1 μm and 0.3-0.5 μm, respectively. The overall thickness of thin-film structure, therefore, is less than two micrometers. This device structure gives a low diffuse scattering of ambient light. The light emitting area is confined to the crossing of the perpendicular electrodes, which are defined to a micrometer accuracy using lithographic technique. The reflection from the aluminum rear electrode is suppressed by using a neutral density filter or a circularly polarizing filter.

The double-insulating-layer type EL devices have the following advantages:
1. Double-insulating layers can protect the phosphor layer against impurities and moisture from outside to ensure higher stability.
2. In this structure, direct electron flows from electrodes to the phosphor layer are prevented, resulting in a high breakdown electric field.
3. Trapped charges at the phosphor layer/insulating layer interfaces cause internal polarization, which increases the effective electric field under ac drive conditions.

As a result, luminous efficiency and luminance are increased.

Emission colors can be controlled by adding different luminescent centers. ZnS:Mn gives yellow emission with the highest luminance[34]. In the ZnS-based EL devices activated by rare-earth ions[34),38),75)], ZnS:Tb,F gives green emission, ZnS:Tm,F gives blue emission, and ZnS:Sm,F gives reddish-orange emission. In the CaS- and SrS-based EL devices[50)-56)], SrS:Ce gives blue-green emission, CaS:Ce gives green emission, and CaS:Eu gives red emission. It should be noted that copper, which is used in powder EL, is not used in ac thin-film EL because copper ions migrate under a high electric field ($\sim 10^8$ V/m), causing deterioration of the EL device characteristics.

On the basis of the above discussion, the EL emission mechanism is indicated in Fig. 3, which shows an energy-band diagram of the EL device. The EL emission occurs in the following way.
1. Above the threshold voltage, electrons are injected from the interface states between the phosphor layer and insulating layer by high-field-assisted tunneling.
2. The injected electrons are accelerated and gain kinetic energy large enough to excite luminescent centers or the host lattice.
3. High-energy electrons, which are called hot electrons, directly excite luminescent centers through the impact-excitation mechanism. When these electrons in the excited states of the luminescent centers make radiative transitions to the ground state, EL emission is realized.
4. The hot electrons travel through the phosphor layer and are finally trapped at the phosphor layer/insulator layer interface states on the anode side, causing polarization.
5. When the polarity of the ac voltage wave forms is reversed, the same process takes place in the opposite direction in the phosphor layer.

Since the tunnel injection is temperature insensitive, ac thin-film EL devices can be used over a wide temperature range from -100 to 100 °C.
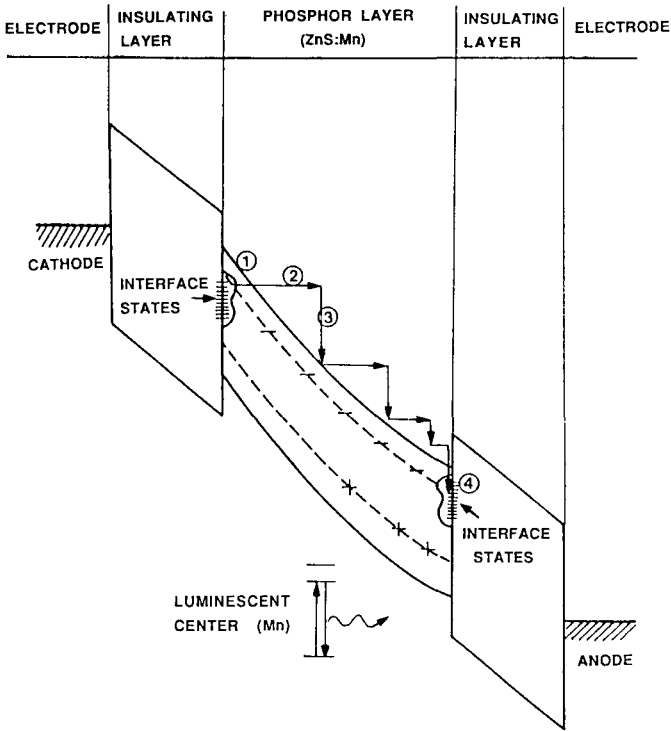
Fig. 3. Energy-band diagram of the double-insulating-layer-type ac thin-film EL device and the EL emission mechanism; Circled numbers refer to the corresponding features described in the text (Ref. 13)

This EL emission mechanism is generally accepted for ZnS-based EL devices[12),13),76)-78)]. In CaS- or SrS-based EL devices, however, an additional mechanism has been proposed[79)-82)]. This additional mechanism is characterized by a field-induced ionization of luminescent centers and subsequent trapping of low energy electrons, resulting in EL emission.

Figure 4 shows typical luminance versus voltage (L-V) and luminous efficiency versus voltage ($\eta$-V) characteristic curves of ZnS:Mn EL devices. This L-V curve features a threshold voltage $V_{th}$ below which little light is emitted, a steeply rising characteristic above threshold, and finally a saturation region. The threshold voltage is defined by the voltage corresponding to a luminance of 1 cd/m². As indicated in the figure, $L_{30}$ is defined by the luminance at 30 V above $V_{th}$. This value is very important because under practical drive conditions, the drive voltage is usually set at 30 or 40 V above $V_{th}$. On the other hand, the luminous efficiency $\eta$ increases just above $V_{th}$ and has a maximum in the voltage region where a steep increase of luminance takes place. Above this voltage region, $\eta$ decreases slowly.

This highly non-linear L-V characteristic provides a device with the capability to be electrically addressed at a very high multiplexing ratio while maintaining excellent contrast. This is just what is required for the matrix addressing of high-information-content flat-panel displays. The typical performance level achievable with this technology in the commercially available 640x480 thin-film EL display units is a luminance level of 100 cd/m$^2$ and contrast ratio of 15:1 in a 500 lux ambient with a 60-Hz frame rate. Because these displays have wide viewing angles (>160°) and operate at video rates, thin-film EL technology has all the characteristics required to produce high-information-content flat-panel displays with the image quality of the CRT. In fact, because of the photolithographic definition of the pixels in thin-film EL displays, the visual acuity, the image linearity, and the freedom from flicker makes today's thin-film EL technology superior to some features of the CRT. In addition, the solid state nature of thin-film EL displays make the extremely rugged which is often a desirable characteristics for a flat panel display when used in portable applications.
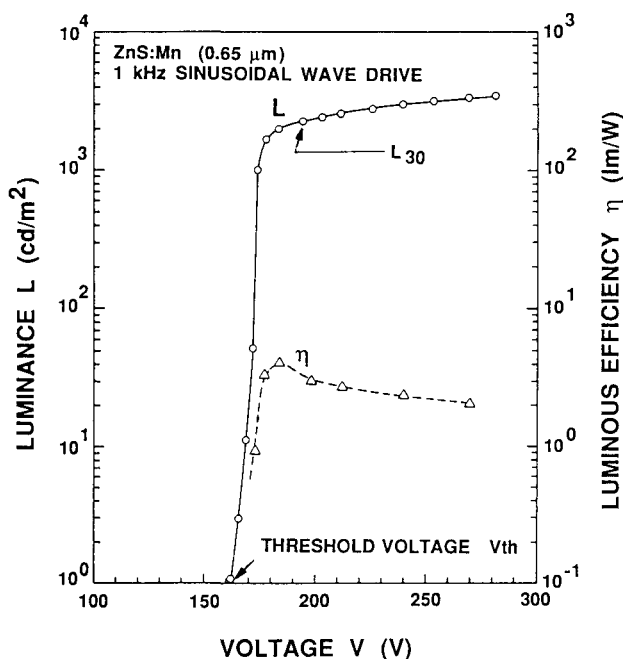


Fig. 4. Typical luminance vs. voltage (L-V) and luminous efficiency vs. voltage (η-V) characteristics for double-insulating-layer-type ac thin-film EL devices (Ref. 13)

## 3.2. ac Powder EL

This type of EL device was first developed by Sylvania in the first era of EL devices. Now they are used as backlights of liquid-crystal displays. The device structure

is shown in Fig. 5(a). The phosphor layer (50-100 μm) consists of a suitably doped ZnS powder (5-20 μm grains) suspended in a dielectric, which acts as a binder as well. The phosphor layer is sandwiched between two electrodes, one of which is transparent, and is supported by a substrate, consisting of either glass or flexible plastic. As a dielectric, an organic material with a large dielectric constant, such as cyanoethylcellulose, or low melting glass is used. An insulating layer may be placed between the phosphor layer and the rear electrode to avoid catastrophic dielectric breakdown. The important point is that the ZnS grains should be isolated from each other. In the case of good isolation, an insulating layer is not necessary.

Electric fields of $10^6$-$10^7$ V/m are necessary to obtain EL emission. Luminance increases proportionally with frequency up to 10 kHz, but lifetime decreases in the same proportion. As shown in Fig. 5(b), the luminance level is about 100 cd/m$^2$ at a voltage of 400 V and frequency of 400 Hz and luminous efficiency is about 1 lm/W.
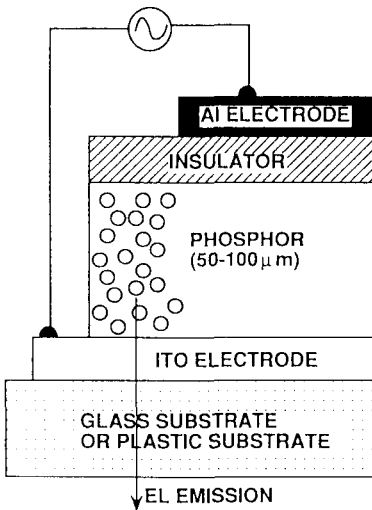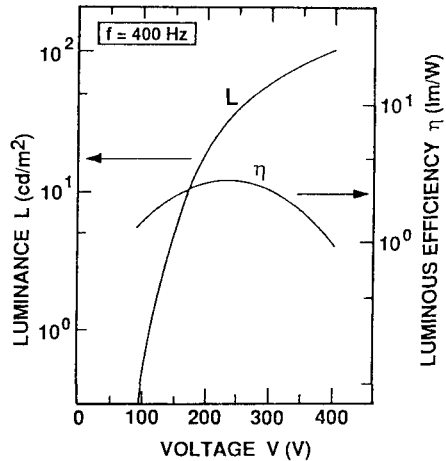


(a) EL DEVICE STRUCTURE    (b) L-V and η-V CHARACTERISTICS

Fig. 5. ac powder EL structure and electro-optical characteristics: (a) cross-sectional EL device structure; (b) Luminance vs. voltage (L-V) and luminous efficiency vs. voltage (η-V) characteristics

Emission colors can be controlled by adding different kinds of luminescent centers. As shown in Fig. 6, a combination of Cu and Cl (ZnS:Cu,Cl) gives either blue (~460 nm) or green (~510 nm) emission, depending on the relative amount of Cl. This EL emission is caused by the recombination transition of D-A (donor-acceptor) pairs, where Cu constitutes an acceptor and Cl constitutes a donor. The combination of Cu and Al (ZnS:Cu,Al) gives green and the addition of Mn to Cu and Cl (ZnS:Cu,Cl,Mn) gives yellow (~590 nm). An advantage of this type of EL device is easy control of emission colors, by mixing different phosphors with different emission colors.
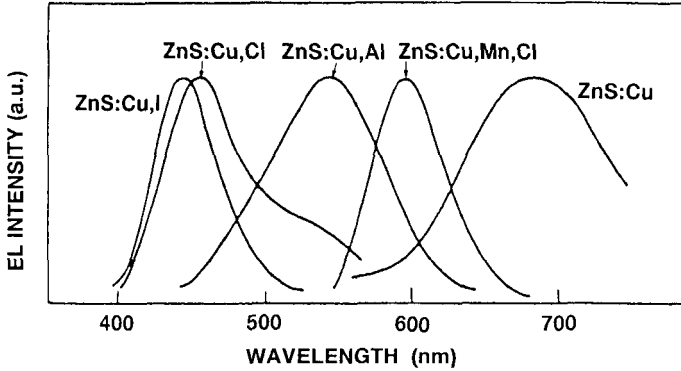
Fig. 6. EL emission spectra of ac powder EL displays

The EL emission mechanism[83)-85)] is shown in Fig. 7. As shown in Fig. 7(a), when the electric field exceeds the threshold electric field $E_{th}$, EL emission begins in the form of a pair of small bright spots. With the increase in electric field, these bright spots elongate to form comet-shaped emissive regions. This behavior is understood in the following way. EL powders fired at high temperatures have the hexagonal structure but subsequent cooling transforms them into the cubic (zinc blende) structure. Then copper exceeding the solubility limit precipitates on defects in ZnS particles. The result is embedded $Cu_xS$ conducting needles.



(a) EL EMISSION          (b) ENERGY BAND DIAGRAM
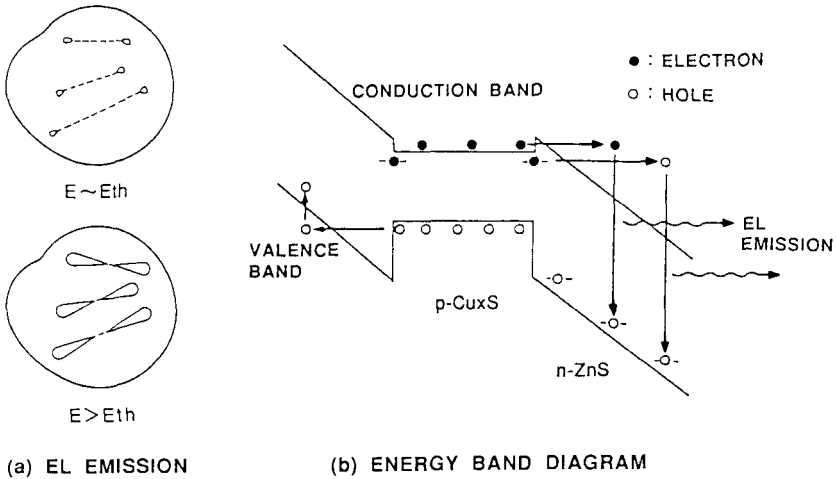
Fig. 7. EL emission mechanism and schematic energy-band diagram of ac powder EL device: (a) EL emission from a ZnS:Mn particle; (b) energy-band diagram (Refs. 83 and 84)

Between these $Cu_xS$ precipitates and ZnS powder hetero-junctions are formed, as shown in Fig. 7(b). These $Cu_xS$ conducting needles act to concentrate an applied electric field at their tips, and therefore an applied field of $10^6$-$10^7$ V/m can induce a local field of $10^8$ V/m or more. This electric field is strong enough to induce tunneling of holes from one end and electrons from the other. The holes are trapped on Cu recombination centers, and upon reversal of the fields the emitted electrons recombine with the trapped holes to produce light. Thus EL emission occurs along the $Cu_xS$ precipitates. Larger particle sizes lead to longer needles and greater field enhancement.

Lifetime is a key issue for the application of this EL device. The half-life, defined by the time when the luminance becomes 1/2 the initial value, now exceeds 2500 hours when driven at a voltage of 200 V and frequency of 400 Hz through the improvement of phosphor treatment conditions, encapsulation, and drive conditions. However, it is very difficult to have both long lifetime and high luminance simultaneously because they are trade-off characteristics.

## 3.3. dc Thin-Film EL

This type of EL device has the simplest structure: a thin film of phosphor layer with electrodes on both sides. Several attempts have been carried out by depositing a thin-film phosphor layer of ZnS:Mn, ZnS:Cu,Cl, and ZnS:Mn,Cu to increase stability and luminance, but no good results were obtained. Since the basic problem with this device is a tendency toward catastrophic failure, employment of a current-limiting layer should be considered. Kobayashi et al.[86),87)] succeeded in fabricating a stable ZnS:Mn EL device by inserting a thick resistive powder layer made of $MnO_2$ as a current-limiting layer between the phosphor layer and rear electrode. The cross-sectional structure is shown in Fig. 8. They called this device dc thin-film-powder hybrid EL. The luminous efficiency was 0.8 lm/W and the lifetime was more than 20 000 hours.
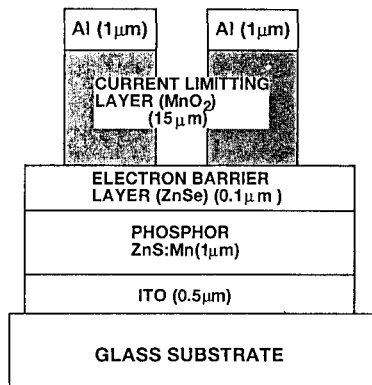


Fig. 8. Cross-sectional structure of dc thin-film/powder hybrid EL device (Ref. 86) .

Application to a green-emitting ZnS:TbOF EL devices was also carried out[88)]. A luminance $L_{100}$ and a luminous efficiency $\eta_{100}$ were 30 cd/m$^2$ and 0.27 lm/W, respectively, at a 50-Hz pulse wave driving.

## 3.4. dc Powder EL

Since the pioneering work by Vecht *et al.*[89]-[91], dc powder EL devices have been extensively studied[92]-[94] in Great Britain. Now commercial panels with the configuration of 640x200 dots are available. The device structure is shown in Fig. 9(a). The phosphor layer (30-50 μm) is made of a fine (0.5-1 μm) Mn-doped ZnS powder and a small amount of binder. Here ZnS powder is deliberately prepared with a $Cu_xS$ coating. In contrast to the ac powder EL case, there is no insulating layer.

To obtain stability and emission uniformity, a forming process is necessary. When a voltage is first applied, a large current flows, the layer heats up, and gradually a narrow region ~1μm thick, adjacent to the transparent anode electrode, begins to luminesce.

As shown in Fig. 9(b) the luminance level is about 500 cd/m² at a voltage of 100 V under a dc drive condition. Under a pulse-wave drive condition at a frequency of 500 Hz with a 1% duty ratio, almost the same luminance level is realized as that of the dc drive case. Luminous efficiency is not high with values of 0.2-0.3 lm/W. In encapsulated, moisture-resistant devices, the half-life is about 1000 hours in dc drive and 5000 hours in pulse-wave drive.
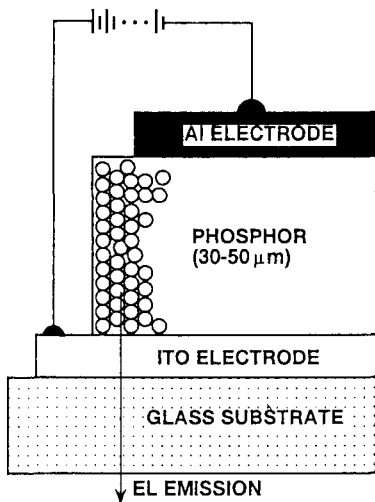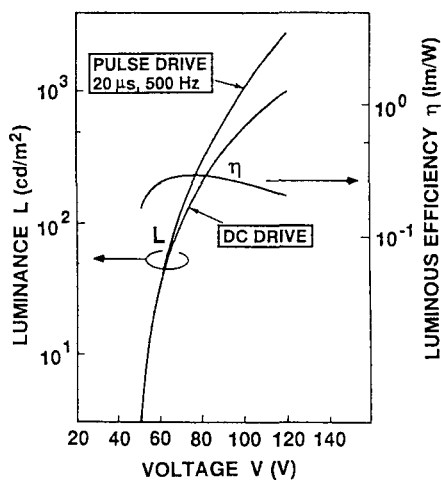


(a) EL DEVICE STRUCTURE          (b) L-V and η-V CHARACTERISTICS

Fig. 9. dc powder EL structure and electro-optical characteristics: (a) cross-sectional EL device structure; (b) Luminance vs. voltage (L-V) and luminous efficiency vs. voltage (η-V) characteristics

EL emission spectra of dc powder EL devices are shown in Fig. 10. The emission color of ZnS:Mn,Cu is yellow (~590 nm). In ZnS-based EL devices activated by rare-earth ions, $Tm^{3+}$ gives blue emission, $Tb^{3+}$ and $Er^{3+}$ give green emission, and $Nd^{3+}$ and $Sm^{3+}$ give red emission. In CaS- and SrS-based EL devices, SrS:Ce,Cl gives blue-green emission, CaS:Ce,Cl gives green emission, and CaS:Eu,Cl gives red emission.
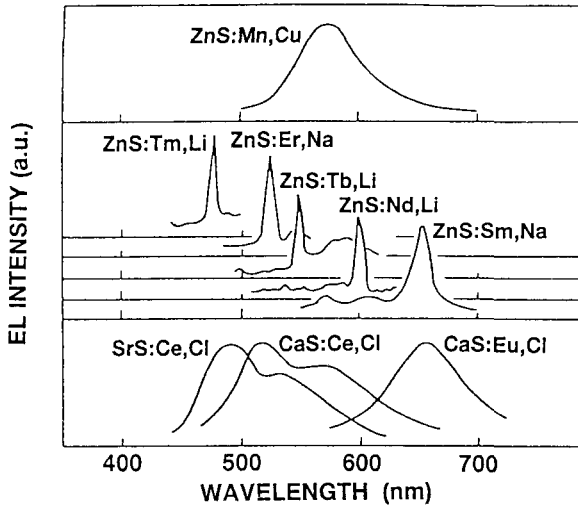
Fig. 10. EL emission spectra of dc powder EL displays

Figure 11(a) describes the microscopic model of dc powder EL. In the forming process[93], electromigration drives all copper out of a region adjacent to the anode, creating a highly resistive copper-free region (formed region) near the anode. As a result, a high electric field of $10^8$ V/m is created in this region. As shown in Fig. 11(b), under a high electric field, electrons, which have tunneled out of the $Cu_xS$ at the edge of the formed region, are accelerated and excite $Mn^{2+}$ luminescent centers by impact. When the excited electrons make transitions radiatively to the ground state, EL emission is realized.



(a) MICROSCOPIC MODEL    (b) ENERGY BAND DIAGRAM
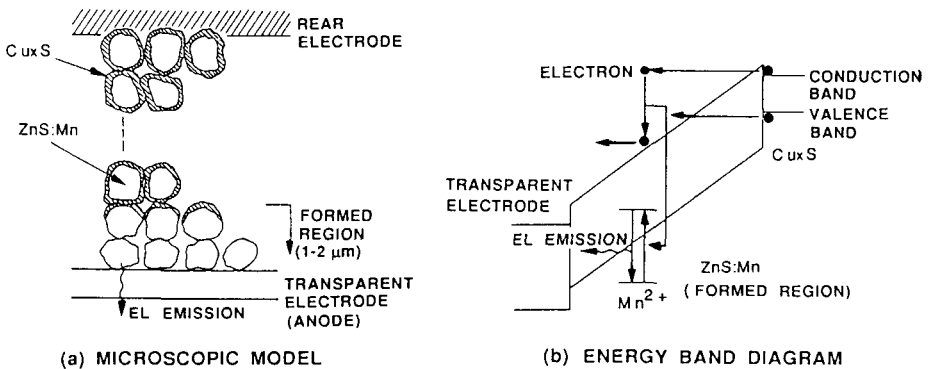
Fig. 11. Microscopic model of dc powder EL and energy band diagram for EL emission mechanism: (a) microscopic model; (b) energy band diagram

## 3.5. Organic Thin-Film EL

Figure 12 shows the structure of an organic thin-film EL diode device[95),96)].
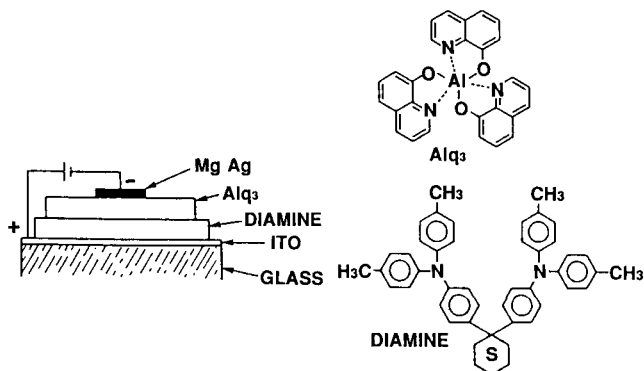


Fig. 12. Configuration of organic EL diode device and molecular structures of Alq3 and diamine (Ref. 95)

The substrate is an ITO-coated glass and the first organic layer (about 75 nm) is a hole-transport layer made of amorphous diamine film of molecular structure. The second organic layer (about 60 nm) is the luminescent layer as well as an electron-transport layer, made of 8-hydroxyquinoline aluminum (Alq3). The rear electrode is a mixture of Mg and Ag with an atomic ratio of 10:1.
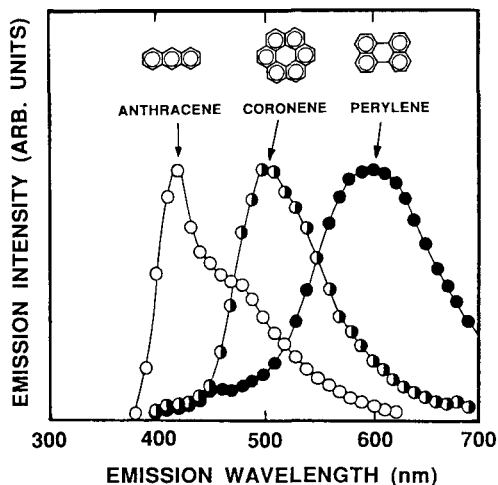


Fig. 13. EL emission intensities of three-layered organic EL diode devices with emitter materials; open circles are for anthracene, half-black and half-opened circles are for coronene and black circles are for perylene. Chemical structures of these are shown above. (Ref. 97)

The emission color of undoped $Alq_3$ was green, and a luminance of more than 1000 $cd/m^2$ and a luminous efficiency of 1.5 lm/W were achieved at a dc pulse drive voltage of 10 V. In the device with an $Alq_3$ layer doped with fluorescent molecules, the EL quantum efficiency was about 0.025 photons/electron. The EL emission color was tuned from blue-green to orange-red by a suitable choice of dopants as well as by changing the concentration of the dopant. The electron-hole recombination and emission zones were confined to about 5 nm near the hole-transport interface.

Adachi *et al.*[97)-101)] introduced a three-layer structure made of a hole-transport layer, a luminescent layer, and an electron-transport layer. By separating the luminescent function from the hole- or electron-transport layers, it became possible to select luminescent layer materials freely to obtain different emission colors. Figure 13 shows the results: By changing the luminescent layer material from anthracene to coronene to perylene, the emission color changed from blue to green to red. Here, an aromatic diamine and a perylene tetracarboxylic acid derivative were used for the hole- and electron-transport materials, respectively.

A matrix-drivability of organic thin-film EL diode display was confirmed[102)] by fabricating a 16x16 dot matrix EL cell using a MgIn thin-film cathode.

The lifetime is a key issue for the application of this EL diode device.

# 4. PHYSICS OF AC THIN-FILM EL DEVICES

This chapter discusses the physics of ac thin-film EL devices with the double-insulating-layer structure. First, typical display characteristics of thin-film EL devices[22),103)] are described: The electrical characteristics, including current-voltage (I-V) and phase difference-voltage ($\varphi$-V) characteristics, electro-optical characteristics, polarization characteristics, and stability characteristics, such as luminance-voltage (L-V) shift with respect to time and long-time behavior of luminance. Based on these results, an ideal model for the thin-film EL in terms of an equivalent-circuit[12),76)] is introduced, and device performances, such as transferred charge density, power dissipation (or input power to an EL device) and luminance, are expressed[12),104)] in terms of device parameters such as layer thickness, dielectric constant, dielectric breakdown strength, threshold field, and luminous efficiency. Then the standard EL measurement and evaluation methods[105)] are detailed, which are recommended by the 125th Research Committee[106)] on Mutual Conversion between Light and Electricity, Japan Society for the Promotion of Science, followed by the detailed discussions on the physical and chemical properties of phosphor materials and luminescent centers of color thin-film EL devices[13),38),52),53),56)]. This chapter concludes with the recent analysis on electronic transport in high electric field in terms of Monte Carlo simulation[107)-112)] and the lucky-drift model[113)-117)].

As mentioned in the introduction, light emission in a solid caused by an applied electric field is called electroluminescence (EL). The fundamental difference between cathode ray tube (CRT) displays and thin-film EL displays becomes obvious when considering how the excitation energy is provided to the light emitting phosphor. In CRT's luminescent centers of a light emitting phosphor are excited by the impact of high energy (~20 keV) electrons accelerated in vacuum. In a thin-film EL display the luminescent centers of the phosphors are excited by electrons that have acquired the excitation energy in the phosphor itself because of the applied electric field.

Actually there are good reasons to make a distinction between high-field and low-filed EL, as they are physically fundamentally different. A thin-film EL display is based upon high field (> $10^8$ V/m) electroluminescence. Majority charge carriers, usually electrons, are accelerated in an electric field to an energy of 2-3 eV or more. Light emission is obtained when the electrons excite luminescent centers and emission originates usually from transition between localized states, such as $3d^5$ of $Mn^{2+}$ in ZnS:Mn. On the other hand, a light emitting diode (LED) is based upon low-field (~$10^6$ V/m) EL, which originates from the potential energy provided to electron-hole pairs in a p-n junction. To achieve sufficient diffusion length of the minority carriers and radiative recombination, single crystalline materials are needed. Polycrystalline films can be used in high-field EL, which is a considerable advantage of thin-film EL displays.

## 4.1. Typical Display Characteristics of Thin-Film EL Devices

### 4.1.1. Electrical Characteristics

Figure 14 shows the current density versus voltage (I-V) and phase difference versus voltage ($\varphi$-V) characteristics under 1-kHz sinusoidal-wave drive conditions. The I-V profile is given by two straight lines linked with a kink, the voltage of which corresponds to the threshold voltage $V_{th}$. The profile of the phase difference $\varphi$ between current and voltage indicates that below the threshold voltage, only the displacement current flows with 90° phase difference. On the other hand, above the threshold voltage, conduction current

in phase with the voltage starts to flow, and with the increase in voltage the phase difference decreases from 90°, indicating that more in-phase conduction current flows. The impedance of the EL device can be estimated from the I-V characteristics curve with the following results: Below the threshold voltage, the estimated capacitance is equal to the total capacitances of the insulating layer, the phosphor layer, and the insulating layer in series, with the phosphor layer being a capacitor. This indicates that the phosphor layer has high resistivity and acts as an insulator. Above the threshold voltage, the estimated capacitance is equal to the total capacitances of only the insulating layers in series, with the phosphor layer being shunted. This indicates that the phosphor layer loses its insulating characteristics, and electrons at the interface states between the phosphor layer and the insulating layers are injected into the conduction band through a tunneling effect.
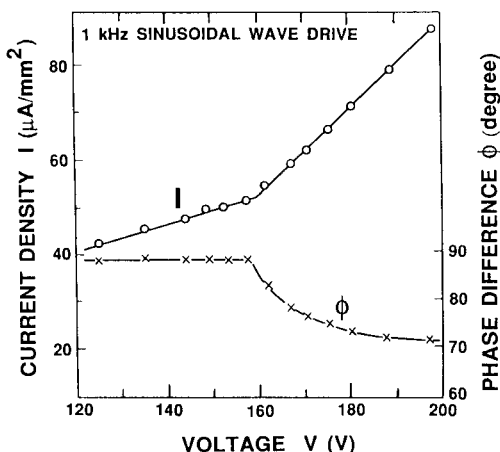


Fig. 14. Current density vs. voltage (I-V) and phase difference vs. voltage ($\phi$-V) characteristics of an ac thin-film EL device with a double-insulating-layer structure

### 4.1.2. Electro-Optical Characteristics

Figure 15 shows time-dependent characteristics of the voltage wave form V, the current wave form I, and the EL emission wave form L under triangular-wave drive conditions. As indicated in Section 4.1.1, below the threshold voltage $V_{th}$ only a constant displacement current flows and no EL emission occurs. On the other hand, above $V_{th}$ an additional current flows in the time period when the voltage is larger than $V_{th}$. This additional current corresponds to an in-phase (dissipative) current that flows through the phosphor layer, causing EL emission, as indicated in the EL-emission wave form L. The rise time and decay time of L for a ZnS:Mn thin-film EL device are of the order of several $\mu$s and several ms, respectively. As shown in Fig. 15, there are two EL emissions in one cycle, and luminance is proportional to the drive frequency up to several kHz.

Above $V_{th}$, the average electric field in the phosphor layer becomes $1.3$-$1.8 \times 10^8$ V/m. As indicated above, only above this electric field can electrons flow in the phosphor layer. Since EL excitation is due to this electron flow, the current and the transferred charge are important parameters in the analysis of the EL emission mechanism. It has been

verified experimentally[76],[105],[118] that the electric field of the phosphor layer is kept at a constant value above the threshold voltage (clamp effect). Therefore, the excess voltage is placed on the insulating layers, indicating the importance of insulating layers against dielectric breakdown of the EL device.
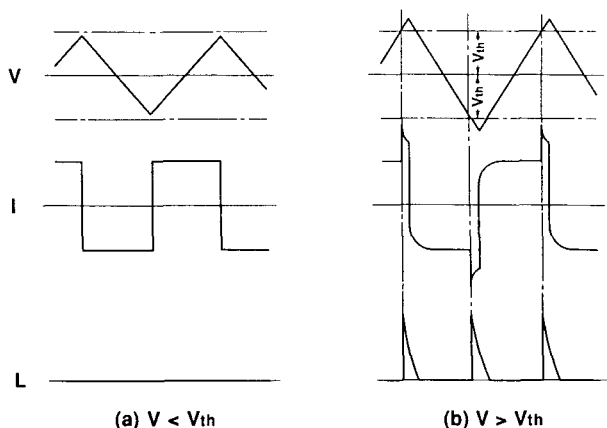


Fig. 15. Schematic characteristic diagrams of voltage wave form V, current wave form I and EL emission wave form L under triangular-wave drive conditions for double-insulating-layer type ac thin-film EL devices: (a) $V < V_{th}$; (b) $V > V_{th}$
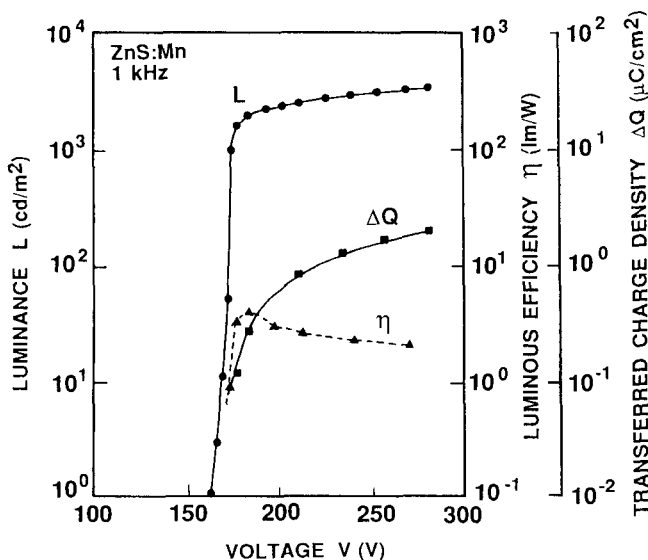


Fig. 16. Typical luminance vs. voltage (L-V), luminous efficiency vs. voltage ($\eta$-V) and transferred charge density vs. voltage ($\Delta Q$-V) characteristic curves of ZnS:Mn EL devices at 1-kHz sinusoidal drive

Figure 16 shows luminance versus voltage (L-V), luminous efficiency versus voltage (η-V) and transferred charge density-voltage (ΔQ-V) characteristic curves of ZnS:Mn EL devices at 1-kHz sinusoidal wave drive. As discussed in Section 3.1, above the threshold voltage, luminance rises rapidly because of increased transferred charge in the phosphor layer. The sharp increase in luminance is due to tunnel injection of electrons from trap states at the phosphor layer/insulating layer interface. The luminous efficiency η increases just above the threshold voltage, has a maximum and decreases slowly. The transferred charge density ΔQ increases linearly as a function of the voltage above the threshold voltage, which is more explicitly shown in the linear L-V and ΔQ-V curves in Fig. 17 for the ZnS:Mn device driven at 125 and 250 Hz sinusoidal waves[105].
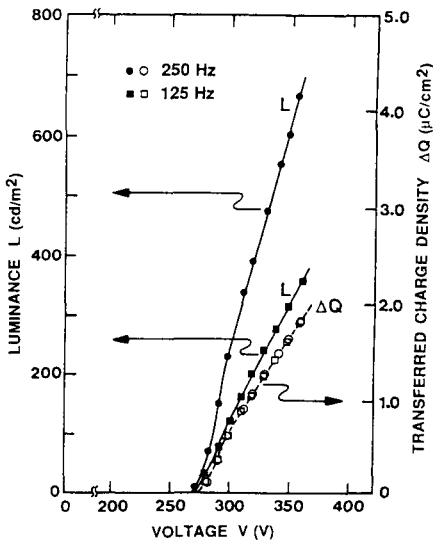


Fig. 17. L-V and ΔQ-V characteristics in linear scales for 125- and 250-Hz sinusoidal wave drive (Ref. 105)
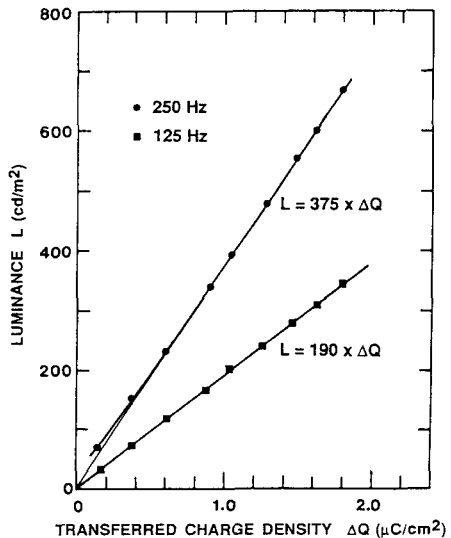
Fig. 18. L- ΔQ characteristics for 125- and 250-Hz sinusoidal wave drive (Ref. 105)

In Fig. 18, the relationship between luminance and transferred charge density is depicted for the two drive frequencies, showing that the luminance L is proportional to the product of the drive frequency f and the transferred charge density ΔQ over a wide range. Here, the proportionality constant depends on the phosphor layer properties, such as crystallinity, concentration of luminescent centers, distribution of luminescent centers and space charge.

As indicated above, the luminance is proportional to the transferred charge density within the phosphor layer[12),105),119)-121)], so that an increase in the transferred charge is necessary to improve luminance. Furthermore, the excitation probability of the luminescent centers by hot electrons should be improved, where the excitation probability is a function of the energy received by hot electrons from the electric field, i.e., a function of the product of the electric field and mean free path. The electric field is limited by the clamp electric field, while the mean free path depends on the crystallinity of the phosphor-

layer thin film. From these arguments, an increase in transferred charge density and better crystallinity are necessary to improve luminance.

Figure 19 shows the phosphor-layer thickness $d_{EL}$ dependence of luminance $L_{60}$ and luminous efficiency $\eta_{60}$ of EL devices[122] prepared by atomic layer epitaxy under a 1-kHz sinusoidal wave drive condition.
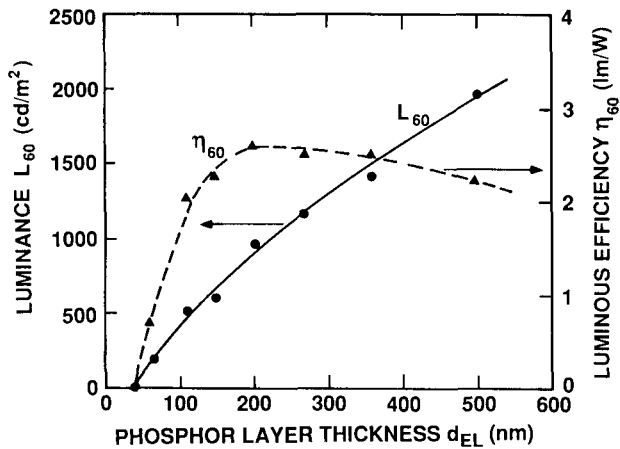


Fig. 19. Phosphor-layer thickness $d_{EL}$ dependence of luminance $L_{60}$ and luminous efficiency $\eta_{60}$ of ALE-prepared ZnS:Mn EL devices (Ref. 122)
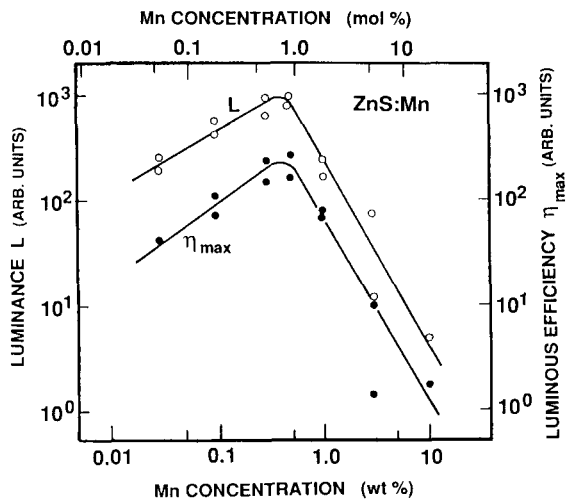


Fig. 20. Mn concentration dependence of luminance $L$ and maximum luminous efficiency $\eta_{max}$ of EBE-prepared ZnS:Mn EL devices (Ref. 123)

From the figure, thickness of the dead layer is estimated to be approximately 30 nm, which is much smaller than that of electron-beam evaporated films[123),124)]. When $d_{EL}$ is larger than the dead layer thickness, the luminance $L_{60}$ increases linearly with $d_{EL}$. On the other hand, the luminous efficiency $\eta_{60}$ increases when $d_{EL}$ is just above the dead-layer thickness, then stays nearly at a constant value to a thickness of about 500 nm with an average luminous efficiency of 2.5 lm/W.

EL luminance and luminous efficiency strongly depend on the luminescent-center concentration, as shown in Fig. 20 for a ZnS:Mn EL device[123),124)]. In the low Mn concentration region, the luminance L and the maximum luminous efficiency $\eta_{max}$ increase with increasing Mn concentration and reach maximum at a Mn concentration of 0.45 wt%. This increase is attributed to the increase in Mn luminescent centers. The luminance-voltage (L-V) hysteresis characteristics, the so-called memory effect, is observed for a Mn concentration of more than 0.5 wt%. In the high Mn concentration region above 0.5 wt%, both L and $\eta_{max}$ decrease rapidly. Two mechanisms may be responsible for this sharp decrease: One is the decrease in the mean free path of electrons, which is due to the scattering of hot electrons by the Mn centers or the decrease of the crystallinity in the phosphor layer. The other is the increase in the non-radiative transition probability of the excited Mn centers. Both mechanisms are present in the ZnS:Mn thin-film EL devices.

Regarding the luminance improvement it is important to consider a light-trapping effect[12)] in a ZnS:Mn ac thin-film EL device with a double-insulating-layer structure. As shown in Fig. 21, a ZnS:Mn phosphor layer with a refractive index n of 2.3 is sandwiched by insulating layers with smaller values of refractive indices, such as $Y_2O_3$ (n=1.9), $Al_2O_3$ (n=1.63), $Si_3N_4$ (n=2.0) or $SiO_2$ (n=1.46). Furthermore, the refractive index of glass is 1.53, larger than the refractive index of air, 1.0.



INSULATING LAYER
PHOSPHOR LAYER
ZnS:Mn (n = 2.3)
INSULATING LAYER

GLASS SUBSTRATE
(n = 1.53)
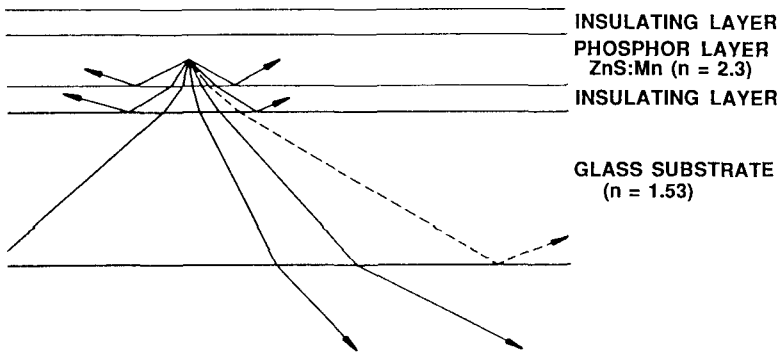
Fig. 21. Schematic representation of light-trapping effect in ZnS:Mn (refractive index: $n=2.3$) ac thin-film EL devices with double-insulating-layer structure; refractive indices of typical insulating-layer materials are as follows: $Y_2O_3$, $n=1.9$; $Al_2O_3$, $n=1.63$; $Si_3N_4$, $n=2.0$; and $SiO_2$, $n=1.46$ (Ref. 12)

Therefore, a large part of the EL emissions from the phosphor layer do not go through the glass substrate into air, rather they are trapped within the EL device because of total reflection. The measure for this effect is the optical light-outcoupling efficiency $\eta_{opt}$. In the estimation of $\eta_{opt}$ we take into account for simplicity only the ZnS phosphor layer which has the largest refractive index. By assuming that light is reflected at the metal rear electrode, we obtain

$$\eta_{opt} = \int_0^{\arcsin(1/2.3)} \sin\theta d\theta = 1 - [1 - (1/2.3)^2]^{0.5} \approx 0.1 \tag{1}$$

This is thus an important factor that can be increased if the surface of ZnS film is rough. Excessive surface roughness may reduce contrast ratio because of increased diffuse scattering. It should be mentioned that the contrast ratio of thin-film EL display is good and it can further be enhanced in strong illumination by using neutral density filters or circular polarizers.

On the other hand, when seen from the side edge of the EL devices, a very bright EL emission can be observed. An application of this edge emission was proposed[125] in the field of electrophotographic printers, i.e., thin film edge-emitter arrays for the optical image bar in place of a scanning laser with a rotating mirror or LED arrays. (Detailed discussion is given in Section 9.3.)

### 4.1.3. Polarization Characteristics

When the thin-film EL device with double-insulating-layer structure is driven by a series of voltage pulses, the light output of the device at each pulse is strongly affected by the polarity of the preceding pulse voltage[22],[103]. Figure 22 shows a schematic illustration of this phenomenon. As is clear from this figure, when the polarity of the succeeding pulse is inverted, a large light output is observed. On the other hand, if the polarity of the succeeding pulse is the same, the observed light output is very low. This behavior is due to the polarization of electrons at the phosphor layer/insulating layer interface states, which was observed to persist for a few minutes under a normal room light condition and for more than 10 hours in the dark.
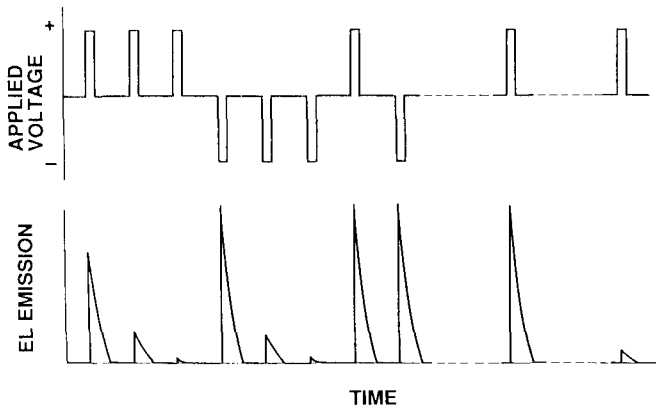


Fig. 22. Schematic illustration of drive voltage polarity effect on EL emission in thin-film EL devices with a double-insulating-layer structure (Ref. 103)

The cause of this polarization is as follows. As explained in Section 3.1, the voltage pulse creates a strong electric field which accelerates the electrons within the phosphor layer. As these electrons travels across the phosphor layer, they excite the Mn luminescent centers. Having traveled across the phosphor layer, the electrons accumulate at the interface between the phosphor layer and the insulating layer. These electrons remain at the

interface for a rather long period of time even after the electric field is removed, resulting in a polarization. Consequently, if the polarity of the next pulse is in the same direction as that of the first pulse, the effective inner electric field across the phosphor layer is lowered by the superposition of the previous counter polarization. On the other hand, when the polarity of the next pulse is inverted, the effective inner electric field is enhanced by additive polarization. Thus light output from the device is affected by the polarity of the preceding pulse.

### 4.1.4. Stability

Figure 23 shows time-dependent characteristics of the luminance vs. voltage (L-V) curve from the start of drive operation to 140 hours of drive operation[22],[103]. The L-V curve shifts to higher voltages with increasing operation time without changing the curve form, but the saturation luminance does not change. The L-V curve was found to settle asymptotically to a final curve after a certain operation time, approximately 80 hours in this EL device. Therefore, this shift is not an indication of degradation but an indication of stabilization due to aging effect. This stabilizing process was found to be accelerated by increasing the ambient temperature and by simultaneously applying a suitable voltage above the threshold voltage on the device. For example, if the aging operation was performed at around 200°C in the saturation region of the L-V curve, this stabilizing process was completed in an hour.
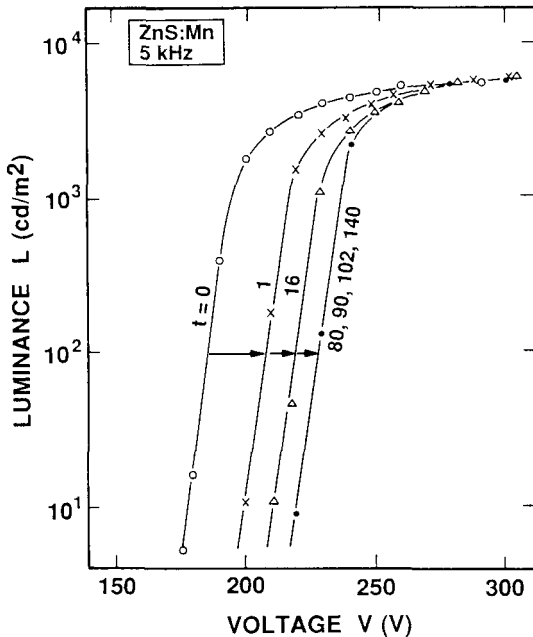
Fig. 23. Time dependence of L-V characteristics curves of typical ZnS:Mn thin-film EL devices deposited by electron-beam evaporation method (Refs. 22 and 103)

We note that the thin-film EL device became extremely stable after completion of this stabilization process[22),103)]. No change in luminance is observed, as shown in Fig. 24, during a continuous operation over 20000 hours at a constant operating voltage.
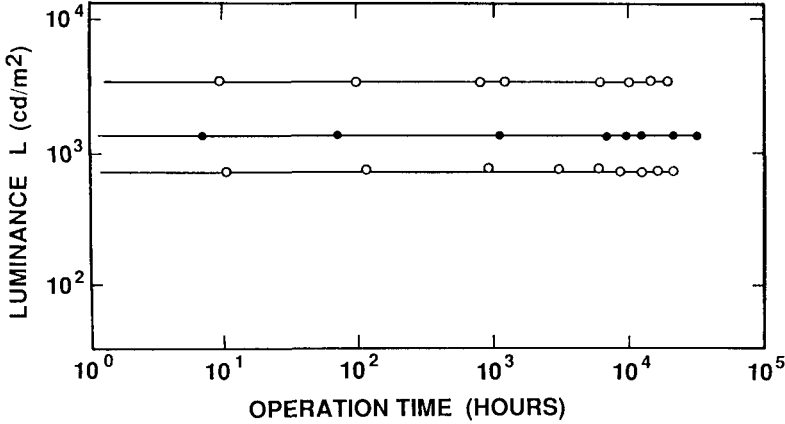


Fig. 24 Luminance vs. operation time characteristics at constant voltage operations in the double-insulating-layer type ZnS:Mn EL devices (Refs. 22 and 103)

### 4.2. Ideal Model for Thin-Film EL Devices

The above arguments lead to the following simple equivalent-circuit model of the thin-film EL structure shown in Fig. 25. Alt[12)] demonstrated that this simple model contains the essential phenomenological physics of a thin-film EL device and in practice this model has been found to model accurately the most significant characteristics of a thin-film EL device. This model treats the insulating layers of the device as perfect capacitors. The first and second insulating layers are incorporated into one effective insulating layer with the effective capacitance per unit area, $C_I$, given by

$$C_I = \frac{C_{I1}C_{I2}}{C_{I1} + C_{I2}} \qquad (2)$$

where $C_{I1}$ and $C_{I2}$ are capacitances per unit area of the first and second insulating layers, respectively. The thin film phosphor also behaves as a capacitor below the threshold voltage $V_{th}$ with the capacitance per unit area $C_{EL}$. However, above the threshold voltage real (dissipative) current flows in the phosphor layer and gives rise to the light emission. Therefore, the phosphor layer is described as a capacitor in parallel with a non-linear resistor with the I-V characteristic shown in Fig. 26. In an ideal case, this non-linear resistor can be simulated by back-to-back Zener diodes. The luminance of the device is proportional to the power consumed in this resistive branch with the proportionality constant being the experimentally determined luminous efficiency $\eta$ in units of lumens per watt (lm/W).
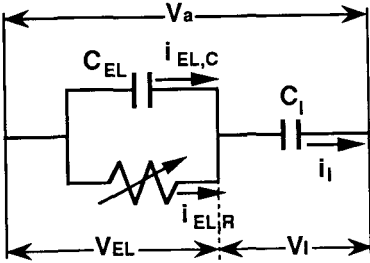
Fig. 25. Equivalent circuit model of double-insulating-layer type ac thin-film EL device
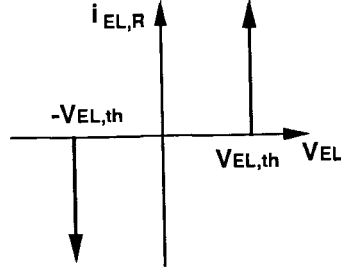
Fig. 26. Ideal I-V characteristics of the non-linear resistor of the phosphor layer

The analysis[12),104)] that follows will first compute the transferred charge density in the resistive branch above the threshold voltage and the energy dissipated per unit area by this charge flow. The final solution will show the dependence of device performance on structure parameters such as layer thickness, dielectric constant, dielectric breakdown strength, threshold field, and luminous efficiency. Even though this model is certainly idealized, all the predicted dependencies are correct, and actual thin-film EL devices can be designed with the help of this model.

First, let us define the symbols for the voltages across the device

$$V_a = V_I + V_{EL} \tag{3}$$

where $V_a$ is the voltage applied to the entire device, $V_I$ is the portion of the voltage that appears across the insulating layers, and $V_{EL}$ is the voltage across the phosphor (usually ZnS) layer. Below the threshold voltage these voltages are capacitively divided such that

$$V_{EL} = \frac{C_I}{C_I + C_{EL}} V_a \tag{4}$$

$$V_I = \frac{C_{EL}}{C_I + C_{EL}} V_a \tag{5}$$

Now suppose we apply the first pulse $P_1$ shown in Fig. 27 and that the magnitude of this pulse is greater than the threshold voltage, $V_{th}$.

Initially the voltage across the layer is divided capacitively as given in Eqs. (4) and (5), so that

$$V_{EL,i1} = \frac{C_I}{C_I + C_{EL}} V_a \tag{4a}$$

$$V_{I,i1} = \frac{C_{EL}}{C_I + C_{EL}} V_a \tag{5a}$$
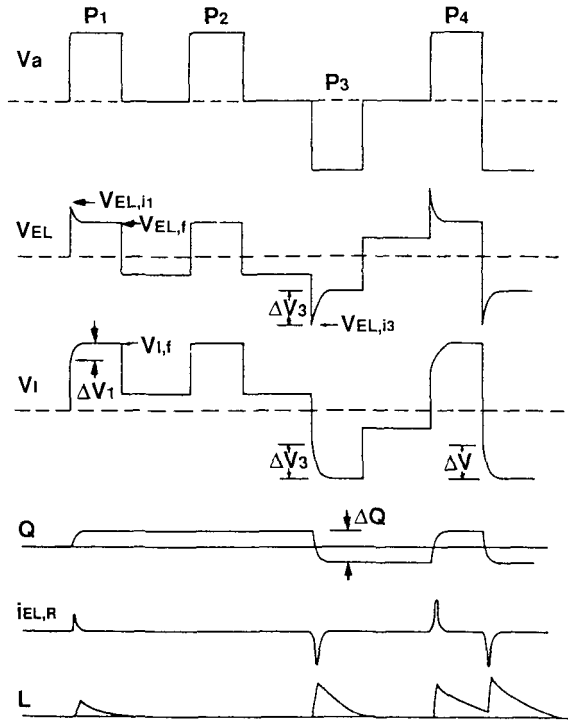
Fig. 27. Wave forms indicating a particular pulse excitation voltage sequence $V_a$, and the resulting changes in phosphor-layer voltage $V_{EL}$, insulating-layer voltage $V_I$, charge density Q, transferred charge density $\Delta Q$, dissipative current $i_{EL,R}$ and EL emission L in a double-insulating-layer type ac thin-film EL device (Ref. 12)

But now the resistive branch turns on and current flows (with accompanying light emission) to discharge the voltage across the phosphor capacitor back to the threshold level. At the same time the resistive branch must supply current to charge up the insulating layer capacitor by an equal voltage increment in order to maintain a constant voltage across the device. Thus we obtain

$$i_{EL,R} = i_I - i_{EL,C} \tag{6}$$

where $i_{EL,R}$ is the current of resistive part of the phosphor layer, $i_{EL,C}$ is the current of capacitive part of the phosphor layer, and $i_I$ is the current in the insulating layer. The final voltage values are

$$V_{EL,f} = V_{EL,th} = \frac{C_I}{C_I + C_{EL}} V_{th} \qquad (7)$$

$$V_{I,f} = V_a - V_{EL,f} = \frac{C_{EL}}{C_I + C_{EL}} V_{th} \qquad (8)$$

The voltage transferred $\Delta V_1$ from the phosphor layer to the insulating layer is given by

$$\begin{aligned} \Delta V_1 &= V_{EL,i} - V_{EL,f} = V_{I,f} - V_{I,i} \\ &= V_{EL,i} - V_{EL,th} \end{aligned} \qquad (9)$$

Or, in terms of the threshold voltage $V_{th}$

$$\Delta V_1 = \frac{C_I}{C_I + C_{EL}} (V_a - V_{th}) \qquad (10)$$

The corresponding transferred charge per unit area, $\Delta Q_1$, that flows in effecting the voltage transfer from the phosphor layer to the insulating layer is given by

$$\Delta Q_I = C_I(\Delta V_1) \qquad (11)$$

$$\Delta Q_{EL,C} = C_{EL}(-\Delta V_1) \qquad (12)$$

$$\begin{aligned} \Delta Q_1 = \Delta Q_{EL,R} &= \Delta Q_I - \Delta Q_{EL,C} \\ &= (C_I + C_{EL})\Delta V_1 \end{aligned} \qquad (13)$$

which leads to the final expression

$$\Delta Q_1 = C_I(V_a - V_{th}) = \int_0^\infty dt i_{EL,R} \qquad (14)$$

Equation 14 thus relates the internal real charge flow to the externally applied voltage and the insulating layer capacitance per unit area. This charge is transferred to the interface between the phosphor layer and the insulating layer and generates an internal electric field which cancels enough of the externally applied field to reduce the electric field in the phosphor layer, $E_{EL}$, to the threshold value, $E_{EL,th}$.

When a second pulse of the same amplitude and polarity, pulse $P_2$, is applied, the initial voltage across the phosphor layer this time is

$$V_{EL,i2} = V_a - V_{I(previous)} = V_a - (V_a - V_{EL,th}) = V_{EL,th} \qquad (15)$$

Thus, no conduction takes place and no light is emitted. The corresponding wave forms for these two pulses are shown in Fig. 27.

Now let us consider what happens when a pulse of the same amplitude and opposite polarity, pulse $P_3$ in Fig. 27, is applied and the stored charge at the interface has not

decayed. Initially both the externally applied electric field and the field from the stored charge add to produce an internal field that is larger than the field associated with the first pulse. Thus more real charge must flow to discharge the voltage across the phosphor layer down to the threshold level. Therefore, the initial and final voltages across the phosphor layer are

$$V_{EL,i3} = \frac{\Delta Q_1}{C_I + C_{EL}} + \frac{C_I}{C_I + C_{EL}} V_a \tag{16}$$

$$V_{EL,f} = V_{EL,th} = \frac{C_I}{C_I + C_{EL}} V_{th} \tag{17}$$

and the transferred voltage for the pulse $P_3$, $\Delta V_3$, is given by

$$\Delta V_3 = 2 \frac{C_I}{C_I + C_{EL}} (V_a - V_{th}) \tag{18}$$

or twice the value for the first pulse. The corresponding transferred charge density $\Delta Q_3$ is given by

$$\Delta Q_3 = 2 C_I (V_a - V_{th}) \tag{19}$$

Succeeding pulses of alternating polarity will also transfer this amount of voltage and charge density. In the steady state, the interface charge density at the end of a voltage pulse is one-half the transferred charge density: one-half the transferred charge neutralizes the previous interface charge, and the remaining half replaces it with an equal amount of opposite polarity. For a steady-state pulse-wave excitation, then, the transferred voltage $\Delta V$ and transferred charge density $\Delta Q$ are given by

$$\Delta V = 2 \frac{C_I}{C_I + C_{EL}} (V_a - V_{th}) \tag{20}$$

$$\Delta Q = 2 C_I (V_a - V_{th}) \tag{21}$$

Next let us calculate the work done per unit area and power consumption (input power) per unit area in this model. To first approximation all real charge is transported across the phosphor layer of thickness $d_{EL}$ at the threshold field, $E_{EL,th}$. Thus the work done per unit area, W, is given by

$$W = 2 C_I (V_a - V_{th}) E_{EL,th} d_{EL} = 2 C_I (V_a - V_{th}) V_{EL,th} \tag{22}$$

Since this transport occurs twice a cycle, the power consumption per unit area, or input power density into an EL device, $P_{in}$, is given by

$$P_{in} = 4 f C_I (V_a - V_{th}) V_{EL,th} \tag{23}$$

The luminance is then computed by multiplying Eq. 23 by the experimentally determined luminous efficiency, $\eta$ as

$$L = \frac{1}{\pi}\eta P_{in} = \frac{4}{\pi}\eta f C_I (V_a - V_{th}) V_{EL,th} \tag{24}$$

Here $\pi$ in the denominator comes from the assumption of perfectly diffusive surface of EL device. (Details of this formulation are given in Section 4.3.) The above equation for luminance assumes a number of simplifications. The luminous efficiency is assumed to be independent of the electric field and phosphor thickness. Experimentally, luminous efficiency does increase with thickness at least over a limited range of thickness, as shown in Fig. 19. It also assumes that all charge is transferred at $V_{EL,th}$, when, in fact, charge will flow at higher voltages, depending on the voltage rise time.

Let us now use Eqs. 23 and 24 along with some typical parameters to calculate the device power consumption and luminance. As a typical example, let us calculate the power consumption per unit area (input power density) of a 10-inch diagonal 640x480 pixel (VGA) thin-film EL display panel with a pixel size of 0.022 cm x 0.022 cm and the following parameters.

$$f = 60 Hz$$
$$C_I = 18 nF / cm^2$$
$$V_a - V_{th} = 40V$$
$$V_{EL,th} = 90V$$

This yields

$$P_{in} = 4 \times 60 \times 18 nF / cm^2 \times 40 \times 90 = 15.5 mW / cm^2 = 155 W / m^2 \tag{25}$$

The area of the display is given by

$$640 \times 480 \times (0.022)^2 cm^2 = 148.7 cm^2 \tag{26}$$

Thus we obtain the total power consumption of the EL panel

$$P(100\%) = 2.30W$$
$$P(50\%) = 1.15W \tag{27}$$

Here 100% means all the pixels are on. As one can see, the power actually consumed to produce light with this technology is quite modest. On the other hand, addressing power consumption from the drive circuits is quite large with a typical value of 10 W (See Section 8.1).

The luminance can be obtained by substituting a typical luminous efficiency value of 2.5 lm/W into Eq. 24

$$L = \frac{1}{\pi}\eta P_{in} = \frac{2.5 \times 155}{3.14} = 123.4 cd / m^2 \tag{28}$$

This result is independent of panel size as long as the panel is refreshed at 60 Hz.

Now we rewrite Eq. 24 in a form that directly shows how the structure parameters influence device performance. Using the relationships

$$C_I = \frac{\varepsilon_0 \varepsilon_I}{d_I} \tag{29}$$

$$V_{EL,th} = E_{EL,th} d_{EL,th} \tag{30}$$

where $\varepsilon_0$ is the dielectric constant of the vacuum and $\varepsilon_I$ is the relative dielectric constant of insulating layer material. Then Eq. 24 becomes

$$L = \frac{4}{\pi} \eta f \varepsilon_0 \varepsilon_I \left( \frac{d_{EL}}{d_I} \right) E_{EL,th} (V_a - V_{th}) \tag{31}$$

Thus in order to optimize the luminance of the EL device with a constant modulation voltage ($V_a$-$V_{th}$), the relative thickness of the phosphor layer to the insulating layer should be maximized and the insulating layer should have a high dielectric constant. The remainder of the terms in the equation are essentially constant. If one is willing to increase the modulation voltage, $V_a$-$V_{th}$, the luminance can be increased further. However, this has two practical limitations. First the major component of the power consumption increases as the square of modulation voltage. Second the dielectric breakdown of the insulating layer places a reliability limit on this voltage. To see this we rewrite Eq. 14 using Eq. 13

$$V_a - V_{th} = \frac{\Delta Q_I - \Delta Q_{EL,C}}{C_I} \tag{32}$$

which states that all the voltage above threshold is transferred to the insulating layer. Thus the maximum voltage excursion is limited by the dielectric breakdown electric field of the insulating layer, $E_{BD}$, or alternately its maximum charge density capacity, $\Delta Q_{max}$, which is equal to $\varepsilon_0 \varepsilon_I E_{BD}$. This term was first introduced by Howard[29]. The $\Delta Q_{EL,C}$ is the charge on the phosphor layer at the threshold. Thus Eq. 31 becomes

$$L = \frac{4}{\pi} \eta f d_{EL} E_{EL,th} (\Delta Q_I - \Delta Q_{EL.C}) \tag{33}$$

In this form it is obvious that the luminance increases with the phosphor layer thickness to a level which is only limited by the insulating layer charge density capacity. Experimentally this has been shown to be the case (Fig. 19).

However, the form of Eq. 31 is preferred since it explicitly shows the influence of the insulating layer capacity and the modulation voltage is limited by power consumption considerations.

As stated above, the ideal model shown in Figs. 25 and 26 accounts for most of the observed thin-film EL device characteristics and can be used in quantitative calculations to predict device performance. However, there is one aspect of device performance not accurately presented by this simple ideal model and that is the time dependence of the

charge transport. For this analysis, an improved equivalent circuit model was proposed by Davidson *et al.*[126),127)] and subsequently Douglas and Wager[128)-131)] at Oregon State University. The Davidson's equivalent model includes insulator and phosphor resistances, $R_{I1}$, $R_{I2}$, $R_{EL}$, and a resistor, $R_D$, in series with the back-to-back diodes, $D_1$ and $D_2$, as a fitting parameter to C-V curves. Douglas and Wager refined this model by adding a parallel resistor-capacitor combination, $C_T$ and $R_T$, in series with the back-to-back diodes $D_1$ and $D_2$ and the resistor $R_D$, as shown in Fig. 28, to accurately describe the wave-form dependence of the turn-on voltage and measured charge, in particular relaxation charge trends. Here the additional $C_T$ and $R_T$ components represent the density of states and the time response for the interface states. The model was proposed in analogy to the modeling done for the interface states of a MOS device. Preliminary work indicates that this model significantly improves the representation of the time response of a thin-film EL device over the basic model shown in Figs. 25 and 26.
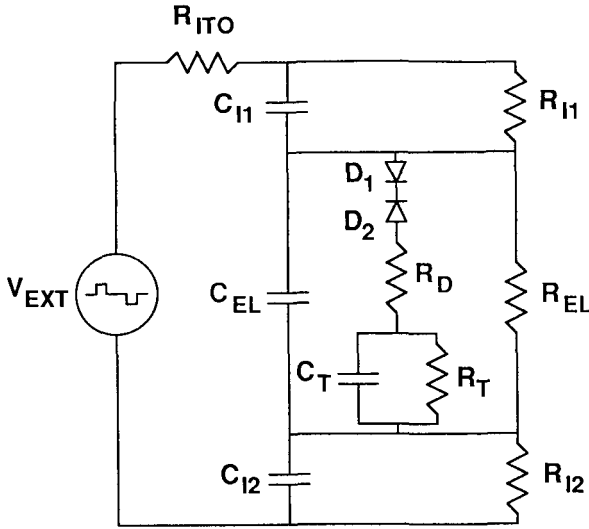


Fig. 28. Improved equivalent circuit model of double-insulating-layer type ac thin-film EL devices (Refs. 128, 129 and 131)

### 4.3. Estimation Methods of Luminous Efficiency

To calculate a luminous efficiency $\eta$ [lm/W], luminance L [cd/m$^2$] and input power density into an EL device, $P_{in}$ [W/m$^2$], must be measured because $\eta$ is expressed in terms of L and $P_{in}$ as

$$\eta[lm/W] = \pi \times \frac{L[cd/m^2]}{P_{in}[W/m^2]} \tag{34}$$

Here a perfectly diffusive EL emission surface is assumed. The derivation of Eq. 34 is as follows. Although the luminance L is usually measured only in the direction normal to the EL emission surface, we need a solid-angle-dependent luminance $L(\omega)$ shown in Fig. 29 in order to estimate all the emission strength.
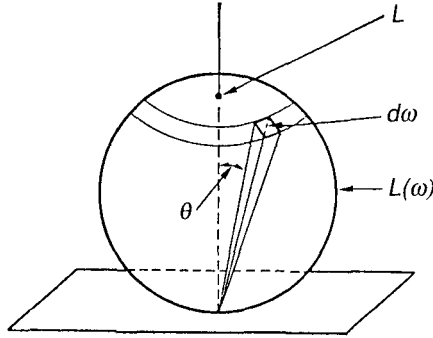


Fig. 29. Definition of solid-angle-dependent luminance $L(\omega)$

Assuming a perfectly diffusive EL emission surface, which is experimentally confirmed to a good approximation, $L(\omega)$ is given by

$$L(\omega) = L\cos\theta \qquad (35)$$

The luminous efficiency $\eta$ [lm/W] is defined by the integral given by

$$\eta[\text{lm/W}] = \int \ d\omega \frac{L(\omega)}{L} \times \frac{L[\text{cd/m}^2]}{P_{in}[\text{W/m}^2]} \qquad (36)$$

Inserting Eq. 35, we find

$$\int \ d\omega \frac{L(\omega)}{L} = \int_0^{2\pi}\int_0^{\pi} d\phi d\theta \sin\theta\cos\theta = \pi \qquad (37)$$

which leads to Eq. 34.

An estimation method of input power density $P_{in}$ is described by Smith[76], Ono *et al.*[105] and Tiku and Smith[132], based on the Sawyer-Tower circuit shown in Fig. 30. Here a sinusoidal-wave drive condition is employed, and $C_t$ is the total capacitance per unit area of the EL device given by

$$C_t = \frac{C_I C_{EL}}{C_I + C_{EL}} \qquad (38)$$

and $C_s$ is the capacitance of sense capacitor. A schematic charge density versus voltage (Q-V) diagram is shown on an oscilloscope, where charge density Q is given by $C_s V_y/A$,

where $V_y$ is the partial voltage of the sense capacitor and A is the pixel area of the EL device. In order that $V_y$ be much smaller than the total voltage V, the condition $C_tA/C_s \ll 1$ must be satisfied. Under this condition accurate Q-V diagrams can be obtained.
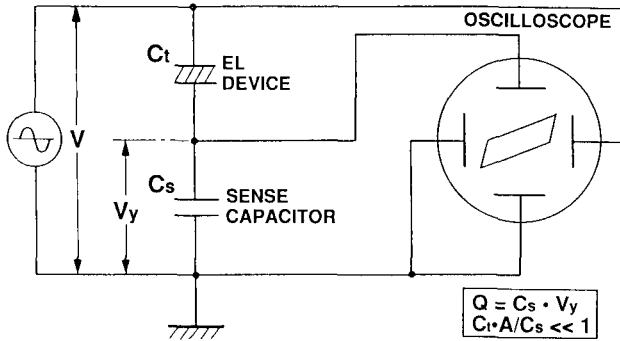


Fig. 30. Charge density vs. voltage (Q-V) characteristic measuring circuit based on Sawyer-Tower circuit (Ref. 105)

As indicated in Section 4.1, below the threshold voltage the EL device can be considered as being a series of capacitors. Then, the Sawyer-Tower circuit acts as a simple capacitive voltage divider, and the Q-V diagram is given by the straight line passing through the origin with a slope $C_t$ given by

$$Q = C_t V \qquad\qquad (39)$$

Above the threshold voltage, a Q-V diagram is represented by a parallelogram[105], as shown in Fig. 31. As the voltage increases from $V_{th}$, the parallelogram spreads out equally from the $Q = C_t V$ straight line. The slope of two sides of the parallelogram crossing the ordinate is given by $C_t$, and that of the remaining sides in the high-voltage region is given by $C_l$, the capacitance per unit area of the insulating layers taken alone. The threshold voltage $V_{th}$ and the threshold charge density $Q_{th}$ can be determined from the point of intersection of two straight lines: the $Q = C_t V$ straight line below the threshold voltage and the straight line in the high-voltage part of the Q-V parallelogram. The equation of the latter straight line in the first quadrant corresponding to EL emission is given by

$$Q - Q_{th} = C_l(V - V_{th}) \qquad\qquad (40)$$

$$Q_{th} = C_t V_{th} \qquad\qquad (41)$$

From these equations, we find

$$Q = C_l(V - V_{EL,th}) \qquad\qquad (42)$$

with

$$V_{EL,th} = \frac{C_I}{C_I + C_{EL}} V_{th}$$

(43)

Figure 31 shows the definitions of the threshold voltage of the whole EL pixel, $V_{th}$, the threshold voltage of the phosphor layer, $V_{EL,th}$, the threshold charge density $Q_{th}$, the transferred charge density $\Delta Q$, and the charge density remaining in the EL pixel, $Q'$, when external voltage becomes 0 V.
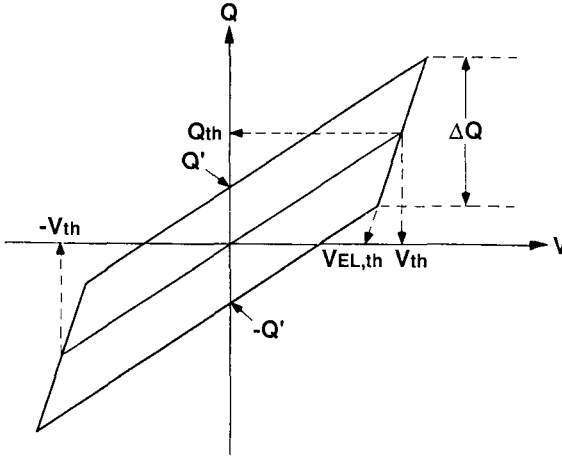


Fig. 31. Charge density vs. voltage (Q-V) characteristic diagram with definitions of physical quantities: $V_{th}$ is the threshold voltage of the EL device; $V_{EL,th}$, the threshold voltage of the phosphor layer; $Q_{th}$, the threshold charge density; $\Delta Q$, the transferred charge density; $Q'$, the remaining charge density in the EL device when V is 0 (Ref. 105)

The area encompassed within the Q-V diagram gives the energy density delivered to an EL pixel per cycle, $E_{in}$, i.e., input power density per cycle. Therefore, the input power density delivered to the EL pixel, $P_{in}$, is just this area times the drive frequency. Assuming a parallelogram form for Q-V diagram, $E_{in}$ and $P_{in}$ are given by

$$E_{in} = 2 \times V_{EL,th} \times \Delta Q = 4 \times V_{th} \times Q'$$

(44)

$$P_{in} = f \times E_{in} = 2 \times f \times V_{EL,th} \times \Delta Q = 4 \times f \times V_{th} \times Q'$$

(45)

When a Q-V diagram cannot be approximated by a parallelogram, $E_{in}$ and $P_{in}$ must be evaluated numerically, for example, using a wave memory and a personal computer[105].

Since luminance depends on the drive frequency and drive wave forms, it is recommended that the frequency and drive wave form be indicated when luminance values are discussed. Recommended drive wave forms are sinusoidal waves and pulse waves of alternate polarity with frequencies of 50 or 60 Hz, or 1 kHz. Furthermore, voltage should be indicated in zero-to-peak values, rather than the rms (root-mean-square) values, since luminance depends on the peak voltage values.

## 4.4. Recommended Standard Measuring and Evaluation Methods of EL Device Characteristics

As indicated in the discussions of Section 4.3, it is evident that a luminance of the thin-film EL devices depends on drive voltage, drive wave forms and drive frequency. Therefore, it is desirable to explicitly quote these conditions in comparing luminance values reported from different institutions. For this purpose, the 125th Research Committee on Mutual Conversion between Light and Electricity, Japan Society for the Promotion of Science set up an EL Subcommittee to discuss the details of the measuring and evaluation methods of thin-film EL device characteristics. The following is the translation of the report[106] of the EL subcommittee, entitled as the recommended standard measuring and evaluation methods of EL device characteristics.

### 4.4.1. Introduction

Electroluminescent device characteristics, such as luminance, threshold voltage, luminous efficiency, contrast ratio and lifetime, depend strongly on the measuring conditions and drive methods. In order to properly compare the values for the EL characteristics it is desirable to set common and standard measuring conditions. In the following the recommended standard measuring and evaluation methods are detailed. Since these methods are primarily for ac thin-film EL devices, proper extension measures should be taken for the analysis of EL device characteristics of dc thin-film, ac powder and dc powder EL devices
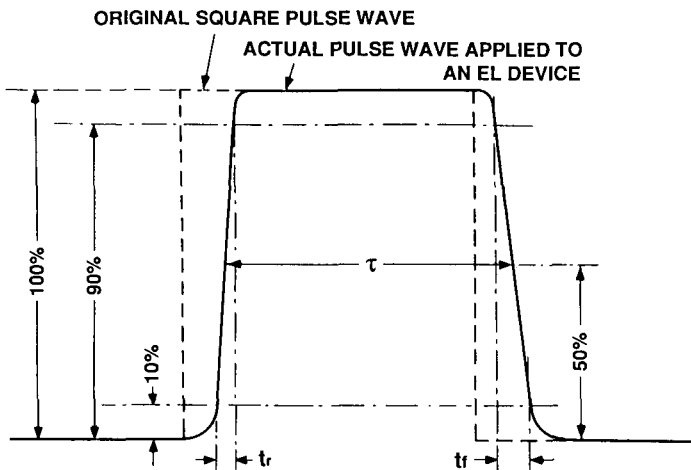


Fig. 32. Definitions of pulse width $\tau$, rise time $t_r$ and fall time $t_f$ of the actual pulse drive wave form applied to an EL device (Ref. 106)

### 4.4.2. Drive Wave Forms

Recommended drive wave forms are sinusoidal waves and square pulse waves of alternate polarity with frequencies of 50 or 60 Hz, or 1 kHz. Furthermore, voltage values should be indicated in zero-to-peak values ($V_{0p}$), rather than in rms (root-mean-square) values, since luminance depends on the peak voltage value. When square pulse waves of

alternate polarity are used for driving, the following parameters should be specified as defined in Fig. 32. The pulse width is defined by the full width at the half maximum of the actual (deformed) pulse drive wave form applied to an EL device, and the rise time $t_r$ and the fall time $t_f$ are defined by the time period corresponding to 10%-to-90% value and 90%-to-10% value, respectively, of the actual voltage. The recommended values for practical applications are $\tau = 40$ μs, $t_r \leq 8$ μs and $t_f \leq 8$ μs.

### 4.4.3. Threshold Voltage $V_{th}$ and Luminance L

By imposing the recommended drive wave forms described above to an EL cell, luminance is measured by a photometer. Here luminance is a photometric term indicating the radiated power in terms of human eye sensitivity, i.e. a physical measure of luminous intensity per unit area, in units of cd/m². Other unit of luminance often used in the literature is foot-Lambert (abbreviated as fL or ft-L) defined by

$$1fL = \frac{1}{\pi} \times \frac{cd}{(ft)^2} = 3.426 cd/m^2 \tag{46}$$

(1) Threshold Voltage $V_{th}$

The threshold voltage $V_{th}$ is defined as the voltage corresponding to the luminance of 1 cd/m².

Another way of defining the threshold voltage is based on the charge density vs. voltage (Q-V) curve obtained by using the Sawyer-Tower circuit. As discussed in Section 4.3, the threshold voltage $V_{th}$ is defined by the voltage corresponding to the threshold charge density $Q_{th}$, i.e., the kink point of the Q-V curve (Fig. 31). This threshold voltage corresponds to the start of the electric field clamp effect in the phosphor layer.

(2) Luminance L

Figure 33 shows a schematic luminance-voltage (L-V) curve for the definition of modulation-voltage-specified luminance values. The drive voltage V is expressed by the sum of the threshold voltage $V_{th}$ and the modulation voltage $V_M$. When reporting luminance, the values for the modulation voltage should be explicitly indicated: $L_{V_M}$ is the luminance at $V_M$ volts above the threshold voltage. For example, $L_{15}$, $L_{30}$ and $L_{60}$ are shown in Fig. 33. In practical EL panels, the modulation voltage $V_M$ is usually set between 30 and 60 V.

In order to properly compare luminance data measured at different institutions, the following experimental parameters should be presented together with the luminance value.

(a) Drive wave forms including the pulse width τ, rise time $t_r$ and
   fall time $t_f$ for pulse wave drive
(b) Drive frequency f
(c) Ambient temperature $T_a$
(d) Phosphor layer thickness $d_{EL}$

In addition, luminance L should be used instead of brightness B which was often used in the literature. Here we refer to the definitions of luminance and brightness given in McGraw-Hill Dictionary of Scientific and Technical Terms, Third Edition.

Luminance :  The ratio of the luminous intensity in a given direction of an
                  infinitesimal elements of a surface containing the point under
                  consideration, to the orthogonally projected area of the element
                  on a plane perpendicular to the given direction.
                  Formerly known as brightness.

Brightness :   The characteristic of light that gives a visual sensation of more
                or less light
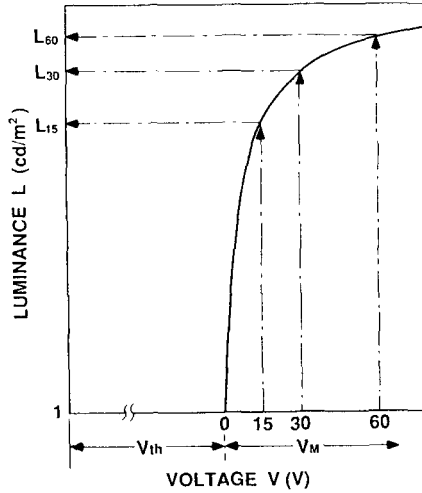


Fig. 33. Definition of modulation-voltage-specified luminance. The drive voltage V is expressed by the sum of the threshold voltage $V_{th}$ and the modulation voltage $V_M$ (Ref. 106)

### 4.4.4. Luminous Efficiency $\eta[lm/W]$ and Power Efficacy $\eta[W/W, \%]$

The input power density $P_{in}[W/m^2]$ and luminance $L[cd/m^2]$ must be measured for the estimation of luminous efficiency $\eta[lm/W]$. The input power density to an EL cell can be estimated from the charge density vs. voltage (Q-V) diagram shown for the sinusoidal wave drive in Fig. 31. As discussed in Section 4.3, by assuming a parallelogram form for the Q-V diagram, the input power density $P_{in}$ is given by

$$P_{in} = f \times area\ of\ the\ parallelogram$$
$$= 2 \times f \times V_{EL,th} \times \Delta Q = 4 \times f \times V_{th} \times Q' \qquad (47)$$

with

$$V_{EL,th} = \frac{C_I}{C_I + C_{EL}} V_{th} \qquad (48)$$

Here, $V_{EL,th}$ is the threshold voltage of the phosphor layer, $\Delta Q$ is the transferred charge density in the phosphor layer, $V_{th}$ is the threshold voltage of the EL device, and $Q'$ is the remaining charge density in the EL device when the external drive voltage is set to 0 V. Using the measured values for $V_{EL,th}$, $\Delta Q$, $V_{th}$ and $Q'$, the input power density is obtained. For the square pulse wave drive case, $V_{th}$ and $Q'$ can be measured using the Sawyer-Tower circuit in a similar way. However, the Q-V diagram is no longer

approximated by a parallelogram, so that a numerical evaluation of $P_{in}$ is necessary, for example, by using a wave memory and a personal computer[105].

There are other methods to obtain input power density using a wave-memory, where wave-form data of voltage and current in one cycle are stored. Performing the Fourier transform of these wave-form data, the input power density is evaluated from the following equation

$$P_{in} = \sum_n V_n I_n \cos \phi_n / A \tag{49}$$

where $V_n$, $I_n$, and $\phi_n$ are the amplitudes of voltage, current and phase difference between $V_n$ and $I_n$, respectively, in each Fourier component, and A is the pixel area of EL device. Another way of estimating $P_{in}$ using wave memory is directly integrating over one period of operation T

$$P_{in} = \frac{1}{T} \int_0^T dt VI / A \tag{50}$$

Once the input power density $P_{in}$ [W/m$^2$] and luminance L[cd/m$^2$] are obtained, the luminous efficiency $\eta$[lm/W] can be estimated from the following equation under the assumption of a perfectly diffuse EL emission surface:

$$\eta[lm/W] = \pi \times \frac{L[cd/m^2]}{P_{in}[W/m^2]} \tag{51}$$

Since the luminous efficiency depends on the drive voltage, the modulation voltage $V_M$ should be explicitly indicated just like the case for luminance: $\eta_{V_M}$ is the luminous efficiency measured at $V_M$ volts above the threshold voltage. Examples are $\eta_{15}$ and $\eta_{30}$. In addition, $\eta_{max}$ is also used to indicate the maximum luminous efficiency.

On the other hand, power efficacy $\eta$[W/W, %] is estimated from luminance and emission spectrum data, and is expressed in units of W/W or %.

When reporting the luminous efficiency data, the following items should be explicitly indicated.

(a) Measuring method of input power density $P_{in}$
(b) Modulation-voltage-specified luminous efficiency, such as $\eta_{15}$, $\eta_{30}$, or $\eta_{max}$
(c) Ambient temperature $T_a$

### 4.4.5. CIE Color Coordinates x and y

Any color sensation can be reproduced by the judicious combination of three monochromatic components. The Commission Internationale de l'Eclairage (CIE) has adopted a standard colorimetry which represents the attributes of color by a three-dimensional diagram. The Cartesian vectors of this tridimensional diagram are derived from spectral tristimulus values, $\bar{x}(\lambda)$, $\bar{y}(\lambda)$ and $\bar{z}(\lambda)$, shown in Fig. 34. The curve $\bar{y}(\lambda)$, which is equal to the photopic response of the eye, is normalized at a peak at 550 nm.

The CIE color coordinates, x, y and z, are defined by the ratios:

$$x = \frac{X}{X+Y+Z}$$
$$y = \frac{Y}{X+Y+Z}$$
$$z = \frac{Z}{X+Y+Z} \tag{52}$$

where X, Y and Z are calculated by the following integrations over the entire visible spectrum

$$X = \int d\lambda \phi(\lambda)\bar{x}(\lambda)$$

$$Y = \int d\lambda \phi(\lambda)\bar{y}(\lambda)$$

$$Z = \int d\lambda \phi(\lambda)\bar{z}(\lambda) \tag{53}$$

Here $\phi(\lambda)$ is the EL emission spectrum of interest.
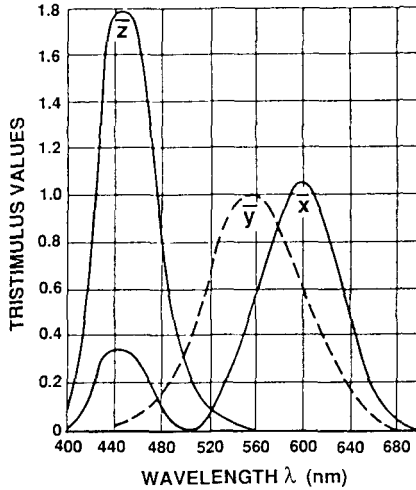


Fig. 34. CIE standard color mixture curves for x(λ), y(λ) and z(λ)

Since the sum of x, y and z is unity, it is sufficient to identify only x and y to automatically imply z. In other word, the color map may be expressed as a two-dimensional projection into the xy plane. This is the standard CIE chromaticity diagram shown in Fig. 35. The upper arc is the locus of saturated colors. All the colors and shades that the eye can resolve are enclosed between the area of saturated colors and the straight line labeled "magenta." The central region appears white. A black body assumes at

different temperatures various shades of whiteness as shown by the arc labeled "black body locus." Regions of three primary colors, red, green and blue, are specified by RED, GREEN and BLUE, respectively.

CIE color coordinates x and y can be calculated using Eqs. 52 and 53 from the emission spectrum data measured by a photometer. Data for x and y are plotted in the chromaticity diagram shown in Fig. 35.
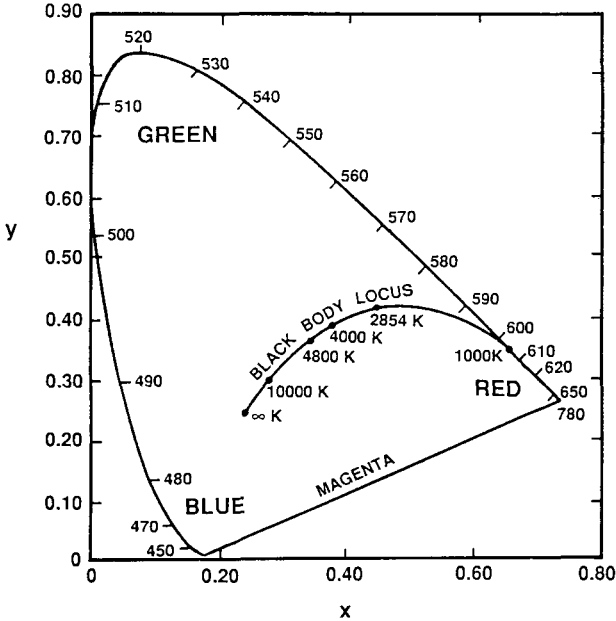


Fig. 35. CIE chromaticity diagram with regions of three primary colors indicated

### 4.4.6. Contrast Ratio CR

A light is emitted to the EL device at an angle $\theta$ from the normal direction to the device surface, and luminance in the direction normal to the EL device surface is measured. At the same time, illuminance in units of lux on the EL device surface is measured. Recommended angle of incident light is 45°. A contrast ratio is defined by the luminance ratio of emitted pixel to non-emitted pixel.

When reporting the contrast ratio data, the following items should be explicitly indicated.

(a) Ambient illuminance in units of lux at the EL device surface
(b) Angle of incident light, $\theta$
(c) Luminance value

## 4.4.7. Lifetime

The luminance after completing the annealing process is defined as the initial luminance. An EL device is driven at a constant voltage $(V_{th}+V_M)$ with a recommended drive wave form, and the luminance is measured. The life time, or half life, is defined by the elapsed time until the luminance becomes 50% of the initial luminance.

When reporting the life-time data, the following items should be explicitly indicated.

(a) Drive conditions including drive frequency f, initial threshold voltage $V_{th}$, modulation voltage $V_M$, and drive voltage wave form

(b) Ambient temperature $T_a$

(c) Ambient humidity

## 4.4.8. Dielectric Breakdown Strength or Dielectric Breakdown Electric Field $E_{BD}$

By increasing the drive voltage, the dielectric breakdown strength or dielectric breakdown electric field $E_{BD}$ is measured, which is defined by the electric field when a dielectric breakdown occurs in the EL device and EL emission is no longer observable. Since dielectric breakdown is a stochastic process, accumulation of a large number of events is desirable and average values should be used.

When reporting the dielectric breakdown strength data, the following items should be explicitly indicated.

(a) Drive wave forms including pulse width $\tau$, rise time $t_r$ and fall time $t_f$

(b) Drive frequency f

(c) Ambient temperature $T_a$

(d) Ambient humidity

(e) Threshold voltage $V_{th}$

## 4.5. Physical and Chemical Properties of Phosphor Host Materials and Luminescent Centers

All phosphors consist of a host material and a light-emitting dopant called an activator or a luminescent center. The classical thin-film EL phosphor uses ZnS for the host material and the Mn atom for the light emitting dopant. We discuss the general characteristics that these materials must possess to form an efficient phosphor system[13],[38],[52],[53],[56]. Detailed discussion on the materials that have been found to form useful thin-film EL phosphors are given in Chapter 7.

In order to be an efficient thin-film EL phosphor, the host material should have the best possible crystalline order to allow electron acceleration to a kinetic energy sufficient for impact excitation. In order for the luminescent center (activator) atoms to emit light efficiently, they should be incorporated into a substitutional lattice site, otherwise the excited center will lose its energy non-radiatively to a nearby lattice defect. Finally, it should be noted that the typical dopant concentration of luminescent centers in a thin-film EL phosphors is on the order of one percent. This level is several orders of magnitude larger than that found in semiconductor transistor devices. In order to maintain the required good crystallinity at these dopant levels, it is emphasized that the need to match both the geometric size and the valence of the host cation with that of the dopant[52]. If there is a geometric mismatch, the dopant atoms will have to fit into a less efficient interstitial site and if there is a valence mismatch, this will have to be compensated by an additional co-activator ion.

With these concepts in mind, let us discuss the requirements for phosphor host materials and luminescent centers (activators) in detail.

## 4.5.1. Phosphor Host Materials

Phosphor host materials must satisfy the basic requirement of having a large enough band gap to emit visible light from the doped luminescent centers without significant absorption. Furthermore, they must hold a high electric field of about $10^8$ V/m, which is necessary for EL emission. This limits the class of possible materials to large band gap semiconductors with energy band gap larger than 2.5 eV and insulators. The classical CRT host materials, the II-VI compounds and the rare earth oxides and oxysulfides, were considered to be good thin-film phosphor host materials in the beginning. However, thin-film process technology tends to restrict the set of viable host materials to be a smaller subset, because practical thin-film EL phosphors must resist a maximum process temperature of approximately 550°C, consistent with the glass substrate properties. On the other hand, CRT powder phosphors are usually processed above 1000°C to promote good crystallization. Thus, the more refractory CRT phosphors are not usually good candidates for thin-film EL phosphors.

In addition, EL host materials must have the requirement of providing a medium for the efficient transport of high energy (> 2 eV) electrons. To date, only the wide-gap semiconductors of II-VI compounds have demonstrated this capability; IIb-VIb compounds such as ZnS and IIa-VIb compounds such as CaS and SrS. Empirically, the oxide phosphors with their larger band gaps (> 4.5 eV) do not seem to have the capability to transport significant current densities of hot electrons. Thus the EL phosphor host materials used in today's devices have band gaps in the range of 3 to 4.5 eV. Table 3 summarizes the material parameters of II-VI compound phosphor host materials and Fig. 36 shows band structures of ZnS[133)-135)] and alkaline-earth sulfides CaS[136),137)] and SrS[137),138)].

Table 3  Properties of II-VI compound phosphor host materials (Refs. 52 and 53)

| Item | IIb-VIb compound | IIa-VIb compound | |
|---|---|---|---|
| Material | ZnS | CaS | SrS |
| Melting point (°C) | 1800-1900 | 2400 | >2000 |
| Band gap (eV) | 3.6 | 4.4 | 4.3 |
| Transition type | Direct | Indirect | Indirect |
| Crystal structure | Cubic zinc blende or Hexagonal wurtzite | Rock salt (NaCl type) | Rock salt (NaCl type) |
| Dielectric constant | 8.3 | 9.3 | 9.4 |
| Lattice constant (Å) | 5.409 | 5.697 | 6.019 |
| Ionic radius (Å) | 0.74 | 0.99 | 1.13 |
| Ionicity | 0.623 | >0.785 | >0.785 |

ZnS has the cubic zinc-blende crystal structure when processed at low temperatures or hexagonal wurtzite crystal structure when processed at high temperatures. The band structure is a direct-transition type with both the conduction band bottom and valence band top at Γ point. The band gap energy is 3.6 eV, which is wide enough to pass all the visual spectrum of light, but not so wide as to inhibit the avalanche multiplication process of electrons and thus restrict the number of carriers available for impact excitation of the luminescent centers. The Mn dopant is readily incorporated into the ZnS lattice as its valence and size allow it to go in substitutionally for the Zn atoms. In addition to the yellow emission[38)] of the Mn center in ZnS, the rare earth fluorides also can be used[38)] as luminescent centers in ZnS and emit light that spans the spectrum.
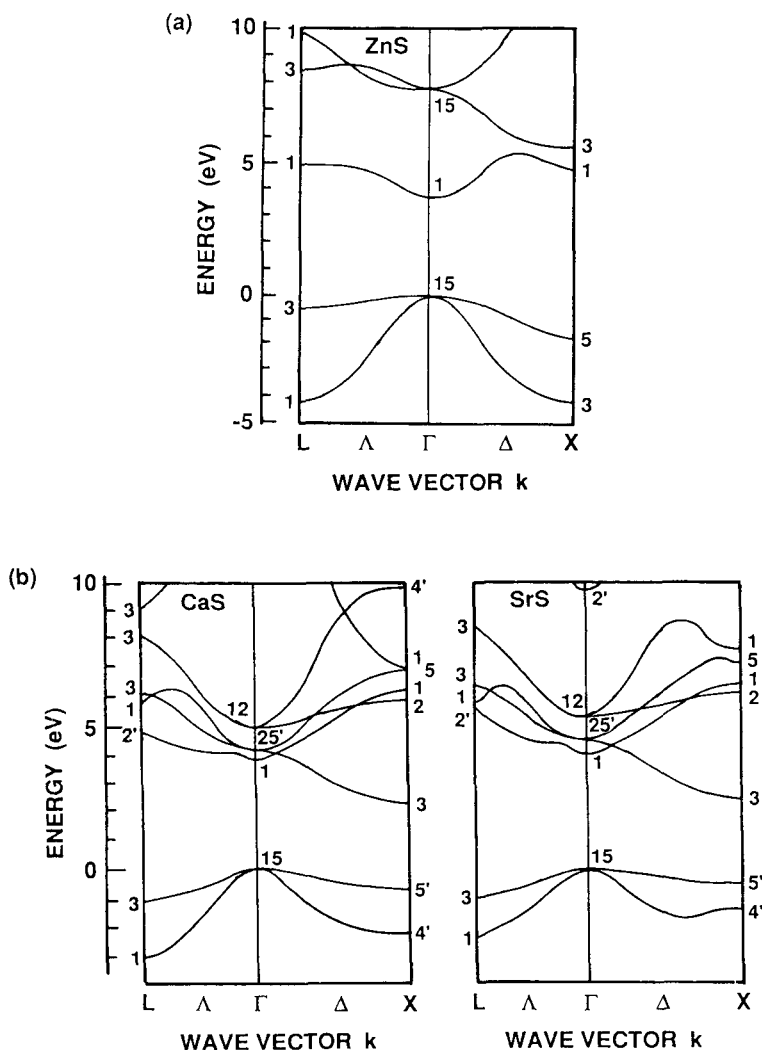
Fig. 36. (a) Band structure of ZnS and (b) band structures of alkaline-earth sulfide CaS and SrS (ZnS: Ref. 134; CaS: Ref. 136 and SrS: Ref. 138)

On the other hand, the more ionic IIa-VIb compounds CaS and SrS have the rocksalt or sodium chloride crystal structure[52),53),56)]. The band structure is an indirect-transition type with the conduction band bottom at X point and valence band top at Γ point. The band gap energies of CaS and SrS are 4.4 and 4.3 eV, respectively. The band gaps are

wide enough to pass all the visible spectrum and to have the high avalanche fields needed for the impact excitation mechanism. The ionic radii of $Ca^{2+}$ and $Sr^{2+}$ are very close to those of rare-earth luminescent center ions (Table 5). Furthermore, their chemical properties are very similar. A processing obstacle for these materials is their refractory nature which means a higher heat treatment is required to promote good crystallization. Nevertheless, these materials are expected to be good candidates for accepting rare-earth ions as luminescent centers, providing an excellent alternative to the classic ZnS host material. However, since these phosphor materials have hygroscopic characteristics, encapsulation is necessary.

Other candidates of phosphor host materials are alkaline-earth thiogallates, $MGa_2S_4$ (M: Ca, Sr or Ba). They were known to be relatively efficient cathodoluminescent phosphors[139] when activated with $Ce^{3+}$ and $Eu^{2+}$. Recently these thiogallates have been successfully applied to thin-film EL devices and bright blue emissions with good color purity have been obtained[4],[140] using $CaGa_2S_4$:Ce, $SrGa_2S_4$:Ce and $BaGa_2S_4$:Ce. Table 4 lists properties of alkaline-earth thiogallates, showing that these thiogallates have band gap energy of 4.1-4.4 eV, comparable to those of the alkaline-earth sulfides. The dielectric constant of these thiogallate compounds is about 15, which is much larger than that of alkaline-earth sulfides or zinc sulfide. In addition, they are less susceptible to hydrolysis than alkaline-earth sulfides.

Table 4  Properties of alkaline-earth thiogallates (Ref. 4)

| Item | $CaGa_2S_4$ | $SrGa_2S_4$ | $BaGa_2S_4$ |
|---|---|---|---|
| Crystal structure | Orthorhombic | Orthorhombic | Cubic |
| Lattice constant (Å) | a=20.09 | a=20.84 | a=12.66 |
|  | b=20.09 | b=20.49 |  |
|  | c=12.11 | c=12.21 |  |
| Melting point (°C) | 1150 | 1200 | 1200 |
| Dielectric constant | 15 | 14 | 15 |
| Band gap (eV) | 4.2 | 4.4 | 4.1 |

### 4.5.2. Luminescent Centers

To be an efficient EL phosphor, the luminescent center must have a large cross section for the impact excitation. In addition, the luminescent center must be stable in the high electric-field environment associated with the electroluminescence phenomenon. Because of this latter requirement, certain classic light emission centers, which have excellent performance when excited by an electron beam in a CRT, have very poor performance when used as a thin-film EL phosphor. The best example of this is the poor thin-film EL performance of the donor-acceptor center associated with the copper doping of ZnS, whereas this same center is the activator in the efficient green CRT phosphor, P1. This is probably due to the fact that the shallow donor and acceptor levels are unstable in high electric fields because electrons can tunnel out of these levels. On the other hand, the Mn levels are very deep. In fact, it has been shown that the electrons never leaves the Mn atom. To date, all efficient thin-film EL luminescent centers are atomic in nature with deep energy levels, i.e., isolated luminescent centers. And transition-metal ions, such as Mn (yellow), and rare-earth ions, such as Tb (green), Sm (red), Eu (red), Ce (blue-green) and Pr (white), are found to be suitable luminescent centers.

The rare-earth ions have an open 4f shell, which is screened by the outer electrons in the $5s^2 5p^6$ closed shells. Therefore, the 4f electrons of rare-earth ions in the host materials are not greatly influenced by crystal fields. Two different types of luminescent transitions can be observed: a parity-forbidden f-f intrashell transition, and the parity-allowed f-d transition. Examples of EL emission due to f-f transition are the green emission from $Tb^{3+}$, red emission from $Sm^{3+}$, blue emission from $Tm^{3+}$, and white emission from $Pr^{3+}$. Both $Eu^{2+}$ and $Ce^{3+}$ produce EL emission due to f-d transitions. The 5d electrons are easily affected by the crystal field. Clearly, then, excited energy levels depend on the host material, and the EL emission color can be varied by changing it.

To effectively dope with transition metals or rare-earth elements, it is very important to match chemical properties and ionic radii between the cations of the host phosphor materials and the luminescent centers. Table 5 compares the ionic radii of host materials ($Zn^{2+}$, $Ca^{2+}$, $Sr^{2+}$) and rare-earth luminescent-center ions. Since rare-earth ions have different valences and ionic radii from those of $Zn^{2+}$, it is difficult to dope them uniformly into the ZnS host at high concentrations. To overcome this difficulty, doping methods featuring the addition of charge compensators[53] or molecular luminescent centers[20],[33] have been proposed, and fluorides or sulfides of these luminescent centers have been used.

Table 5 Ionic radii of host materials and luminescent centers (Ref. 13)

| Ion | Radius (Å) | Ion | Radius (Å) | Ion | Radius (Å) |
|-----|-----------|-----|-----------|-----|-----------|
| $Zn^{2+}$ | 0.74 | $Ce^{3+}$ | 1.034 | $Gd^{3+}$ | 0.938 |
| $Ca^{2+}$ | 0.99 | $Pr^{3+}$ | 1.013 | $Tb^{3+}$ | 0.923 |
| $Sr^{2+}$ | 1.13 | $Nd^{3+}$ | 0.995 | $Dy^{3+}$ | 0.908 |
| $Mn^{2+}$ | 0.80 | $Sm^{3+}$ | 0.964 | $Ho^{3+}$ | 0.894 |
| | | $Eu^{3+}$ | 0.950 | $Er^{3+}$ | 0.881 |
| | | $Eu^{2+}$ | 1.09 | $Tm^{3+}$ | 0.869 |

## 4.6. High-Field Electronic Transport in Thin-Film EL Devices

The operation of ac thin-film EL devices in high-field regime depends on the physics of hot electron transport in the active phosphor layer. The aim of the transport theories is to predict the fraction of carriers which can attain a definite energy, say, the energy required to impact excite a $Mn^{2+}$ ion, 2.12 eV. We note that this energy value of 2.12 eV is the energy of the emitted photon associated with yellow EL emission from $Mn^{2+}$, i.e., the energy difference between the $^4G$ ($^4T_1$) first excited state and the $^6S$ ($^6A_1$) ground state. The actual energy required to excited (optically or electrically) $Mn^{2+}$ from the $^6S$ ($^6A_1$) ground state to the $^4G$ ($^4T_1$) first excited state is a little larger than 2.12 eV. The minimum energy is 2.24 eV corresponding to the zero-phonon line, and significant absorption begins at 2.30-2.34 eV. In the following analysis, however, 2.12 eV is used as a representative value for the required energy to impact-excite $Mn^{2+}$. There are currently two approaches: One is band-structure dependent and often based on Monte Carlo simulation[107]-[112], while the other relies on a mean free path for high-energy electrons determined by energy loss to phonons, known as the lucky-drift model[113]-[117]. Both approaches have been used to elucidate high-field transport in electroluminescent

devices. The Monte Carlo method[141),142)] as applied to semiconductor transport is a simulation of the trajectories of individual carriers as they move through a device under the influence of external forces and subject to random scattering events due to various electron-phonon interactions. The duration of the carrier free flights between successive collisions and the scattering events involved are selected stochastically in accordance with the given transition probabilities describing the microscopic processes. On the other hand, lucky drift approach[143)] was first proposed by Ridley[144)-146)] for semiconductors in general, and a non-local version of this model was applied to ZnS by Ridley and El-Ela[147),148)]. Subsequent analyses by Burt[149)] and coworkers[150),151)] showed that this is an analytical version of Baraff's theory[152)] when applied to impact ionization. Bringuier[113)] used the lucky-drift model to calculate the impact excitation luminescence in ZnS:Mn. He subsequently applied this model to the detailed analysis of high-field electron transport in ZnS-type electroluminescence[114)-117)].

### 4.6.1. Monte Carlo Simulation

Two contradictory views existed regarding high-field transport in ZnS:Mn thin-film EL devices based on Monte Carlo simulation. Brennan[107)] performed an ensemble Monte Carlo simulation of steady-state hot electron transport in bulk ZnS, including a full band structure calculation for the density of states in the first two conduction bands and a treatment of electron-phonon scattering. He concluded that very few carriers are available with sufficient energy to excite Mn luminescent centers in ZnS at a field of $1 \times 10^8$ V/m. This result cannot explain the high luminance and high luminous efficiency of commercial ZnS:Mn EL devices. On the other hand, Mach and Müller[153)] concluded from their Monte Carlo calculations that the electrons in ZnS thin-film EL devices undergo ballistic or loss-free transport, resulting in extremely high-energy electrons. Here, a single, parabolic conduction band was assumed and only polar optical phonon scattering was considered for electron scattering mechanism.

### (1) Non-Parabolic Multivalley Model

Bhattacharyya et al.[108),109)] resolved this apparent contradiction using a more realistic ensemble Monte Carlo simulation of transient and steady-state electron transport in the active ZnS phosphor layer at high electric fields. They used a non-parabolic multivalley model with $\Gamma$, L and X valleys and they considered the electron scatterings due to polar optical phonons, acoustic phonons (through deformation potential coupling), intervalley scattering, ionized impurities and neutral impurities.

In this model, the conduction band is approximated by non-parabolic multivalley ($\Gamma$, L and X) bands, with the dispersion relation

$$\gamma(E) = E(1 + \alpha_n E) = \frac{\hbar^2 k^2}{2m_n^*} \tag{54}$$

where $\alpha_n$ and $m_n^*$ are the nonparabolicity parameter and the effective mass of valley n, respectively, while k is the wave vector. Between the collisions, the crystal momentum changes according to the local field, while the velocity of the particle is given by

$$\mathbf{v} = \frac{1}{\hbar} \frac{\partial E}{\partial \mathbf{k}} \tag{55}$$

The duration of the free flight $t_r$ is given by

$$t_r = -\frac{1}{\Gamma}\ln(r) \tag{56}$$

where r is a random number uniformly distributed between 0 and 1 obtained from the computer random number generator, and the total scattering rate $\Gamma$ is given by

$$\Gamma = \Gamma_{pop} + \Gamma_{ac} + \Gamma_{iv} + \Gamma_{imp} + \Gamma_{self} \tag{57}$$

where $\Gamma_{pop}$, $\Gamma_{ac}$, $\Gamma_{iv}$ and $\Gamma_{imp}$ are the scattering rates due to polar optical phonons, acoustic phonons, intervalley scattering and impurities (both ionized and neutral), respectively. The $\Gamma_{self}$ is the self scattering rate corresponding to a fictitious scattering mechanism that changes with time so that the total rate $\Gamma$ is constant[141]. Self-scattering does not change the carrier momentum and energy, and thus does not affect the carrier's trajectory. Its inclusion is necessary to simplify the random free flight time selection, which is central to the Monte Carlo technique.

Several thousand particles are simulated simultaneously and ensemble analysis are performed to obtain the quantities of interest, such as the energy, velocity and carrier stabilization. The ZnS material parameters used in the Monte Carlo calculation are collected in Tables 6 and 7 after Brennan[107]. Table 6 gives the valley-independent parameters and Table 7 gives the valley-dependent parameters of ZnS.

Table 6  Bulk material parameters of ZnS (Ref. 107)

| Parameter | Value |
|---|---|
| Polar optical-phonon energy (eV) | 0.044 |
| Sound velocity (cm/s) | $5.20 \times 10^5$ |
| Low-frequency dielectric constant | 8.32 |
| High-frequency dielectric constant | 3.60 |
| Mass density (g/cm$^3$) | 4.08 |
| Neutral impurity density (cm$^{-3}$) | $1 \times 10^{20}$ |

Table 7  Valley-dependent parameters of ZnS (Ref. 107)

| Parameter | $\Gamma$ | L | X |
|---|---|---|---|
| Effective mass ($m_n^*/m_0$) | 0.28 | 0.222 | 0.40 |
| Nonparabolicity $\alpha_n$ (eV$^{-1}$) | 0.690 | 0.650 | 0.360 |
| Valley separation (eV) | —— | 1.449 | 1.454 |
| Number of equivalent valleys | 1 | 4 | 3 |

Figure 37 shows the calculated scattering rates[109] for the $\Gamma$ valley at 300 K due to various scattering mechanisms as a function of energy. For the ionized impurity scattering rate calculation, an impurity concentration of $1 \times 10^{19}$/cm$^3$ was used. For electron energies less than about 1.7 eV, polar optical phonon scattering is the dominant scattering

mechanism, whereas above 1.7 eV intervalley scatterings are most important. The $\Gamma$ to X intervalley scattering rate is larger than the $\Gamma$ to L intervalley scattering rate because of the larger X valley effective mass. Acoustic phonon scattering and ionized impurity scattering are of negligible significance in determining the overall scattering rate of heated carriers relevant to ac thin-film EL performance. It is noted that the $\Gamma$ valley scattering rate due to neutral impurities is too small (approximately $10^{11}$/s) to be plotted on Fig. 37, even for a density of $10^{20}$/cm³ (corresponding to an atomic doping concentration of 0.5% in cubic ZnS, which is the approximate Mn concentration), indicating that neutral impurity scattering can be ignored.
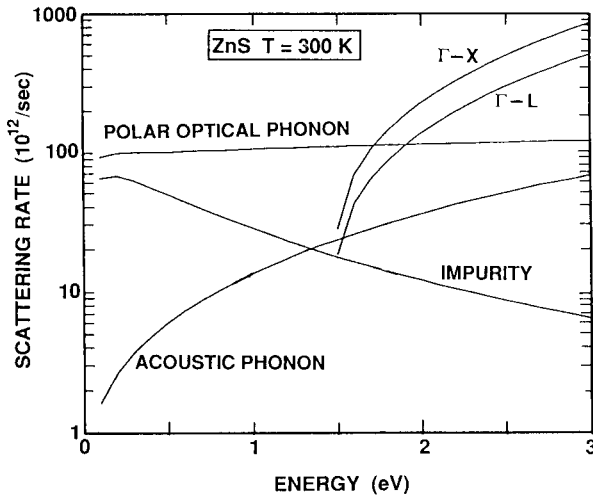


Fig. 37. Calculated scattering rates for the $\Gamma$ valley at 300 K due to various scattering mechanisms as a function of energy (Ref. 109)

When the parabolic bands for the $\Gamma$, X and L valleys were used together with only polar electron-phonon interaction, the ensemble Monte Carlo simulation exhibited electron run away, consistent with ballistic or loss-free transport, at a field $1\times10^7$ V/m and higher, in agreement with the results of Mach and Müller[153]. However, when conduction-band nonparabolicity and the non-polar electron-phonon interaction were included in the Monte Carlo simulation, electron run away was no longer observed and electron distribution became stable, i.e., non-polar interaction and nonparabolicity stabilized the electron distribution by increasing the scattering rate. Furthermore, the inclusion of higher valleys and the associated intervalley scattering completely stabilized the simulated results for all fields considered.

Figures 38 and 39 show the steady-state electron energy distribution n(E) as a function of energy considering the total energy (kinetic and potential) of the electrons. In Fig. 38, the sum of the electron populations in the three different valleys are plotted for three values of electric field, 1, 1.5 and $2\times10^8$ V/m. For comparison, the estimated Mn impact excitation rate taken from the calculation of impact excitation cross section $\sigma(E)$ by

Shen and Xu[154], which is based on the full band structure. To calculate the impact excitation rate, a value of 500 μs is used for the radiative lifetime of $Mn^{2+}$. (We note when a more realistic value for the impact cross section is used, the radiative lifetime is estimated[155] to be 1.3-1.8 ms.)
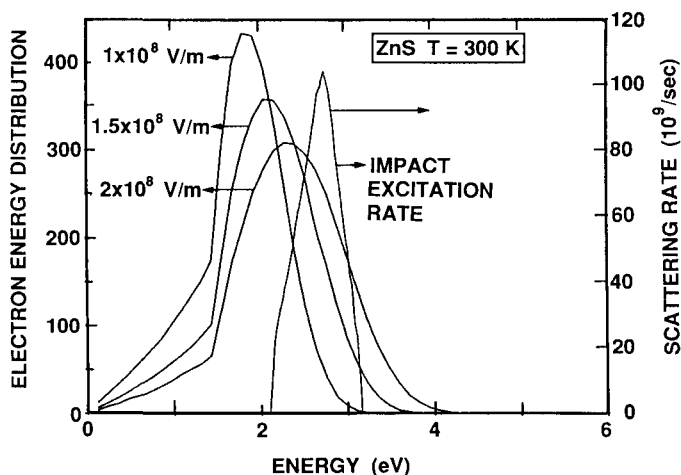


Fig. 38. Steady-state electron energy distribution n(E) and Mn impact excitation rate R(E) as a function of energy (Sum of the electron populations in three different valleys) (Ref. 109)
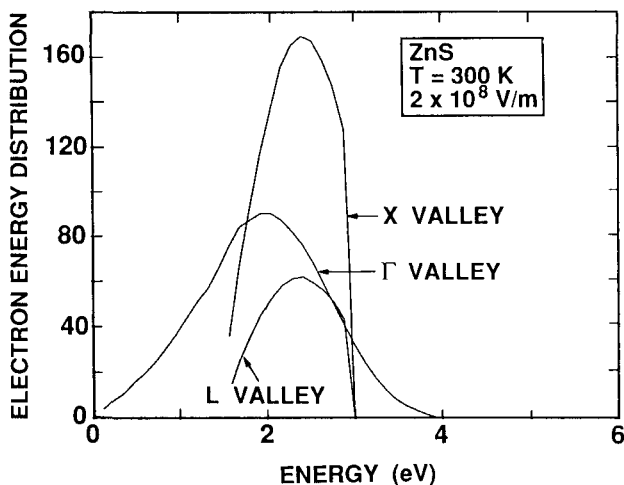


Fig. 39. Steady-state electron energy distribution in individual valleys ($\Gamma$, L and X) as a function of energy for an electric field of $2\times10^8$ V/m (Ref. 109)

Figure 39 shows the electron population in individual valleys for an electric field of $2 \times 10^8$ V/m. The electron energy distribution n(E) in the $\Gamma$ and X valleys are comparable and much higher than that of L valley because of the difference in intervalley scattering rates.

As seen from Figs. 38 and 39, at fields on the order of $1 \times 10^8$ V/m and larger, a significant fraction of the total electron population, n(E), resides at energies exceeding the threshold for Mn luminescence excitation (i.e., 2.1 eV). Figure 38 shows that the peak of the electron energy distribution n(E) versus energy curve shifts towards higher energy with the increase in the electric field. This trend implies that at higher phosphor fields, the carriers are heated to higher average energies. There is a substantial overlap of the hot electron distribution with the Mn excitation cross section, a desirable situation for efficient excitation of luminescent center impurities.

These results indicate that at fields in the range of $1.5$-$2 \times 10^8$ V/m, corresponding to the field-clamping regime in ZnS ac thin-film EL devices, the average electron energy exceeds 2 eV, and thus there is an adequate supply of energetic carriers for efficient electroluminescence to occur. Brennan's Monte Carlo simulation[107] shows that only 1% of the electrons exceed 2.1 eV at an electric field of $1 \times 10^8$ V/m while the lucky-drift modeling of Bringuier[113] gives 27% at $1 \times 10^8$ V/m and 72% at $2 \times 10^8$ V/m. On the other hand, Monte Carlo simulation of Bhattacharyya et al.[108),109)] gives 26% at $1 \times 10^8$ V/m, 50% at $1.5 \times 10^8$ V/m and 65% at $2 \times 10^8$ V/m. From a comparison of the Mn impact excitation rate with the electron energy distribution, it is found that the percentage of electrons between 2.1 and 3.2 eV, for which the impact excitation cross section is significant (See Fig. 38), is 26%, 50% and 54% for electric fields of 1, 1.5 and $2 \times 10^8$ V/m, respectively. Since the impact excitation rate decreases to zero above 3 eV, higher energy electrons cannot excite the luminescent centers.

As shown in Fig. 38, the Monte Carlo simulation for the electric field of $1.5 \times 10^8$ V/m has a distribution which peaks at approximately 2 eV with a high energy tail that extends out to approximately 3.5 eV. This is inconsistent with the hot electron luminescence experiments by Douglas et al.[157),158)] which showed that the high-energy tail extended out to 3.7 eV. Douglas et al.[157)] argued that the disagreement between experiment and the simulation may be due to the unrealistic density of states associated with the nonparabolic three-valley model used to model the ZnS conduction bands. In this model, the density of states monotonically increases, which is not the case for the realistic density of states. The scattering rate increases as the density of available final states increases. Therefore, the monotonic increase in the nonparabolic three-valley characteristic leads to an unrealistically high scattering rate and an effective cooling of the electron distribution. To obtain realistic results in the Monte Carlo simulation, a full band structure density of states must be included.

*(2) Full-Band Model*

Pennathur et al.[112)] performed a full-band Monte Carlo simulation of the high-field electron transport in the ZnS phosphor layer of an ac thin-film EL device. A full band energy dispersion relation computed using an empirical (local) pseudopotential band structure of ZnS was used to describe carrier dynamics. For the effective masses of the valleys in the first conduction bands, the values obtained from the pseudopotential band structure calculations were used: the $\Gamma$, L and X valley effective masses are $0.20m_0$, $0.53m_0$ and $0.46m_0$, respectively. In addition, all the pertinent electron scattering mechanisms were included: polar optical phonon scattering, scattering due to acoustic

phonons, intervalley scattering, ionized impurity scatterin, band-to-band impact ionization and impact excitation of $Mn^{2+}$.
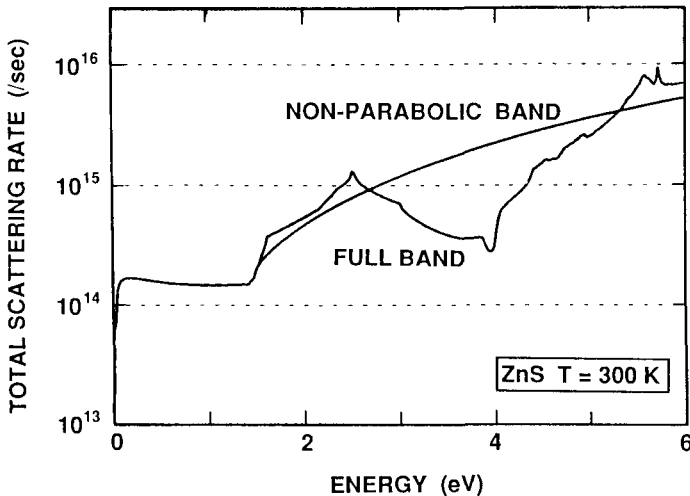


Fig. 40. Total scattering rate as a function of electron energy for a non-parabolic and full band models of the ZnS conduction band (Ref. 112)

The total scattering rate as a function of the total electron energy for a three-valley non-parabolic model of the conduction band is shown in Fig. 40 indicated as non-parabolic band. This model provides a reasonable estimate for the scattering rate for low energy electrons (i.e. less than 1.5 eV), but is not valid for high energy electrons because it does not accurately reflect the true density of conduction band states at high energies. An accurate esimate of the conduction band density of states is important because the scattering rates due to nonpolar deformation potential scattering and intervalley scattering (the dominant mechanisms above 1.5 eV) are proportional to the density of final states. A more realistic full-band density of states begins to decrease above 2.5 eV, and subsequently increases again above about 4 eV, with the onset of higher energy conduction bands. Accordingly, Pennathur *et al.* corrected the scattering rates for energies above 1.5 eV by scaling the non-parabolic scattering rate by a ratio of the pseudopotential to non-parabolic density of states, thereby forcing the scattering rate to behave as if it is modulated by the density of states. The result is also shown in Fig. 40 indicated as full band. Note that the scattering rate differences between the two curves arise exclusively from differences in the density of states above 1.5 eV. Above 4.3 eV, additional differences are due to the inclusion of impact ionization scattering in the full band model, discussed below.

In the absence of the inclusion of band-to-band impact ionization, a significant number of electrons gain energy from the field at a faster rate than they lose energy to the crystal lattice for electric fields in the phosphor layer in excess of $1.5 \times 10^8$ V/m, which leads to the unphysical runaway of carriers to extremely high energies. Note that in the discussion of the non-parabolic multivalley model[108),109)] there was no electron runaway

because of the monotonic increase in the density of states (and hence the scattering rates) implicit in such a model, as shown in Fig. 40. The unrealistically large density of states of the non-parabolic multivalley model at high energies leads to a cooling of the electron distribution. Correcting the scattering rates using the full band density of states, however, results in a decreasing scattering rate as energy increases over an energy range of approximately 2.5 eV to 4 eV, as indicated in Fig. 40. In order to prevent electron runaway from being observed in the Monte Carlo simulation, an additional scattering mechanism that has a stabilizing effect on the electron distribution is required. Hence, impact ionization is included.
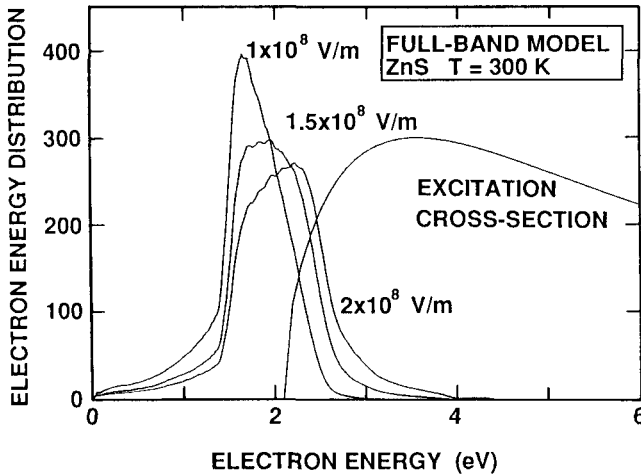


Fig. 41. Electron energy distribution at three different electric fields in the phosphor layer plotted along with the excitation cross section of $Mn^{2+}$ luminescent centers (Ref. 112)

The simulated electron energy distribution for three different electric fields in the phosphor layer is shown in Fig. 41. The distribution becomes hotter (i.e., increasing average energy) with increasing the electric fields in the phosphor layer. For manganese luminescent centers with an excitation threshold energy of about 2.1 eV, it is seen that a considerable number of electrons in the ensemble are energetic enough to cause impact excitation. From the distribution shown in Fig. 41, it is estimated that about 18%, 38% and 51% of the electrons possess energy above 2.1 eV at fields of $1 \times 10^8$ V/m, $1.5 \times 10^8$ V/m and $2.0 \times 10^8$ V/m, respectively. These values are smaller than those of non-parabolic band model calculation by Bhattacharyya et al.[108),109)] The internal luminescence excitation intensity is proportional to a convolution of the electron energy distribution function with the impact excitation cross-section of the luminescent centers in the phosphor. The excitation cross-section (in arbitrary units) for $Mn^{2+}$ centers in ZnS is also shown in Fig. 41. An increasing overlap of the excitation cross-section with the electron energy distribution is observed with increasing the electric fields in the phosphor layer.

### 4.6.2. Lucky-Drift Model Calculation

The two basic transport modes considered in the lucky-drift theory[113)-117),143)-151)] are as follows:

1. The ballistic mode, which is spatially defined by the optical-phonon mean free path $\lambda$, and temporally by the electron-phonon collision rate $1/\tau_m$.
2. The drift mode, which is characterized by the energy relaxation length $\lambda_E$, and the energy relaxation rate $1/\tau_E$.

The first is a collision-free mode (ballistic flight), while the second occurs after the electron has suffered one collision, for the reason that once it has collided, it will be deflected and the probability of other collisions occurring will be greatly increased. In the ballistic mode, the electron travels with its group velocity $v_g(E)$, so that $\lambda = v_g\tau_m$, while in the drift mode the motion is governed by a field-dependent drift velocity $v_d(E)$, and $\lambda_E = v_d\tau_E$. The lucky-drift model may be applied provided that $\tau_E >> \tau_m$ and $\lambda_E >> \lambda$, which should be true for wide-gap semiconductors in the high-field regime. When those two inequalities are fulfilled, each collision results in an appreciable momentum loss for the electron, while it loses but little energy. Over the energy relaxation length, the carrier (electron in the present case) drifts in the field losing its momentum and direction, but conserves much of its energy.

Now let us discuss the high-field transport in ZnS in detail[114)-117)]. First, we discuss[116)] the important effect of phonon in terms of electron-phonon interaction. Then more detailed transport models are introduced[116)] to calculate the fraction of electrons capable of impact exciting $Mn^{2+}$ centers.

### (1) Electron-Phonon Interaction

In a ZnS:Mn thin-film EL device, an electron in the conduction band travels in an electric field $F\sim1\times10^8$ V/m. In atomic units, this corresponds to $F\sim0.01$ V/Å, which is much smaller than atomic fields, so that the usual band-structure-related concepts should retain their validity. In this electric field regime, the average drift velocity of electrons saturate at $v_s\sim10^5$ m/s, a value which is almost independent of temperature and semiconductor materials. Scattering with impurities, which controls the mobility at low field, can no longer stabilize the electron drift in this saturation region. Only the electron-phonon (electron-lattice) interaction can do so. There are two phonon modes: acoustic mode with the energy $\hbar\omega$ varying from zero (at $k=0$, $\Gamma$ point) to a maximum at the Brillouin zone edge, and optical mode with the energy $\hbar\omega$ being almost constant with a value close to that of the zone-edge acoustic phonons.

An electron can interact with the lattice in two ways. In ionic compounds, longitudinal vibrations give rise to a polarization which acts on the electron in the form of a macroscopic electric field. Where it is present, this polar interaction usually dominates. On the other hand, in covalent crystals such as Si, a displacement of the atomic nuclei disturbs the periodic potential felt by an excess (conduction) electron and alters electron motion, without resulting in a macroscopic electric field. This interaction is called the deformation-potential interaction, which is also present in ionic solids, though it is usually much weaker than the polar interaction.

The energy exchange between electron and phonon is described by the electron-phonon interaction Hamiltonian, where the electron can emit or absorb one phonon at a time. Because the phonons are bosons, the probability of the phonon occupation number changing from n to n+1 is proportional to n+1, and that from n to n-1 is proportional to n. Therefore the ratio of the phonon emission rate $r_e(n \rightarrow n+1)$ to the phonon absorption rate $r_a(n \rightarrow n-1)$ is given by $(n+1)/n$. Because $r_e>r_a$, the electron experience a net energy loss to the lattice which stabilizes the electron drift.

Hot electrons in high electric field lose energy only to optical phonons and also, though less, to zone-edge acoustic phonons, because of the following reasons. First, let us consider the requirements of crystal momentum ($\hbar\mathbf{k}$) and energy conservation. A low-energy electron confined in the central valley experiences small momentum transfer $\Delta\hbar\mathbf{k}$, and the associated phonons lie near the zone center. Since its energy E is on the average lower than $\hbar\omega = 44$ meV (optical-phonon energy in ZnS), it mainly exchanges acoustic phonons with lattice. The situation is different for a high-energy electron, whose wavevector is a fraction of the Brillouin zone edge and whose energy E largely exceeds 44 meV. Energy relaxation of such electrons is dominated by the coupling to high-frequency modes, whether optical or zone-edge acoustic. From now on $\omega$ denotes the angular frequency (assumed independent of $\mathbf{k}$) of such modes. In the present analysis, the phonon energy $\hbar\omega = 44$ meV is assumed in ZnS, for simplicity. Necessary material parameters for ZnS are as follows: The polar coupling constant with optical phonons $\alpha$ is equal to 0.69 and the intervalley separation $E_i$ is 1.45 eV. At temperature T the phonon occupation number $n(\omega)$ is given by

$$n(\omega) = \frac{1}{\exp(\hbar\omega/kT)-1} \tag{58}$$

where k is the Boltzmann constant. For ZnS at 300 K, $n(\omega)=0.223$. The analytical expression for the saturation drift velocity $v_s$ of the lucky-drift theory[113] is given by

$$v_s = \left[\frac{\hbar\omega}{(2n+1)m^*}\right]^{1/2} \tag{59}$$

which yields $1.38\times10^5$ m/s at 300 K for $\Gamma$ valley electrons, in rough agreement with the Monte Carlo value of $v_s=0.75\times10^5$ m/s. As indicated at the beginning of this subsection, this velocity is the average of the drift velocity $v_d(E)$ over the energy distribution.

In order to assess the electron-phonon coupling in typical working conditions, the electron-phonon scattering rate $1/\tau$ is necessary, which is given by

$$\frac{1}{\tau} = r_e + r_a \tag{60}$$

$$\frac{r_e}{r_a} = \frac{n+1}{n} \tag{61}$$

From these, the average energy loss of the electron per unit time is derived as

$$\hbar\omega(r_e - r_a) = \frac{\hbar\omega}{(2n+1)\tau} \tag{62}$$

At steady state this loss offsets the potential energy gained by drifting down field yielding

$$\frac{\hbar\omega}{(2n+1)\tau} = qFv_s \approx 10^{13}\, eV/s \tag{63}$$

By substituting n=0.223 and $\hbar\omega$ = 44 meV into Eq. 63, we find $1/\tau \sim 3.2 \times 10^{14}$ s$^{-1}$, or an electron mean free time $\tau \sim 3$ fs. This high value for the scattering rate calls for an examination of transport models.

## (2) Transport Models

The rate obtained above and the drift velocity that enters Eq. 63 are averaged quantities. Competition between field heating and lattice scattering determine not only the average energy $E_{av}$ but also the nonequilibrium energy distribution function. Fluctuations from the average energy, arising from electrons gaining more energy from the field than is lost to the phonons, occur over a small elapse of time. The energy balance condition is obtained by setting the following equation to zero:

$$\frac{dE}{dt} = qFv_d - \frac{\hbar\omega}{2n(\omega)+1} \times \frac{1}{\tau(E)} \tag{64}$$

where $1/\tau(E)$ is the energy-dependent scattering rate. Figure 42 compares the electron average energies $E_{av}$ obtained from Eq. 64 with those obtained by Monte Carlo simulations[107)-110)] as a function of electric field F.
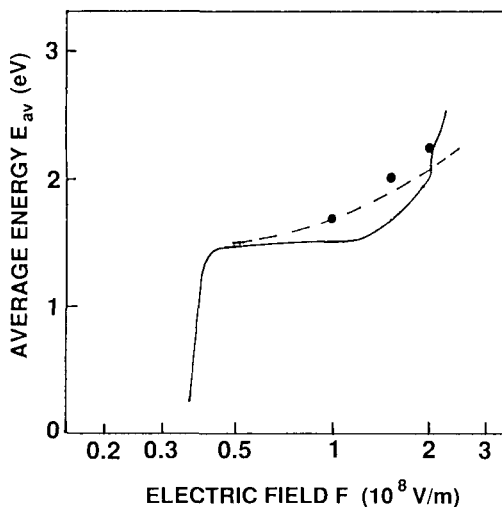


Fig. 42. Comparison of electron average energies $E_{av}$ as a function of electric field F obtained through the energy balance equation of the lucky-drift theory: solid line, using the scattering rate of Ref. 107; dashed line, using the scattering rate of Refs. 108 and 109; solid circles, actual Monte Carlo-calculated $E_{av}$ values of Refs. 108 and 109 (Ref. 116)

The standard approach to estimate the scattering rate $1/\tau$ is by means of the Golden rule, i.e., the first order perturbation theory:

$$\frac{1}{\tau} = \frac{2\pi}{\hbar} \Big| < f \big| H_{e-ph} \big| i > \Big|^2 N(E) \qquad (65)$$

where the $H_{e-ph}$ is either polar or nonpolar electron-phonon interaction Hamiltonian, and $N(E)$ is the density of available conduction-band states at the final energy E. We first draw the broad features and later highlight some details. The polar scattering rate peaks at about $2.2\alpha\omega$ for $E\sim3\hbar\omega$ and then slightly decreases in a parabolic band structure, where $\alpha$ stands for the polar (Fröhlich) coupling constant, which is 0.69 for $\Gamma$ valley of ZnS. This gives $1/\tau = 0.9\times10^{14}$ s$^{-1}$. Calculations performed in nonparabolic bands[107)-110)] lead to $1/\tau = 10^{14}$ s$^{-1}$ at $E\sim3\hbar\omega$ followed by a slight increase due to enhancement of the density of states $N(E)$ by nonparabolicity. It should be noted that the presence of satellite valleys above $E_i$ = 1.45 eV does not affect the polar scattering rate, because the polar interaction forbids large wave vector transfer $\mathbf{k'}-\mathbf{k}$ during an electron-phonon collision, resulting in the confinement of electrons inside the lower-energy valley. The calculation of Bringuier[113)] for the scattering rate balancing the energy gain in a field $F\sim1\times10^8$ V/m showed that polar scattering was unable to stabilize the electron drift in typical operating conditions. Hence some workers[153),156)] concluded that in electroluminescent materials electrons could run away, i.e. attain arbitrarily high energies, with the only limitation being the creation of electron-hole pair (band-to-band impact ionization). Actually, there is another (nonpolar) electron-phonon interaction, namely, the deformation-potential interaction. Contrary to the polar interaction, which does not allow large wave vector transfer $\mathbf{k'}-\mathbf{k}$ during a collision and thereby leads to (ineffective) forward scattering at high energies, the nonpolar interaction has a strength which is independent of the wave vectors $\mathbf{k}$ and $\mathbf{k'}$, thereby allowing all transitions in $\mathbf{k}$ space. When the electron energy is high, scattering to satellite valleys with high energy becomes possible owing to the isotropic nature of the deformation-potential interaction. In ZnS the density of states $N(E)$ in L and X satellite valleys are much larger than those in the lower ($\Gamma$) valley, so that $1/\tau$ suddenly increases as soon as E becomes larger than the intervalley separation energy $E_i$=1.45 eV. This leads[107)] to $1/\tau = 7\times10^{14}$ s$^{-1}$ at $E \sim 2.7$ eV, which is enough to balance the energy obtained form the field. Although this conclusion is based on the use of the Golden rule, it is qualitatively unchanged if the first-order perturbation theory is replaced by the full-order perturbation theory (Dyson's equation), as was done by Brennan[107)].

According to Eq. 64, the slow increase of $1/\tau$ below the intervalley separation energy $E_i$ followed by the sharp increase beyond $E_i$ yields an average energy $E_{av}$ rapidly increasing with the field till $E_i$ is reached, followed by a slow increase in $E_{av}$ above $E_i$, as shown in Fig. 42. This means that there is a transition from polar to nonpolar scattering at the energies of interest in ZnS-based electroluminescent devices. Drift at fields $\sim 2\times10^8$ V/m is controlled by the nonpolar interaction.

The existing numerical simulations[107)-110)] are in good agreement as shown in Fig. 42. Hence the more conventional transport model developed by Bhattacharyya et al.[108),109)] may be used with equal confidence in view of the assumptions regarding the electron-phonon interaction. The main difference of their model with Brennan's[107),110)] lies in the use of a multivalley density of states instead of a pseudopotential-derived band structure. The differences with Brennan's model (See Fig. 42) are only quantitative, as shown in Table 8 which illustrates the fraction of electrons capable of impact exciting $Mn^{2+}$

centers. The higher density of states of the multivalley model at high energy cuts down the high-energy tail of the distribution[112),157)].

Table 8  Fraction of electrons beyond 2.12 eV, P(2.12 eV), at 300 K for electric field of 1 or $2 \times 10^8$ V/m, according to different models (Ref. 116)

| Item | Brennan (1988, 1994) (Refs. 107, 110) | Bringuier (1991) (Ref. 113) | Bhattacharyya et al. (1993) (Refs. 108,109) |
|---|---|---|---|
| Calculation method | Numerical (Monte Carlo) | Analytical (Lucky drift) | Numerical (Monte Carlo) |
| Parameters | Empirical pseudopotential band structure | Mean free path | Non-parabolic multivalley band structure |
| P(2.12 eV) at $F=1 \times 10^8$ V/m | ~1% | 27% | 26% |
| P(2.12 eV) at $F=2 \times 10^8$ V/m | ~50% | 72% | 65% |

The following values are used to obtain the lucky-drift predictions in Table 8: $\tau = 2 \times 10^{-15}$ s and $v_g = 1.5 \times 10^6$ m/s at the energy of interest (2 eV). Here $\tau$ is taken from Brennan's Monte Carlo simulation[107)] and the group velocity $v_g$ is a parabolic-band estimate. Then, the estimated fractions of electrons above 2.12 eV in the lucky drift analysis agrees fairly well with those of Bhattacharyya et al.[108),109)] based on Monte Carlo simulation in spite of the crudeness of the lucky-drift approach. The detailed correspondence between the lucky-drift and Monte Carlo descriptions can be found in Ref. 117.

It should be noted that only when "lucky-drift" arguments[113),114)] were applied to Brennan's raw results[107)] became it clear that he correctly predicted[110)] a high impact efficiency at fields around $2 \times 10^8$ V/m. Brennan[107),110)] used the electron distribution function f(E) in his analysis, while Bhattacharyya et al.[108),109)] and Bringuier[104)-117)] used the electron number distribution function n(E), which is the product of the electron distribution function f(E) and the density of states N(E). Since the density of states is very large at high energies, the product of f(E) and N(E) can lead to a much greater percentage of carriers in the high energy tails of the number distribution function n(E), even though f(E) itself is very small. This result is included in the Brennan's calculation in Table 8.

Before concluding this section, a brief discussion is given on the application of this method to alkaline-earth sulfides CaS and SrS. The values for the polar coupling constant[136),159)] with optical phonons $\alpha$ for CaS and SrS are 1.15 and 1.3, respectively, which are much larger than the value for ZnS, 0.69. Therefore, alkaline-earth sulfides are more polar by factor of ~2, so that the field for $E_{av}$ to reach $E_i$ should be larger by a factor of ~2 (Eqs. 63 and 64). The values for the intervalley separation $E_i$ in CaS and SrS are 1.0 and 1.55 eV, respectively. As shown in Table 3 and Fig. 36, CaS and SrS have indirect bandgap[136)-138)], and the high-energy valley is $\Gamma$, whose density of states is usually smaller than that of the low-energy X valley. Hence intervalley transitions are not expected to dominate the scattering rate at high energies in those phosphors. On the other hand,

intravalley nonpolar scattering in X valley is expected to dominate the scattering rate because of the larger density of states of the X valley, and no sharp transition in $1/\tau$ at $E_i$ is expected. To establish the above statements one needs to verify that the effective mass of the $\Gamma$-valley is indeed smaller than that of the X-valley, which has not yet been reported.

### 4.6.3.  Hot-Electron Luminescence Experiments

Douglas et al.[157),158)] measured hot-electron luminescence in an evaporated thin-film EL device in the structure Al/SiON/ZnS:Mn/SiON/ITO/glass, and they found that the hot-electron luminescence spectrum extends out to the ZnS band gap for all the electric fields sufficient for tunnel emission from interface states. If the luminescence originates from hot-electron intraband transitions, this implies that a substantial fraction of the hot electrons transiting the ZnS phosphor layer possess energies up to 3.7 eV. This result seems in agreement with that of Monte Carlo simulations Bhattacharyya et al.[108),109)] and the lucky drift modeling of Bringuier[113)-117)], in which the average energy of the electron distribution is approximately 1-2 eV with high energy tails out to 3-4 eV for a phosphor electric field of $1.5\text{-}2.0\times10^8$ V/m. On the other hand, hot-electron luminescence result contradicts with ballistic electron transport results of Müller and co-workers[153),158)]. However, for more realistic comparisons, physics of electron-phonon couplings at high energy must be elucidated.

# 5. MATERIALS REQUIREMENTS

In this chapter, the requirements of materials used in thin-film EL devices with double-insulating-layer structure are discussed in terms of optical, electrical, and physical characteristics. There are two device structures used in practical thin-film EL panels: (a) a conventional device structure and (b) an inverted device structures. Figure 43 shows the conventional device structure consisting of metal electrode/insulating layer/phosphor layer/insulating layer/transparent electrode/glass substrate. On the other hand, Fig. 44 shows the inverted device structure consisting of transparent electrode/insulating layer/phosphor layer/insulating layer/metal electrode/glass substrate and color filters on the covering glass substrate.

METAL ELECTRODES

INSULATOR

RGB PHOSPHORS

INSULATOR

ITO ELECTRODES
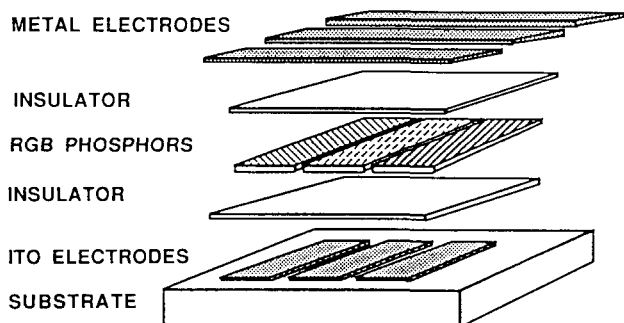
SUBSTRATE

Fig. 43. Device structure of a conventional thin-film EL devices with patterned phosphors

RGB FILTERS

ITO ELECTRODES

INSULATOR

WHITE PHOSPHOR

INSULATOR

METAL ELECTRODES
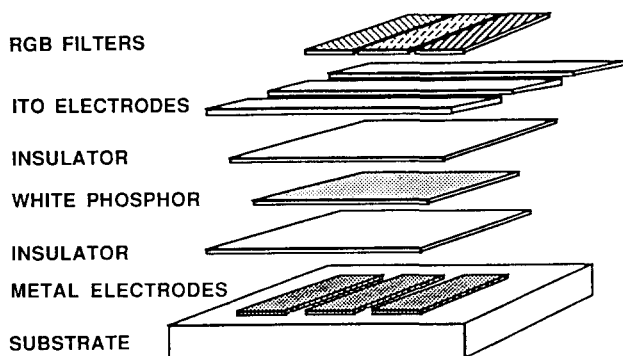
SUBSTRATE

Fig. 44. Device structure of an inverted thin-film EL devices with patterned color filters

## 5.1. Glass Substrates

The characteristics and surface conditions of the glass substrates control the properties and reliability of EL devices. During EL fabrication, severe processing

conditions are used, such as high-temperature (~550 °C) annealing and immersion in acid or alkaline fluids, and so the glass substrates must be heat resistant and acid and alkali resistant. Furthermore, diffusion of alkali-metal ions from the glass into the phosphor layer must be prevented, because they deteriorate the EL characteristics. This has led to non-alkaline, phosphosilicate or aluminosilicate glasses being used for EL devices. A final requirement is that the glass surface be as smooth as that for photomasking.

Physical properties required of the glass substrates are as follows:
1. high transmission coefficient in the visible-light region
2. thermal expansion coefficient that matches that of the deposited films
3. high softening temperature, i.e., above 650°C
4. low or no alkali-metal content
5. high electrical resistivity

Much of the thin film EL work done to date has used Corning 7059 glass: it is a non-alkaline, phosphosilicate glass with high thermal resistivity[160]. The softening temperature of this glass is, however, 598°C, and glass substrates with higher softening temperature are desired. Other non-alkaline glasses used in practical panels are aluminosilicate glasses, such as Hoya NA-40 and Asahi AN glasses.

In Finlux thin-film EL displays, soda lime glass[161)-163)] is used with an ion barrier layer of ALE-grown amorphous $Al_2O_3$. An $Al_2O_3$ layer 50 nm thick eliminates the influence of the high sodium concentration of the glass material, even when subjected to severe heat treatment conditions.

## 5.2. Transparent Conducting Films

Large conductivity values and high transmittance in the visible light region are necessary for transparent conducting films for EL devices, and indium-tin-oxide (ITO: $In_2O_3$-10wt% $SnO_2$) is best suited. Since ITO can be easily etched by normal lithographic techniques, it is suitable for fine patterning (~8 lines/mm) necessary for high-information content flat panel displays.

A small electrical resistance is required for EL devices. Presently the sheet resistance of typical ITO thin films is about 5-10 $\Omega$/square. The sheet resistance can be decreased by increasing the film thickness, which in turn increases the slope of the etching edge of the ITO stripes, causing a decrease in the breakdown electric field of the first insulating layer deposited just above the ITO electrode. From experiments it has been found that the film thickness should be less than 150 nm. Then the resistivity must be smaller than $10^{-4}$ $\Omega$cm, which is the smallest value obtainable at present.

Since high conductivity of ITO is due to oxygen deficiency, care must be taken regarding the environmental conditions. When heated in air, i.e., in high oxygen-partial-pressure condition, oxidization proceeds to reduce the degree of oxygen deficiency, resulting in high resistance. On the other hand, when heated at low oxygen-partial-pressure condition, such as in vacuum, the degree of oxygen deficiency increases, resulting in the precipitation of metal fine particles, in blackening of the films and in decrease in transmittance. These can be prevented when ITO is covered by stable protection thin films. However, heating in the reverse environmental conditions recovers the original ITO characteristics.

In addition to ITO, $CdSnO_3$ and ZnO are used in laboratory samples.

## 5.3. Insulating Layers

The most important role of the insulating layers is to protect the phosphor layers from electric breakdown in the electric field of more than $2 \times 10^8$ V/m, so that insulating layer films must have no significant defects in areas in excess of 200 cm². In addition, they must satisfy critical mechanical requirements in terms of adhesion and stress over process temperatures that range up to 550°C. Furthermore, they must prevent metal-ion diffusion into the phosphor layer and provide interface states at the boundary of the phosphor layer and the insulating layer. From these interface states, electrons are injected into the conduction band of the phosphor layer through tunneling when the applied electric field is larger than the threshold electric field.

The following properties are required to produce reliable and efficient thin-film EL devices[12),13),29),132)]:

1. high dielectric constant $\varepsilon_0 \varepsilon_r$
2. high dielectric breakdown electric field $E_{BD}$
3. small number of pinholes and defects
4. good adhesiveness
5. small $\tan\delta$.

Here $\varepsilon_0$ and $\varepsilon_r$ are the dielectric constant of a vacuum and relative dielectric constant, respectively; $\tan\delta$ is a measure of dissipative characteristics defined by $1/(2\pi f CR)$, where f is the drive frequency, C is the capacitance, and R is the resistance of the insulating layer. We now look into some of these requirements in detail.

### 5.3.1. Dielectric Constant

Below threshold a thin-film EL device acts as an ideal capacitor and Maxwell's equations impose the following boundary conditions at the interface between the individual film layers:

$$\varepsilon_0 \varepsilon_I E_I = \varepsilon_0 \varepsilon_{EL} E_{EL} \tag{66}$$

where $E_I$ and $E_{EL}$ are the electric field in the insulating layer and the phosphor layer, respectively, and $\varepsilon_I$ and $\varepsilon_{EL}$ are the relative dielectric constant of the insulating layer and the phosphor layer, respectively. Using Eq. 66 and the relation

$$V_a = E_I d_I + E_{EL} d_{EL} \tag{67}$$

the fraction of the applied voltage $V_a$ imposed across the phosphor layer, $V_{EL}$, can be calculated as

$$V_{EL} = E_{EL} d_{EL} = \frac{\varepsilon_I d_{EL}}{\varepsilon_I d_{EL} + \varepsilon_{EL} d_I} \times V_a \tag{68}$$

Therefore, to maximize $V_{EL}$, the dielectric constant of the insulating layer $\varepsilon_I$ should be as large as possible and the thickness, $d_I$, as small as device reliability will allow. In addition, this can lead to lower device operating voltage because a proportionally smaller voltage will appear across the insulating films. This feature is illustrated in Fig. 45, where the maximum trapped charge density $Q_{max}$ ($=\varepsilon_0 \varepsilon_r E_{BD}$) at the phosphor layer/insulating layer interface and the threshold voltage $V_{th}$ are plotted against the relative dielectric

constant $\varepsilon_r$ of insulating layer materials. Here the threshold voltage $V_{th}$ is estimated by taking 0.7 μm for the phosphor layer thickness, 0.4 μm for the insulating layer thickness and $1.5 \times 10^8$ V/m for the threshold electric field $E_{EL,th}$ of the phosphor layer .
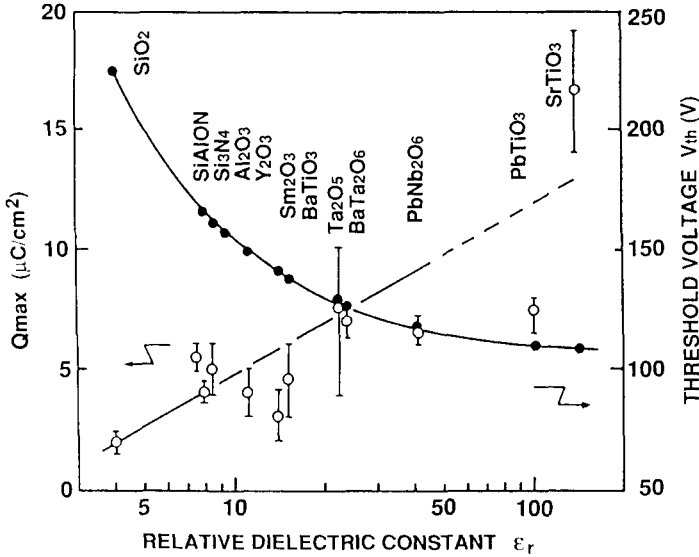


Fig. 45. Maximum trapped charge density at the interface $Q_{max}$ and threshold voltage $V_{th}$ as a function of the relative dielectric constant er of the insulating layers

### 5.3.2. Dielectric Breakdown Strength

The threshold field in a ZnS:Mn thin-film EL phosphor is approximately $1.5 \times 10^8$ V/m. From Eq. 66 the insulating layer must therefore withstand an electric field given by

$$E_I = \frac{\varepsilon_{EL} E_{EL}}{\varepsilon_I} = \frac{8.3 \times 1.5 \times 10^8 \, \text{V/m}}{\varepsilon_I} \tag{69}$$

where $\varepsilon_{EL} = 8.3$ for ZnS is used. Thus another possible advantage of an insulator with a higher dielectric constant is better reliability due to operation at lower field levels. There are two groups of dielectric materials used in thin-film EL devices: (a) amorphous oxides and nitrides, such as $Al_2O_3$, $SiO_2$, $Y_2O_3$, $TiO_2$, $Si_3N_4$, and $Ta_2O_5$; (b) ferroelectric materials, such as $BaTiO_3$ and $PbTiO_3$. Group-(a) dielectric materials have a small dielectric constant and high breakdown electric field. On the other hand, group-(b) dielectric materials have a large dielectric constant and low breakdown electric field. To characterize dielectric materials for insulating layers, a figure of merit is introduced[29], which is the product of dielectric constant and breakdown electric field, $\varepsilon_0 \varepsilon_r E_{BD}$. This figure of merit is equal to the maximum trapped charge density $Q_{max}$ at the phosphor

layer/insulating layer interface. Table 9 lists figures of merit for typical insulating layer materials[164] and also relative dielectric constants $\varepsilon_r$ and breakdown electric fields $E_{BD}$. The numbers should be taken as typical values because there are variations, depending on the deposition conditions and methods. Figure 46 relates $\varepsilon_r$ and $E_{BD}$.

Table 9. Relative dielectric constant $\varepsilon_r$, breakdown electric field $E_{BD}$, figure of merit defined by $\varepsilon_0 \varepsilon_r E_{BD}$ (= the maximum trapped charge density), and breakdown mode of typical insulating-layer materials

| Material | Deposition method* | $\varepsilon_r$ | $E_{BD}$ ($10^8$ V/m) | $\varepsilon_0 \varepsilon_r E_{BD}$ ($\mu C/cm^2$) | Breakdown mode** |
|---|---|---|---|---|---|
| $SiO_2$ | Sputtering | 4 | 6 | 2 | SHB |
| SiON | Sputtering | 6 | 7 | 4 | SHB |
| SiON | PCVD | 6 | 7 | 4 | SHB |
| $Al_2O_3$ | Sputtering | 8 | 5 | 3.5 | SHB |
| $Al_2O_3$ | ALE | 8 | 8 | 6 | SHB |
| $Si_3N_4$ | Sputtering | 8 | 6-8 | 4-6 | SHB |
| SiAlON | Sputtering | 8 | 8-9 | 5-6 | SHB |
| $Y_2O_3$ | EBE | 12 | 3-5 | 3-5 | SHB |
| $Y_2O_3$ | Sputtering | 12 | 3-5 | 3-5 | SHB |
| $BaTiO_3$ | Sputtering | 14 | 3.3 | 4 | SHB |
| $Sm_2O_3$ | EBE | 15 | 2-4 | 3-5 | SHB |
| $Ta_2O_5$-$TiO_2$ | ALE | 20 | 7 | 12 | SHB |
| $BaTa_2O_6$ | Sputtering | 22 | 3.5 | 7 | SHB |
| $Ta_2O_5$ | Sputtering | 23-25 | 1.5-3 | 3-7 | SHB |
| $PbNb_2O_6$ | Sputtering | 41 | 1.5 | 5 | SHB |
| $TiO_2$ | ALE | 60 | 0.2 | 1 | PB |
| $Sr(Zr,Ti)O_3$ | Sputtering | 100 | 3 | 26 | PB |
| $SrTiO_3$ | Sputtering | 140 | 1.5-2 | 19-25 | PB |
| $PbTiO_3$ | Sputtering | 150 | 0.5 | 7 | PB |

*EBE: Electron-beam evaporation, ALE: Atomic layer epitaxy
PCVD: Plasma (-excited) chemical vapor deposition
**SHB: Self-healing breakdown mode; PB: Propagating breakdown mode

### 5.3.3. Film Breakdown Characteristic

It has been found that thin-film EL insulating layers exhibit two distinctly different film breakdown patterns. One pattern is a propagating arc that destructively grows in size until significant microscopic damage is done to the films. The other pattern is the so called "self-healing" localized discharge that clears the film defect by causing a microscopic open circuit to occur around the breakdown site. These two types of breakdown holes are schematically shown in Fig. 47 as breakdown holes in ramp tests[164] and are also indicated for each insulating material in Table 9. Because all thin film devices have some microscopic defects, it is necessary that thin-film EL insulating layer materials have the self-healing breakdown characteristic. Generally, dielectric thin films with large dielectric constants or not fully oxidized or not fully nitrified dielectric thin films tend to have a propagating breakdown mode. Coupled with other dielectric thin films, insulating layers with the propagating breakdown mode can be converted into the self-healing type.
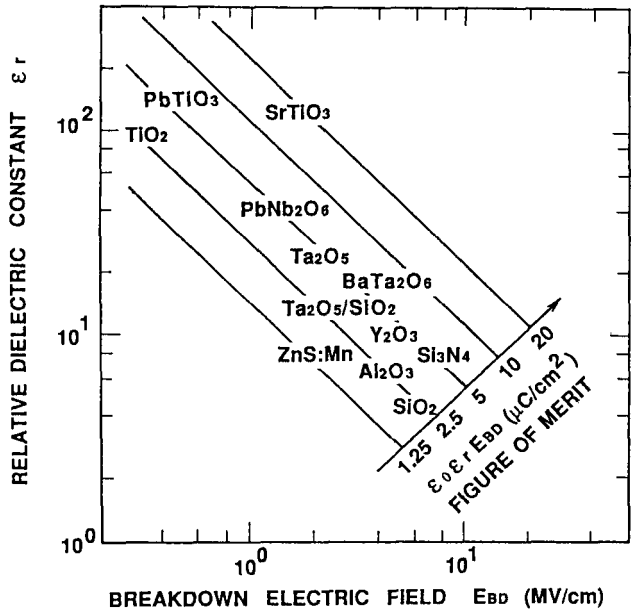
Fig. 46. Relative dielectric constant versus breakdown electric field ($\varepsilon_r$ - $E_{BD}$) characteristics of typical dielectric materials for thin-film EL devices (straight lines indicate constant figure of merits) (Ref. 164)
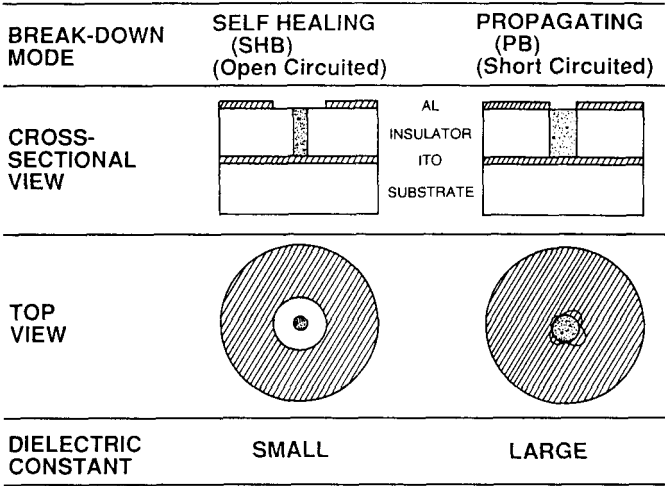


Fig. 47. Schematic illustration of dielectric breakdown holes in the thin-film capacitors (Ref. 164)

### 5.3.4. Film Morphology

Again because of the high field nature of the thin-film EL device, it is desirable to have a very smooth interface between the various film layers. Any asperity will lead to a high field region that may lead to localized breakdown of the device structure. Therefore, it is preferable to have either a very fine grained insulating layer morphology or even better, an amorphous structure. In fact, the amorphous structure leads to better device stability by eliminating possible grain boundary diffusion paths for ions or moisture.

### 5.3.5. Film Stress and Adhesion

The adhesion between the various layers of a thin-film EL device is stressed by the requirement either to deposit or to anneal the ZnS phosphor layer at 500°C in order to achieve good crystallinity for phosphor efficiency. Sputtered insulator films in particular often have a high degree of internal stress which can lead to film peeling. A careful selection of materials and process is required to avoid this potential problem.

### 5.3.6. Practical Examples

Yttrium oxide ($Y_2O_3$) was the insulator used by Inoguchi *et al.*[22] when they first announced the achievement of reliable thin film EL device performance in 1974. As seen in Table 9, $Y_2O_3$ has a moderately high dielectric constant of 12, it has quite good adhesion to ZnS, and a fair breakdown strength with self healing characteristic. For several years after the Sharp report $Y_2O_3$ was the standard EL insulator. However, crystalline nature of the material caused thin-film EL devices built with $Y_2O_3$ to be sensitive to moisture and ionic intrusion. In addition, this crystalline nature caused nonuniformity in the phosphor thin films deposited on top of them, resulting in non uniform luminance. These apparently led Sharp to favor amorphous $Si_3N_4$ and $Al_2O_3$ dielectrics[2],[32] even though these materials have lower dielectric constants and compromise device performance. Apparently their reliability is significantly superior to $Y_2O_3$. However, $Y_2O_3$ is still used as one component of double insulator film structures because of its excellent ZnS adhesion characteristics.

Barium titanate ($BaTiO_3$) was used extensively by the IBM group in their investigations[165],[166]. This material is amorphous and presumably more resistant to ion migration than $Y_2O_3$, plus its dielectric constant is somewhat higher. It represents the first in a series of attempts to improve device performance by utilizing high dielectric constant material. A recent report by Fujita et al.[164] summarizes the characteristics of several of these materials including $Ta_2O_5$, $PbTiO_3$, $BaTa_2O_6$, and $SrTiO_3$ (See Table 9). However, one of the disappointing features of their investigation is the tendency of materials with high dielectric constants to have lower breakdown strength as shown in Table 9. Thus the figure of merit for all of these materials tend to be in the 3 to 7 $\mu C/cm^2$ range even if the dielectric constant is very large. In other cases a material with otherwise good characteristics will have a propagating breakdown mode (i.e., $SrTiO_3$). Thus attempts to significantly lower the operating voltages of thin-film EL devices by using high index insulators has had only mixed success.

Another thrust has been to use combinations of different insulator materials to produce a composite with superior properties. An example of this is the silicon-aluminum oxynitride (SiAlON) reported by Tiku et al.[132],[167]. This composite has excellent adhesion to the ZnS, which is a problem for pure $Si_3N_4$ or $Al_2O_3$. Sharp uses a $SiO_2/Si_3N_4$ layer[2] to achieve good adhesion to the ITO electrodes. Lohja has reported essential improvement using an ALE-grown $Al_2O_3/TiO_2$ mixed insulating layers[161]. This composite insulator approach appears to be the preferred commercial solution to achieve all the insulator requirements listed above.

## 5.4. *Phosphor Layers*

All phosphors consist of a host material and a luminescent center. The requirements for the phosphor host materials are as follows:
1. They have a large enough band gap to emit visible light from the doped luminescent centers without significant absorption.
2. They must hold a high electric field of the order of $10^8$ V/m without electric breakdown and they must have insulating characteristics below the threshold voltage.
3. They must withstand a post annealing temperature of 550°C.

Phosphor host materials satisfying the above requirements are limited to II-VI compounds, such as IIb-VIb compounds such as ZnS and ZnSe, and IIa-VIb compounds such as CaS, SrS, and SrSe, and alkaline earth thiogallates, $CaGa_2S_4$, $SrGa_2S_4$ and $BaGa_2S_4$.

On the other hand, luminescent centers must satisfy the following requirements.
1. They must be properly incorporated into host materials and emit visible lights.
2. They must have a large cross section for the impact excitation.
3. They must be stable in the high electric field of the order of $10^8$ V/m.

Luminescent centers satisfying the above requirements are isolated luminescent centers, and transition metals such as Mn and rare-earth elements such as Tb, Sm, Tm, Eu and Ce are found to be suitable.

Detailed discussions on phosphor host materials and luminescent centers have already been given in Section 4.5.

## 5.5. *Metal Electrodes*

The requirements for the rear electrode materials in the conventional thin-film EL structure shown in Fig. 43 are as follows:
1. good adhesiveness to the insulating layer
2. no metal-ion migration at high electric field
3. an ability to prevent breakdown spread when dielectric breakdown of the phosphor layer or insulating layers occurs
4. low resistivity.

Among the materials satisfying these conditions, aluminum (Al) is considered to be the best. Deposition of Al thin films can be done by thermal heating, electron-beam evaporation (EBE) and sputtering methods. One disadvantage in their use is their high reflectivity of light, so that mirror-type reflection occurs. This reflection can be suppressed by a smoke filter of 50-70% or by circularly polarizing filters. Since Al films have specular reflection, the latter works very well. Then no incident light going into the EL cell can come out from the glass plate and only the EL emissions are effectively taken out from the EL devices.

On the other hand, in the inverted thin-film EL structure shown in Fig. 44, in which the metal electrode is deposited first on the glass substrate, additional requirements for the lower metal electrode are as follows:
5. high-temperature resistance not to be deformed above 550°C during annealing, i.e., high melting point
6. thermal expansion coefficient that matches that of glass substrate
7. small reflection coefficient in the visible light region to obtain good contrast.

Table 10 lists the characteristics of several metal electrodes. Since the melting point of Al is 660°C, Al is not suitable for the metal electrode in the inverted device structure: Al

cannot stand the high-temperature annealing process at 550 °C resulting in creasing[47]. One more important feature of the metal electrode is the effect on the insulating layer characteristics during the annealing process. Experiment on the current-voltage characteristics in test samples with the structure $Al/Si_3N_4/SiO_2$/metal electrode/glass substrate revealed that the leak current of the insulating layer was the lowest in the tungsten (W) and molybdenum (Mo) samples[47]. Therefore, Mo and W are suitable for the metal electrodes in the inverted device structure.

Table 10 Physical properties of typical metal electrodes (Ref. 47)

| Metal | Resistivity $(10^{-6}\ \Omega \cdot cm)$ | Melting point (°C) | Reflection coefficient* (%) | Expansion coefficient- $(10^{-6} \cdot deg^{-1})$ |
|---|---|---|---|---|
| Al | 2.24 | 660 | 90 - 92 | 23 |
| Mo | 4.3 | 2615 | 55 - 57 | 5.0 |
| Ta | 11.0 | 2998 | 40 - 57 | 6.5 |
| W | 4.3 | 3380 | 46 - 51 | 4.5 |
| Glass | —— | —— | —— | 4.7 |

*Data in the visible-light region

# 6. MATERIALS DEPOSITION METHODS

## *6.1. Phosphor Layer Deposition Methods*

In this chapter deposition methods used in fabricating phosphor layers of thin-film EL devices, especially ZnS:Mn EL devices, are discussed[104),168),169)], with emphasis on the deposition conditions, crystal structures, and their relations to electro-optical characteristics. Furthermore, a brief discussion on the deposition conditions of other thin-film phosphor materials, ZnS:Tb,F, CaS:Eu and SrS:Ce, will be given.

Thin-film processes to deposit thin-film phosphors are divided into two groups: physical vapor deposition (PVD) methods and chemical vapor deposition (CVD) methods. The former include evaporation methods, such as electron-beam evaporation (EBE)[104),123),124),170)] and thermal evaporation, sputtering[35),36),171)-178)] and multi-source deposition (MSD)[179)-183)]. The latter include atomic-layer epitaxy (ALE)[30),121),122),161)-163),184)-198)], metal-organic chemical vapor deposition (MOCVD)[39),199)-208)] and low-pressure hydride-transport chemical vapor deposition (HT-CVD)[209)-213)] with halogen transport of Mn. Among these, EBE and ALE are now used to fabricate commercial ZnS:Mn EL display panels.

Whichever the process is used, it is necessary to produce films with excellent stoichiometry and the best possible crystallinity in order to permit the maximum acceleration of the electrons so that they can gain sufficient energy to impact-excite the luminescent centers. Otherwise, film imperfections will scatter the electrons before they can obtain sufficient kinetic energy. This requirement implies that the processing should be done at high temperatures where large grain growth will occur.

## *6.1.1. PVD (Physical Vapor Deposition) Methods*

### *(1) Evaporation (Electron-Beam Evaporation and Thermal Evaporation) Method*

The evaporation technique[104),123),124),170)] is useful for non-refractory materials that will vaporize at a reasonable temperature, reasonable being less than 1400°C for thermal sources and less than 2200°C for electron-beam sources. Typically, evaporation can produce good film stoichiometry for elements and simple compounds. Specifically, the evaporation technique has difficulty producing good films of complex phosphors like rare earth oxysulfides because of the widely varying vapor pressures and chemical reactivities of the constituent components of these compounds. On the other hand, the classical II-VI compounds form excellent films by evaporation. The kinetics of the evaporation, material transport and film condensation are shown in Fig. 48. The strength of the chemical bonding of these II-VI compounds are weak enough that the heat of evaporation is sufficient to largely dissociate the molecule. The individual atomic species are then transported to the substrate in a line of sight trajectory provided that the pressure level is low enough to permit collisionless transport. The atoms then recombine on the substrate to form the original II-VI compound. A feature of this recombination at the substrate is that it can be controlled to produce very stoichiometric films by adjusting the substrate temperature. The mechanism here is that the vapor pressure of the consituent atoms, for example Zn and S, is high enough for substrate temperatures above 200°C that neither Zn nor S will adhere to other similar atoms. Thus the film growth proceeds by formation of alternate layers of Zn and S atoms and stoichiometry is automatically achieved.

For ZnS:Mn thin-film EL devices, post-deposition thermal annealing is performed in vacuum at approximately 550 °C. Thermal annealing improves the phosphor layers because it removes strains in the films, enhances crystallinity of the grains, and accelerates Mn diffusion.
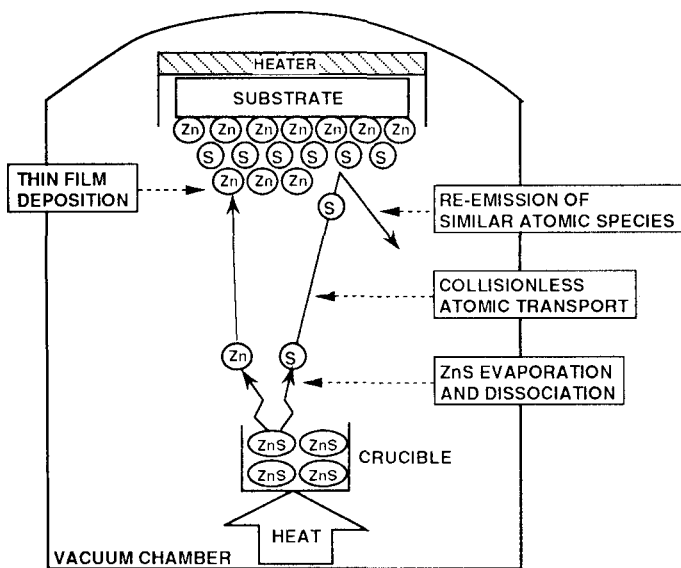


Fig. 48. ZnS evaporation kinetics (Ref. 104)

For CaS- and SrS-based EL devices, the EBE method is mainly used[51)-55)] with higher substrate temperature of 400-600°C and sulfur coevaporation to realize stoichiometric thin films.

*(2) Sputtering Method*

Sputtering[35),36),171)-178)] is complimentary to evaporation in that this process is ideal for forming films of complex composition but perhaps less able to form good II-VI compounds. The process is not done at high vacuum but rather in the 10 millibar pressure range where a plasma discharge is used to physically sputter the material off the face of a target material and this material is then transported to the substrate through the gas of ions, electrons and molecules of the discharge medium (typically Ar).

An intrinsic characteristic of this process is that the composition of the substrate film will, in the steady state, be the same as the target material. This is the reason why complex materials are excellent candidates for sputtering deposition. However, this composition equivalency is only in the "alloy" sense and the crystal structure of the film may have no relationship whatsoever to the target material. Sputtered films also tend to incorporate some of the discharge gas in the crystal structure which tends to further degrade the crystal perfection. This, combined with typically slow deposition rate (relative to evaporation) which allow the background gas (such as $H_2O$) to chemically

react with the films during growth, tends to make it more difficult to form good films with excellent stoichiometry. The II-VI compounds are difficult to deposit because the sulfur atom is less reactive than the oxygen containing background gases and it is difficult to avoid forming an oxysulfide rather than a pure sulfide. Therefore, usually sputtering of II-VI compounds is performed in a partial pressure of $H_2S$ gas to actively suppress oxide formation[174].

Sputtering is suitable for in-line processes, because both the insulating layers and the phosphor layer can be grown by the same deposition method[171),172),174]. In the case of ZnS:Mn, however, the crystallite diameter of the deposited films is not large, and stoichiometric ZnS films are difficult to obtain[176] because of the reason discussed above. As a result, a bright ZnS:Mn EL device has not been realized yet.

On the other hand, for ZnS:Tb,F, the brightest green-emitting EL devices are realized by sputtering[35),36),178]. In the ZnS:Tb,F EL device, ionic radius mismatch of 25% (See Table 5) makes it very difficult to incorporate Tb ions into the ZnS host lattice without creating lattice defects. To overcome this difficulty, sputtering process is very effective because sputtering imparts a kinetic energy of several eVs to the nucleating atoms during the film growth. The ion bombardment during sputtering must influence both the crystal growth of the ZnS and the Tb dopant incorporation site in such a way that the Tb dopant is more effectively incorporated into the thin-film phosphor.

*(3) MSD (Multi-Source Deposition) Method*

In this method[179)-183], evaporation sources for Zn, S and Mn are placed in a vacuum chamber having a pressure of $10^{-5}$ to $10^{-6}$ Torr. By independently controlling the temperatures of these sources, highly crystalline and stoichiometric ZnS:Mn films can be obtained[180].

Figure 49 shows a cross-sectional transmission electron microscopic (TEM) picture[179] of deposited ZnS:Mn film on a glass substrate. From this figure we found that columnar polycrystals of ZnS extended from the bottom to the top surface. The grain size of these columns was approximately 100 to 200 nm.



Fig. 49. Transmission electron micrograph of a cross-section of a MSD-prepared ZnS:Mn thin film (Ref. 179)

The X-ray diffraction patterns and transmission electron diffraction measurements showed that the crystal structure was hexagonal (wurtzite) with a (002) preferred orientation. The luminance $L_{80}$ was 5300 cd/m$^2$ and the luminous efficiency η was 3.18 lm/W under a 5-kHz sinusoidal excitation for the thin-film EL device with a phosphor layer thickness of 900 nm and the threshold voltage of 99 V

Recently a new technique of sulfur vapor pressure control[183] has been successfully incorporated into the MSD method. The sulfur vapor is supplied from the sulfur furnace through the bellows valve, which is installed outside of the MSD chamber. The sulfur vapor can be controlled over a wide pressure range of 0.01-1 Pa by the temperature of the sulfur furnace and the bellows valve. The ZnS films grown by MSD have mixtures of cubic and hexagonal phases. The ZnS films deposited at higher sulfur vapor pressure (~0.85 Pa) show smooth surfaces, and have a uniform grain size of about 200 nm. Stable ZnS:Mn thin-film EL devices with good performance have been obtained for the devices prepared at sulfur vapor pressures higher than 0.1 Pa. Luminance $L_{30}$ and luminous efficiency $η_{30}$ at 30 V above the threshold voltage of 180 V are 300 cd/m$^2$ and 3.5 lm/W, respectively, at 60-Hz pulse wave driving.

SrS:Ce thin-film fabrication has been achieved with MSD, and good crystallinity was obtained[181],[182].

### 6.1.2. CVD (Chemical Vapor Deposition) Methods

The chemical vapor deposition process differs from the above physical vapor deposition processes in that the source materials are converted to gases externally to the actual deposition chamber. The substrates are then heated to a sufficient temperature inside the deposition chamber so that the source gases chemically react on the substrates to form the desired thin film compounds. Thus the deposition rate is not controlled by the physical arrival rate of the consituent atoms, but rather by the chemical reaction rate. This process technology is used extensively in the manufacturing of integrated circuits for materials such as $SiO_2$ and $Si_3N_4$.

### (1) ALE (Atomic Layer Epitaxy) Method

The basic idea behind ALE[30],[161]-[163],[184]-[198] is to ensure a surface-controlled growth instead of the source-controlled growth used in conventional thin film techniques. In ALE it really is a question of material growth instead of material transfer. The ALE process is carried out stepwise by separate surface reactions, each forming one atomic layer only. It can be applied to compound materials either on amorphous or on single crystal substrates. In the ALE process the heated substrates are exposed sequentially to the vaporized reactants. As well as compounds of the elements, elemental components of the final compound can be used as reactants. In each step, such a reaction is possible for one chemisorbed atomic layer only. Sufficiently high temperature prevents the condensation of extra reactant on the substrate.

The source materials[190] for the metals used in the growth of sulfide materials for EL phosphors are $ZnCl_2$, $Zn(CH_3COO)_2$, $Zn(thd)_2$, $Ca(thd)_2$ and $Sr(thd)_2$, where thd is 2,2,6,6,-tetramethyl-3,5-heptanedione. The non-metallic source material is $H_2S$. For the luminescent center deposition, manganese compounds $MnCl_2$, $Mn(thd)_2$ and $Mn(CO)_5$ have been used for yellow emission, $Ce(thd)_3$, for blue-green emission, $Tb(thd)_3$, $Eu(thd)_3$ and $Pr(thd)_3$, for green, red and white emissions, respectively.

As shown in Fig. 50, the ALE growth process for ZnS is based on the exchange reaction

$$ZnCl_2(ads) + H_2S(g) \rightarrow ZnS(s) + 2HCl(g) \qquad (70)$$
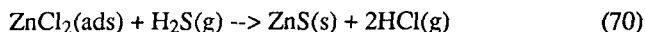
Here ads stands for adsorbed state and g stands for gaseous state. The growth consists of the following steps: $ZnCl_2$ is introduced in vapor phase. Provided that the substrate temperature is not too high (~500°C), cation-anion bonds allow $ZnCl_2$ to adhere as a monolayer on an anion surface, such as oxygen or sulfur. The substrate temperature is, however, kept high enough to prevent the formation of zinc to zinc bonds on the surface and therefore no more than one layer of $ZnCl_2$ is formed. Excess $ZnCl_2$ vapor is subsequently flushed away and then $H_2S$ is introduced as vapor. Through reaction of $H_2S$ with the adsorbed $ZnCl_2$, ZnS is formed and HCl is liberated. After flushing away excess HCl, the cycle is repeated. The growth is insensitive to pressure and substrate materials, but the substrate temperature is important. The temperature must be sufficient for chemisorption but not too high to lead to the desorption of the monolayer.

Manganese doping is performed by transporting $MnCl_2$ by Ar gas. Large area thin-film EL panels are prepared in a flow type reactor.
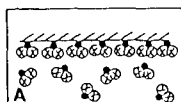


A    SURFACE WITH OXYGEN ATOMS IS SUBJECTED TO ZnCl2 VAPOR. ZnCl2 COVERAGE IS MADE BY Zn-O BONDS.
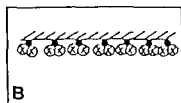
B    EXCESS ZnCl2 VAPOR IS SWEPT AWAY.
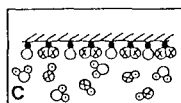
C    SURFACE IS SUBJECTED TO H2S VAPOR. AN EXCHANGE REACTION RELEASES Cl FROM THE SURFACE, AS HCl VAPOR, AND DELIVERS S TO THE Zn SURFACE TO FORM A MONOATOMIC S SURFACE LAYER.
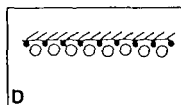
D    EXCESS H2S IS SWEPT AWAY.
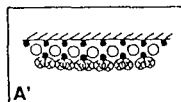
A'   STEP A IS REPEATED FOR THE S SURFACE.

Fig. 50. Growth mechanism of the atomic-layer epitaxy (ALE) process for ZnS using $ZnCl_2$ and $H_2S$ as reactants (Ref. 30)

There are some advantages in using $ZnCl_2$ and $H_2S$ as source materials. First, the probability of re-evaporation of Zn from the surface will decrease, because the surface is covered with a non-metallic layer. Second, molecules containing only one S atom as $H_2S$ are more reactive than two- or poly-atomic forms, which are typical on non-metals.

The ALE process has several unique features compared with conventional thin film techniques. The first is that it requires no thickness monitoring. Thickness is determined by counting the number of reaction steps, provided only that the dose of reactant in each step is high enough to produce a full monolayer coverage. It also possesses high

chemical stability; weak chemical bonds are automatically eliminated in each reaction step, which results in highly stable and stoichiometric films. Another advantage is the high uniformity of layers even in ultra thin structures. A final advantage of the ALE method is a possibility to prepare the whole insulating layer/phosphor layer/insulating layer stack in one continuous process. This is important when moisture sensitive alkaline earth sulfides are processed.

From X-ray measurements of ZnS films[191], shown in Fig. 51, it was found that ZnS thin films grown at 350 °C have the cubic (zinc blende) crystal structure and films grown at 500 °C have the hexagonal (wurtzite) structure. This crystal structure dependence on the growth temperature was confirmed by the electroreflectance measurements[195]. It was found that crystal structure of polycrystalline ZnS thin films grown from zinc acetate at 300-375 °C were mainly cubic, while the ZnS thin film layers grown from zinc chloride at 425-500 °C were predominantly hexagonal.
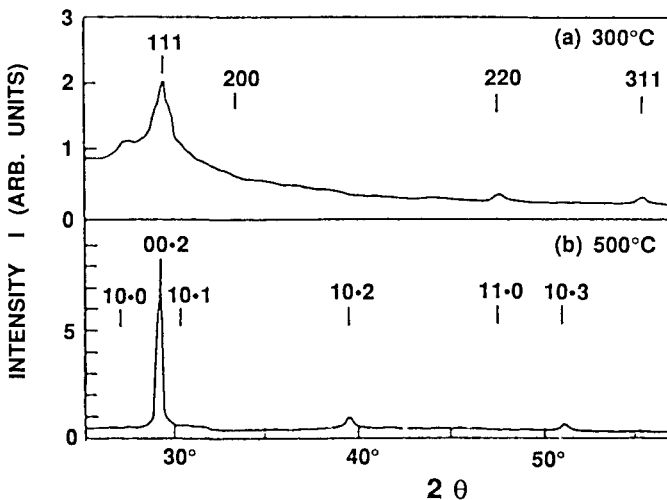


Fig. 51. X-ray diffraction patterns of ALE EL devices: (a) 350°C; (b) 500°C (Ref. 191).

Figure 52 shows crystallite size versus phosphor layer thickness $d_{EL}$ of ZnS:Mn films prepared by ALE, EBE, MOCVD and HT-CVD methods. The crystallite size of ALE-prepared ZnS:Mn is large from the start of the deposition[192] and two to three times larger than that of other deposition methods, indicating the best crystallinity of ALE thin films. In the EBE films small grains are present in the so-called dead layer, i.e. a zone of poor crystallinity at the beginning of the growth. From the data[122] of phosphor layer thickness dependence of the luminance (Fig. 19) the dead layer of ALE-EL thin films was approximately 30 nm. The average luminous efficiency was 3 lm/W, with the maximum being 8 lm/W.

Because of the hexagonal crystalline structure of the ALE-ZnS:Mn films, the peak wavelength of an emitted light of ALE-EL device is slightly different from that of an EL device based on a vacuum evaporated or sputtered ZnS:Mn film. The shift of wavelength is from 585 nm, typical of a device with a cubic ZnS:Mn layer, to 580 nm, which changes the color of the display from orange yellow to a bright yellow.
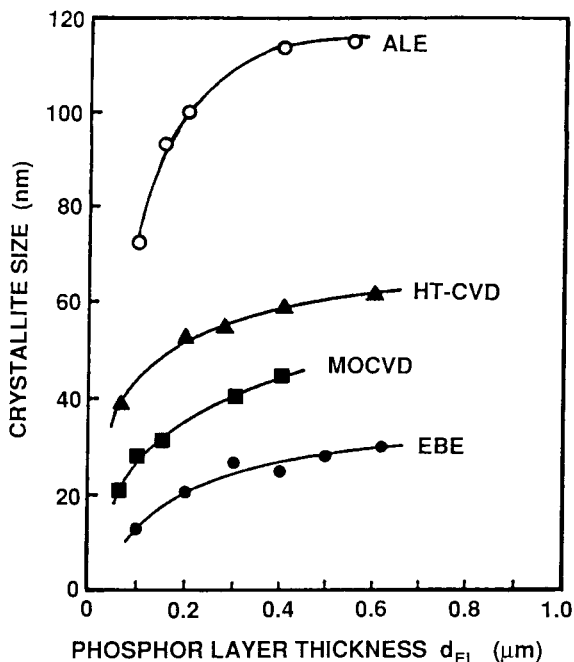
Fig. 52. Crystallite size versus phosphor layer thickness $d_{EL}$ of ZnS:Mn thin films prepared by ALE, HT-CVD, MOCVD and EBE methods (Refs. 191, 204 and 210)

Application to green emitting ZnS:TbS$_x$ devices was successfully carried out with an industrially applicable luminance level[196]. Here, the phosphor layer was grown from ZnCl$_2$, H$_2$S and highly volatile terbium compound. For Tb doping, Tb(thd)$_3$ was chosen, because it offers a sufficient vapor pressure even below 200°C and a good thermal stability. High luminance was obtained by concentrating terbium to layers separated by pure ZnS, i.e., by depositing alternately Tb-rich layers and Tb-free ZnS layers.

The ALE method has been successfully applied to the deposition of SrS- and CaS-based EL devices[189]. The growth reaction in this case is

$$M(thd)_2(g) + H_2S(g) \longrightarrow MS(s) + 2Hthd(g) \qquad (71)$$
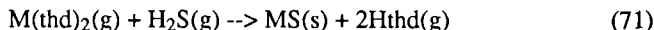
where M is either Ca or Sr ion. Based on this, blue-green emitting SrS:Ce EL devices were grown[197],[198] using Sr(thd)$_2$ and Ce(thd)$_3$ as source materials and good luminous efficiency and sufficient stability for display application were realized. The filtered blue luminance[198] was among the best reported values.

*(2) MOCVD (Metal Organic Chemical Vapor Deposition) Method*

The MOCVD[39],[199]-[208] offers several advantages, such as lower growth temperature and easy control of stoichiometry and impurity concentration. The growth

rate and incorporation of impurities are mainly controlled by mass-transfer of source materials with subsequent thermal decomposition on the substrate. Strict control of source material flow and temperature distribution in the substrate becomes a practical problem in developing an uniform film over a large area. Figure 53 shows a schematic illustration of the low-pressure MOCVD growth system[201] for ZnS:Mn thin-film EL devices. The reactor consists of a silica tube containing a graphite pedestal heated by high-frequency induction. For Zn, dimethyl-zinc (DMZ) was used and for sulfur, either $H_2S$ with a 5% mixture in hydrogen or diethylsulfide (DES) was used. Hydrogen serves as a carrier gas for the reactants. For Mn, tricarbonylmethyl-cyclopentadienyl-Mn (TCM) was used.

Cross-sectional TEM images revealed that in the MOCVD-prepared film very pronounced columnar grains were grown, which extended from the bottom to the top of the film. Crystallite size vs. phosphor layer thickness characteristics are shown in Fig. 52, showing that the crystallite size of MOCVD-grown ZnS:Mn is larger than that of EBE but smaller than that of HT-CVD and ALE. The X-ray diffraction analysis showed that the MOCVD films had hexagonal wurtzite crystal structure.
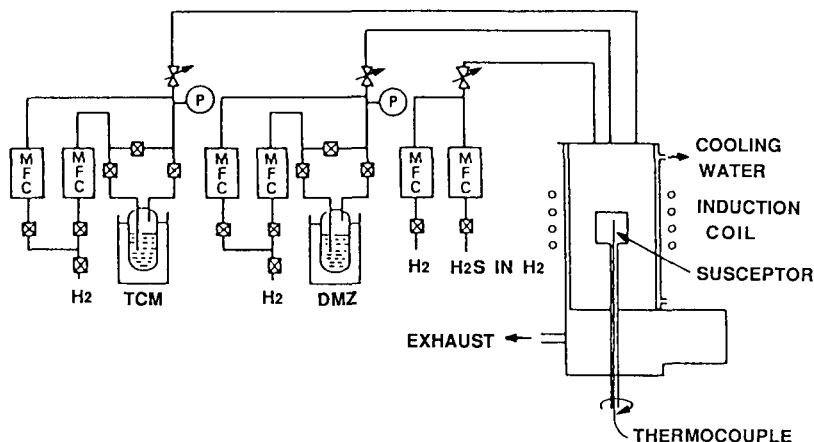


Fig. 53. Schematic illustration of low-pressure MOCVD growth system (Ref. 201)

New Mn sources, di-$\pi$-cyclopentadienyl-Mn (CPM) and bis-methyl-cyclopentadienyl-Mn (BCPM), were studied[204] and both were efficiently decomposed at the optimum growth temperature of ZnS, 280-350°C. The EL devices with CPM have the largest luminance. The maximum luminance and luminous efficiency were 4300 $cd/m^2$ and 4.8 lm/W, respectively, under a 1-kHz sinusoidal drive in the device with 500 nm phosphor-layer thickness.

Table 11 summarizes source materials, optimum process temperatures and crystal structures of MOCVD-prepared ZnS:Mn thin films.

ZnS-based color EL devices have been fabricated[39] by MOCVD. In particular, use of $SmCl_3$ as a source material of luminescent center gave a much brighter and better purity red EL emission than $SmF_3$.

Table 11   Source materials, optimum process temperature and crystal structure of MOCVD-prepared ZnS:Mn thin films

| Source materials | | | Optimum process | Crystal |
|---|---|---|---|---|
| Zn | S | Mn | temperature | structure |
| DMZ | $H_2S$ | TCM | 300°C | zinc blende |
| DEZ | $H_2S$ | CPM | 350°C | zinc blende |
| DEZ | $H_2S$ | BCPM | 350°C | zinc blende |
| DEZ | $CS_2$ | —— | 400°C | wurtzite |
| Zn[$(C_2H_5)_2NCS_2$]$_2$ | | TCM | 400°C | wurtzite |
| DEZ | ZES | TCM | 550°C | wurtzite |

DMZ: Dimethylzinc, $Zn(CH_3)_2$
DEZ: Dietylzinc, $Zn(C_2H_5)_2$
DES: Diethylsulfide, $S(C_2H_5)_2$
TCM: Tricarbonyl methylcyclopentadienyl manganese, $(CH_3C_5H_4)Mn(CO)_3$
CPM: Di-$\pi$-cyclopentadienyl manganese, $(C_5H_5)_2Mn$
BCPM: Bis-methyl cyclopentadienyl manganese, $(CH_3C_5H_4)_2Mn$

*(3) HT-CVD  (Hydride- or Halogen-Transport Chemical Vapor Deposition) Method*
        The halide or hydride transport CVD has a high potential in growing epitaxial II-VI compound thin films.  This method is convenient for large quantity production, because a hot wall method can be utilized.  Good-quality ZnS:Mn (ZnS:Tb) phosphor layers can be prepared by using a low-pressure HT-CVD system[209)-213)] with halogen transport of Mn (Tb) and hydrogen transport of ZnS.  This system with a horizontal reactor is schematically shown in Fig. 54.
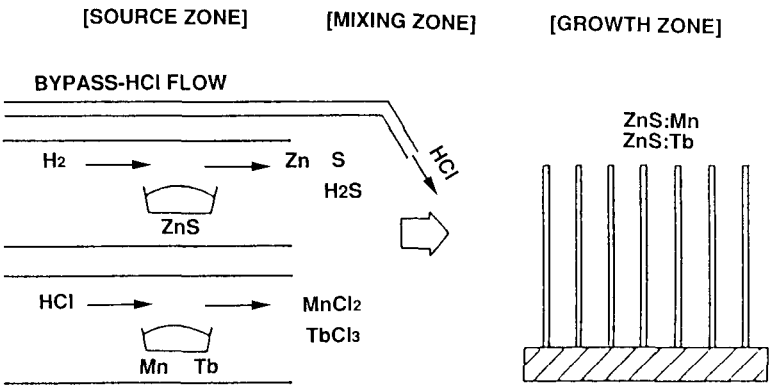


Fig. 54.  Growth process of low-pressure HT-CVD system (Ref. 213)

        The component elements Zn and S are transported as vapor and/or gaseous hydride by passing $H_2$ over the ZnS powder source.  The Mn (Tb) is transported as gaseous halide by passing HCl over the Mn (Tb) source.  The source temperature is taken to be

between 700 and 1000°C. These gases are brought together in the growth zone, where the substrates have been placed on a quartz holder.

From the results of X-ray diffraction and reflection high-energy electron diffraction (RHEED) analysis, the following results have been obtained. The undoped ZnS films have the cubic (zinc blende) crystal structure with a strong (111) orientation. The Mn- or Tb-doped ZnS films have hexagonal (wurtzite) crystals with a (001) preferred orientation. The thin-films show columnar crystals with large grains. Crystallite size vs. phosphor layer thickness characteristics are shown in Fig. 52, showing that the crystallite size of HT-CVD-grown ZnS:Mn is larger than that of MOCVD and EBE but smaller than that of ALE. The ZnS:Mn device made by this method shows high yellow luminance and high stability without any degradation in actual operation over 50000 hours. Film thickness variation can be controlled[209),210)] within ±2%, resulting in uniform EL emission over a wide area.

Figure 55 shows luminance versus voltage (L-V) characteristic curves[210)] of ZnS:Mn under a 1-kHz sinusoidal excitation. In the inset, film-thickness dependence of luminance $L_{50}$ and luminous efficiency $\eta$ is shown. EL devices with film thickness as small as 0.26 μm show steep L-V characteristics, and the maximum luminous efficiency is 4.4 lm/W in the device with 0.5 μm film thickness.
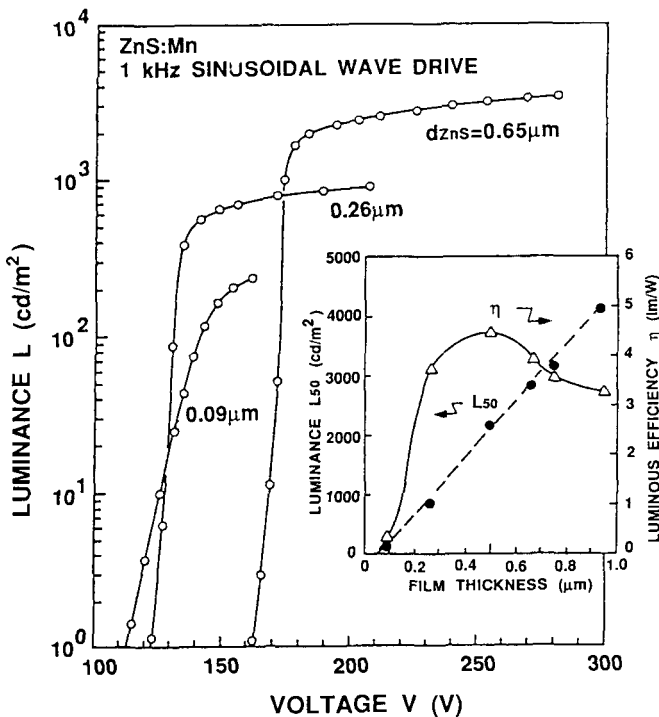


Fig. 55. Luminance versus voltage (L-V) characteristics and the film-thickness dependence of luminance $L_{50}$ and luminous efficiency of a thin-film EL device fabricated by the HT-CVD method (Ref. 210)

Figure 56 compares L-V characteristics[47] of HT-CVD- and EBE-prepared EL devices under a 100-Hz pulse wave drive condition, showing that a saturated luminance of the HT-CVD device is higher by 30% than that of the EBE device, and the threshold voltage of the HT-CVD device is lower by 25 V than that of the EBE device. These improved characteristics is attributed to better quality of HT-CVD prepared thin films.
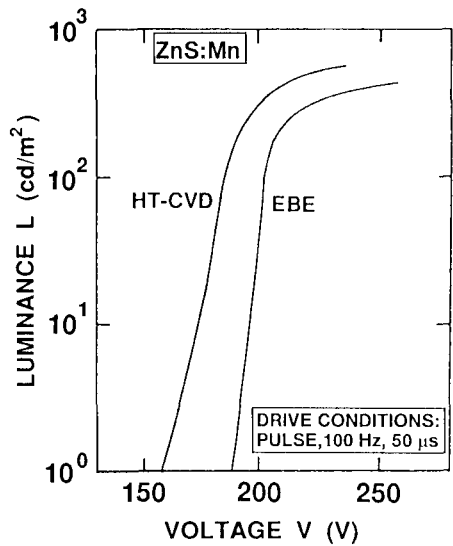


Fig. 56. Comparison of luminance versus voltage characteristics curves of thin film EL devices prepared by EBE and HT-CVD methods (Ref. 47)

Application to green-emitting ZnS:Tb,F deposition was carried out successfully[211] by introducing a bypass-HCl flow system shown in Fig. 54.

Table 12 Comparison of deposition methods used for ZnS:Mn EL devices (Ref. 169)

| Conditions and characteristics | Physical vapor deposition | | | Chemical vapor deposition | | |
|---|---|---|---|---|---|---|
|  | Sputtering | EBE | MSD | MOCVD | HT-CVD | ALE |
| Deposition rate (Å/min.) | >100 | >1000 | ~300 | >100 | >100 | 10-50 |
| Substrate temperature (°C) | 200 | 200 | 300 | 300-500 | 500 | 500 |
| Crystal structure | z.b.** | z.b. | z.b. | wur.**;z.b. | wur. | wur. |
| Peak emission wavelength (nm) | 585 | 585 | 585 | 585;580 | 580 | 580 |
| Luminance (cd/m²)* | >1500 | >3000 | >3000 | >3000 | >3000 | >3000 |
| Luminous efficiency (lm/W)* | ~2 | ~3 | ~3 | >4 | >4 | ~3 |

*1-kHz excitation        **z.b.: zinc blende, wur.: wurtzite

### 6.1.3. Summary of Phosphor Deposition Methods

Table 12 summarizes deposition conditions of phosphor layers and luminescent characteristics of ZnS:Mn EL devices. By the low-temperature physical vapor deposition (PVD) methods, thin columnar ZnS:Mn thin-film crystals with cubic zinc blende crystal structure were obtained with orange-yellow EL emission. On the other hand, by the high-temperature chemical vapor deposition (CVD) methods, large-grain columnar ZnS:Mn thin-film crystals with hexagonal wurtzite crystal structure were obtained with yellow EL emission. The luminous efficiency was larger in the CVD-prepared EL devices.

### 6.2. Insulating Layer Deposition Methods

Originally electron-beam evaporation was used to fabricate insulating layers because of easiness of evaporation materials and evaporation sources, in particular oxide sources such as $Y_2O_3$ were used. However, these insulating films tended to have deficiencies such as too much porosity and oxygen deficiency resulting in low breakdown electric field. With the development of sputtering which enabled thin film deposition of high melting-temperature materials and reactive deposition, sputtering has become the standard deposition method of oxide as well as nitride insulating layers. In particular, reactive sputtering was extensively adopted throughout the deposition of these insulating layers to assure the film purity and reproducibility of film characteristics and uniformity of EL luminance. In addition, sputtering can be applied to large area devices with uniform thickness.

Atomic layer epitaxy (ALE) is also used to deposit high-quality insulating layers[190]: The ALE-grown $Al_2O_3$, $Al_2O_3/TiO_2$ and $Ta_2O_5/TiO_2$ are good insulating layers. They are pinhole-free and their breakdown voltages are as high as $3 \times 10^8$ V/m. The source materials are $AlCl_3$, $TiCl_4$ and water. The resulting films are amorphous since the process temperatures (450-500°C) are not sufficient for crystallization of these reactive oxides.

With a plasma-CVD method[214] it becomes possible to deposit good quality $Si_3N_4$ and SiON insulating thin films at low temperature. Furthermore, electron cyclotron resonance (ECR) plasma CVD method[215] is promising because of possibility of realizing insulating thin films with high-breakdown electric field and long-time stability.

### 6.3 ITO (Indium-Tin-Oxide) Deposition Methods

For the deposition of ITO, physical vapor deposition method such as electron-beam evaporation, thermal evaporation and sputtering and chemical vapor deposition method have been investigated. Sputtering, in particular magnetron sputtering, is now the standard deposition method for high-quality ITO films[216),217)], because of the good characteristics of the deposited thin films and the high production yield. Control of oxygen partial pressure during deposition is important.

# 7. PHOSPHOR MATERIALS AND LUMINESCENT CENTERS OF COLOR THIN-FILM EL DEVICES

This chapter discusses in detail the recent developments of thin-film EL phosphors for three primary colors (red, green and blue) and for white. Primarily II-VI compounds are used as thin-film EL phosphor materials: $ZnS^{34)-38)}$ activated by manganese (Mn) or rare-earth elements (RE), and alkaline-earth sulfides CaS and $SrS^{50)-55)}$ activated by cerium (Ce) or europium (Eu). Recently, ternary compound phosphors have been developed for thin-film EL. Cerium doped alkaline-earth thiogallates[4),140)], in particular, are efficient blue EL phosphors. Furthermore, these phosphors have been combined to obtain white-light emitting phosphors[57),62)-64),67),218)], which are useful for multicolor thin-film EL panels when used with color filters. This chapter concludes with a discussion on luminance requirements[219),220)] for primary colors based on the American National Standards Institute/Human Factor Society (ANSI/HFS) 100-1988 standard and on the European Broadcasting Union (EBU) standard.

## 7.1. Color Thin-Film EL Devices Based on ZnS Phosphors

### 7.1.1. Yellow- or Orange-Yellow-Emitting ZnS:Mn

The ZnS:Mn EL device shows the highest luminance and luminous efficiency (See Table 13). This can be explained by the fact that Mn has both the right valence (+2) and a similar ionic-radius size to the Zn atoms (only 8 % difference) in the ZnS lattice (See Table 14). This valence matching leads to high solid solubility without using charge compensators. As a result, Mn can be distributed uniformly in ZnS by substituting very nicely even at low process temperatures, and large impact cross section ($2x10^{-16}$ $cm^2$) is realized. In fact, Mn is miscible in the ZnS lattice over a wide solid solution range, because ZnS and MnS have the same crystal structure. These conditions lead to high luminance and high luminous efficiency (2-4 lm/W). The $3d^5$-energy-level configurations of $Mn^{2+}$ are the $^6S$ ($^6A_1$) ground state and the $^4G$ ($^4T_1$) first excited state.
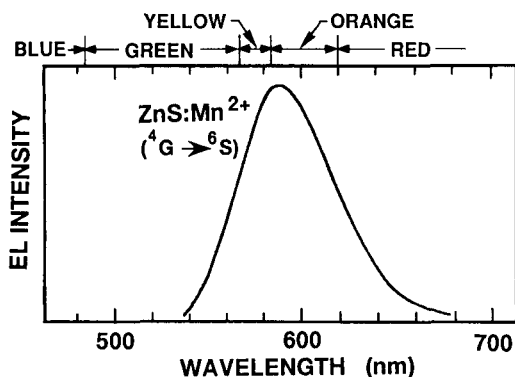
Fig. 57. EL emission spectrum of a ZnS:Mn thin-film EL device (Ref. 11)

As shown in Fig. 57, a broad orange-yellow emission with a peak around 585 nm for cubic ZnS:Mn is realized when the transition from $^4G$ ($^4T_1$) to $^6S$ ($^6A_1$) occurs. This d-d transition is partially allowed under the perturbation of the crystal field around $Mn^{2+}$.

The CIE color coordinates of this emission are x=0.50 and y=0.50. We note that this orange-yellow emission with a peak around 585 nm is realized in the cubic ZnS with the zinc-blende crystal structure when deposited at low temperatures by electron beam evaporation or sputtering. On the other hand, yellow emission with a peak around 580 nm is realized in the hexagonal ZnS with the wurtzite crystal structure when deposited at high temperatures by atomic layer epitaxy, halogen-transport chemical vapor deposition or multi-source deposition (See Section 6.1, for detail).

Since the emission spectrum of ZnS:Mn is very broad, ranging from green to red as shown in Fig. 57, a bright red emission can be obtained by using a red filter. Tuenge and Kane[40] reported a bright red EL emission by using an inorganic thin-film long-wavelength pass filter made of cadmium sulfoselenide (CdSSe). They obtained a luminance ($L_{35}$) of 75 cd/m$^2$ and luminous efficiency of 0.8 lm/W at a 60-Hz pulse-wave driving. The CIE color coordinates are x=0.65 and y=0.35, which indicates that the color gamut is very close to that of the color-CRT red phosphor $Y_2O_2S$:Eu whose CIE color coordinates are x=0.624 and y=0.337.

Green emission can be also obtained by filtering out the green component of the ZnS:Mn spectrum. Okibayashi et al.[47] obtained filtered yellowish-green luminance of 80 cd/m$^2$ with the CIE color coordinates of x=0.45 and y=0.55 at 60-Hz pulse driving.

### 7.1.2. Multicolor-Emitting ZnS:RE,F (RE: Rare-Earth Elements)

Rare-earth ions have been the most important luminescent centers for multicolor electroluminescent devices since Lumocen devices were first reported[20),33]. Figure 58 shows that most rare-earth-doped ZnS EL devices yield EL emissions in the visible-light region[38),75),218].
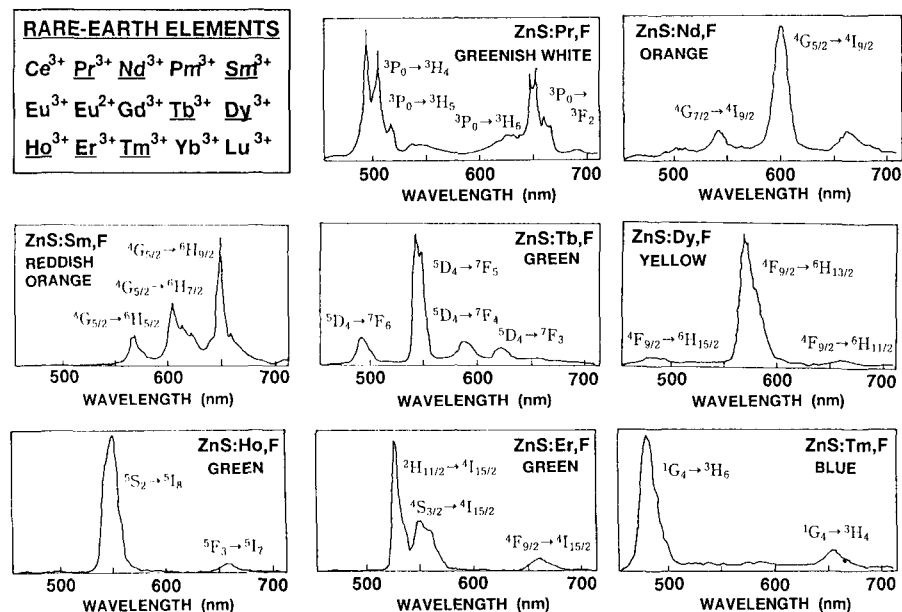


Fig. 58. EL emission spectra of ZnS:RE,F thin-film EL devices (RE: Rare-earth elements) (Ref. 75)

The EL emission spectra consist of line spectra due to (4f) inner-shell transitions. For the three primary-color representations, ZnS:Sm,F is used for red; ZnS:Tb,F, for green; and ZnS:Tm,F, for blue. As shown in the box in the upper left corner of Fig. 58, the valence of rare-earth ions is usually +3, so that charge compensation is necessary.

Table 13 lists the maximum reported luminances and luminous efficiencies of these EL devices.

Table 13  Luminance and luminous efficiency of color thin-film EL devices (Ref. 13)

| Phosphor layer material | Emission color | CIE color coordinates | | Luminance $L(cd/m^2)$ | | Luminous efficiency $\eta(lm/W)(1\ kHz)$ |
|---|---|---|---|---|---|---|
| | | x | y | 1 kHz | 60 Hz | |
| ZnS:Mn | Yellow | 0.50 | 0.50 | 5000 | 300 | 2-4 |
| ZnS:Sm,F | Reddish-orange | 0.60 | 0.38 | 120 | 8 | 0.05 |
| ZnS:Sm,Cl | Red | 0.64 | 0.35 | 200 | 12 | 0.08 |
| CaS:Eu | Red | 0.68 | 0.31 | 200 | 12 | 0.05 |
| ZnS:Mn/Filter | Red | 0.65 | 0.35 | 1250 | 75 | 0.8 |
| ZnS:Tb,F | Green | 0.32 | 0.60 | 2100 | 125 | 0.5-1 |
| ZnS:Mn/Filter | Yellow-green | 0.45 | 0.55 | 1300 | 80 | —— |
| CaS:Ce | Green | 0.27 | 0.52 | 150 | 10 | 0.1 |
| ZnS:Tm,F | Blue | 0.11 | 0.09 | 2 | <1 | <0.01 |
| SrS:Ce | Blue-green | 0.19 | 0.38 | 900 | 65 | 0.44 |
| ZnS/SrS:Ce | Bluish-green | 0.26 | 0.47 | 1500 | 96 | 1.3 |
| ZnS/SrS:Ce/Filter | Greenish-blue | 0.10 | 0.26 | 220 | 14 | 0.2 |
| CaGa$_2$S$_4$:Ce | Blue | 0.15 | 0.19 | 210 | 13 | —— |
| SrS:Ce,Eu | Eggshell-white | 0.41 | 0.39 | 540 | 32 | 0.4 |
| SrS:Ce/CaS:Eu | Paper-white | 0.35 | 0.36 | 280 | 17 | —— |
| ZnS:Mn/SrS:Ce | Yellowish-white | 0.42 | 0.48 | 2450 | 225 | 1.3 |

Table 14  Ionic radii of host materials and luminescent centers (Ref. 13)

| Ion | Radius (Å) | Ion | Radius (Å) | Ion | Radius (Å) |
|---|---|---|---|---|---|
| $Zn^{2+}$ | 0.74 | $Mn^{2+}$ | 0.80 | $Eu^{2+}$ | 1.09 |
| $Ca^{2+}$ | 0.99 | $Ce^{3+}$ | 1.034 | $Tb^{3+}$ | 0.923 |
| $Sr^{2+}$ | 1.13 | $Sm^{3+}$ | 0.964 | $Tm^{3+}$ | 0.869 |

*(1)  Green-Emitting ZnS:Tb,F*

The ZnS:Tb,F green-emitting EL devices are second in luminance[35] to ZnS:Mn device (See Table 13). The $Tb^{3+}$ ion has an ionic radius of 0.923 Å, which is 25% larger than that of $Zn^{2+}$ ion (Table 14). This size mismatch makes thermal diffusion of Tb ions into the ZnS lattice difficult. To overcome this difficulty, sputtering process was found to be very effective[35],[37],[171],[221] because sputtering imparts a kinetic energy of several eVs to the nucleating atoms during the film growth. The ion bombardment during

sputtering must influence both the crystal growth of the ZnS and the Tb dopant incorporation site in such a way that the Tb dopant is more effectively incorporated into the thin-film phosphor. Atomic-layer epitaxy[196] was also found to be effective in uniform doping of $TbS_x$ luminescent center at high concentration, and luminance level of ALE $ZnS:TbS_x$ became almost the same as that of sputtered ZnS:Tb,F.

Figure 59 shows the emission spectrum of the green emitting ZnS:Tb,F, showing that this phosphor is a line emitter which is the characteristics of an f-f transition. The CIE color coordinates are very close to the standard color CRT green (See Fig. 67). Because green is near the maximum of the eye sensitivity curve, this phosphor is expected to have monochrome as well as color applications.
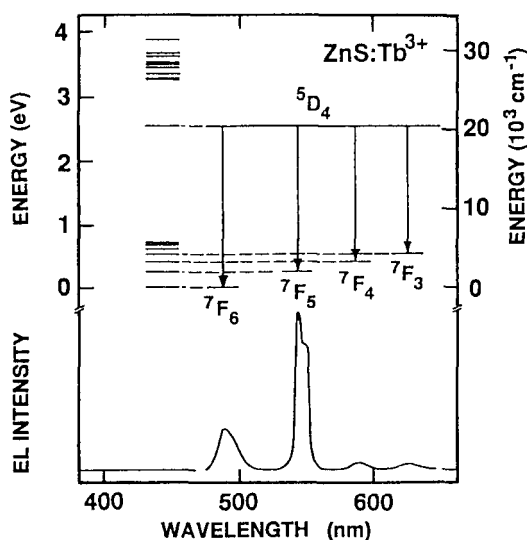


Fig. 59. EL emission spectrum of the green emitting $ZnS:Tb^{3+}$ thin film EL device with corresponding energy levels to emission peaks (Ref. 38)

The charge-compensation problem was studied extensively to find ways to increase luminance, and fluorine (F) or chlorine (Cl) was introduced. It was found that co-doped Re,F luminescent centers were effective[222] in increasing luminance. Furthermore, the role of F in ZnS:Tb,F has received a particular attention[37],[223)-226]. In these experiments, the luminance of sputtered ZnS:Tb,F was studied as a function of the luminescent-center concentration in the sputtering targets and the sputtered phosphor films. It was found that not only the Tb concentration but also the F concentration affect luminance. As shown in Fig. 60, the highest luminance was obtained when the [F]/[Tb] ratio was close to unity[37],[224)-226]. This is reasonable, considering that a $Tb^{3+}$ ion replaces a $Zn^{2+}$ ion and an $F^-$ ion acts as a charge compensator for the excess positive charge. Furthermore, recent studies have shown that TbOF complex luminescent centers[226)-231] are even more effective in increasing luminance and luminous efficiency (~1 lm/W).
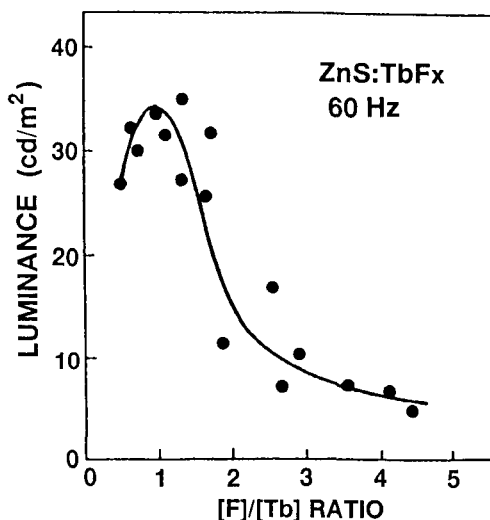
Fig. 60. Luminance versus [F]/[Tb] ratio in green-emitting ZnS:Tb,F thin-film EL devices (Ref. 226)

Recent reports on luminance stability of ZnS:Tb,F is encouraging. Tuenge[232] reported an 8% decrease in luminance after about 3000 hours at 1-kHz operation, which roughly corresponds to only 2 % in 10 000 hours at 60 Hz. The shift in threshold voltage was also reported to be on an acceptable level. Okamoto and Watanabe[223] found that increased non-radiative relaxation, which is responsible for luminance degradation, can be considerably reduced by post-annealing at about 600°C.

### (2) Red-Emitting ZnS:Sm

In attempting to increase the luminance of red-emitting ZnS:Sm,F EL devices, the ionic radius difference (30% mismatch) and valence difference must also be taken into account. Since Sm has a valence of +3, most of the investigations utilized a co-activator with a valence of -1 in an attempt to charge compensate so that a valence match to the divalent Zn can be achieved. Typically, this has been a halogen[38] such as fluoride (F) or chlorine (Cl), but also phosphorus (P) has been used[233]. The ZnS:Sm,F, which was the activator/co-activator dopant first investigated by Chase *et al.*[33] emits an reddish-orange color with the CIE color coordinates x=0.60 and y=0.38. Therefore, ZnS:Sm,F does not achieve the deep red of the standard color CRT red phosphor. The chromaticity was first improved[233] using P as a co-activator instead of F, resulting in red emission with the CIE color coordinates x=0.63 and y=0.36. The chromaticity was further improved[39] using Cl as a co-activator, resulting in red emission from ZnS:Sm,Cl with the CIE color coordinates x=0.64 and y=0.35. The chromaticities of these latter two thin-film EL phosphors are quite close to the standard color CRT red phosphor and thus they appear to better meet the requirements for a full-color thin-film EL display than ZnS:Sm,F. The reason of chromaticity shifts can be interpreted from the following arguments. As shown in Fig. 61, the $Sm^{3+}$ ion has three line emissions due to multiple $^6H_J$ (J=9/2, 7/2 and 5/2)

final transition states. The relative intensities of the transitions to these multiple final states is apparently affected by the local crystal fields, which are, in turn, modified by the co-activators. We note that the Cl co-activator gives rise to the sharpest lines which implies that the local environment of the Sm ions for this co-activator is the most regular.
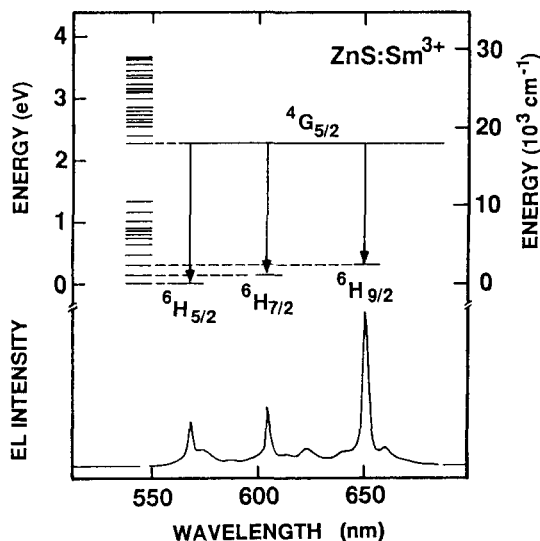


Fig. 61. EL emission spectrum of red-emitting $ZnS:Sm^{3+}$ thin-film EL device with corresponding energy levels to emission peaks (Ref. 38)

The maximum luminance reported for ZnS:Sm is 1000 cd/m$^2$ at 5-kHz driving by using ZnS:Sm,Cl[39], which extrapolates to approximately 12 cd/m$^2$ at 60 Hz. This luminance level is at least a factor of four smaller than the minimum requirements given in Table 15. Therefore, ZnS:Sm is not a good candidate for a red EL phosphor.

*(3) Blue-Emitting ZnS:Tm,F*
The only blue phosphor reported to date is ZnS:Tm,F. Although the color purity is very good, with x=0.11 and y=0.09, the luminance level is very low with 2 cd/m$^2$ at 1-kHz driving[34]. This is due to the poor ionic-radius and valence matching between Zn$^{2+}$ and Tm$^{3+}$. This is disappointing since Schrader et al.[234] pointed out that ZnS:Tm is a fairly efficient blue CRT phosphor. As shown in Fig. 62, the emission spectrum of ZnS:Tm$^{3+}$ consists of three manifolds in the blue, red, and infrared portions of the spectrum. Apparently one of the causes for the relative inefficiency of ZnS:Tm as a thin-film EL phosphor is that the EL emission spectrum is more concentrated in the infrared at 800 nm, whereas the blue emission dominates the spectra of the powder CRT material, as shown in the photoluminescence (PL) spectrum. Thus, there is still potential that a new process approach for this material may improve its performance as a thin-film EL phosphor. At present, therefore, ZnS:Tm,F is not a satisfactory blue phosphor, although the emission color is pure blue.
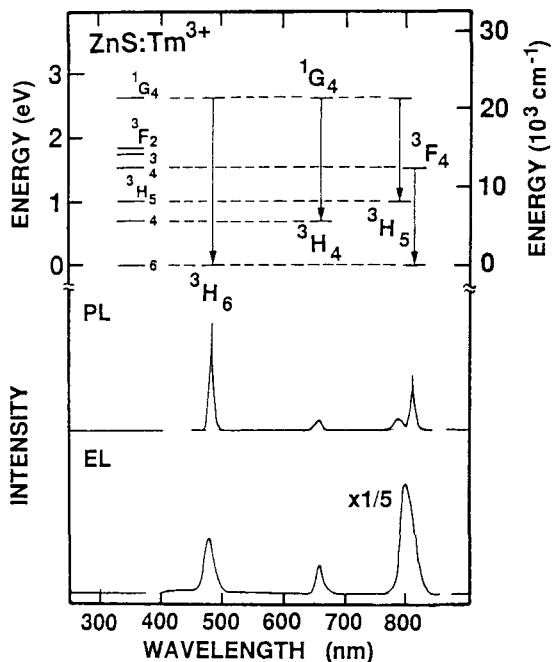
Fig. 62. EL and PL emission spectra of blue-emitting ZnS:Tb,F thin-film EL device with corresponding energy levels to emission peaks (Refs. 38, 294)

## 7.2. Color Thin-Film EL Devices Based on CaS and SrS Phosphors

Alkaline-earth sulfides, such as CaS and SrS, are known as dc powder multicolor EL phosphors[235),236)]. Practical application to thin-film EL devices has become possible thanks to the recent progress in thin-film fabrication technologies. Cerium (Ce) doped strontium sulfide (SrS) was the first alkaline-earth thin-film EL phosphor to be investigated[50)] and report of a 100 times improvement in the luminance over ZnS:Tm,F as a blue phosphor stimulated much of the recent investigations of both SrS and CaS as thin-film EL host material. Now it is possible to obtain red and blue EL emissions with high luminance[50)-57)].

By doping rare-earth elements as luminescent centers into CaS and SrS, primary-color EL emissions can be obtained. The EL emission spectra are shown in Fig. 63, and the maximum luminances and luminous efficiencies are given in Table 13. Since EL emissions from $Eu^{2+}$ and $Ce^{3+}$ luminescent centers are due to f-d allowed transitions, the emission spectra strongly depend on the choice of host phosphor material.
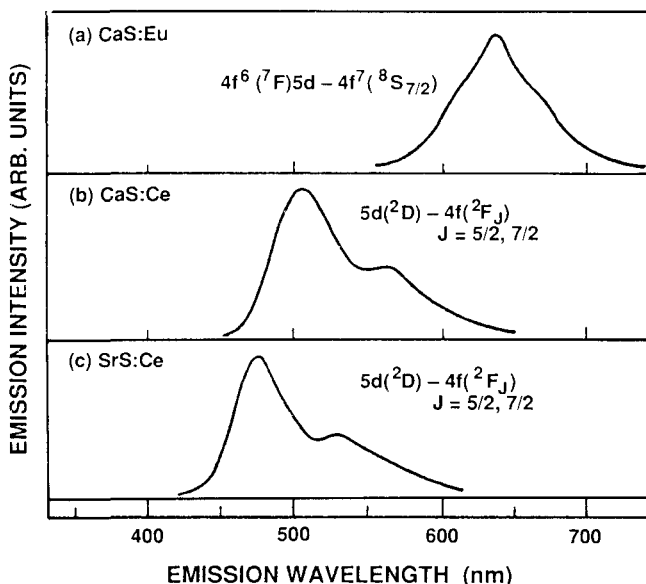
Fig. 63. EL emission spectra of CaS and SrS thin-film EL devices: (a) CaS:Eu; (b) CaS:Ce; (c) SrS:Ce (Refs. 13, 52)

## 7.2.1. Red-Emitting CaS:Eu

CaS:Eu is a promising candidate to achieve a bright red thin-film EL phosphor. Since $Eu^{2+}$ is a stable ion and the ionic radius difference from $Ca^{2+}$ is only 10% (Table 14), Eu can easily be doped into a CaS host. In fact, Eu doped CaS is very similar to Mn doped ZnS. For instance, this center is a broad band emitter due to 5d-4f transition and the 5d electrons are strongly coupled to the host lattice in the same way the d-d transition is for ZnS:Mn. As shown in Fig. 63(a), EL emission from CaS:Eu is deep red with an emission peak around 650 nm. The CIE color coordinates are x=0.68 and y=0.31, providing an even deeper red than the standard color CRT phosphor. These promising features of the CaS:Eu system are balanced by the fact that CaS is somewhat difficult to process because it is a refractory material and also because it tends to react with moisture. The latter means the material must be carefully handled to minimize exposure to a moisture-containing atmosphere and the former implies high temperature processing (such as substrate temperatures of 550 to 700°C). High temperature processing in the electron-beam evaporation method led to luminance increase[53)-57)] to 200 cd/m$^2$ at 1-kHz driving. This extrapolates to a luminance of 12 cd/m$^2$ at 60-Hz driving. This improvement was found to be related to crystalline improvement accompanied by changes in crystalline alignment planes; e.g., in CaS:Eu EL, increasing the temperature changed the crystalline alignment plane from (200) to (220) to (111). This change was attributed to the density of dangling bonds on the alignment plane and the effect of re-evaporation of the deposited atoms[237)].

Thus, at present, CaS:Eu has achieved a higher luminance level than the ZnS:Sm thin-film EL phosphor. However, the CaS:Eu phosphor tends to have a stability problem of luminance degradation[55], which was solved by replacing the insulating layers adjacent to CaS:Eu phosphor from oxides, such as $Ta_2O_5$, to nitrides, such as $Si_3N_4$.

In electron-beam-evaporated CaS:Eu devices, emission and charge density responses were found to be slow[80],[238], which must be remedied before CaS:Eu can be used as a practical red phosphor. Recently, it was found[239] that this slowness could be remedied without changing the color gamut by coactivating CaS:Eu with a small amount (0.05 mol%) of Ce.

### 7.2.2. Green-Emitting CaS:Ce
As shown in Fig. 63(b), the EL emission from CaS:Ce is green and the spectrum is broad and has peaks at 505 and 570 nm. The luminance of CaS:Ce is only 10% that of ZnS:Tb,F and therefore insufficient.

### 7.2.3. Blue-Green-Emitting SrS:Ce
SrS:Ce was the first alkaline-earth thin-film EL phosphor to be investigated[50] and luminance level of blue-green emission was one hundred times larger than that of ZnS:Tm,F. This is due to the fact that the Ce ion is a much better match for the SrS lattice (only 9 % mismatch of ionic radius, Table 14) than the ZnS host lattice. In addition to the size question, the +3 valence of the Ce has to be charge compensated with a co-activator to optimize the performance. Various groups have reported using fluoride (F), chloride (Cl) and potassium (K) as co-activators with fairly similar results. Like the CaS host described above, SrS requires a higher processing temperature and is more chemically unstable than ZnS. Thus, typically deposition at substrate temperature in the 500 to 700 °C range are required and often either excess sulfur or ZnS buffer layers are used[52],[53] to achieve the proper stoichiometry for the SrS thin films. Furthermore, it has been reported that ZnS acts as an effective electron injection layer for SrS[240],[241] which enhances its luminance.

There are at least two issues with this material as a blue thin-film EL phosphor. First, the luminance stability is not as good as ZnS-based phosphors. As described above, in the case of CaS the proper choice of materials for the insulator/phosphor interface greatly improved this characteristics. Perhaps similar results will be good for SrS, but there are no literature reports as yet on this topic.

The second issue is the chromaticity of SrS:Ce, which is blue-green rather than pure blue. This is due to the fact that the 4f ground state is doublet ($^2F_J$ with J=5/2 and 7/2) with one peak in the green at approximately 530 nm and one peak in the blue at 480 nm, as shown in Fig. 63(c) This is actually quite a good color for a multicolor data display since the eye has difficulty with the deeper CRT blue both in sensitivity and depth of focus, but for a video display this blue-green restricts the achievable color gamut. One approach to address this issue is use of a blue filter to obtain pure blue emission with good color purity[57],[61]. However, this is at the expense of reducing the blue luminance by a factor of 5 to 10.

Tanaka et al.[242] reported improving the luminance of blue-green SrS:Ce by using an argon-sulfur post-deposition annealing at 630°C. The device showed luminance of 900 cd/m$^2$ and luminous efficiency of 0.44 lm/W at 1-kHz drive. At 60-Hz-drive, they obtained a luminance $L_{60}$ of 65 cd/m$^2$ and a filtered blue luminance of 6 cd/m$^2$ with the CIE color coordinates of x=0.104 and y=0.147. Luminance was further improved[5]-[7] by employing a ZnS/SrS:Ce multilayered phosphor thin film. The nine alternating ZnS and

SrS:Ce layers were prepared by a reactive evaporation technique. Here ZnS is considered to be the electron acceleration layer and SrS:Ce is the emitting layer. The unfiltered luminance was 96 cd/m$^2$ and blue-filtered luminance was 14 cd/m$^2$ at 60-Hz pulse driving. The corresponding CIE color coordinates for the unfiltered emission were x=0.26 and y=0.47, and for the blue-filtered, x=0.10 and y=0.26. The highest luminous efficiency was 1.3 lm/W for the unfiltered emission, and 0.2 lm/W for the filtered blue emission. This luminance level of filtered blue emission is about 100 times higher than that of ZnS:Tm,F (Table 13). Therefore, SrS:Ce and ZnS/SrS:Ce are promising as blue EL phosphors.

The SrS thin films tend to be sulfur-deficient and easily oxidized[243),244)] as well as being hygroscopic. To cope with these problems, sulfur coevaporation and reduction of oxygen in the target materials have been found to increase the luminance. To prevent moisture from entering the phosphor layer, device structure must be optimized to include different insulating-layer material combinations and accommodate various process conditions.

## 7.3. Color Thin-Film EL Devices Based on Alkaline-Earth Thiogallate Phosphors

The alkaline-earth thiogallates, MGa$_2$S$_4$ (M: Ca, Sr or Ba), activated by Ce$^{3+}$ and Eu$^{2+}$, have been known to be relatively efficient cathodoluminescent phosphors[139)]. They yield deep blue when doped with Ce$^{3+}$ and green when doped with Eu$^{2+}$. These emissions provide significantly better color purities than those attained with alkaline-earth sulfide phosphors. These ternary sulfides were also more chemically stable than the alkaline-earth sulfides; they are also less susceptible to hydrolysis. Recently, these thiogallates have been successfully applied to thin-film EL devices: CaGa$_2$S$_4$:Ce, SrGa$_2$S$_4$:Ce and BaGa$_2$S$_4$:Ce yield deep blue EL emission[4),140),245)-247)]and SrGa$_2$S$_4$:Eu yields deep green EL emission[248),249)]. To deposit thin films with proper stoichiometry, sputtering method is appropriate because the three elements of the ternary material have very different vapor pressures. As shown in Table 4 the thiogallates have an energy band gap of 4.1-4.4 eV, which is comparable to the band gaps of the alkaline-earth sulfides (See Table 3). The dielectric constant of these thiogallate compounds is about 15, which is much larger than that of alkaline-earth sulfides or zinc sulfide. Therefore, high-dielectric-constant insulating layers must be used in fabricating EL devices.

### 7.3.1. Blue-Emitting MGa$_2$S$_4$:Ce (M: Ca, Sr or Ba)

Cerium-doped calcium, strontium and barium thiogallates thin films (CaGa$_2$S$_4$:Ce, SrGa$_2$S$_4$:Ce and BaGa$_2$S$_4$:Ce) were prepared[4),140),245),246)] using rf sputtering method. Post-deposition rapid thermal annealing at temperatures above 650°C was necessary to obtain complete crystallization and EL emission.

Figure 64 shows the EL emission spectrum of the CaGa$_2$S$_4$:Ce EL device, indicating a pure blue emission with a peak at 459 nm. The CIE color coordinates of this emission are x=0.15 and y=0.19. The EL emission peak wavelengths and the CIE color coordinates of SrGa$_2$S$_4$:Ce and BaGa$_2$S$_4$:Ce EL devices are 445 nm with x=0.15 and y=0.10, and 452 nm with x=0.15 and y=0.15, respectively. These data show that ternary thiogallates provide a much deeper blue emission than the SrS:Ce phosphor. .The CIE color coordinates of the SrGa$_2$S$_4$:Ce phosphor has the lowest CIE y value of 0.10 and would provide a color gamut close to that of the standard CRT display. However, the eye response for SrGa$_2$S$_4$:Ce phosphor emission is nearly a factor of two less than that for the CaGa$_2$S$_4$:Ce emission. Thus for equivalent energy efficiency, the CaGa$_2$S$_4$:Ce phosphor

would achieve twice the photopic luminance of the strontium-based host. In addition, blue emission from $CaGa_2S_4$:Ce is good enough for practical purposes. Based on these arguments, $CaGa_2S_4$:Ce has been chosen as the blue phosphor.
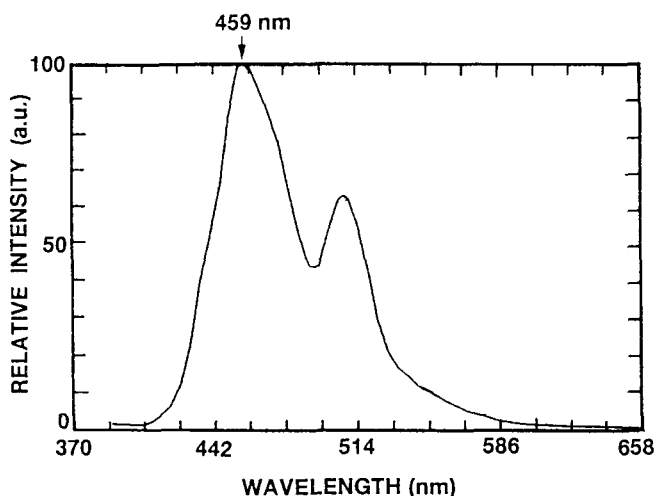


Fig. 64. EL emission spectrum of a blue-emitting $CaGa_2S_4$:Ce thin-film EL device (Refs. 4, 245, 246)
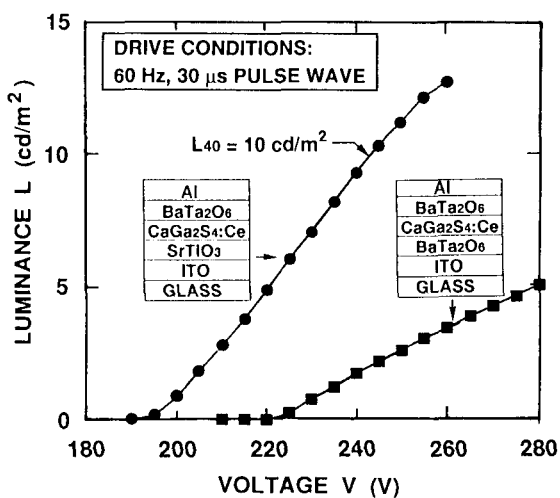


Fig. 65. Luminance versus voltage characteristics of a blue-emitting $CaGa_2S_4$:Ce thin-film EL device (Refs. 4, 245, 246)

Figure 65 shows luminance vs. voltage curves for $CaGa_2S_4$:Ce EL devices. Here, insulating layer materials with high dielectric constants, namely $SrTiO_3$ ($\varepsilon_r = 140$) and $BaTa_2O_6$ ($\varepsilon_r = 22$), were used for the lower insulating layer and $BaTa_2O_6$ was used for the upper insulating layer to increase the electric field across the phosphor layer.

In the EL device with the $SrTiO_3$ lower insulating layer, the maximum luminance of 13 $cd/m^2$ was obtained at a 60-Hz pulse-wave drive, more than twice the value obtained for the otherwise identical $BaTa_2O_6$ lower insulating layer device. This luminance level is the same as for the filtered blue luminance of ZnS/SrS:Ce (Table 13). The former device also realized a 25 V lower threshold voltage. The threshold electric field for the $CaGa_2S_4$:Ce phosphor was about $1.6 \times 10^8$ V/m, about the same as ZnS:Mn phosphor and higher than that for the SrS:Ce phosphor.

Figure 66 shows the results of initial aging measurements at 1 kHz for a sputtered $SrGa_2S_4$:Ce test device compared with that for an electron-beam evaporated SrS:Ce device. The $L_{40}$ luminance of the thiogallate device is maintained at 90% or more of the initial value for 500 hours operation at 1 kHz.
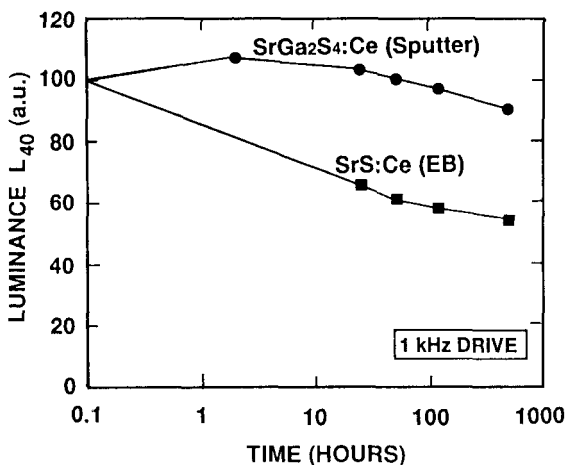


Fig. 66. Comparison of aging characteristics of sputtered $SrGa_2S_4$:Ce and EB-evaporated SrS:Ce thin-film EL devices (Refs. 4, 245, 246)

Aging characteristics of $CaGa_2S_4$:Ce is almost the same as that of $SrGa_2S_4$:Ce described here. Therefore, the stability of these ternary thiogallate phosphors is very good in agreement with the results obtained for these materials when used as CRT phosphors. Although the maintenance for these thiogallate devices are not equivalent to that for commercial ZnS:Mn panels, it is much improved over the strontium sulfide device and adequate for use in prototype color panels. In summary, for the first time the thiogallate blue phosphors have demonstrated sufficient stability, luminance and blue chromaticity to fabricate a full-color thin-film EL display.

The thiogallate blue EL phosphor has demonstrated sufficient stability, luminance and blue chromaticity without the need for filtering enabling the fabrication of full-color thin-film EL panels.

Recently, Inoue *et al.*[247] used molecular beam epitaxy to grow blue-emitting $SrGa_2S_4$:Ce phosphor films. Sr metal and $Ga_2S_3$ compounds were used as source materials. They obtained highly crystalline (orthorhombic crystal structure) and stoichiometric films at the growth temperature of 500-600°C. No post-deposition rapid thermal annealing was necessary to obtain purely blue EL emission with the emission peak of 450 nm and the CIE color coordinates of x = 0.14 and y = 0.13. The luminance level was still low: As-grown samples showed the luminance of 3 cd/m² at a 1-kHz sinusoidal wave drive condition.

### 7.3.2. Green-Emitting SrGa₂S₄:Eu

Benalloul *et al.*[248],[249] used rf magnetron sputtering to prepare $SrGa_2S_4$:Eu thin films. High-temperature post-deposition annealing above 600°C was necessary to obtain good crystallinity. EL emission from $SrGa_2S_4$:Eu is pure green with a broadband spectrum centered at 532 nm. Although the luminance level was low with 2 cd/m² at a 1-kHz sinusoidal wave drive, the EL emission color is a much deeper green, with x=0.26 and y=0.69, compared with the brighter green of ZnS:Tb,F, with x=0.28 and y=0.62.

### 7.4. Summary of Color Thin-Film EL Devices

The above results for the color thin-film EL devices are summarized in Fig. 67, which shows a CIE chromaticity diagram of color thin-film EL devices and relevant properties of suitable thin-film EL phosphors and color CRT phosphors.
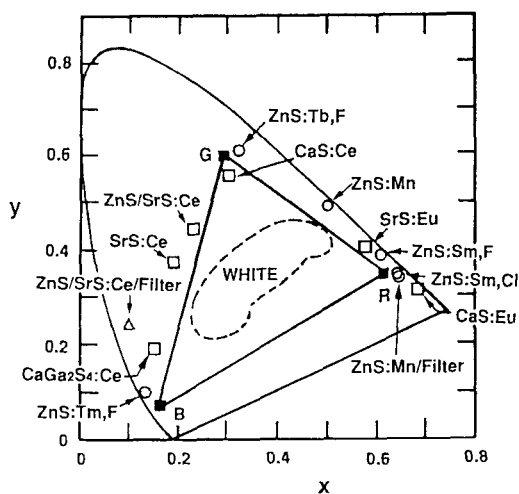


CIE Chromaticity Diagram

### Suitable Thin-Film EL Phosphors

| Color | Phosphor | CIE Color Coordinates | |
|-------|----------|-----|-----|
| | | x | y |
| Red | ZnS:Mn/Filter | 0.65 | 0.35 |
| | ZnS:Sm,Cl | 0.64 | 0.35 |
| | CaS:Eu | 0.68 | 0.31 |
| Green | ZnS:Tb,F | 0.32 | 0.60 |
| Blue | CaGa₂S₄:Ce | 0.15 | 0.19 |
| | ZnS/SrS:Ce/Filter | 0.10 | 0.26 |

### Color CRT Phosphors

| Color | Phosphor | CIE Color Coordinates | |
|-------|----------|-----|-----|
| | | x | y |
| Red | Y₂O₂S:Eu | 0.624 | 0.337 |
| Green | ZnS:Cu,Al | 0.312 | 0.597 |
| Blue | ZnS:Ag | 0.157 | 0.069 |

Fig. 67. CIE chromaticity diagram of color thin-film EL devices, properties of suitable thin-film EL phosphors and color CRT phosphors (Ref. 13)

The most suitable phosphors for multicolor EL devices based on luminance and color gamut are as follows: ZnS:Mn with red filter or ZnS:Sm,Cl or CaS:Eu for red emission; ZnS:Tb,F for green emission; and CaGa$_2$S$_4$:Ce or ZnS/SrS:Ce with blue filter for blue emission. In the figure, R, G, and B (denoted by black squares) represent the color gamut positions of red, green, and blue of color CRTs, respectively, i.e., R for Y$_2$O$_2$S:Eu (x=0.624, y=0.337), G for ZnS:Cu,Al (x=0.312, y=0.597), and B for ZnS:Ag (x=0.157, y=0.069). The CaS:Eu red EL emission and ZnS:Tb,F green EL emission are close to the corresponding CRT emissions. On the other hand, the SrS:Ce or ZnS/SrS:Ce blue-green EL emission is far from the blue CRT emission. By using a blue filter, higher-purity blue emission (indicated by the triangle) can be realized. On the other hand, CaGa$_2$S$_4$:Ce blue EL emission is close to the blue CRT emission and has a reasonable luminance.

### 7.5. White-Emitting Thin-Film EL Devices

A white-emitting phosphor may satisfy two different demands: monochromatic white thin-film EL displays and multicolor or full-color thin-film EL displays by filtering white light through color filters. For this purpose, white-light-emitting EL devices using SrS and CaS have been investigated[57),62)-64),67)].
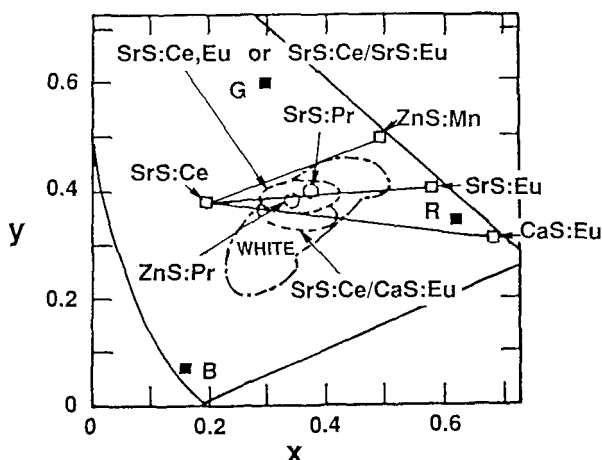


Fig. 68. CIE chromaticity diagram of white-emitting thin-film EL devices (Ref. 13)

Figure 68 shows the CIE color coordinates of several white-emitting EL devices. In particular, SrS:Ce/SrS:Eu and SrS:Ce,Eu devices[63)] produce white emissions because broad blue-green emission from Ce$^{3+}$ and broad orange-red emission from Eu$^{2+}$ are complementary colors. The white emission of Pr originates from one emission band in the bluish green and one in the red, as shown in Fig. 58. As expected from Fig. 63, the emission spectrum of SrS-based white-emitting EL devices is broad enough for them to be suitable for multicolor EL phosphors. The luminance and luminous efficiency of

SrS:Ce,Eu white-emitting phosphor, however, are still low[65),66)], at most $L_{40}=535$ cd/m$^2$ and $\eta_{40}=0.4$ lm/W, respectively, at a 1-kHz sinusoidal wave drive. For the present purpose, at least 3000 cd/m$^2$ at a 1-kHz drive is necessary. On the other hand, from an ergonomics viewpoint, a paper-white emission is more desirable than the eggshell-white emission from SrS:Ce,Eu or SrS:Ce/SrS:Eu. For this purpose, stacked-phosphor layers of SrS:Ce/CaS:Eu were studied[57)], and good color balance of R:G:B=3:6:1 was obtained by using color filters. The luminance level was still low with 280 cd/m$^2$ at a 1-kHz sinusoidal wave drive. Stability improvement of SrS:Ce,Eu thin-film EL phosphor was recently reported[64)].

Another candidate for a white-emitting phosphor is a layered ZnS:Mn/SrS:Ce thin-film phosphor[68)-71),73),74)]. Luminance improvement of ZnS:Mn/SrS:Ce multilayer phosphor was reported by Mauch *et al.*[71)] Nine alternating layers of ZnS:Mn and SrS:Ce totaling 1.5 mm thick were deposited by reactive evaporation. The luminance and luminous efficiency at a 1-kHz pulse drive were $L_{60}=2450$ cd/m$^2$ and $\eta_{60}=1.3$ lm/W, respectively. Pixel luminance levels at 100 Hz pulse drive and the CIE color coordinates of the original yellowish-white emission and the filtered red, green and blue emissions were as follows: L(yellowish-white)=376 cd/m$^2$ (x=0.42, y=0.48), L(red)=36 cd/m$^2$ (x=0.65, y=0.34), L(green)=88 cd/m$^2$ (x=0.27, y=0.63) and L(blue)=13 cd/m$^2$ (x=0.13, y=0.26). These results indicate almost perfect matching to the required color of red, and a reasonable matching of green, whereas the blue component is not saturated enough for true color reproduction.

The measured luminance and luminous efficiency of these white-emitting thin-film EL devices are also listed in Table 13.

## 7.6. Luminance Requirements for Red, Green and Blue Emissions

To estimate the necessary luminance levels[219),220)] needed in subpixels in color displays, the American National Standards Institute/Human Factors Society (ANSI/HFS) 100-1988 standard is usually used, which requires a white luminance of at least 35 cd/m$^2$. In monochrome ZnS:Mn thin-film EL displays, the luminance requirement of 35 cd/m$^2$ is fully sufficient if good contrast (>7:1) is obtained simultaneously.

Table 15   Luminance requirements for red, green and blue EL emissions in color display (Ref. 220)

| Color | Areal luminance (cd/m$^2$ at 60 Hz) | | Required color subpixel luminance (cd/m$^2$ at 60 Hz) | | | | | | Best pixel luminance (cd/m$^2$ at 60 Hz) |
|-------|------|------|-------|------|------|-------|------|------|------|
|       | EBU* | ANSI** | Fill F. | EBU | ANSI | Fill F. | EBU | ANSI | |
| Red   | 10.5 | 9.3  | 22%   | 48   | 42   | 16%   | 67   | 58   | 75 |
| Green | 20.6 | 23.0 | 22%   | 93   | 104  | 22%   | 93   | 104  | 125 |
| Blue  | 3.9  | 2.7  | 22%   | 18   | 12   | 28%   | 14   | 9.6  | 13 |
| White | 35.0 | 35.0 | 66%   | —    | —    | 66%   | —    | —    | — |

*EBU: European Broadcasting Union Standard (R:G:B = 30:59:11)
**ANSI: ANSI/HFS 100-1988 Standard (R:G:B = 27:65:8)
(ANSI: American National Standard Institute)
(HFS: Human Factor Society)
Fill F.: Fill Factor

As for color displays, the ratios for red, green and blue luminances are 30%, 59% and 11%, respectively, in the European Broadcasting Union (EBU) standard. Corresponding figures are 27%, 65% and 8% in the ANSI/HFS 100-1998 standard. The magnitude of the required minimum color subpixel luminance can be estimated based on these standards. For multicolor EL devices with a patterned-phosphor structure, the color subpixel fill-factor can be used to adjust the final color balance. Examples are shown in Table 15 together with the current best pixel luminances.

From the table, we note that satisfactory subpixel luminance levels for all three primary colors have already been attained in laboratory samples at 60 Hz drive operations.

Although the minimum white level of 35 cd/m$^2$ is required in the ANSI/HFS 100-1988 standard, a two times higher luminance level (70 cd/m$^2$) might soon be a requirement in personal computer applications to meet the competition from other flat panel display technologies. In the long run high-definition (HD) TVs may demand about 200 cd/m$^2$ of white luminance. Therefore, continuous efforts for luminance improvements in color phosphors are necessary.

# 8. DRIVE METHODS OF THIN-FILM EL DISPLAYS

The light emitting mechanism of thin-film EL displays with the double-insulating-layer structure requires alternating polarity of the driving electric field for efficient light generation. Therefore, the display has to be driven with an ac drive method. A typical thin-film EL display is an XY-matrix display with M vertical columns and N horizontal rows, as shown schematically in Fig. 69. The cross sections of the X and Y electrodes form the picture elements, pixels, of thin-film EL devices. X electrodes are referred to as column electrodes or data lines, and Y electrodes are referred to as row electrodes or scan lines. These terms are used interchangeably in the following discussion.
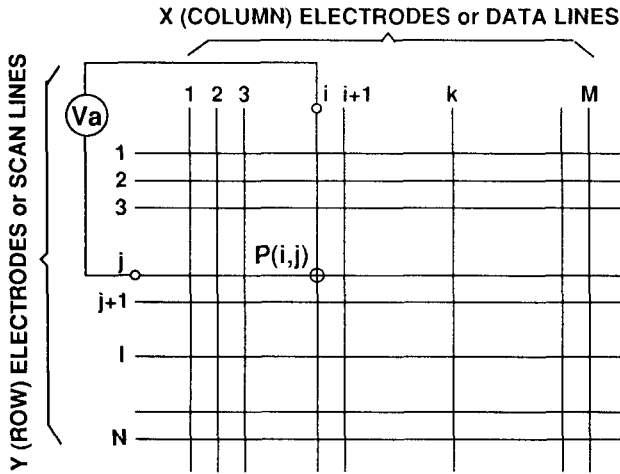


Fig. 69. XY-matrix electrode system of a typical thin-film EL display

Table 16  Selection states and pixel voltages of matrix display panels

| Pixel | Sate of Selection | Pixel Voltage |
|-------|-------------------|---------------|
| P(i, j) | Selected | $V_S = V_a$ |
| P(i, l≠j) | Half Selected (Data (X) Line) | $V_{HX} = V_a \times M/(M+N)$ |
| P(k≠i, j) | Half Selected (Scan(Y) Line) | $V_{HY} = V_a \times N/(M+N)$ |
| P(k≠i, l≠j) | Non Selected | $V_N = 0$ |

Let us select the pixel P(i,j) in the XY-matrix electrode system and impose a voltage $V_a$ for the EL emission, as shown in Fig. 69. Table 16 lists the pixels selection states and pixel voltage, when "off" electrodes are in a floating state and M, N>>1. For the M=N case, a voltage of the half-selected pixels becomes $V_a/2$. In the EL device with the sharp non-linear luminance vs. voltage (L-V) characteristics, $V_a/2$ can be taken much smaller than the threshold voltage $V_{th}$, so that no EL emission occurs at the half-selected and non-selected pixels. In this sense, the sharp non-linear L-V characteristics curve makes thin-film EL displays suitable for matrix driving. A more than three orders of magnitudes

difference in luminance is achieved by an acceptable change in drive voltage (~30 V), and light emission can be generated using voltage pulses having a pulse width of about 30 μs or even less. Drawbacks are the rather high drive voltage ranging from 180 to 240 V in commercial displays, and the substantial capacitance of the thin-film EL structure, which implies significant displacement currents.

There are two refresh-type drive methods for XY-matrix EL displays:

1. Multiplex drive method[31),250)-252)] where each scan line is addressed during the dwell time $t_s$ defined by $t_s = 1/Nf$ (line-at-a-time drive scheme). Here, N is the number of scan lines and f is the drive frequency or drive frame rate.
2. Active matrix drive method[253)-262)] using an active device such as a thin-film transistor (TFT) attached to each pixel.

In the line-at-a-time drive method, an image is generated by scanning the XY-matrix, i.e., the information on the same scan line (row electrode) is written at the same time and each scan line is addressed after the other until the whole screen is written (scanned). A write voltage $V_W$ just below or equal to the device threshold voltage is applied to the selected row (scan line) and at the same time the data information is applied to all columns (data lines), as modulation voltage $V_M$. When a pixel receives both the write and full modulation voltages ($V_W + V_M$) the pixel is fully turned on. A typical write voltage $V_W$ is 160 to 200 V and a typical modulation voltage $V_M$ is 30 to 60 V. Scanning of the whole display is performed at least 60 times a second, giving a frame rate of 60 Hz. For 400-scan lines driven at 60 Hz, the dwell time for each scan line $t_s$ becomes 40 μs. In the case of large scan lines, this drive method has drawbacks of a low duty-ratio driving, resulting in low luminance and occurrence of flickers. However, the response time of EL emission to applied voltage is fast (several microseconds), much faster than that of liquid crystal displays (several tens of milliseconds), so that high luminance can be retained even at low duty ratio driving, such as duty ratio of 1/500 to 1/1000, corresponding to 500 to 1000 scan lines, respectively.

On the other hand, in the active matrix drive method, memory effect is installed to drive circuits for each pixel. As a result, there is no limit to scan-line number even in the refresh type EL displays. However, since an EL display is a capacitive display driven at high voltage, it is necessary to fabricate high-voltage, large-current active drivers in a small area inside each pixel. The active-matrix drive method will be necessary as a future drive method for high-resolution, large information-content displays. R&D of active matrix driven EL displays is in its early stage, so that it takes some more time to reach a practical level.

The information on one data line (column electrode) is determined by the data input to column drivers. The column voltage at the intersection with row electrode is, however, affected by the resistivity of column electrode and the capacitance of thin-film EL structure: Pixels along the column form an RC network. Therefore, the resistivity of column electrodes must be low enough to allow for an RC product much shorter than the dwell time per scan line[263)]. The sheet resistance of ITO is sufficient for column electrodes, although less than 10 Ω/sq. is preferable for a 400 scan-line thin-film EL display. The conductivity of row electrodes is, on the other hand, determined by the fact that the whole line has to be written "at a time". This imposes that row drivers must be able to charge the capacitor formed by the pixels on the scan line within a few microseconds. In commercial half-page displays a current of some 100 mA is needed, and therefore, row electrodes have to be of metal.

## 8.1. Multiplex Drive Methods

In the multiplex drive methods, or line-at-a-time drive methods, the field-refresh drive method[31),250)] and symmetric drive methods, p-n symmetric drive method[251)] and p-p symmetric drive method[252)], have been used to drive thin-film EL displays. To show gray-scale images, frequency modulation method and amplitude modulation method are introduced. The latter method is employed in the recent monochrome thin-film EL display based on ZnS:Mn with 16 gray levels.

### 8.1.1. Field-Refresh Drive Method

#### (1) Field-Refresh Drive Scheme

Figure 70 shows the circuit architecture[2)] of the drive electronics of field-refresh drive method for thin-film EL display unit.
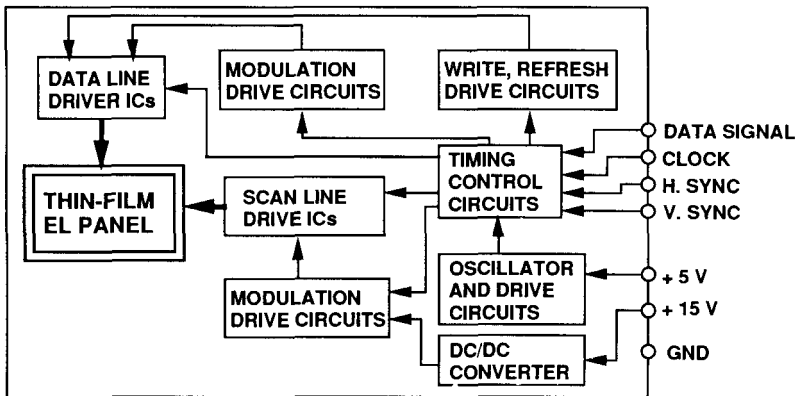
Fig. 70. Circuit architecture of the drive electronics of field-refresh drive method (Ref. 2)

The display information is inputted by applying the following four signals of LS TTL level into the unit.
1. Serial data signal (DATA SIGNAL)
2. Data transfer clock signal (CLOCK)
3. Horizontal synchronizing signal (H. SYNC)
4. Vertical synchronizing signal (V. SYNC)

The power source supplied to this display unit consists of two kinds of voltage, i.e., +5 V for the logic circuit and +15 V for the panel driving circuit. A high voltage of 160-200 V necessary in the writing and refreshing drive sequence is supplied by DC/DC converter which is built within the display unit.

Figure 71 depicts the schematic time sequence of data signal, modulation voltage to the i-th data line (column electrode), write voltages to the scan lines and pixel voltages of the pixels on the i-th column electrode in the field-refresh drive method[31),250)]. The scanning starts by applying a certain (negative) write voltage $V_w$ to the first scan line. The write voltage has to be equal to or a little lower than the threshold voltage $V_{th}$ for the onset of the emission. Simultaneously, a modulation voltage $V_M$ of opposite (positive) polarity is
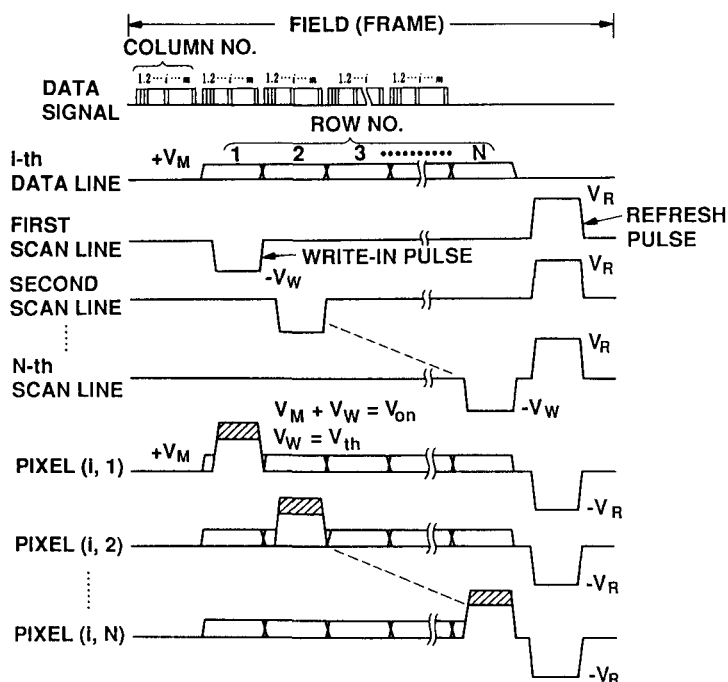
Fig. 71. Time sequence of drive wave forms in the field-refresh drive method (Ref. 31)

applied to the column electrodes (data lines) that intersect with the scan line (row electrode) in pixels in which light emission is desired ("on" pixels). Other column electrodes are grounded. The magnitude of $V_M$ is chosen so that the sum of the write voltage and the modulation voltage is well above the threshold voltage for the emission. The voltage across "off" pixels is equal to $V_W$ and consequently no light is emitted. After the first scan line has been written, which typically lasts a few tens of microseconds, the write voltage is applied to the second scan line. The voltage of the column electrode is varied according to input data so that $V_M$ is applied to "on" column electrodes, and "off" column electrodes are grounded. This procedure is repeated until all the N scan lines have been addressed. Having finished supplying one field of data to the EL device, a field-refresh pulse voltage $V_R$ of opposite polarity is applied to all the scan lines keeping simultaneously column electrodes grounded to conclude the ac cycle of the drive wave forms. In this driving method, there are two emissions per frame time (1/60 Hz).

This drive method utilizes the polarization characteristics of the double-insulating-layer structure described in Chapter 4. Emissive ("on") pixel has polarization in the phosphor layer/insulating layer interface and non-emissive ("off") pixel do not have polarization. When the field refresh pulse of opposite polarity is applied to all the scan lines, in the "on" pixel the internal electric field is larger than the threshold electric field,

resulting in EL emission. On the other hand, in the "off" pixel the electric field is lower than the threshold value, resulting in no EL emission.

Advantage of this drive scheme is that only the single-polarity wave form is necessary to drive the EL device, resulting in a simple drive circuitry. Therefore, push-pull drivers are needed only on the column side, and open-drain drivers composed of high-voltage nMOS FETs and high-voltage diodes can be used for the scan side.

Drawback of the unsymmetrical driving is that different voltage wave forms are applied to pixels at different parts of the EL devices, resulting in the deterioration of L-V characteristics and creation of latent images. The deterioration is characterized by decrease in both the threshold voltage and luminance in the high luminance region[264)-266)].

### (2) Power Consumption

As discussed in Section 4.2, power consumption in thin-film EL matrix displays is rather due to losses in driving electronics and electrodes than to the power dissipation in the phosphor film to generate light. These driving losses are due to current flow through circuit resistance in series with the thin-film EL device capacitance. In the following we first discuss power consumed in the charging process of a series RC network, and calculate the power consumption in a 640x480 thin-film EL display[104)] driven by the field-refresh drive method.

An actual thin-film EL display can be modeled as a series RC network, where the resistance is principally associated with the driver ICs and the panel transparent electrode resistance and the capacitance is mainly due to the thin-film EL device. To charge a capacitor with capacitance C to a certain voltage V through a resistor requires an energy of $W = CV^2$. Half of the energy is dissipated in the resistor, half is stored in the capacitor. It should be noted that the energy dissipation is independent of the value of the series resistance. If the capacitor is now discharged to ground through the series resistance, the stored energy of $CV^2/2$ is dissipated in the resistance and thus the entire $CV^2$ energy supplied by the voltage source is converted to heat. If the voltage source is a time varying signal with frequency f, the power consumption is given by:

$$P = fCV^2 \qquad (72)$$

Now let us use this to calculate the power consumption of a thin-film EL display panel driven by the field-refresh drive method. For the write drivers the power consumption $P_w$ is given by

$$\begin{aligned} P_w &= NfC_{row}V_w^2 \\ &= NfMC_eV_w^2 = fC_pV_w^2 \end{aligned} \qquad (73)$$

where

$N$ = number of scan lines (rows)
$M$ = number of data lines (columns)
$f$ = frame frequency
$C_e$ = capacitance of one pixel element
$C_{row}$ = capacitance of one scan line
$C_p$ = capacitance of the entire panel

The refresh drivers consume the power $P_R$ given by

$$P_R = fC_p V_R^2 \qquad (74)$$

Finally, we calculate the modulation power $P_{mod}$. This term is not only the largest factor, but also its value changes as a function of the number of pixels that are "on". The reason this term is so significant, is that each time a scan line (row) is addressed the modulation drivers charge up a large fraction of the entire panel capacitance.
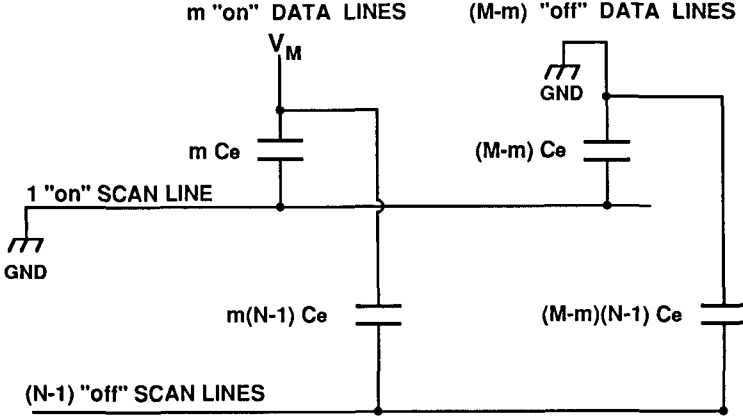


Fig. 72. The equivalent panel-load capacitance of MxN matrix EL display

This can be seen from Fig. 72 which shows the equivalent circuit capacitance seen by the column drivers. The key point here is that the data lines (columns) not only charge the written scan line (row), but also capacitively couple to all the N-1 floating scan lines (rows) which in turn are capacitively coupled to the grounded data lines (columns) to complete the circuit. As can be determined from Fig. 72, the equivalent capacitance that the modulation drivers charge is given by the following expression:

$$C_{mod} = mC_e + \frac{\left[m(N-1)C_e\right] \times \left[(M-m)(N-1)C_e\right]}{m(N-1)C_e + (M-m)(N-1)C_e} \qquad (75)$$

where

$$m \text{ elements are "on"}$$
$$M-m \text{ elements are "off"}$$

This function has a maximum when 50% of the column elements are "on" which is approximately given by

$$C_{mod} = \frac{M}{2}C_e + \frac{M}{4}(N-1)C_e \approx \frac{C_p}{4} \qquad (76)$$

Thus, the maximum power consumption occurs at a 50% screen fill factor (the worst case condition), and is given by

$$P_{mod} = \frac{1}{4} N f C_p V_M^2 \qquad (77)$$

Now let us calculate the maximum addressing power consumption for a 640x480 thin-film EL display with the following parameters:

$$
\begin{array}{ll}
N = 480 & V_W = 180 \text{ V} \\
M = 640 & V_M = 40 \text{ V} \\
C_e = 3.5 \text{ pF} & V_R = 200 \text{ V} \\
C_p = 1075 \text{ nF} & f = 60 \text{ Hz}
\end{array}
$$

Then $P_W$, $P_R$ and $P_{mod}$ are evaluated as

$$P_W = 60 \times (1075 \times 10^{-9}) \times (180)^2 = 2.09 W \qquad (78)$$

$$P_R = 60 \times (1075 \times 10^{-9}) \times (200)^2 = 2.58 W \qquad (79)$$

$$P_{mod} = \frac{1}{4} \times 480 \times 60 \times (1075 \times 10^{-9}) \times (40)^2 = 12.38 W \qquad (80)$$

The total power consumption is then given by

$$P_W + P_R + P_{mod} = 2.09 W + 2.58 W + 12.38 W = 17.05 W \qquad (81)$$

Thus the majority of the worst case power is consumed in the modulation drive.

With the above example as basis for comparison, let us consider some design approaches[104],[245] with respect to drive electronics and EL thin films that can further reduce the power consumption.

(a) Adiabatic Charging: If the capacitance in Fig. 72 is charged in two steps instead of one, the energy dissipated in the series resistance is:

$$W_2 = \frac{1}{2} C \left( \frac{V}{2} \right)^2 + \frac{1}{2} C \left( \frac{V}{2} \right)^2 = \frac{1}{4} CV^2 \qquad (82)$$

However, the final charge state of the capacitor is the same so the stored energy is still $CV^2/2$. Thus, the voltage source has supplied an energy:

$$W_2 = \frac{3}{4} CV^2 \qquad (83)$$

Thus it is possible to save 25% of the power consumption in this manner. This can be carried further by increasing the number of charging steps for the power savings. In the adiabatic limit, 50% of the power can be saved, however, there are practical limitations in terms of the length of time it takes to write a scan line. In the commercial thin-film EL panel, a 4-step modulation wave form (pre-charge, modulation (discharge or boost), write and refresh processes) is employed, resulting in 29% reduction of driving power consumption.

(b) Minimization of the Modulation Voltage: As shown above the power consumption varies as the square of the modulation voltage $V_M$. Thus lower modulation voltages can significantly reduce the power consumption. The modulation voltages for commercial EL panels range from a high of 60 V to 30 V. This causes the modulation power consumption to vary by a factor of four. The magnitude of the modulation voltage depends on the steepness of the luminance vs. voltage characteristics; the steeper the characteristics, the smaller the modulation voltage.

(c) Power Recovery : Using inductive elements[267] in the addressing circuits it is possible to store the energy flowing into and out of the panel capacitance. This is the approach that must be taken if thin-film EL displays are to be used in a battery-operated portable mode.

### 8.1.2. Symmetric Drive Methods

#### (1) P-N Symmetric Drive Method

To improve the drawback of unsymmetrical drive wave forms in the field-refresh drive method, a p-n symmetric drive method[251] has been introduced. This method is also called a field-reversal method, because the polarity of the write pulse voltages is reversed in every succeeding field. Therefore, one cycle in the p-n symmetric drive scheme is composed of two fields. As a result, only one EL emission is realized in each field.

Figure 73 shows the schematic time sequence of data signal, modulation voltage to the i-th data line (column electrode), write voltages to the scan lines and pixel voltages of the pixels on the i-th data line. The scanning procedure is essentially the same as that of the field-refresh drive scheme except the following:
1. The modulation voltage applied to data lines is the pulse voltage of both polarities with the amplitude $V_M/2$.
2. The "on"-pixel voltage $V_{on}$ and "off"-pixel voltage $V_{off}$ are $V_{on} = V_w + V_M/2$ and $V_{off} = V_w - V_M/2$, respectively. Having finished supplying data to the EL device in the first field, the same scanning procedure is performed in the second field by supplying the write pulse voltage of opposite polarity to all the scan lines.

In this way, it becomes possible to realize the symmetric voltage wave forms to each pixel in one cycle made of two fields. Realization of these wave forms requires high-voltage dual-polarity active drivers (nMOS FETs and pMOS FETs) for the scan drivers, instead of nMOS FET and diode arrays in the field-refresh drive method.

In the practical EL displays, the polarity of the write pulse voltages is reversed every scan line to reduce flickering caused by luminance difference between positive and negative write pulses applied to an EL display. Figure 74 shows the actual applied voltage wave forms to pixels (i, j) and (i, j+1) for j = odd case. In the n-p field, positive write pulses are applied to odd-number scan lines and negative write pulses are applied to even-number scan lines, and in the p-n field, the polarity of the write pulses is reversed.
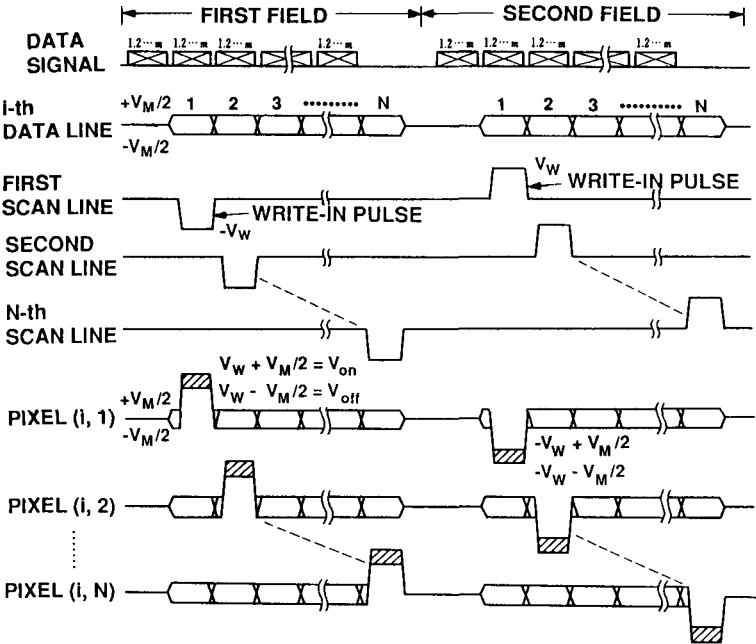
Fig. 73. Time sequence of drive wave forms in the p-n symmetric drive method (Ref. 251)
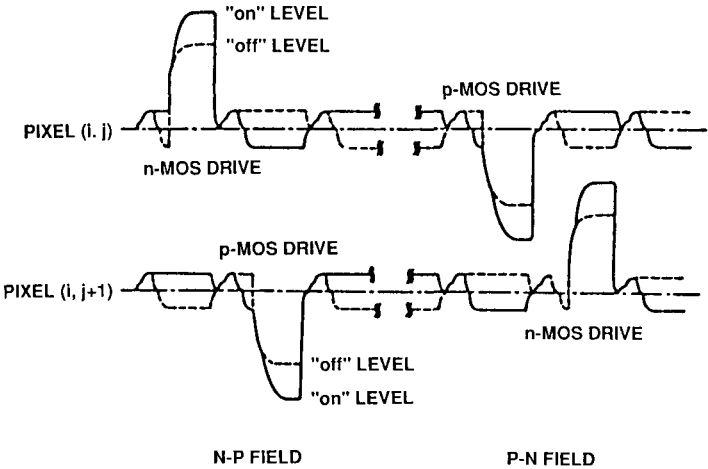


Fig. 74. Actual drive wave forms applied to the adjacent pixels (i, j) and (i, j+1) (Ref. 251)

In addition, modulation voltage is applied in two steps: In the first step, the precharging drive for the whole panel, and in the second step discharging drive for "off" pixels and pull-up charging drive for "on" pixels.

Advantages of the symmetric drive method are as follows:

1. Symmetric pulse wave forms with respect to phase and amplitude can be applied to each pixel, so that long-time reliability is increased and a luminance change with time is substantially reduced.
2. The modulation voltage $V_M$ can be taken to be larger than that in the field-refresh drive method, so that saturation region of the luminance vs. voltage characteristics curve can be utilized. As a result, the "off"-luminance becomes smaller, leading to improvement in contrast ratio and luminance uniformity over the whole display area. This is realized with almost the same luminance value as that of the field-refresh driving, even though there is only one emission in one field.
3. Since the modulation power is averaged over the n-p and p-n field driving, the maximum power consumption is reduced.

*(2) P-P Symmetric Drive Method*

For large-capacity and lower-cost thin-film EL displays, a new drive method has been developed, which is called a bi-directional push-pull symmetric drive method[252] (abbreviated as a p-p symmetric drive method). The availability of integrated high-voltage push-pull drivers has made it possible to realize this new symmetric drive method.

In this drive method the following points have been realized:

1. Reduced drive time (dwell time $t_s$) for increased number of scan lines.
2. Reduced power consumption for increased number of scan lines and increased capacitance.
3. Assured long term reliability and luminance uniformity.

For this drive scheme, the following driver ICs are used: high-voltage push-pull driver ICs both at the scan side and data side, positive write voltage drivers, negative write voltage drivers and modulation and recovery drivers.

In order to reduce the drive time necessary for large EL display with large number of scan lines, two new ideas are implemented: One is the use of push-pull ICs as column driver ICs, making it possible to apply modulation voltage in a single stage, compared to two stages in the conventional drive methods (precharge, and discharge or boost). The other is the overlapping of the modulation pulse application time with the write pulse application time

Now let us calculate the power consumption[245] in the p-p symmetric drive scheme. Figure 75 shows voltage wave forms applied to the i-th data line, the j-th and j+1-th scan lines, and pixels (i, j) and (i, j+1) for the j=odd case. The solid lines are for the lit ("on") states and the broken lines are for the non-lit ("off") states. Positive and negative write voltages are applied to each pixel in two fields: pn field and np field. (Note that the definitions of the pn and np fields are reversed from those in the p-n symmetric drive case.) In order to minimize flickers caused by luminous intensity variation in applying positive and negative pulses to the EL display panel, polarity of write pulse is reversed every scan line.

When the j-th scan line (row) is written in the pn filed, a positive voltage $V_{W1} = V_W + V_M$ is applied to the j-th scan line and the remaining scan lines are floating. Here $V_W$ is the write voltage (less than or equal to the threshold voltage $V_{th}$) and $V_M$ is the modulation voltage.
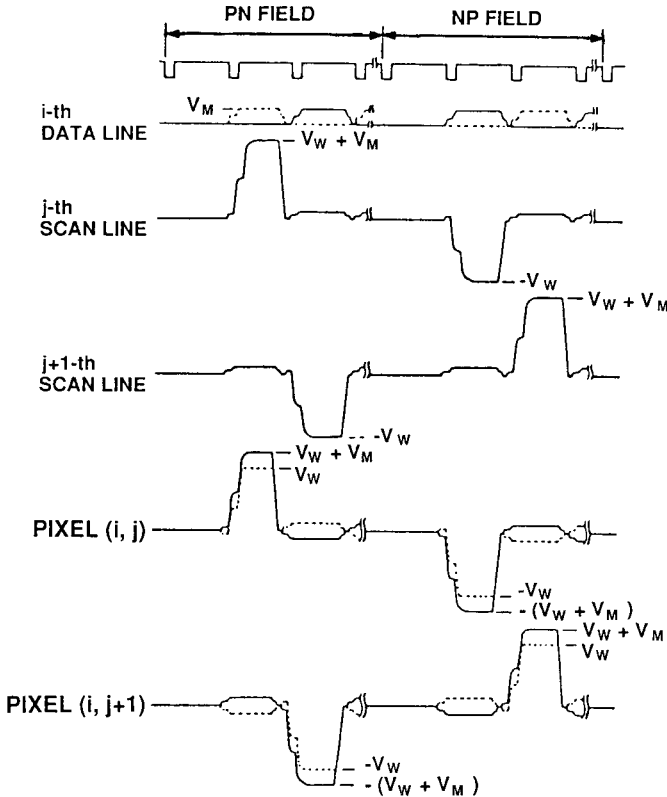
Fig. 75. Time sequence of drive wave forms in the p-p symmetric drive method (Ref. 252)

Since the magnitude of the scan-line voltage is sufficient to generate EL emission (i.e., above $V_{th}$), the data (pixel luminance information) applied to the data-line (column) electrodes is zero volts for an "on" pixel and $V_M$ for an "off" pixel because the data line voltage subtracts from the scan-line voltage of the pixel.

When the next scan line (j+1-th scan line) is written, a negative polarity voltage of magnitude $V_{W2} = V_W$ is applied to the scan line j+1 and again the remaining scan lines float. In this case the polarity and magnitude of data-line (column) voltage are chosen to add to the magnitude of $V_W$ and cause the "on" pixels to emit light, whereas the "off" pixels remain below threshold. This sequence is repeated until the entire frame in the pn field has been written. In the next frame, the np filed, the polarity of the voltages applied to the scan lines is reversed to achieve symmetric drive. Although the switching of the "on" and "off" logic levels of the data-line (column) drivers from line to line seems to be somewhat complicated, the result is that the data-line drivers are simpler in that they only have to switch a unipolar voltage. With this sequence of driving waveforms in mind, the addressing power for this circuit can now be analyzed.

The power consumption to scan half the matrix with a scan-line voltage of $V_{W1}$ is given by

$$P_{W1} = \frac{f}{2} N C_{row} V_{W1}^2 = \frac{f}{2} C_p (V_W + V_M)^2 \tag{84}$$

The power consumption to scan the other half of the matrix with a scan-line write voltage of $V_W$ is given by

$$P_{W2} = \frac{f}{2} N C_{row} V_{W2}^2 = \frac{f}{2} C_p V_W^2 \tag{85}$$

Combining Eqs. (84) and (85), the total write power consumption $P_W$ is given by

$$P_W = P_{W1} + P_{W2} = \frac{f}{2} C_p [(V_W + V_M)^2 + V_W^2] \tag{86}$$

where

$N$ = number of scan lines (rows)
$M$ = number of data lines (columns)
$f$ = frame frequency
$C_e$ = capacitance of one pixel
$C_{row}$ = capacitance of one scan line
$C_p$ = capacitance of entire panel

Next we calculate the modulation power consumption $P_{mod}$. The importance of this term is discussed in detail in Section 8.1.1. The argument there applies here also. Therefore, the equivalent capacitance that the modulation (data-line) drivers charge is given by Eq.(75), whose simplified form is given by

$$C_{mod} = mC_e + \frac{m(M - m) \times (N - 1)}{M} C_e \tag{87}$$

where

$m$ elements are "on"
$M-m$ elements are "off"

If $N \gg 1$, as in N=400 or 480 cases, then we obtain

$$C_{mod} \cong C_p [\frac{m}{M}(1 - \frac{m}{M}) + \frac{m}{M} \times \frac{1}{N}] \tag{88}$$

There are two interesting limits for this function $C_{mod}$. In a typical display pattern for text or graphics the fraction m/M is usually small (10%) in the normal-mode representation or nearly 1 (90%) in the reverse-mode representation. In both of these cases $C_{mod}$ is small. For example, the limiting value of Eq. (88) for small m/M is

$$C_{mod} = \frac{m}{M} C_p$$

(89)

In this limit the modulation power consumption $P_{mod}$ is given by

$$P_{mod} = Nf(\frac{m}{M})C_p V_M^2$$

(90)

The worst case power consumption occurs when m = 0.5 M. In this case, the power consumption is given by

$$P_{mod} = \frac{1}{4} NfC_p V_M^2$$

(91)

Using these equations, let us calculate the power consumption for a 10-inch-diagonal 640x480 pixel (VGA) thin-film EL display with a pixel pitch of 0.30 mm (pixel size of 0.22 mm x 0.22 mm) and the following parameters:

| | |
|---|---|
| N = 480 | $V_W$ = 180 V |
| M = 640 | $V_M$ = 40 V |
| $C_e$ = 3.5 pF | f = 60 Hz |
| $C_p$ = 1.075 μF | |

Table 17 summarizes the calculated power consumption for this display.

Table 17  Calculated power consumption for 640x480 VGA format thin-film EL display (Ref. 245)

| Power component (W) | Typical power (m = 0.1 M) | Maximum power (m = 0.5 M) |
|---|---|---|
| $P_{EL}$ | 0.115 | 0.575 |
| $P_W$ | 2.60 | 2.60 |
| $P_{mod}$ | 4.95 | 12.38 |
| $P_{total}$ | 7.665 | 15.557 |

Here $P_{EL}$ is the input power consumption for EL emission in the symmetric drive method; where the input power per unit area $P_{in}$ is given by

$$P_{in} = 2fC_I(V_a - V_{th})V_{EL,th}$$

(23')

since charge transport occurs once a cycle in the symmetric drive scheme. Then $P_{EL}$ is given by the product of $P_{in}$ and the area of lit pixels. There are several observations to be made: First, the light generation power $P_{EL}$ is a relatively small fraction (< 5%) of the total power consumption of a display. Second, the modulation power is usually the dominant power dissipation term. Also it should be kept in mind that both the write power and modulation power consumption is the result of the flow of displacement current and that a significant fraction of these powers can be saved by various circuit approaches. In fact,

with rather straightforward approaches it is possible to keep the typical power consumption below 5 W for medium-size displays and thus provide for battery operation.

For power consumption reduction, three new methods are introduced in the p-p symmetric drive method:

1. The recovery method: The electric charge for modulation voltage accumulated in the EL panel is taken out and returned through the recovery diodes in the column driver ICs to an external capacitor, resulting in 25% reduction of power consumption.
2. The floating method: Push-pull ICs are used as column driver ICs, and non-selected scan lines are floated, resulting in the reduction of the capacity load to 25% of the original value.
3. The step method: Modulation and write voltages are applied in two steps, resulting in the 25% reduction of power consumption.

To summarize, power consumption in the modulation voltage drive is reduced to 9/64 and power consumption in write procedure is reduced to about 4/5.

Figure 76 shows the relation between power consumption and lit pixel percentage in a 640x400 pixel EL panel driven by the p-p symmetric drive method compared with that of the p-n symmetric drive case. As seen from the figure, the maximum power consumption in the p-p symmetric drive method is reduced from that in the p-n symmetric drive method.
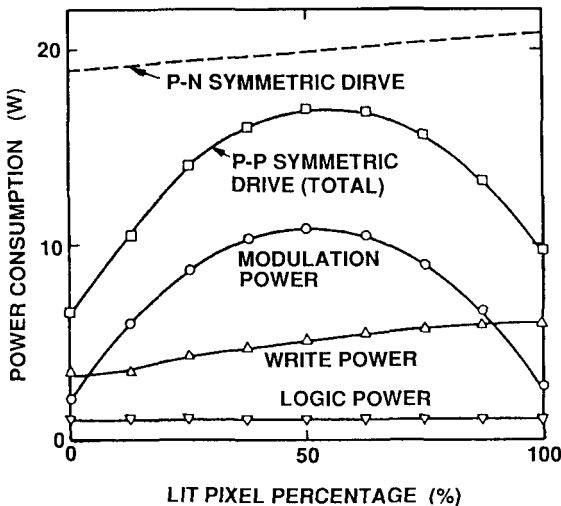


Fig. 76. Power consumption versus lit pixel percentage in a 640x400 pixel EL display panel driven by the p-p symmetric drive method compared with that of the p-n symmetric dive method (Ref. 252)

### 8.1.3. Grayscale Drive Method

The increased use of color terminals for personal computers has raised a demand for video graphic adapter (VGA)-format flat panel displays. Since only monochrome

(ZnS:Mn) EL panel displays of suitable size and speed are available, lack of colors has to be replaced by grayscale in the first place.

There are two ways to achieve grayscale in thin-film EL displays: Pulse amplitude modulation (PAM) method and pulse width modulation (PWM) method. In the former, amplitude of the modulation voltage $V_M$ is varied, and in the latter pulse width of the modulation voltage $V_M$ is varied. The amplitude modulation method is more suitable for thin-film EL displays, because amplitude modulation saves power considerably, which is not the case when pulse width modulation is used. Using amplitude modulation, the power consumption for a 10-inch-diagonal display with 640x480 pixels can be estimated to be less than 15 W in typical cases. If reduced contrast is acceptable in battery mode, typical power consumption may be below 10 W. Recently pulse width modulation of sawtooth-shaped voltage waveforms are introduced, where both amplitude and pulse width can be modulated. Using this method, the commercial 10-inch-diagonal thin-film EL displays with 640x400 or 640x480 pixels can now show sixteen gray-scale images.

Grayscale drivers for thin-film EL displays are still under development. The most advanced pulse amplitude modulation driver now is the Supertex HV08 which gives sixteen different gray shades by a four bit data input. From a driver technology point of view it is important that the accuracy of the chosen voltage considerably exceeds the voltage difference for two adjacent gray levels. If a maximum modulation voltage of 30 V is used, which is quite reasonable, sixteen gray levels implies that the voltage between gray levels is of the order of two volts when amplitude modulation is applied. Consequently the dead voltage band should preferable be below 1 V. For pulse width modulation the requirement is similar but refers to pulse width.

The same arguments hold for the thin-film EL structure because variations in luminance level must not interfere with the grayscale pattern displayed. Over a short distance, maybe just a few centimeters, it is necessary that luminance variations are well within one gray level. Over the whole display larger variations can be tolerated, but variations should be kept within some 30% to 50%.

Grayscale implies a tight control of the thickness of the films in the thin-film EL structure. The operation on the steep portion of the luminance vs. voltage characteristics is critical to variations in threshold voltage. Therefore, films have to be deposited to a thickness accuracy of about two percent depending on the steepness of the luminance vs. voltage characteristics.


## 8.2. Active-Matrix Drive Method

Active matrix addressing, in particular with thin-film transistors (TFTs), of a flat panel display is needed whenever the display element itself lacks a suitable threshold characteristics. This is true for twisted nematic liquid crystal displays (LCDs), but also for the earlier ac powder EL displays[253]. With the advent of the ac thin-film EL display with their sharp threshold characteristics, interest in active driven EL displays disappeared. Recently, however, interest in the subject has awakened again, probably stimulated by the work on TFT-driven LCDs. In particular, amorphous-Si (a-Si) or polycrystalline-silicon (poly-Si) TFTs for LCDs have recently advanced rapidly. TFTs for thin-film EL displays have to be high-voltage resistant. Other requirements include small off current, high on/off ratio, long term stability, good uniformity and good reproducibility. For these purposes, CdSe TFT[254)-258], poly-Si TFT[259),260], a-Si TFT[261], single-crystal silicon (Si) MOS TFT[262] have been studied. Among these a-Si, poly-Si and single-crystal Si MOS TFTs are promising candidates for high-resolution TFT-driven EL displays because conventional

LSI techniques for MOS devices can be utilized. In addition, with a-Si TFTs it is easy to extend to large area displays because its mature technologies of TFTs for LCDs can be utilized.

Advantages of TFT-driven EL displays are as follows:

1. A high-voltage drive frequency independent of the frame rate can be used so that low efficiency EL phosphors, such as blue phosphor, can be driven with higher frequency to obtain higher luminance.
2. 100%-duty-ratio drive is possible because of storage capacitor for providing frame-period driving at each picture element.
3. Low voltage external drivers can be used because high-voltage part of the driving is done within the active matrix.

### 8.2.1. a-Si TFT Driven EL Display

Suzuki et al.[261] used a-Si TFTs to drive a 32x32-pixel prototype EL display with ZnS:Mn phosphor as a feasibility check of full-color EL displays as depicted in Fig. 77.
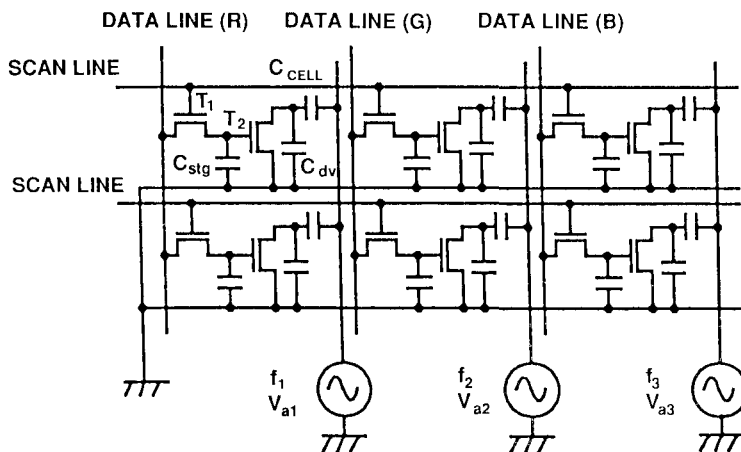


Fig. 77. Circuit configuration of a TFT-driven full-color EL display (Ref. 261)

We use the drive characteristics of TFT-driven EL displays using circuit configuration shown in Fig. 77. Here, each of R, G and B pixel groups can be driven independently at a suitable ac frequency higher than the frame frequency so that red and/or blue pixels which have inadequate luminances in the conventional drive scheme would offer enough luminance for full-color display application.

The basic driving scheme is discussed by using an equivalent circuit shown in Fig. 78: $T_1$ and $T_2$ denote the addressing and EL driving TFTs, respectively. $C_{stg}$ is a data storage capacitor and $C_{dv}$ is a dividing capacitor introduced parallel to $T_2$ to reduce the stress to the TFT due to the applied ac voltage ($V_a$). $C_{cell}$ indicates the EL cell and $C_p$ is a parasitic capacitance induced mainly by the overlap capacitance due to the inverted staggered structure TFT. The data line (drain bus) is connected to the drain of $T_1$ and the scan line (gate bus) is connected the gate of $T_1$. The source of $T_1$ is connected to the gate

of $T_2$ and $C_{stg}$, and the drain of $T_2$ is connected to the EL cell, and the source of $T_2$ is grounded. $V_g$ is the gate voltage to the EL driving TFT $T_2$, $V_{ds}$ is the drain-source voltage of $T_2$ and $V_{cell}$ is the voltage of the EL cell.

When a large enough gate voltage (scan voltage) is applied to the gate of $T_1$, $T_1$ is turned on and the capacitance $C_{stg}$ is charged up by the drain (data) voltage. The $C_{stg}$ voltage, or the gate voltage $V_g$, depends on the pulse width of the gate voltage. When $V_g$ is large enough, $T_2$ is turned on and the whole voltage $V_a$ is applied to the EL cell, i.e., $V_{cell} = V_a$, which is larger than the threshold voltage, resulting in EL emission. With the progress in discharging of the capacitor $C_{stg}$, the gate voltage $V_g$ decreases, and eventually $T_2$ is turned off. Then, the applied voltage $V_a$ is capacitively divided by $C_{cell}$ and $C_{dv}$, so that $V_{cell} = V_a \times C_{dv}/(C_{cell}+C_{dv})$, which is smaller than the threshold voltage, resulting in no EL emission. In this way, TFT-addressed EL displays are driven by the line-at-a time drive scheme.
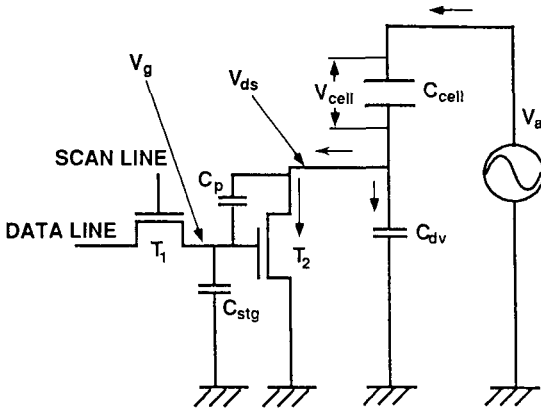


Fig. 78. Equivalent circuit of one pixel of a TFT-driven EL display (Ref. 261)

Two structures of a TFT-driven EL display are possible:
1. A side-placed TFT type, where TFTs are placed besides the EL cell on the same plane. In this type, better reliability can be expected because of a smaller possibility of electrical breakdown, compromised by a lower pixel resolution.
2. A stacking TFT type, where TFTs are placed on top of the EL cells, which was first proposed by Vanfleteren et al.[257]. This type offers a larger aperture ratio and a higher pixel resolution, compromised by a larger possibility of occurrence of electrical breakdown.

The luminance vs. gate voltage (L-$V_g$) relation[261] is shown in Fig. 79. When $V_g$ is just above 7 V a steep rise of luminance was observed and the EL device showed its full luminance above $V_g = 12$ V. The lower the applied voltage $V_a$, the higher the switching voltage $V_g$. This is due to the drop of the voltage allocated to the EL cell. The luminance vs. applied voltage characteristics with TFT driving for $V_g$=15 V are essentially the same as those without TFT driving, i.e., with conventional drive method.

The frequency characteristics[261] of an a-Si TFT driven EL are shown in Fig. 80 for a TFT with channel dimension of W/L=8 and field-effective mobility of 0.8 cm$^2$/Vs, where W and L are the channel width and channel length of the TFT, respectively.
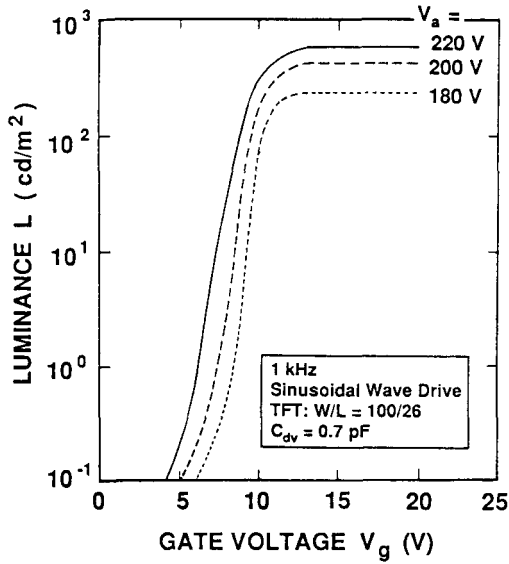
Fig. 79. Luminance vs. gate voltage (L-$V_g$) characteristics for different values for $V_a$ (Ref. 261)
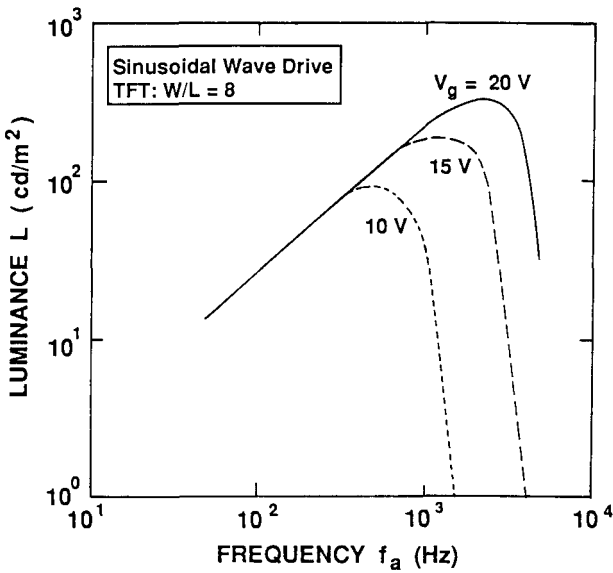


Fig. 80. Luminance vs. frequency (L-$f_a$) characteristics for different values for gate voltage $V_g$ (Ref. 261)

The luminance increases linearly with increasing drive frequency $f_a$ in the low frequency region and falls down steeply in the higher frequency region. Application of higher gate voltage allows higher frequency driving. Figure 80 indicates that it is possible to drive EL display up to 2 kHz for $V_g$=15 V and up to 3 kHz for $V_g$=20 V.

### 8.2.2.  Single-Crystal Si  MOS TFT Driven EL Display

Khormaei et al.[262] fabricated a fully functional 128x128 pixel ZnS:Tb green emitting EL display driven by single-crystal Si MOS TFTs built on insulator wafers. Using conventional IC processing technique of SOI (silicon on insulator), they succeeded in making a very high resolution active-matrix EL display with above 1000 lines per inch (24 μm pitch). They used the ALE process for the EL cell fabrication.

Use of SOI allows inclusion of the peripheral digital circuitry, which opens up the possibility for high resolution displays with very small dimensions. A further benefit of SOI wafers is that wafers can be processed by conventional CMOS foundries.

In the present active matrix design, the EL cell is placed on top of the pixel circuit, with the lower EL electrode connected to the pixel circuit. The upper electrode is a common conductor for all the pixels and is connected to the AC source.
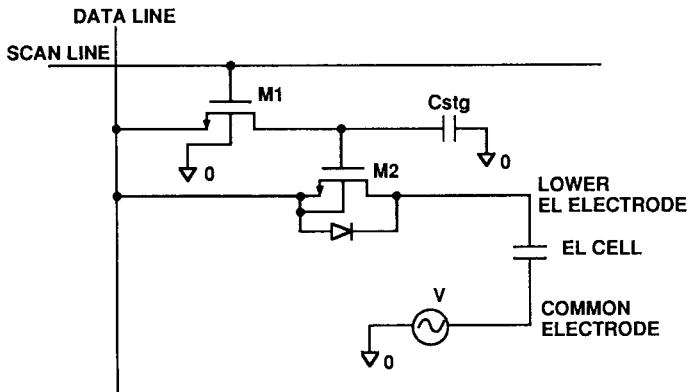


Fig. 81.  Pixel circuit design of an EL display driven by single-crystal silicon MOS TFTs on SOI (Ref. 262)

The pixel circuit is shown in Fig. 81. M1 is the low-voltage transistor for the control of data storage and can be either NMOS or PMOS. M2 is a high-voltage transistor fabricated by a double-diffused MOS (DMOS) structure developed for this purpose[268]. The voltage across EL is the difference between the voltage on the common electrode and the DMOS drain voltage. This high-voltage transistor either blocks the high voltage, resulting in an "off" pixel, or grounds the lower electrode resulting in full voltage across the EL cell, and an "on" pixel. Here the following method is used: Only the required voltage is blocked to change the EL cell from an "on" state to the "off" state, in other words, to shift the peak-to-peak voltage across the EL cell to below the luminance threshold voltage.

A typical luminance-voltage (L-V) characteristic curve for an EL cell driven at 10 kHz is shown in Fig. 82. Note that to completely cross from "off" to "on" states, a modulation

voltage of only about 40 V is required. In this application, since the blocking is only at one polarity, twice the modulation voltage (80 V) is required.
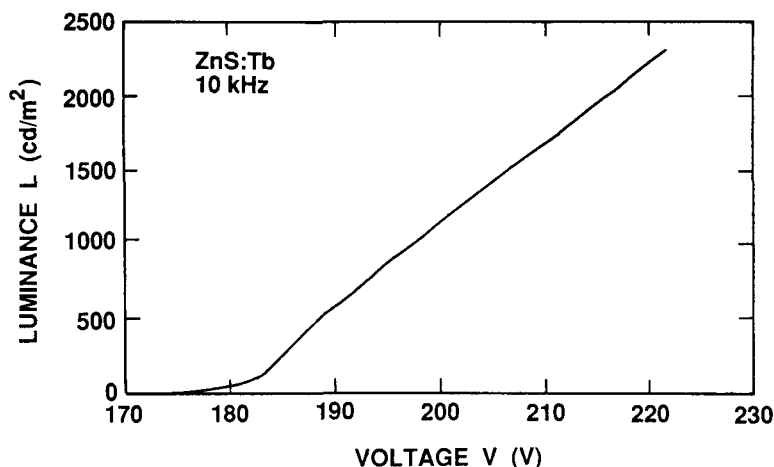


Fig. 82. Luminance-voltage (L-V) characteristics at 10 kHz drive (Ref. 262)

Test matrices of both 28x28 matrix with 100 μm pixel pitch and 128x128 matrix with 24 μm pixel pitch were fabricated successfully. The resulting displays showed good performance. The active matrix circuitry was combined effectively with the EL thin films resulting in initial devices with high reliability and excellent optical performance. This work establishes the path for a full 1280x1024 pixel active-matrix EL display at 1000 lines per inch with the peripheral circuitry. The "on" luminance of the initial device was more than 2000 cd/m$^2$ at 10 kHz excitation with the contrast ratio of well above 100:1. This luminance level corresponds to 12 cd/m$^2$ at 60-Hz driving. The pixel data were updated at 60 Hz rate with no sign of data loss to the leakage. Furthermore, an approach for achieving full-color EL displays was established by combining successfully white phosphor (ZnS:Mn/SrS:Ce) with SOI substrate.

# 9. EL DISPLAY PANELS AND OTHER APPLICATIONS

## 9.1. Monochrome Thin-Film EL Panels

### 9.1.1. Character Displays

Figure 83 shows a large information board[269] installed at Helsinki International Airport in March 1983. It consists of 3000 ALE-EL modules with dimensions 3 m x 2.2 m x 0.2 m. The active area is 2.6 m x 1.6 m and consists of 16 character lines with 45 character positions plus two positions for blink modules on each line. The board operates 24 hours a day at a luminance of 115 $cd/m^2$ and the contrast ratio 10:1 at 5000 lux ambient illumination. Based on a statistics of 50000 hours of continuous operation the mean time between failure (MTBF) for a thin-film module is more than $2x10^6$ hours.

The character module is an ac thin-film EL display designed for viewing distances up to 25 m. The light emitting area, 40 mm x 55 mm, is an 8x11 dot matrix. A redundancy feature has been realized by dividing each pixel into 25 subpixel In the case of breakdown or delamination of the thin film, only the affected subpixel will be lost.

The thin-film layers of EL display are grown by the ALE process. The dielectric layers are a mixed $Al_2O_3/TiO_2$ compound. Front and rear electrodes are transparent ITO conductors. The benefit of a fully transparent EL structure is that a black backing layer can be applied outside the EL layers. The component is unsealed and protection against humidity is made by using a thin-film passivation layer made of $Al_2O_3$. Contrast enhancement is realized by applying an anti-reflection coating with a transmission of 62% in front of the EL glass.
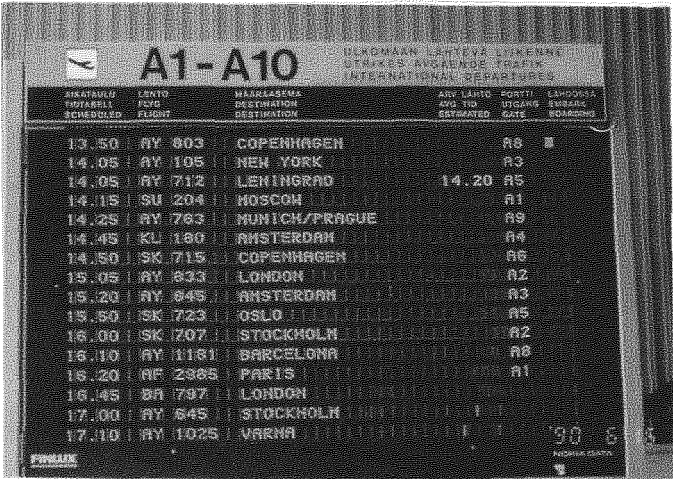
The 8x11 matrix is multiplexed as a 4x22 matrix. The electronic part of the module consists of three main components: a data line driver, a scan line driver hybrid and microprocessor hybrid including a character generator and a frame frequency controller.

The information board exhibits excellent readability, high contrast and wide viewing angle. The modularity of the system permits its use to all kinds of indoor information systems where the merits of electroluminescence are needed. The application of thin-film EL devices in large area displays is unique and demonstrates the general applicability and the reliability of EL devices in actual working conditions.

### 9.1.2. Graphic Displays

A wide variety of monochrome yellow-emitting thin film EL displays are now commercially available[245],[270]. These include the 512x256 half-page display which has become the standard flat panel display for industrial measurement and control applications. The whole series of standard-size half-page displays for personal-computer-based applications including the 640x200 (CGA: Computer graphics adapter), 640x350 (EGA: Enhanced graphics adapter), 640x400, and 640x480 (VGA: Video graphics array) were developed and are in production.

A new generation of products is now available in the market place with enhanced features. These include a series of small- to medium-sized EL displays which consume very low power (less than or equivalent to a backlit LCD). Large area displays such as the 1024x768 and 1024x864 displays have been developed for workstation applications. The present generation of EL display products has additional features such as dimming and contrast controls, gray scale (VGA) and a low power operation mode[271]. In 1993 the first multicolor EL product[3] was introduced to the market place. Figure 84 shows a typical monochrome 640x400 EL display and Table 18 lists the specifications of commercially available thin-film EL displays.

Fig. 83.  ALE-EL based large information board installed at Helsinki International Airport
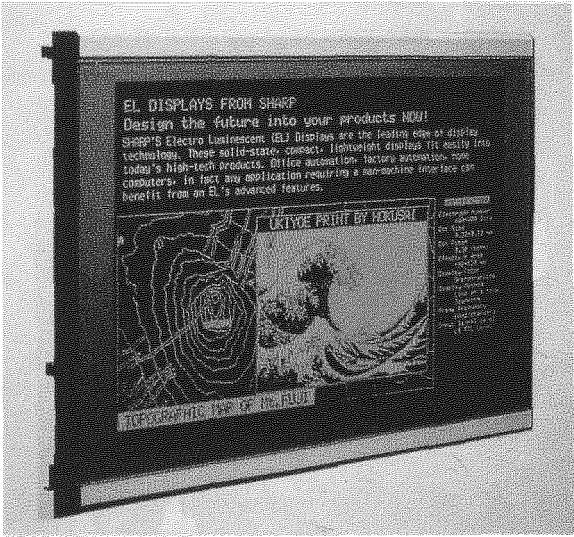


Fig. 84.  Photograph of orange-yellow-emitting ZnS:Mn EL display with 640x400 pixels in normal-mode representation (Courtesy of Sharp Corporation)

Table 18  Specifications of commercial thin-film EL displays (ZnS:Mn)

| Items | SHARP | | Planar and Planar International | |
|---|---|---|---|---|
| | LJ280U32 | LJ640U48 | EL751214MS | EL7768MS |
| Display format (pixels) | 1280x1024 | 640x480 | 1024x800 | 640x480 |
| Display area (mm x mm) | 255.9x204.7 | 191.9x143.9 | 345x292 | 206.4x154.8 |
| (Inch diagonal) | (13) | (9.4) | (18) | (10) |
| Pixel size (mm) | 0.14x0.135 | 0.22x0.22 | 0.236x0.236 | 0.23x0.23 |
| Pixel pitch (mm) | 0.20x0.20 | 0.30x0.30 | 0.338x0.338 | 0.32x0.32 |
| Luminance (cd/m$^2$) | 85 | 100 | 70 | 120 |
| (Luminance (fL)) | (25) | (30) | (20) | (35) |
| Frame frequency (Hz) | 70 | 60 | 60 | 60 |
| Viewing angle (°) | >120 | >120 | >160 | >160 |
| Power consumption (W) | 23(typ) | 13(typ) | 60(max) | 12(typ) |
| Operating temp. (°C) | -5 - 55 | 0 - 55 | 10 - 55 | 0 - 55 |
| Weight (g) | 1300* | 660* | 3000** | 708 |

*EL panel unit with DC/DC converter      **EL panel monitor

Half-page thin-film EL displays are now manufactured in volumes. There is, however, a demand for full-page flat panel displays with some 800 scan lines and 1000 columns. Then new driving concepts seem inevitable. One possibility is to drive a 1000x800 matrix as two 1000x400 matrixes by dividing column electrodes in half[272]. The only major change in this case in comparison to a 400 scan-line display is that every column electrode has to be contacted from the same side of the panel as is commonly done already in larger liquid crystal displays. It is possible to drive more than 400 scan lines, but modulation power consumption $P_{mod}$ in the worst case condition has to be considered because it increases with the square of number of scan lines given by the following equation by rewriting Eq. 91 in Section 8.1.2:

$$P_{mod} = \frac{1}{4}NfC_pV_M^2 = \frac{f}{4} \times M \times N^2 \times C_e \times V_M^2 \tag{92}$$

Here the relation

$$C_p = M \times N \times C_e \tag{93}$$

is used, where $C_p$ is the capacitance of the entire panel and $C_e$ is the capacitance of one pixel element. And f is the drive frequency or frame frequency and $V_M$ is the modulation voltage. Note that $P_{mod}$ is the largest power consumption factor. Let us compare a 1000x800 to a "double" 1000x400 matrix.

$$M = 1000, N = 800 \rightarrow P_{mod} = \frac{f}{4} \times 1000 \times (800)^2 \times C_e \times V_M^2 \tag{94}$$

$$M = 2000, N = 400 \rightarrow P_{mod} = \frac{f}{4} \times 2000 \times (400)^2 \times C_e \times V_M^2 \tag{95}$$

It is easily seen that dividing the matrix into two parts saves about one half of the modulation power consumption. There is still another point to be made. Frequency has been assumed to be the same in both cases. The shorter dwell time $t_S$ (=1/Nf) per line in the 1000x800 case requires considerably reduced column electrode sheet resistance. Yet, one may ask how many lines can be driven directly in a thin-film EL display without being forced to double the cost of column drivers. Physically it might be possible to transfer the excitation charge in the phosphor within some 10 μs, which would allow multiplexing of 1000 lines. At least at present it seems likely that full-page matrices will first be realized by dividing the columns in half.

On a longer run the possibilities to build still larger displays must be evaluated. There are likely to be color displays for TV applications. Longer and narrower electrodes will impose heavy requirements on driving. Yet there are possibilities of very large displays provided that the electrode pitch is large enough to allow for metal reinforcement (metal bus-bar) of the transparent ITO electrode.

## 9.2. Multicolor Thin-Film EL Panels

Based on the progress in color phosphor materials described in Chapter 7, several kinds of multicolor thin-film EL structures have been proposed[58),59),75),219),273),274)], and a large number of prototype multicolor and full-color thin-film EL display panels have already been developed. In this section, recent developments are described in detail.

There are four types of multicolor thin-film EL panel structures under consideration[13)]:

1. stacked-phosphor structure
2. patterned-phosphor structure
3. broadband-spectrum or white phosphor with patterned color filters
4. dual-substrate structure

Schematic cross-sectional structures of the first three panel structures are shown in Fig. 85. The dual-substrate structure[4)] is a hybrid of the stacked- and patterned-phosphor structures.
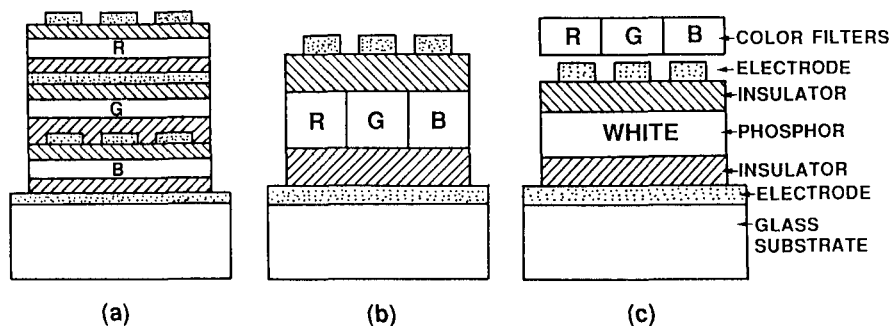


Fig. 85. Schematic structures of multicolor thin-film EL panels: (a) stacked-phosphor structure; (b) patterned-phosphor structure; (c) broadband-spectrum or white phosphor with patterned color filters (Ref. 13)

Stacked-phosphor structure implies that at least one intermediate transparent electrode pattern must be used. Power consumption in this case is necessarily higher than that when phosphors are in one plane, and therefore this structure is not suitable for practical multicolor displays. In the patterned-phosphor structure (similar to the CRT), the phosphors are deposited in three subsequent processes separated by the necessary lithographic steps. Consequently, each pixel is divided into three subpixels and each emits one of the primary colors. The structure with broadband-spectrum or white phosphor with patterned color filters (similar to LCDs) is probably the simplest. Pixels are divided into three subpixels, in each of which light is filtered to one of the primary colors. To avoid parallax, filters have to be placed close to the light-emitting films.

Chronological lists of recent publications on multicolor thin film EL panel, categorized into the four types, are given in Table 19.

Table 19 Recent publications on multicolor thin-film EL display panels

1. Stacked-phosphor structure
  (1) R.E. Coovert et al. (Tekronix), SID 82 Digest (1982), p.128 (Ref. 275).
  (2) R.E. Coovert and C.N. King (Tektronix), Proc. SPIE*, Vol. 386 (1983), p.63 (Ref. 276).
  (3) Y. Oishi et al. (Osaka Univ.), Japan Display '83 (1983), p.570 (Ref. 277).
  (4) W.A. Barrow et al. (Planar), SID 86 Digest (1986), p.25 (Ref. 41).

2. Patterned-phosphor structure
  (1) Y. Yamauchi et al. (NTT), SID 87 Digest (1987), p.230 (Ref. 42).
  (2) C.N. King et al. (Planar), Eurodisplay '87 (1987), p.14 (Ref. 58).
  (3) Brunel et al. (CNET), Eurodisplay '87 (1987), p.238 (Ref. 278).
  (4) W.A. Barrow et al. (Planar), SID 88 Digest (1988), p.284 (Ref. 60).
  (5) M. Yamamoto et al. (Matsushita), Japan Display '89 (1989), p.228 (Ref. 43).
  (6) T. Konishi et al. (NEC Kansai), SID 91 Digest (1991), p.271 (Ref. 44).
  (7) R.T. Tuenge and S. Kane (Planar and David Sarnoff), SID 91 Digest (1991), p.279 (Ref. 40).
  (8) C. Laakso et al. (Planar and Planar Intern'l), 1991 IDRC** (1991), p.43 (Ref. 45).

3. Broadband-spectrum or white phosphor with patterned color filters
  3.1. Broadband-spectrum phosphor (SrS:Ce + CaS:Eu) with patterned color filters
    (1) S. Tanaka et al. (Tottori Univ.), SID 87 Digest (1987), p.234 (Ref. 61).
  3.2. Broadband-spectrum phosphor (ZnS:Mn) with patterned color filters
    (1) N. Tsurumaki et al. (Komatsu), Eurodisplay '90 (1990), p.212 (Ref. 46).
    (2) K. Okibayashi et al. (Sharp), SID 91 Digest (1991), p.275 (Ref. 47).
    (3) J. Haaranen et al. (Planar and Planar Intern'l), SID 92 Digest (1992), p.348 (Ref. 48).
    (4) D. Cramer et al. (Planar Intern'l), SID 93 Application Digest (1993), p.57 (Ref. 3).
  3.3. White phosphor (SrS:Ce,Eu) with patterned color filters
    (1) J. Mita et al. (Oki), SID 91 Digest (1991), p.290 (Ref. 65).
    (2) Y. Tanaka et al. (NEC Kansai), Japan Display '92 (1992), p.721 (Ref. 66)
  3.4. White phosphor (ZnS:Mn/SrS:Ce) with patterned color filters
    (1) T. Nire et al. (Komatsu), SID 92 Digest (1992), p.352 (Ref. 68).
    (2) A. Matsuno et al. (Komatsu), Japan Display '92 (1992), p.717 (Ref. 69).
    (3) M. Leppänen et al. (Planar Intern'l), Eurodisplay '93 (1993), p.229 (Ref. 72).

4. Dual-substrate structure (ZnS:Mn/Filter + ZnS:Tb + $CaGa_2S_4$:Ce)
  (1) W.A. Barrow et al. (Planar and David Sarnoff), SID 93 Digest (1993), p.761 (Ref. 4).
  (2) W.A. Barrow et al. (Planar), 1994 IDRC** (1994), p.448 (Ref. 8).

*SPIE: Society of Photo-Optical Instrumentation Engineers
**IDRC: International Display Research Conference

This table shows a historical trend; stacked-phosphor structure —> patterned-phosphor structure —> broadband-spectrum or white phosphor with patterned color filters. In particular, the filtered, inverted thin-film EL structure[3),46)-49),68),69),72)] with the transparent electrode on top of the thin-film stack seems the most promising approach for multicolor thin-film EL panels. This is the structure of the EGA-format multicolor EL panel with 640x350 pixels put on the market by Planar International[3)] in 1993.

### 9.2.1. Stacked-Phosphor Structure

Historically, this was the first device structure to be investigated[275)-277)]. Structures of this type take advantage of the fact that the thin-film EL layers are transparent and, therefore, light from one layer can be transmitted through another layer. Two examples are shown in Fig. 86(a) and (b). Figure 86(a) shows a single-substrate implementation of a stacked-phosphor structure. This is essentially a stack of two EL devices with a common middle transparent electrode shared by both devices. This was first reported in 1982 for a green/yellow device[275), 276)]. Figure 86(b) shows a dual-substrate version[41)] of a stacked-phosphor structure where each substrate has a separate independent EL device, with the rear electrode of each device required to be transparent. The two substrates are put together with the thin films facing each other in order to minimize parallax.



(a) SINGLE-SUBSTRATE STRUCTURE          (b) DUAL-SUBSTRATE STRUCTURE
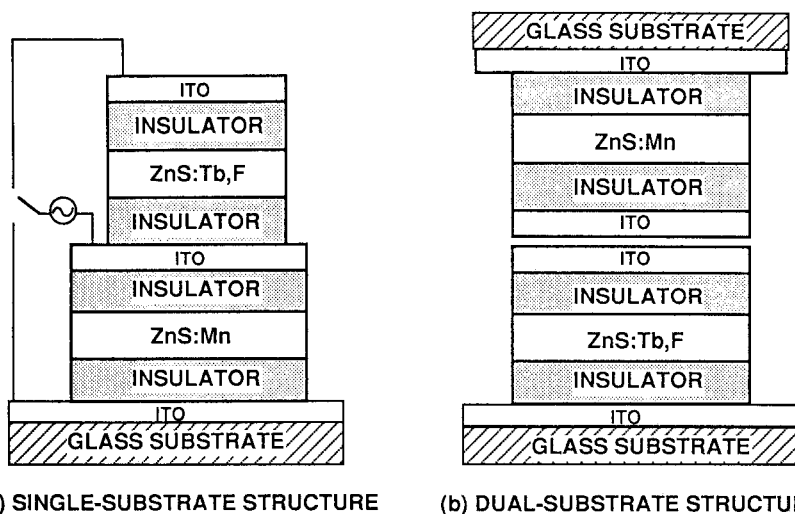
Fig. 86. Structures of stacked-phosphor type multicolor thin-film EL display panels: (a) single-substrate structure (Ref. 275); (b) dual-substrate structure (Ref. 41)

A major advantage of the stacked-phosphor structure is the capability of fabricating a multicolor display without suffering the loss of resolution that normally accompanies a color display, i.e., shadow mask CRT or patterned filter LCD. In addition, from a process point of view, this type of structure maintains the relatively simple photo-patterning requirements of monochrome EL; only the electrodes need to be patterned and, thus, the active layers of the device are continuous thin films that can be deposited in one

processing pass. A major disadvantage of the stacked-phosphor structure devices has to do with the performance of the transparent electrodes. For the structure shown in Fig. 86(a), the common middle electrode, usually made of ITO, does not have the necessary self-healing characteristics for good device reliability. Another problem is their rather high resistance in comparison to the aluminum rear electrodes used for monochrome EL devices. This places constraints on the maximum size of the device that can be built without experiencing significant voltage drop along the transparent electrodes which leads to luminance non-uniformity.

The device structure shown in Fig. 86(b) was used to fabricate a multicolor 320x240 six-inch-diagonal matrix-addressed display[41], where filtered ZnS:Mn was used for red phosphor and ZnS:Tb,F was used for green phosphor. The resulting CIE color coordinates were x=0.644 and y=0.345 for red emission and x=0.321 and y=0.585 for green emission. This device structure completely overcomes the first disadvantage listed above for the transparent electrodes, i.e., self-healing characteristics of the rear electrode are realized. This device structure also tends to maximize the area-averaged (areal) luminance by increasing the effective pixel fill factor. However, this structure still suffers some limitations to the resistance of the transparent electrode system.

While the stacked-phosphor structure appears to be quite effective for dual-color panels, it has problems when extended to three colors. The single-substrate version shown in Fig. 86(a) has yet another self-healing problem introduced with the third device stack. The dual-substrate structure shown in Fig. 86(b) encounters severe parallax problems if three substrates are used. Thus, as will be discussed below, the stacked-phosphor structure evolves to a hybrid structure (dual-substrate structure) for a full-color device.

### 9.2.2. Patterned-Phosphor Structure

The patterned-phosphor structure is perhaps the more traditional approach to build multicolor devices. As shown in Fig. 43 in Chapter 5, in this structure photolithographically patterned phosphor layers corresponding to three primary colors are placed on the same plane. The advantages of this structure over the stacked-phosphor structure include a drive circuitry that is essentially the same as the monochrome EL devices, simpler deposition processes, easy extension of the device structure from two colors to three and the use of standard electrodes. In terms of the electrodes, a self-healing aluminum rear electrode can be used to avoid any reliability problem and the RC time constant of a panel is essentially the same as that of a monochrome panel and, thus, no reduction in the maximum panel size is incurred. In addition, even though the areal (averaged) luminance tends to be reduced because of a smaller fill factor for the pixels, the pixel luminance is higher than that of the stacked-phosphor structure because the rear aluminum electrode reflects more light forward than the transparent electrodes of the stacked-phosphor structure. Disadvantages of the patterned-phosphor structure are lower resolution, lower areal luminance due to the smaller pixel fill factor and difficulty in phosphor-layer patterning. However, in some cases, the problem of lower areal luminance can be solved by refreshing the display at a higher frequency.

Yamauchi et al.[42] was the first to report a two-color TFEL device with this structure. They fabricated a red/green EL display utilizing wet chemical etching and lift-off techniques to pattern the phosphors. They reported that this additional photoprocessing did not degrade the performance of the individual phosphor stripes in comparison to continuous films. Shortly thereafter, Brunel et al.[278] also reported the fabrication of a dual-color yellow/green display. In their case they utilized the ion beam etching technique to pattern the phosphor layers.

King *et al.*[58] and Barrow *et al.*[60] reported the fabrication of a prototype 6-inch diagonal multicolor display panel with 320x240 pixels by patterning phosphor layers of red (ZnS:Sm,Cl), green (ZnS:Tb,F), and blue (SrS:Ce). They utilized another dry etching technique called reactive ion etching. The CIE color coordinates of three primary colors and white were x=0.65 and y=0.34 for red, x=0.30 and y=0.59 for green, x=0.20 and y=0.39 for blue and x=0.40 and y=0.40 for white.

Yamamoto *et al.*[43] fabricated a prototype 10-inch-diagonal three-color (orange-yellow/yellow/green) EL display panel with 512x384 pixels. Its structure is shown in Fig. 87. In order to protect the first phosphor layer of ZnS:Mn from being etched, an intermediate layer was placed between the first phosphor layer and the second phosphor layer of ZnS:Tb, made of BaTa$_2$O$_6$. Furthermore, CH$_3$OH and Ar were used as dry etchants for good selectivity.
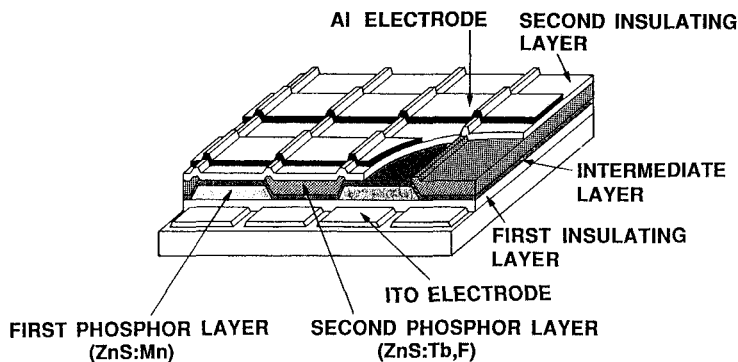


Fig. 87. Structure of a patterned-phosphor type multicolor thin-film EL panel (Ref. 43)

Konishi *et al.*[44] developed a 9.3-inch-diagonal multicolor (yellow/green) EL display panel with 320x400 pixels by patterning phosphor layers of ZnS:Mn and ZnS:Tb,F. They used a co-evaporation method and balanced the green and yellow luminance vs. voltage (L-V) characteristics by regulating the phosphor layer thicknesses and Mn concentration. They used a sputter dry etching method with only Ar gas to form the stripes of the phosphor layers.

Tuenge and Kane[40] developed a 10-inch-diagonal 640x200 pixel multicolor display panel with a red/green patterned phosphor structure. They also used the dry etch process. The green phosphor was ZnS:TbS$_x$ with the CIE color coordinates x=0.32 and y=0.61. For the red phosphor, ZnS:Mn was used together with a CdSSe thin film color filter, resulting in red emission with the CIE color coordinates x=0.65 and y=0.35. The color filter was placed between the glass substrate and the lower ITO transparent electrode to prevent chromaticity shifts at different viewing angles, i.e., to prevent parallax. Another benefit of this filter layer is the reduction in reflected ambient light that it provides. Only red light is reflected which increases the contrast ratio of the red pixel. A diffuse reflectance of 5% was measured for CdSSe-filtered red monochrome panel compared to a diffuse reflectance of about 15% for an unfiltered ZnS:Mn panel. In a red EL panel a contrast ratio of 10:1 was obtained in a 500 lux ambient without any additional contrast enhancing filters. Hence, neither a polarizing filter nor a contrast

enhancing black layer, which reduce luminance by at least a factor of 2, are required to achieve a high-contrast display.

Laakso et al.[45] developed a 9-inch-diagonal multicolor (red/green/yellow) display with 640x200 color pixels by combining atomic layer epitaxy, sputtering, and evaporation thin-film deposition methods. An inorganic CdSSe filter was incorporated to achieve a deep red by filtering the yellow emission of ZnS:Mn. This filter was also used as a self-aligning photomask for defining the ZnS:Mn stripes. A pinhole-free barrier layer made of ALE-prepared $Al_2O_3$ or $SiO_2$ covering the filter allowed standard wet etching of the ITO column electrodes without damage to the red filter. The lower insulator and ZnS:Tb are sequentially grown by atomic layer epitaxy, whereas the ZnS:Mn and upper insulator were deposited in an in-line vacuum coater using electron-beam evaporation. The red filter and both phosphors were sputter etched. The subpixel luminances of red and green were 50 and 30 cd/m$^2$, respectively, and areal luminance of yellow was 25 cd/m$^2$ under a 90 Hz drive condition. Typical power consumption was about 13 W.

Table 20 summarizes display specifications, color phosphor configurations and etching methods of phosphor patterning of patterned-phosphor-structure multicolor EL panels.

Table 20   Specifications of prototype multicolor EL displays in patterned-phosphor structure

| Item | Barrow et al. (1988) (Ref. 60) | Yamamoto et al.(1989) (Ref. 43) | Konishi et al. (1991) (Ref. 44) | Tuenge and Kane (1991) (Ref. 40) | Laakso et al. (1991) (Ref. 45) |
|---|---|---|---|---|---|
| Display area (mm x mm) | 122x91 (6-in. diag.) | 205x154 (10-in. diag.) | 192x120 (9.3-in. diag.) | 10-in. diagonal | 195x122 (9-in. diag.) |
| Pixel number | 320x240 | 512x384 | 320x400 | 640x200 | 640x200 |
| Color phosphor   Red | ZnS:Sm,Cl | ——— | ——— | ZnS:Mn/filter | ZnS:Mn/filter |
|    Green | ZnS:Tb,F | ZnS:Tb,F | ZnS:Tb,F | ZnS:TbS$_x$ | ZnS:Tb |
|    Blue | SrS:Ce | ——— | ——— | ——— | ——— |
|    Yellow | ——— | ZnS:Mn | ZnS:Mn | ——— | ——— |
| Etching method | Reactive ion etching | Sputtering Ar+CH$_3$OH | Sputtering Ar | Dry etching | Sputtering |

These results tend to substantiate the fact that the thin-film EL phosphor layers can be patterned by several different techniques without damaging the performance of the phosphor which is the major issue in the feasibility of this type of phosphor structure. However, the ZnS-based phosphors are much more easily etched than the alkaline-earth-sulfide-based phosphors.

### 9.2.3. Broadband-Spectrum or White Phosphor with Patterned Color Filters

Combining a broadband-spectrum phosphor or a white-light-emitting phosphor having red, green, and blue spectral components, with color filters makes it possible to obtain multicolor EL devices. This structure has the following advantages:
1. A single broadband-spectrum or white phosphor is used in the device, so that matching of threshold voltages for the individual color subpixels is guaranteed.
2. This structure maintains the simple device fabrication sequence of a monochrome thin-film EL display without breaking vacuum, minimizing defect levels.

3. Multicoloring can be achieved by laminating patterned color filters to the EL device at the end of the process, so that organic color filters can be utilized similar to those used in the fabrication of color LCD panels.

The disadvantage of this approach from the performance perspective is that it requires a very high luminance broadband phosphor.

This subsection discusses recently developed multicolor thin-film EL panels, which are based on SrS:Ce (+CaS:Eu) and ZnS:Mn broadband-spectrum phosphors, or SrS:Ce,Eu and ZnS:Mn/SrS:Ce white-light-emitting phosphors.

*(1) Broadband-Spectrum Phosphor (SrS:Ce + CaS:Eu) with Patterned Color Filters*

A prototype multicolor thin-film EL device using CaS:Eu and SrS:Ce phosphors and interference color filters has been fabricated[61] in the hybrid device structure. As shown in Fig. 88, the hybrid device structure consists of two device structures (like a stacked-phosphor structure) with one of the devices having a patterned-filter structure. In the present structure, a chromaticity problem with the blue phosphor was solved by placing blue/green color filters in front of the SrS:Ce phosphor to produce blue and green with good color purities. In the front layer, CaS:Eu was used for the red pixels. The resultant emission colors were very close to those of a color CRT. Luminances and the CIE color coordinates of filtered primary colors at a 1-kHz drive condition were as follows: L(red)=21 cd/m$^2$ (x=0.69, y=0.31), L(green)=70 cd/m$^2$ (x=0.31, y=0.62) and L(blue)= 14 cd/m$^2$ (x=0.13, y=0.12). The white luminance was 105 cd/m$^2$.
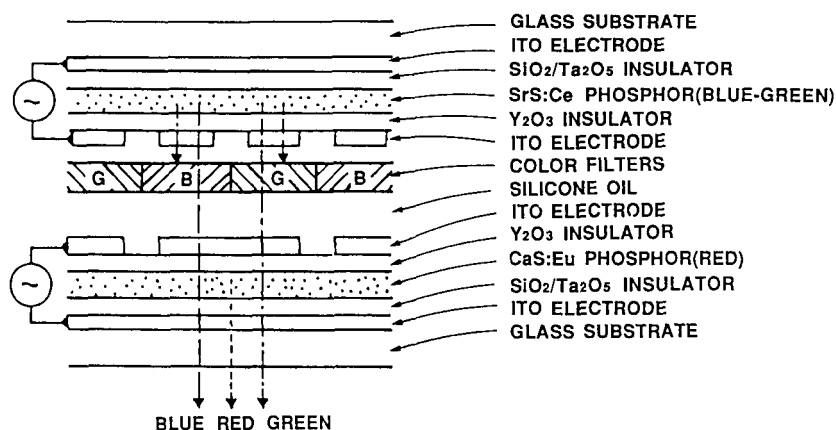


Fig. 88. Cross-sectional view of a multicolor thin-film EL device in the hybrid device structure with color filters (Ref. 61)

*(2) Broadband-Spectrum Phosphor (ZnS:Mn) with Patterned Color Filters*

As shown in Fig. 57, ZnS:Mn is a good candidate for a broadband-spectrum phosphor with high luminance. Okibayashi *et al.*[47] fabricated a prototype 9-inch-diagonal multicolor (green/red) EL device with 320x200 pixels. The ZnS:Mn phosphor layer was deposited by hydride-transport chemical vapor deposition (HT-CVD), and organic color filters were utilized.
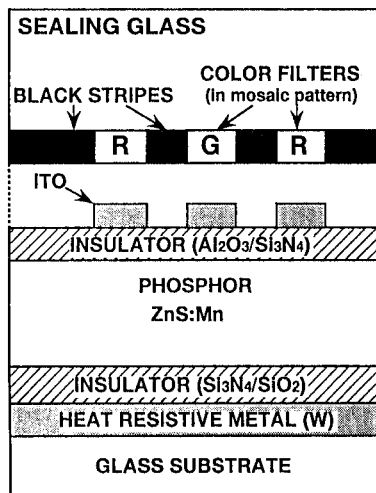
Fig. 89. Inverted, double-insulating layer-type
multicolor thin-film EL panel structure (Ref. 47)
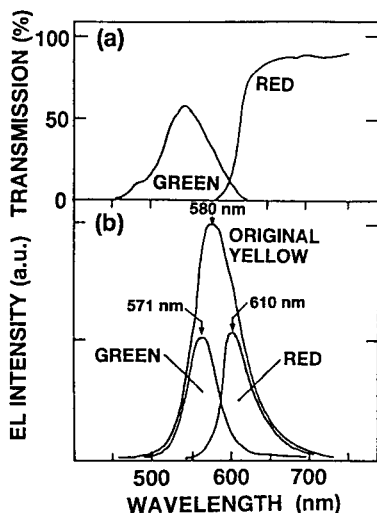


Fig. 90. Color filter characteristics and EL
spectra of filtered green and red emissions
(Ref. 47)

As depicted in Fig. 89, an inverted, thin-film multicolor EL panel structure was employed with a heat-resistive tungsten lower electrode and an ITO upper electrode. Green and red color filters were deposited on the sealing glass on top of the upper electrodes. This placement was adopted to avoid high-temperature degradation of color filters during the phosphor-layer annealing process at approximately 550°C. This structure's red and green pixels are easy to drive because each pixel has the same luminance-versus-voltage characteristics (those of ZnS:Mn). Furthermore, a black matrix was formed by overlapping green and red color filters, increasing the contrast ratio. Figure 90 shows the transmission characteristics of the green and red color filters along with the EL emission spectra for the ZnS:Mn's original yellow emission, and the filtered green and red emissions. The luminances and the CIE color coordinates of filtered EL emissions under a 60-Hz drive condition were L(green) = 80 cd/m$^2$ (x=0.45, y=0.55) and L(red) =30 cd/m$^2$ (x=0.66, y=0.34). Here, the original yellow luminance was 200 cd/m$^2$.

Haaranen et al.[48] developed a 9-inch-diagonal multicolor (red/green/yellow) EL display panel with 640x200 pixels. Both the red and green emissions are obtained by filtering the broadband emission from ZnS:Mn phosphor. The ZnS:Mn layer and insulating layers were deposited by atomic layer epitaxy. An inverted thin-film EL structure was used with the transparent electrodes on top of the thin-film stack. Figure 91 and Table 21 compare[49] the device structures and display characteristics of (a) the conventional thin-film EL structure with patterned color phosphor films and (b) the inverted thin-film EL structure with patterned color filters for the color phosphor film with a broadband emission spectrum. Note the opposite viewing directions. The structure shown in (a) is that for the red/green/yellow multicolor displays[40),45)] discussed in Section 9.2.2.

METAL ELECTRODES
(Aluminum)

INSULATOR

YELLOW PHOSPHOR

GREEN PHOSPHOR

INSULATOR

ITO ELECTRODES

BARRIER LAYER

RED FILTER

GLASS SUBSTRATE

VIEWING DIRECTION

(a) CONVENTIONAL EL STRUCTURE

VIEWING DIRECTION

RED FILTER

GREEN FILTER

ITO ELECTRODES

INSULATOR

YELLOW PHOSPHOR

INSULATOR

METAL ELECTRODES
(Molybdenum)

GLASS SUBSTRATE

METAL
BUS BAR
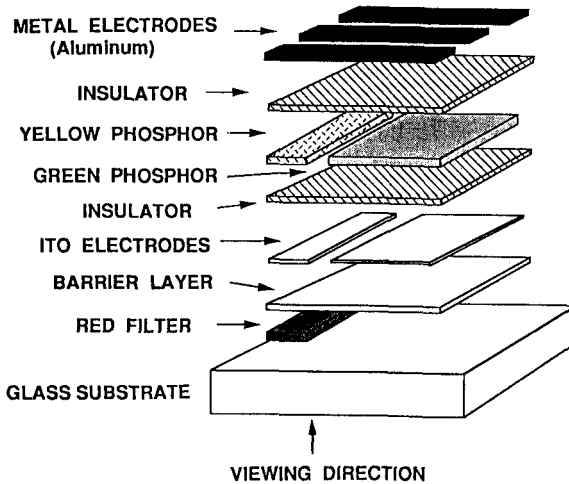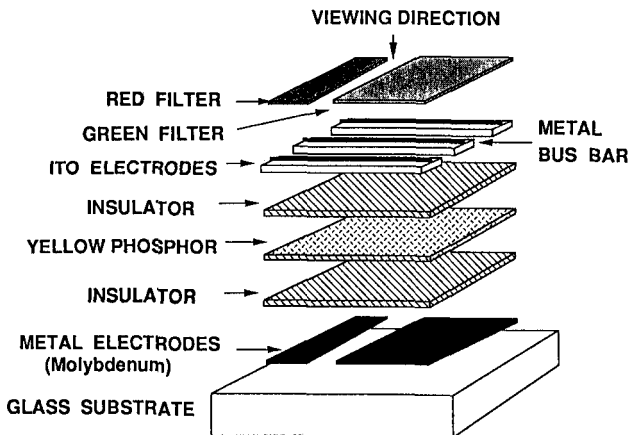
(b) INVERTED EL STRUCTURE

Fig. 91. Multicolor (red/green/yellow) thin-film EL display structures: (a) conventional, with patterned color phosphors; (b) inverted, with patterned color filters and a broadband-spectrum phosphor (Ref. 49)

The inverted structure (b) has the following benefits:
1. Relatively simple organic patterned color filters can be used.
2. The absorption of ambient light in the patterned color filters and in the rear metal electrode yields excellent contrast when metals with low reflection coefficient are used as rear electrodes.

3. A narrow metal bus-bar can be placed on top of the transparent ITO
   column electrode to increase the conductivity. As a consequence the
   RC time constant of the column electrode does not impose limitations
   to using higher refresh rates to increase luminance. In addition, the
   power dissipation in the column electrodes can be reduced substantially.

Table 21  Display characteristics comparison of red/green/yellow multicolor thin-film EL displays in conventional and inverted device structures

| Item | | (a) Conventional EL structure (Patterned phosphors) (Ref. 45) | (b) Inverted EL structure (Patterned filters) (Ref. 48) |
|---|---|---|---|
| Display area (mm x mm) | | 195x122 | 192x122 |
| Pixel number | | 640x200 | 640x200 |
| Pixel pitch (mm x mm) | | 0.30 x 0.61 | 0.30 x 0.61 |
| Display thickness (mm) | | 6 | 4 |
| Color | Red | ZnS:Mn/CdSSe filter | ZnS:Mn/filter |
| phosphor | Green | ZnS:Tb | ZnS:Mn/filter |
| Areal | Red | 12 | 5 |
| luminance | Green | 13 | 10 |
| (cd/m$^2$) | Yellow | 25 | 15 |
| (Drive frequency (Hz)) | | (90) | (90) |
| CIE color | Red | (0.65, 0.35) | (0.62, 0.37) |
| coordinates | Green | (0.32, 0.61) | (0.46, 0.53) |
| (x, y) | Yellow | (0.47, 0.48) | (0.53, 0.47) |
| Contrast ratio  (500 lux ambient) | | 7:1 | 14:1 |
| Viewing angle (°) | | >160 | >140 |
| Power dissipation (W) | | 13 | 13 |

As indicated in Table 21, a remarkable characteristic of the display in the inverted thin-film EL structure is the excellent contrast it provides without any additional contrast-enhancement filter. The contrast ratio was 14:1 at 500 lux ambient and 6:1 at 1000 lux ambient, values comparable to those achieved with monochrome thin-film EL displays when a circular polarizer is used. In the actual display, the combination of a light-absorbing molybdenum rear electrode and organic (dyed polyimide) patterned color filters on the front glass was employed. Areal luminances and the CIE color coordinates of yellow, red, and green emissions under a 90-Hz symmetric driving were L(yellow) = 15 cd/m$^2$ (x=0.53, y=0.47), L(red) = 5 cd/m$^2$ (x=0.62, y=0.37), and L(green) = 10 cd/m$^2$ (x=0.46, y=0.53). The subpixel luminances of the red and green subpixels were both 30 cd/m$^2$. Although the luminance level may appear low, visual appearance was very good because of excellent contrast.

In the inverted thin-film EL display, a narrow metal bus-bar is placed on the column ITO electrode to reduce the electrical resistance. In addition, employment of tape-automated bonding (TAB) and chip-on-glass (COG) technologies made it possible to reduce the display thickness to 4 mm.

Based on these technologies, Cramer *et al.*[3] have fabricated the first commercial 9-inch-diagonal multicolor thin-film EL display with 640x350 pixels (EGA version), whose specifications are given Table 22.

Table 22  Specifications of the commercial multicolor thin-film EL display panel (Ref. 3)

| Luminance-related specifications | | Panel-related specifications | |
|---|---|---|---|
| On luminance* (min) | 15 cd/m$^2$ (full yellow) | Display area | 179.5 mm x 122.5 mm (9 inch diagonal) |
| Off luminance* (max) | 0.15 cd/m$^2$ | Pixel number | 640x350 |
| Contrast ratio | 20:1 (500 lux ambient) 10:1 (1000 lux ambient) | Panel size | Width: 228.5 mm Height: 158.5 mm Depth:   18.3 mm |
| CIE color coordinates (x, y) | Yellow: (0.53, 0.47) Red:    (0.62, 0.37) Green: (0.46, 0.53) | Panel weight | 640 g (with PS**) |
| Viewing angle | ≥140° | Power display only with PS** | 11 W (typ), 15 W (max) 15 W (typ), 25 W (max) |
| Gray scale No. of colors | 3 levels 8 + black | Operating temp. | 0 to 55°C |
| *90 Hz drive | | **PS: power supply | |

This display is capable of producing red, orange, yellow, greenish-yellow and green on a black background in addition to half levels of red, yellow and green, as shown in Fig. 92. The contrast ratio is 20:1 at 500 lux ambient and 10:1 at 1000 lux ambient, so it is sufficient without additional contrast-enhancement filters. Therefore this multicolor display is suitable in the application areas where color highlighting is needed, but the premium for full-color is not justified, such as industrial and process control, test and measurement equipment, medical monitoring equipment and navigation electronics.

*(3) White Phosphor (SrS:Ce,Eu) with Patterned Color Filters*

Mita *et al.*[65] developed a prototype multicolor EL device by stacking a white-light-emitting EL device with SrS:Ce,Eu phosphor and low-cost electro-deposited color filters. The SrS:Ce,Eu white phosphor was prepared by the electron-beam evaporation method with sulfur co-evaporation.  When sputtered $Si_3N_4/SiO_2$ thin films were used as insulating layers, the maximum luminance and luminous efficiency were $L_{40} = 535$ cd/m$^2$ and $\eta_{40} = 0.4$ lm/W, respectively, at a 1-kHz sinusoidal wave drive. The luminances and the CIE color coordinates of three primary colors after passing through the electro-deposited color filters were $L_{40}$(red) = 135 cd/m$^2$ (x=0.63, y=0.36), $L_{40}$(green) = 175 cd/m$^2$ (x=0.33, y=0.60), and $L_{40}$(blue) = 41 cd/m$^2$ (x=0.13, y=0.27).

Tanaka *et al.*[66] developed a 4.7-inch-diagonal white thin-film EL display with 320x240 pixels and discussed the possibility of its use as a full-color EL display. SrS:Ce,Eu as used for the white phosphor.  Under a 100-Hz pulse drive condition, the pixel luminances and the CIE color coordinates of three primary colors after passing through color filters were $L_{60}$(red) = 12.8 cd/m$^2$ (x=0.67, y=0.33), $L_{60}$(green) = 23.4 cd/m$^2$ (x=0.27, y=0.65), and $L_{60}$(blue) = 5.5 cd/m$^2$ (x=0.12, y=0.20), while the original
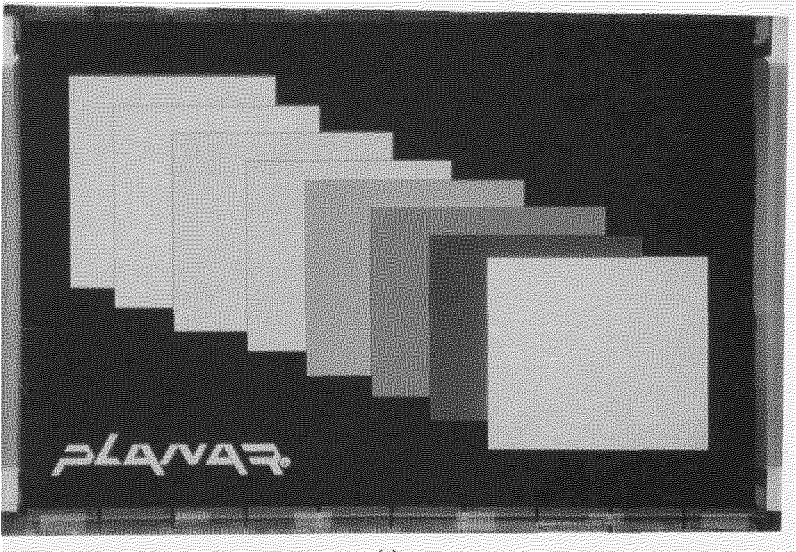
(a)
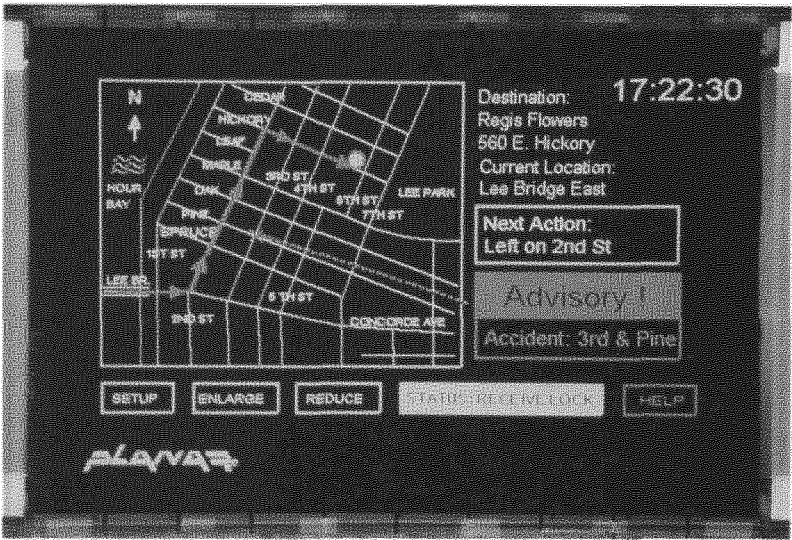


(b)

Fig. 92. Color pictures of the first commercial 9-inch-diagonal multicolor thin-film EL display with EGA format: (a) 8 color representation; (b) application as a personal computer screen (Courtesy of Planar International)

white luminance was $L_{60}$(white) = 61.5 cd/m$^2$ with the CIE color coordinates of x=0.34 and y=0.42.

## (4) White Phosphor (ZnS:Mn/SrS:Ce) with Patterned Color Filters

Another approach to obtain white emission is the use of layered ZnS:Mn/SrS:Ce phosphor, as described in Section 7.5. Based on this, prototype multicolor RGB thin-film EL panels have been fabricated[68],[69]. Nire et al.[68] and Matsuno et al.[69] used a ZnS:Mn/SrS:Ce/ZnS:Mn stacked phosphor to fabricate a prototype 4.4-inch-diagonal RGB multicolor EL display with 213x200 pixels. As shown in Fig. 93, the inverted EL structure and patterned color filters were used. Both SrS:Ce and ZnS:Mn phosphor layers were grown by multi-source deposition method with sulfur addition. To reduce the resistivity of the ITO transparent electrode, a Cu/Al metal bus bar was employed. Pixel luminances and the CIE color coordinates of three primary colors under the 60-Hz field-refresh drive condition were as follows[68]: $L_{40}$(red) = 23 cd/m$^2$ (x=0.56, y=0.40), $L_{40}$(green) = 37 cd/m$^2$ (x=0.36, y=0.57), and $L_{40}$(blue) = 6 cd/m$^2$ (x=0.24, y=0.37). The original yellowish-white luminance was 125 cd/m$^2$ at 60-Hz driving. However, areal luminances[69] with 14% fill factor at 180 V ($L_{20}$) were reduced to $L_{20}$(red) = 0.68 cd/m$^2$, $L_{20}$(green) = 1.2 cd/m$^2$, and $L_{20}$(blue) = 0.3 cd/m$^2$. As a result, the luminance of white emission was 2.1 cd/m$^2$ with the CIE color coordinates x=0.42 and y=0.47. In spite of the low luminance, fine visibility was achieved because ambient light was absorbed by the color filters and black stripes, resulting in good contrast.
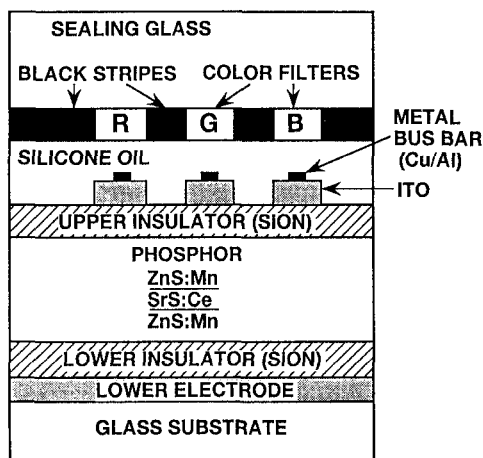


Fig. 93. Cross-sectional view of the RGB multicolor thin-film EL display in the inverted structure (Ref. 68)

Leppänen et al.[72] discussed device characteristics of their multicolor RGB thin-film EL display with a layered ZnS:Mn/SrS:Ce phosphor in an inverted and filtered EL structure. They evaluated the performance in two device structures: a conventional thin-film EL structure and an inverted thin-film EL structure with a molybdenum metal rear electrode. The phosphor layers and insulating layers were grown by ALE. The molybdenum rear electrode in the inverted structure reduced the total luminance by about

35% compared to the luminance value in the conventional EL structure with reflecting aluminum electrode. For the estimation of luminance levels of the blue emission, two blue filters were used: filter B1, for high color purity, and filter B2, for high luminance. In the conventional thin-film EL test device with an aluminum rear electrode, pixel luminances $L_{40}$ and the CIE color coordinates of the original yellowish-white, and filtered red, green, and blue emissions at a 60-Hz pulse-wave drive were as follows: $L_{40}$(yellowish-white) = 220 cd/m$^2$ (x=0.44, y=0.48), $L_{40}$(red) = 29 cd/m$^2$ (x=0.61, y=0.38), $L_{40}$(green) = 62 cd/m$^2$ (x=0.30, y=0.62), and $L_{40}$(blue/B1) = 5.5 cd/m$^2$ (x=0.13, y=0.19) or $L_{40}$(blue/B2) = 14 cd/m$^2$ (x=0.16, y=0.31). The obtained color purities are suitable for multicolor RGB EL panels, but for full-color applications, a deeper blue color is necessary. Based on the luminance values of the conventional EL structure with an aluminum rear electrode, they estimated areal luminances of red, green, blue and white (all pixels on) for a multicolor RGB EL display in the inverted device structure with a molybdenum rear electrode. Estimated areal luminances and the CIE color coordinates of white were 13.1 cd/m$^2$ and (x=0.38 , y=0.48) for B1 filter, and 14.3 cd/m$^2$ and (x=0.36, y=0.48) for B2 filter.

Table 23 summarizes display specifications of prototype multicolor EL displays with broadband-spectrum or white phosphors with patterned color filters. Here, compared items include device structure, rear electrode material, pixel number, color phosphor material, pixel luminance and the CIE color coordinates.

Table 23 Comparison of prototype multicolor EL display panels based on broadband-spectrum or white phosphors with patterned color filters

| Item | Broadband spectrum phosphor | | White phosphor | |
|---|---|---|---|---|
| | Okibayashi et al. (1991) (Ref. 46) | Haaranen et al. (1992) (Ref. 47) | Tanaka et al. (1992) (Ref. 64) | Nire et al. (1992) (Ref. 66) |
| Device structure | Inverted | Inverted | Conventional | Inverted |
| Rear electrode | Tungsten | Molybdenum | Aluminum | ITO |
| Display area (mm x mm) | 192x120 | 192x122 | 96x72 | 95.8x59.9 |
| Pixel number | 320x200 | 640x200 | 320x240 | 213x200 |
| Color phosphor | ZnS:Mn | ZnS:Mn | SrS:Ce,Eu | ZnS:Mn/SrS:Ce |
| Pixel luminance (cd/m$^2$) White | —— | —— | 61.5 | 92 |
| Yellow | 200 | —— | —— | — |
| Red | 30 | 30 | 12.8 | 23 |
| Green | 80 | 30 | 23.4 | 37 |
| Blue | —— | —— | 5.5 | 6 |
| Drive frequency (Hz) | 60 | 90 | 100 | 60 |
| CIE color coordinates (x, y) White | —— | —— | (0.34, 0.42) | (0.42, 0.47) |
| Yellow | (0.53, 0.47) | (0.53, 0.47) | —— | —— |
| Red | (0.66, 0.34) | (0.62, 0.37) | (0.67, 0.33) | (0.56, 0.40) |
| Green | (0.45, 0.55) | (0.46, 0.53) | (0.27, 0.65) | (0.36, 0.57) |
| Blue | —— | —— | (0.12, 0.20) | (0.24, 0.37) |

### 9.2.4. Dual-Substrate Structure (ZnS:Mn/Filter + ZnS:Tb + CaGa₂S₄:Ce)

*9.2.4. Dual-Substrate Structure (ZnS:Mn/Filter + ZnS:Tb + CaGa$_2$S$_4$:Ce)*

Employing the newly developed blue phosphor CaGa$_2$S$_4$:Ce Barrow *et al.*[4),245),246)] fabricated a prototype 10-inch-diagonal full-color panel with a VGA format (640x480 pixels). As shown in Fig. 94, a dual-substrate thin-film EL structure was employed.
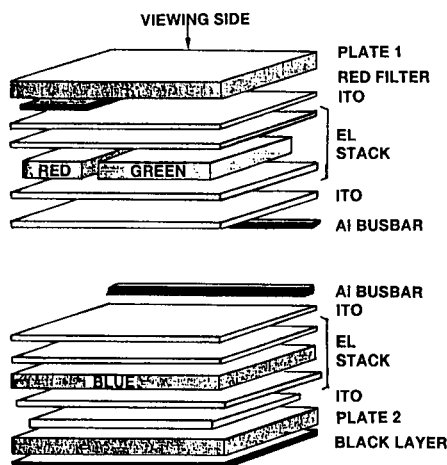


Fig. 94. Cross-sectional view of the dual-substrate full-color thin-film EL panel (Refs. 4, 245, 246)

The front (top) substrate consists of patterned red and green phosphors. The red color is obtained by filtering the ZnS:Mn emission as described in Section 7.1.1. The green emitter was ZnS:Tb phosphor film deposited by atomic layer epitaxy. The green/red substrate has the conventional patterned-phosphor structure with the exception that the rear row electrode is a transparent ITO instead of aluminum. Narrow aluminum bus bars are added in parallel with the ITO row electrodes on both substrates to enhance conductivity. The rear substrate is a monochrome blue-emitting EL panel with transparent top and bottom electrodes. The CaGa$_2$S$_4$:Ce film is used as a blue emitter. A black layer was applied to the back of the rear substrate to ensure high contrast without the need for a circular polarizing filter. The red and green substrates are aligned and sealed together in close proximity to achieve a wide viewing angle with no parallax.

The luminances L$_{40}$ and the CIE color coordinates of the test devices for the three primary colors at 60 Hz are as follows: L$_{40}$(red) = 68 cd/m$^2$ (x=0.65, y=0.34), L$_{40}$(green) = 100 cd/m$^2$ (x=0.31, y=0.60) and L$_{40}$(blue) = 10 cd/m$^2$ (x=0.15, y=0.19), yielding the ratio of the red, green and blue luminance capabilities to be 6.8:10:1. If equal-size RGB subpixels are employed in the full-color panel, the blue luminance would need to be further enhanced to balance the maximum capabilities for the other two primaries in order to achieve the desired 3:6:1 RGB ratio. The dual-substrate panel structure, however, allows the blue subpixel to be nearly the same size as sum of the red and green subpixel areas while maintaining a high fill factor for the red and green. As a result, it becomes possible to increase the blue luminance to achieve the desired 3:6:1 RGB luminance ratio. Another advantage of the dual-substrate panel structure is that the drive electronics can be independently optimized for each substrate. The threshold voltage of

the blue phosphor, therefore, need not match that established for the red and green phosphors. By splitting the column electrodes on the blue substrate, a higher refresh frequency can be used, yielding increased blue luminance. A further advantage of the dual-substrate structure is that each of the red/green and blue substrates can be processed and tested separately before they are sealed, which is expected to produce higher manufacturing yields.

Color reproduction characteristics of the dual-substrate full-color thin-film EL panel is shown in Fig. 95, which indicates that the color range of the full-color EL panel is very close to that for the color CRT. The EL red and green primaries are more saturated than those for the color CRT, while the EL blue approaches the CRT blue. A white color areal luminance of 10 cd/m$^2$ with the CIE color coordinates of x=0.37 and y=0.37 was achieved for a VGA color panel with all three phosphors on.
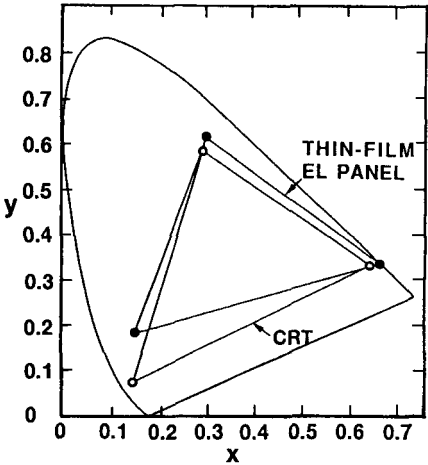


Fig. 95. Color reproduction characteristics of the full-color thin-film EL panel (Ref. 4)

Table 24  Specifications of prototype full-color thin-film EL panel (VGA format) (Ref. 4)

Luminance-related specifications

| Phosphor | Red | ZnS:Mn/Filter |
| | Green | ZnS:Tb |
| | Blue | CaGa$_2$S$_4$:Ce |
| Subpixel luminance L$_{40}$ (cd/m$^2$) | Red | 68 |
| | Green | 100 |
| | Blue | 10 |
| Drive frequency (Hz) | | 60 |
| CIE color coordinates (x, y) | Red | (0.65, 0.34) |
| | Green | (0.31, 0.60) |
| | Blue | (0.15, 0.19) |

Panel-related specifications

| Display size | | 10 inch diagonal |
| Number of pixels | | 640x480 |
| Number of colors | | 16 |
| Color pixel pitch (mm) | | 0.31 |
| Subpixel size (mm x mm) | Red | 0.060x0:210 |
| | Green | 0.170x0.210 |
| | Blue | 0.210x0.210 |
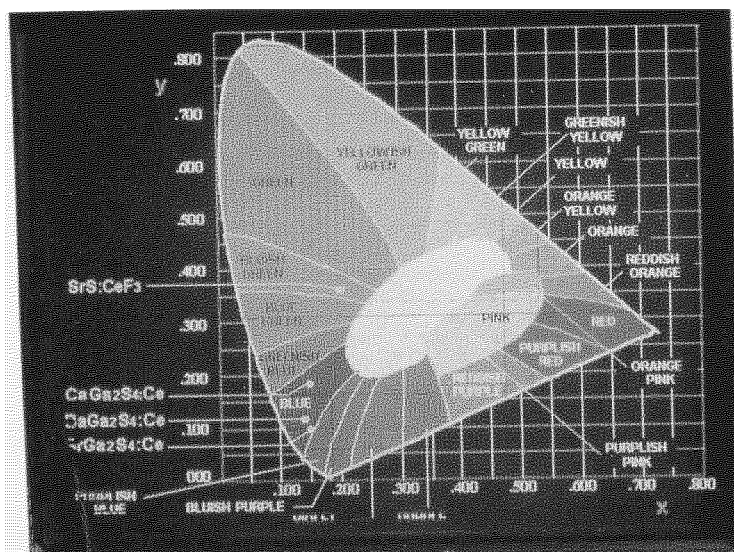
Fig. 96. Color pictures of the prototype full-color EL panel (Courtesy of Planar Systems)

Table 24 summarizes specifications of the prototype dual-substrate full-color thin-film EL panel and Fig. 96 shows color pictures of the prototype full-color EL panel.

Based on this technology, the first commercial full-color, 320x256 pixel, thin-film electroluminescent display monitor has been developed[8]. The Ce activated calcium thiogallate blue phosphor in combination with the high fill factor of the dual-substrate structure and double driven rows has for the first time enabled sufficient blue luminance for a practical full-color thin-film EL monitor. ALE thin films have enabled all wet etching of the phosphors, making color thin-film EL panel fabrication very cost competitive. Chip-on-glass (COG) packaging of the row and column drivers has made the high density interconnects possible in a very compact and rugged package.

In the developed full-color display monitor, the dual-substrate structure has made it possible to obtain high fill factors: The blue fill factor is 48%, the red, 13%, and the green, 35%. The ratios have been chosen to provide a good white with the available luminances of the individual red, green and blue phosphors.

In the red/green substrate, ALE-prepared $Al_2O_3$ thin films are used as the lower insulating layer and the thin wet-etch barrier. The conformal nature of the ALE process with extremely low defect density is critical in both of these areas. The barrier between the red and green phosphors is a 600 Å ALE $Al_2O_3$ thin film. This thin layer is sufficient to protect the green ZnS:Tb phosphor during wet etch of the ZnS:Mn yellow phosphor which is deposited and patterned immediately after the green. Also in the blue substrate, ALE $Al_2O_3$ thin films are used as the lower and upper insulating layers.

The first commercial full-color thin-film EL display monitor is designed with two operating modes: Low power mode and high luminance mode. In the low power mode the display is driven at a 60-Hz frame rate, and in the high luminance mode the display is driven at a 180-Hz frame rate. In both cases, a pair of blue rows is driven simultaneously on the blue substrate, effectively doubling the blue frame rate and thereby doubling its luminance. The white luminance in the high luminance mode was 30 cd/m$^2$ with the CIE color coordinates of x=0.35 and y=0.35. The contrast ratio at this luminance is greater than 20:1 in a 200 lux ambient. This high contrast ratio is achieved due to the low reflectance nature of the transparent thin-film structure. The overall performance of the first full-color EL display monitor is summarized in Table 25.

Table 25    Specifications and performance characteristics of the first commercial full-color thin-film EL display monitor (Ref. 8)

Panel-related specifications

| Item | | Specifications |
|---|---|---|
| Display area (mm x mm) | | 96.0 x 76.8 |
| (Inch diagonal) | | (4.8) |
| Number of color pixels | | 320 x 256 |
| Color pixel pitch (mm x mm) | | 0.30 x 0.30 |
| Monitor size (mm x mm x mm) | | 162 x 138 x 45 |
| Weight (g) | | 500 |
| Fill factor (%) | Red | 13 |
| | Green | 35 |
| | Blue | 48 |

Luminance-related performance characteristics

| Item | | Low power mode | High luminance mode |
|---|---|---|---|
| Subpixel luminance (cd/m²) | Red | 23 | 70 |
| | Green | 17 | 51 |
| | Blue | 2 | 6 |
| Areal luminance (cd/m²) | Red | 3 | 9 |
| | Green | 6 | 18 |
| | Blue | 1 | 3 |
| | White | 10 | 30 |
| Drive frame rate (Hz) | | 60 | 180 |
| Typical power (W) | | 5 | 15 |
| Contrast ratio (200 lux ambient) | | 10:1 | 20:1 |

## 9.3. Other Applications

### 9.3.1. Edge Emitter Light Source for Electrophotographic Printers

The edge emitter concept[125),279),280)] takes advantage of the light guiding nature of the thin-film EL device structure to extract light from the edge of the film stack rather than the face as in typical display applications, as described in Section 4.1.2.

As shown in Figs. 97 and 98, in edge emission the light is collected from an effective emission length on the order of 1 mm rather than the 1 μm thickness of a typical thin-film EL display. In practice this leads to an edge emission luminance that is one to two orders of magnitude larger than the normal thin-film EL face emission and can be optimized by reducing the internal scattering in the thin-film EL film stack.
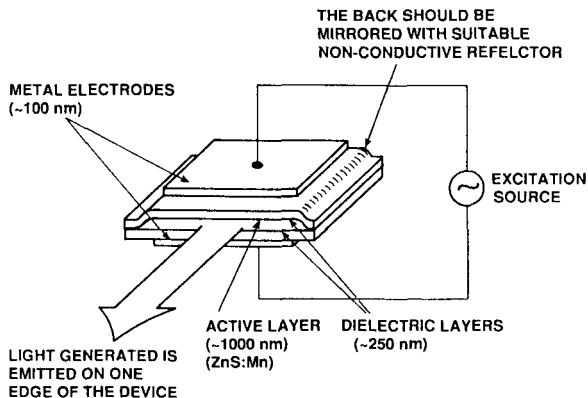


Fig. 97. Schematic illustration of the thin-film EL edge emitter concept (Ref. 125)
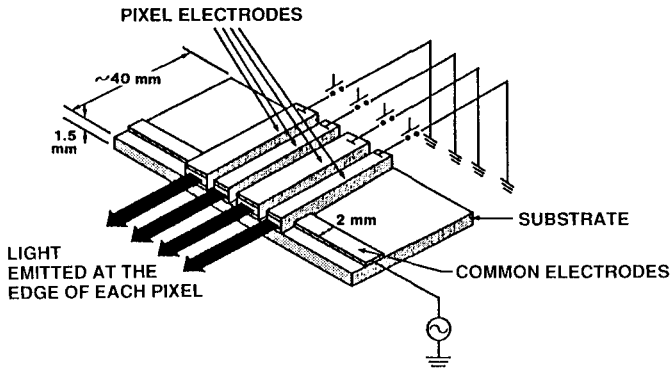
Fig. 98. Schematic arrangement of an edge-emitter (Ref. 125)

Because of the small capacitance of the single line of pixels in an EL light bar, it is easy to drive the edge emitting devices at frequencies in the 1 to 10 kHz range which further increases the luminance. Thus edge emission from a thin-film EL device gives rise to the possibility of building a completely solid state, high resolution "light bar" with a radiance in excess of 250 milliwatts per $cm^2$ that can be used to expose the photo receptor in electrophotographic printer applications.

In fact, Edge Emitting Technologies Inc. (EET) has been formed to build a printer head based on an EL light bar that will produce laser-writer-quality copies for personal computer applications. EET feels that EL edge emitter will not only be cost competitive but also have performance advantages over today's laser printers in the area of size, ruggedness, resolution, and gray scale capability. Because of the high frequency drive and the very small EL "pixel" height of the light bar, gray scale can be obtained by either modulating the duty cycle of the EL device or spatial fill factor of the written pixel, or both. These "digital" gray scale approaches are simpler to implement than the analog techniques used in typical gray scale thin-film EL displays.

### 9.3.2. Thin-Film Cold Cathode

A new thin-film cold cathode has been developed[281)-284)] by utilizing hot electrons produced in II-VI compounds such as ZnS by a high electric field. Figure 99 schematically shows the cross-sectional structure of the ZnS-based thin-film cold cathode device[281),282)]. The device is a single insulating structure which consists of an ITO-coated glass substrate, an insulating layer of $Ta_2O_5$ (thickness 300-500 nm), a ZnS layer (about 500 nm) and a Au electrode (about 10 nm). Here, ZnS thin film is an electron acceleration layer and no luminescent centers, such as Mn, are added in order to avoid scattering of hot electrons. The thickness of Au electrode was set at approximately 10 nm, which is less than the mean free path of the electrons (~20 nm), to achieve electron tunneling through the Au film. The device produced planar and pulsated electron emissions with energies of more than 2.7 eV. The maximum emission current and stored charge density were 28 nA/$cm^2$ and 1.2 µC/$cm^2$, respectively, at a 5-kHz sinusoidal wave driving. Cathodoluminescence was observed with a luminance of 160 cd/$m^2$ for a

green-emitting ZnO:Zn phosphor and 85 cd/m$^2$ for a blue-emitting ZnS:Ag phosphor for a 5-kHz driving.
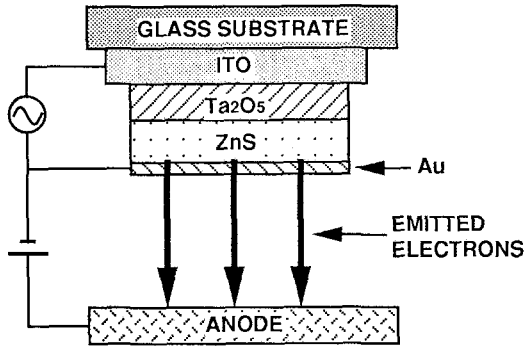


Fig. 99.  Cross-sectional structure of ZnS-based thin-film cold cathode device (Ref. 281)

Because of the simple structure made of stacked polycrystalline or amorphous thin films and easiness of large area fabrication, it is expected that these thin-film cold cathode devices can be applied to flat panel displays, microvacuum tubes which must reliably operate at very high speeds or radiometric circumstances, electron sources of surface analyzing apparatus.

### 9.3.3.  LCD Backlight

Figure 100 shows the device structure of ac powder EL used as a backlight[285] for liquid crystal displays.
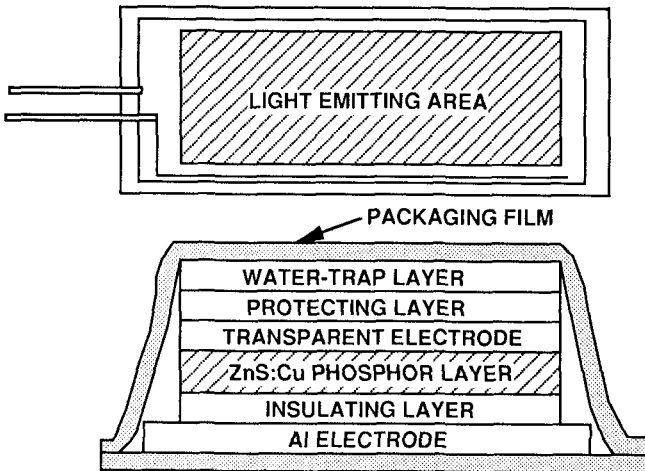


Fig. 100.  Structure of an ac powder EL device for LCD backlight

In order to reduce the weight an ITO-coated polyester film is used instead of a glass as substrate. Behind a phosphor layer is placed an insulating layer with high dielectric constant, such as $TiO_2$ and $BaTiO_3$. This insulator of several tens of micrometer thick increases the effective voltage of the phosphor layer. The whole device is covered by a waterproof packaging film and in addition a water-trap layer is placed. Phosphor for a green-emitting EL is ZnS:Cu. On the other hand, phosphor for a white-emitting EL is blue-green emitting ZnS:Cu,Cl mixed with organic red dyes.

An ac powder EL device has a detrimental characteristics of fast decreasing luminance with increasing operation period caused by an impedance increase due to decrease in device capacitance. However, since luminous efficiency do not decrease as much as luminance, improved DC/AC inverters with constant-power characteristics[285] are implemented to minimize luminance decrease with operation time. As a result, a green-emitting EL device with an initial luminance of 150 cd/m$^2$ (125 V and 1300 Hz drive) has a half life of 12000 hours and a white-emitting EL device with an initial luminance of 195 cd/m$^2$ (125 V and 1000 Hz drive) has a half life of 2500 hours in the test conditions of 25°C and 60% relative humidity.

# 10. RELIABILITY

In considering the reliability of thin-film EL devices, three important factors must be taken into account:
1. Electrical reliability with respect to electric breakdown
2. Long-time reliability
3. Shifts in luminance-voltage (L-V) characteristic curve with operation

Electrical breakdown properties depend strongly on the electrical properties of the insulating-layer materials and the thin-film fabrication processes. For long-time reliability, the hygroscopic, adhesive and photolithographic resistant properties of phosphor layer and dielectric-layer materials must be taken into account, and proper choices of passivation and sealing materials are essential. Shifts in luminance-voltage (L-V) characteristics curve with operation time are not suitable because they result in luminance deterioration. With proper choices of the insulating-layer structure and crystallinity control of the phosphor-layer films it has become possible to obtain EL devices[212] with no shifts in L-V characteristics curve. In addition, effects of various stresses on the performance of EL panels and display units should be considered[104].

## 10.1. Electrical Reliability

As discussed in Chapter 5, the requirements of the insulating layers are high dielectric constant $\varepsilon_0 \varepsilon_r$ and high breakdown electric field $E_{BD}$, i.e., a large figure of merit defined by $\varepsilon_0 \varepsilon_r E_{BD}$, which is equal to the maximum storage charge density, $Q_{max}$. When insulators with high $Q_{max}$ are used, a low-voltage drive becomes possible. However, insulators with high $Q_{max}$ tend to have a low reliability, and propagating-type electric breakdown often occurs. Several multilayered structures[286],[287] of insulating layers have been proposed to overcome this difficulty.
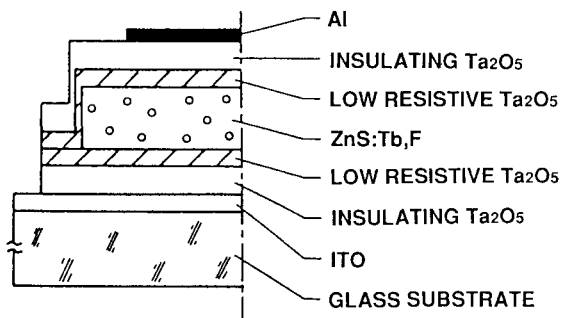


Fig. 101. EL device structure employing insulating and low resistive Ta$_2$O$_5$ thin films (Ref. 286)

Figure 101 shows an EL device structure with stacked insulating layers made of insulating Ta$_2$O$_5$ and low-resistive Ta$_2$O$_5$ thin films. These Ta$_2$O$_5$ films can be prepared by changing sputtering deposition conditions. In this structure, insulating Ta$_2$O$_5$ films provide electrical insulation and low-resistive Ta$_2$O$_5$ films give increased charge generation and better adhesiveness between the phosphor layer and insulating layers. Another

combination of the insulating layers is a $SiO_2/Ta_2O_5$ stacked structure[287] of the order $Al/SiO_2/Ta_2O_5$/phosphor layer/$Ta_2O_5/SiO_2$/ITO/glass substrate. Here the $SiO_2$ layers act as electrically insulating layers and the $Ta_2O_5$ layers serve as partly conductive layers. In addition to these examples, $SiO_2$, $TiO_2$, and CaS are used as buffer thin films between electrodes and insulating layers or between insulating layers and the phosphor layer to stabilize EL operation[288],[289].



SEALING GLASS LID
REAR ELECTRODE, Al
$Al_2O_3$
SILICON OXINITRIDE
ZnS:Mn PHOSPHOR LAYER
SILICON OXINITRIDE
$SiO_2$
TRANSPARENT ELECTRODE, ITO

SILICONE OIL FILLING SPACE

GLASS SUBSTRATE
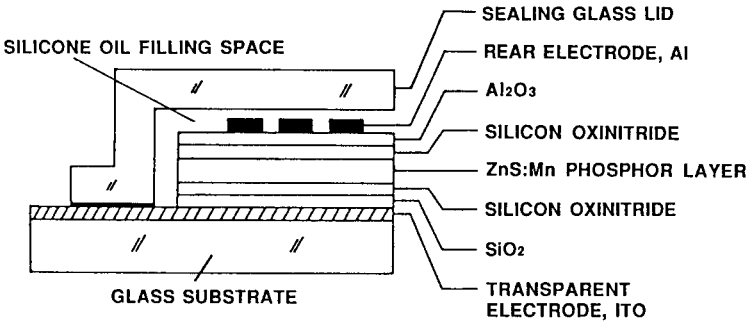
Fig. 102. Cross-sectional structure of commercially available thin-film EL devices (Ref. 2)



THIN-FILM EL STRUCTURE

| Al |
| $Al_2O_3$ |
| SiNO |
| ZnS:Mn |
| SiNO |
| $SiO_2$ |
| ITO |
| GLASS |

| Al |
| $SiO_2$ |
| SiNO |
| ZnS:Mn |
| SiNO |
| $SiO_2$ |
| ITO |
| GLASS |

BREAKDOWN VOLTAGE (V)

NUMBER OF SAMPLES
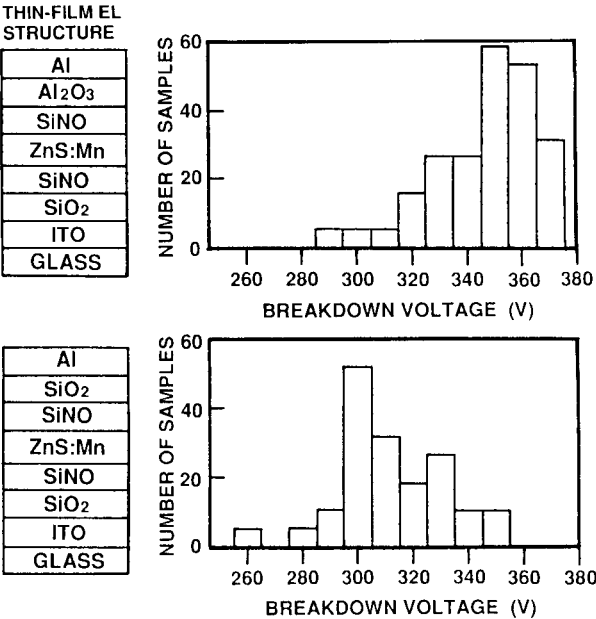
Fig. 103  Comparison of breakdown voltage distribution of thin-film EL panels (Ref. 2)

In commercial EL devices of Sharp, composite insulating layers[2] are employed to increase the breakdown voltage and environmental resistivity of the panel. This is shown in Fig. 102, where the first insulating layer consists of silicon-oxynitride/$SiO_2$ stacked layers and the second insulating layer, of $Al_2O_3$/silicon-oxynitride. Films of $Al_2O_3$ and silicon-oxynitride are well known for their high packing density feature by physically and chemically stable insulating properties. Structuring of composite insulating films by combining insulators of high individual qualities proved that eminent enhancement of insulating property and environmental resistivity could be realized.

The average DC breakdown voltage of the improved version of thin-film EL panel exceeded 320 V, which offers an ample safety margin for the electric breakdown of the panel. Figure 103 shows the distribution of breakdown voltage[2] of the improved panel measured under application of DC voltage. For comparison, measured results of the panel whose upper insulating layer has different structure are shown. As these figures clearly show, the breakdown voltage is higher in the case when $Al_2O_3$ film is placed next to the Al rear electrode than the case of $SiO_2$ film in contact with the Al electrode. This is probably due to the better adhesiveness of $Al_2O_3$ to Al. Another advantage noteworthy of the composite insulating layer of silicon-oxynitride/$Al_2O_3$ is in its excellent resistivity to chemicals. This property is essential for the enhancement of the productivity of thin-film EL panels in the forming process of Al electrode stripes by chemical etching.

In ALE-prepared EL devices, improvement in reliability was realized[161] by replacing $Al_2O_3$ by mixed dielectric layers of $Al_2O_3$/$TiO_2$: The ratio of the breakdown voltage to the operation voltage increased from 1.6 to 2.6, giving an ample safety margin for the electric breakdown of the panel. The mixed dielectric layers of $Al_2O_3$/$TiO_2$ also improved moisture resistivity characteristics in damp-test conditions..

## 10.2. Long-Time Reliability

The lifetime-determining factors of EL devices are the peeling of thin films and the formation of very small dielectric breakdown holes. These small breakdown holes result from local defects in the thin films during the first stage of the drive annealing process. These holes are approximately 30 μm in diameter and their number does not increase with annealing time. Therefore, they do not cause any practical troubles. Proper control of process conditions is important to decrease the defects.

On the other hand, peeling of the thin films is caused by moisture (water) leaking into the phosphor layer/insulating layer interface through pinholes[290]. During EL drive operation, ionization of the water occurs from hot-electron impact in the phosphor layer, generating $H^+$ and $OH^-$ ions. The $H^+$ ions will combine at the interface to form hydrogen gas. The gas pressure lifts the second insulating layer from the phosphor layer, leading to peeling of the thin films. With longer drive periods, peeling proceeds rapidly, and it affects the lifetime of EL devices. To avoid this, proper control of atmospheric conditions, especially humidity control, during and after the deposition process is necessary. In particular, encapsulation of EL devices by sealing is very effective to prevent moisture from entering into them. Sealing methods include oil sealing, gas sealing, vacuum sealing, and resin sealing. Among these, the oil sealing method is the best. In commercial EL display devices, silicone oil and silica gel powders are placed in the glass-sealed EL devices as shown in Fig. 102. Furthermore, since in the double-insulating-layer structure the phosphor layer is sandwiched by insulating layers, it is possible to prevent moisture from entering the phosphor layer. By employing the structures discussed above, a long lifetime, of more than 20000 hours, has been realized.

The drive method is also important to obtain long-time reliability[262],[265]. In the beginning, a field-refresh drive method[31] was employed, as discussed in Section 8.1. As is shown in Fig. 71, unsymmetrical drive voltage waveforms are created at different parts of the EL devices so that the luminance versus voltage characteristics deteriorate and latent images are created. The deterioration is characterized by decreases in both threshold voltage and luminance within the high luminance region[264]-[266].

To overcome this difficulty, the p-n symmetric drive method[251] and the p-p symmetric drive method[252] have been introduced, as discussed in Section 8.2. As shown in Figs. 73 and 75, the drive wave forms are symmetric at all pixels, no charge accumulation is created, resulting in no latent images. In addition, these symmetric drive methods allow a higher voltage to be applied to EL devices than that in the field-refresh method, so that saturation regions of the L-V characteristic curves can be utilized. This makes it possible to realize a uniform luminance over the whole area of the EL device, and the luminance change with time is substantially reduced.

### 10.3. Shifts in Luminance-Voltage (L-V) Characteristics Curve with Operation

There are three kinds of L-V shifts during the aging process of EL devices:
1. positive shift: L-V curve shifts towards higher voltage.
2. negative shift: Threshold voltage shifts toward lower voltage.
3. no shift: Essentially no shift in L-V curve with small softening at the shoulder.
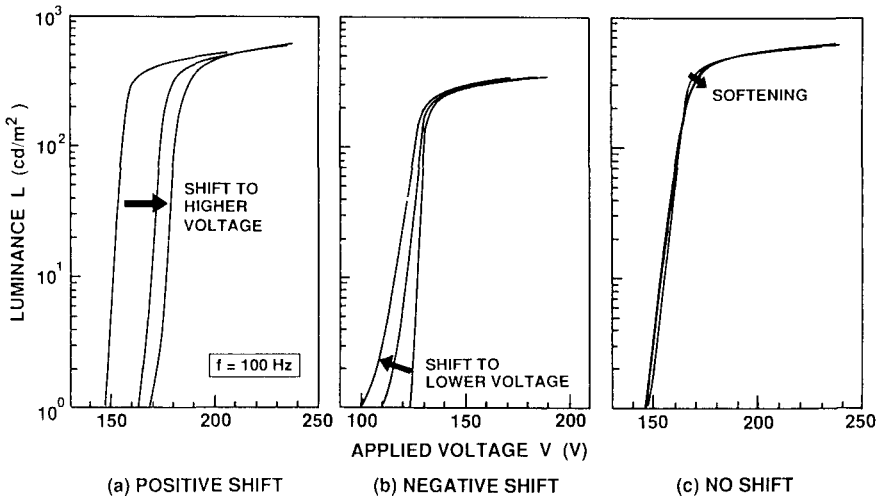


Fig. 104. Shifts in luminance vs. voltage (L-V) characteristics curves during drive operation: (a) positive shift (Refs. 103 and 212); (b) negative shift (Refs. 193 and 212); (c) no shift (Ref. 212)

Figure 104 shows these L-V shift characteristics. Fig. 104 (a) is for an EBE-prepared ZnS:Mn device[103], [212] and Fig. 104 (b) is for an ALE-prepared ZnS:Mn device[193]. In the EBE films L-V characteristic curve shifts to higher voltage with aging time (positive shift). The amount of L-V voltage shift and stabilization time depends on the

deposition conditions and insulating layer materials, and stabilization time is 10-30 hours in typical devices. Sputtered ZnS:Mn thin films yields the same L-V shift results as those of EBE ZnS:Mn thin films. On the other hand, in the ALE-prepared films threshold voltage shifts to lower voltage (negative shift), and this behavior persists for a long time. These L-V shifts are caused by changes in high-electric-field electronic conduction characteristics, which are governed by tunneling injection currents from the trap states at the phosphor layer/insulating layer interface and space-charge-controlled currents or avalanche currents in the bulk ZnS phosphor layer. These L-V shift behaviors depend not only on phosphor-layer thickness, Mn concentration and insulating layer materials, but also on phosphor layer quality. In the co-evaporated ZnS:Mn films, L-V characteristics instability was significantly reduced through two thermal post-deposition methods[291] which increased the sulfur content of the ZnS thin-film layer. Both approaches involved thermal treatment of the deposited ZnS film before the second insulator deposition: one method was to anneal the sample in an $H_2S$ atmosphere and the other was to heat the sample in an enclosed volume with solid sulfur present. These improvements support the assertion that the observed instabilities are mainly due to sulfur vacancies. Worst case differential aging after 1000 hours of operation was well within the requirements of 16-level gray scale monitors. In the HT-CVD films it became possible to obtain EL devices without any threshold shift as shown in Fig. 104 (c) for more than 20000 hours by controlling crystallinity of the phosphor layer, and selecting proper insulating layer structure and combinations of insulating layer materials[212],[213].

## 10.4. Display Resistance to Environmental Stresses

Display resistance[104] to environmental stresses such as pressure, temperature, and temperature/humidity is very important to assure EL device reliability. The present status is listed in the following.

### 10.4.1. Pressure
The solid state nature of the thin-film EL device is essentially immune to pressure variation or elevation changes. The limiting feature is the mechanical integrity of the seal technology. Typical epoxy seals for commercial panels will easily withstand 12000 m elevation and submersion to -2500 m. Militarized versions will withstand elevations greater than 30000 m and overpressures of 4 atmospheres.

### 10.4.2. Temperature
The characteristics of a non-operating thin-film EL panel are unaffected when subjected to temperature extremes from -55 to 125°C. Typically, commercial thin-film EL display units are specified to operate from 0°C to 55°C, the limitation being due to the electronics rather than the panel. However, thin-film EL display systems with militarized electronics have been designed to operate over the temperature range of -40 to 85°C.

### 10.4.3. Temperature/Humidity
This is primary a stress on the panel seal and interconnect technologies. Both commercial and military display units can pass the Mil 202F, method 106 10 day temperature and relative humidity test in which the operating unit is cycled from -10°C to +65°C at 90% RH when above 25°C.

## 11.  CONCLUSIONS AND FUTURE PROSPECTS

Thin-film electroluminescence, in comparison with competing flat-panel display technologies such as liquid crystal displays (LCDs), plasma display panels and vacuum fluorescent displays, possesses many important features required of a flat panel technology: excellent visual characteristics, a rugged and compact device with a simple multicolor display structure.  Other superior characteristics are as follows:
1. Good display qualities from an ergonomics viewpoint
   • an emissive display with large viewing angle and good contrast
   • a possibility of resolution higher than 8 lines/mm
2. Temperature-independent emission
   • suitable for automotive equipment used under very severe temperature requirements
3. All-solid devices
   • rugged and vibration resistant
   • suitable for personal computers used under very severe vibrational conditions, such as in military equipment or spacecraft
4. Low-power, thin and lightweight devices
   • lowest power consumption among emissive flat-panel displays
   • thickness of less than 30 mm and weight of less than 700 g in EL display units

Ten years have passed since volume production[2] of monochrome (yellow) thin-film EL display panels started in 1983, and they have gained a wide marketplace acceptance.  Now they are available from Sharp, Planar Systems and Planar International.  During these years, performance improvements of EL displays have been carried out aiming at higher luminance, larger size, finer resolution and gray-scale capability.  In addition, price has been reduced substantially.  Today, the product range covers a great variety of sizes and resolutions, ranging from small battery-operated displays to full-page displays for workstation.  However, volume production is still small compared with that of liquid crystal displays because of the high cost, and so the cost reduction is necessary.  In addition, further reduction of power consumption and further increase in display sizes are in demand for monochrome EL displays.  The biggest challenge today is realization of multicolor and full-color EL display panels.

Regarding the cost reduction, simplification of drive circuits, which amounts to one-third of the cost, is most important.  In this context, drivers with higher number of outputs, larger ASIC-chips and the use of tape-automated-bonding (TAB) and chip-on-glass (COG) technologies are important.  As a result of these developments, EL panel can be made as thin as 4 mm in depth.  Improvements of device structures and deposition conditions are also important.  Lower temperature processes with good crystallinity are desired for cost reduction and continuous processes without breaking the vacuum are necessary for better thin-film qualities.  In addition, reduction of process steps is imperative to increase yields and throughputs, in particular, in the developments of color displays.

Since an EL display is a capacitive device, a large current is necessary in driving.  Therefore, power consumption reduction in the electrodes and drive circuit system is effective to low-power driving.  Employment of resonating circuits using inductances has made it possible to realize low-power-consumption EL display panels[245] such as 7-inch-diagonal 320x128 display with 1.47 W and 9-inch-diagonal 640x400 display with 6 W.  These displays are now applied to battery-driven portable equipment.

Display size and display capacity are limited by the RC time constant, current capacity of driver ICs and power dissipation in the electrode system, where R is the

electrode resistance and C is the panel capacitance. In the present device structure and technology, the largest possible display size would be 14-inch-diagonal and several hundred thousand pixels. In the conventional thin-film EL device structure the power consumption would be about 100 W, while in the inverted thin-film EL device structure with metal bus-bars on ITO electrodes the power consumption would be reduced to 40-45 W. For the 20-inch-diagonal-class EL displays, the split electrode technique[272),292)] is employed to realize an 18-inch-diagonal 1024x864 display by driving independently the upper and lower parts of the display. For the realization of EL display panels larger than 20-inch-diagonal size, pasting mechanically four EL displays side-by-side would be a solution.

The color display development status and future prospects are the next topic. First we discuss the color phosphor materials. As for three primary colors, the following phosphors are the solutions now: $ZnS:Tb,F$ for green, filtered $ZnS:Mn$ for red and recently-developed[4)] $CaGa_2S_4:Ce$ for blue. Recently, broadband spectrum or white phosphors have been investigated vigorously because of the prospect of realization of multicolor or full-color EL displays with the use of color filters. For this purpose, the brightest yellow-emitting $ZnS:Mn$ phosphor with a broadband emission spectrum and a multi-layered $ZnS:Mn/SrS:Ce$ phosphor[71)] with a yellowish-white emission are good candidates. However, luminance improvement is still necessary.

Next, we discuss multicolor and full-color thin-film EL panels. The performance of the red/green/yellow thin-film EL display[48)] based on the inverted, patterned color filter device structure using $ZnS:Mn$ phosphor was found to be excellent and the first commercial multicolor thin-film EL display[3)] based on this technology was put into the market in 1993. This display will be a noteworthy cost-effective alternative for demanding multicolor flat panel applications where highlighting is needed and the presence of blue color is not crucial. Furthermore, full-color capability of thin-film EL display was demonstrated in 1993 by using a dual substrate EL panel structure[4)]. This structure combines patterned red/green phosphors on one substrate with a new blue phosphor, $CaGa_2S_4:Ce$, on a separate substrate in a stacked configuration, which couples the unfiltered blue emission with saturated red and green EL emission to produce a color gamut approaching that of the color CRT. Based on this technology, the first commercial full-color, 320x256 pixel, thin-film electroluminescent display monitor[8)] was developed in 1994.

These all-solid, emissive color displays equipped with superior EL characteristics of fast response and wide viewing angle should find application fields not only in displays for personal computers but also in edge emitters for printers, opto-electronic (OE) ICs, and input/output equipment with high value-added qualities. Further development work, however, is needed to improve individual color phosphor. Strong research efforts are justified by the prospects of simple, multiplexed full-color thin-film EL displays with lower power consumption.

Now let us turn to the discussion on new developments in EL device structures, in particular phosphor layer structures. Recently multi-layered phosphor structures have been proposed[5)-7),70),71),73),74),196),293)-295)] to obtain higher luminance and higher luminous efficiency by assigning separately to different layers the roles of the phosphor layer of being a host for luminescent centers for EL emission, providing interface states with insulating layers for the high-field electron tunnel injection and being a hot electron acceleration layer. In the device[5)-7)] with ten layers of $ZnS/SrS:Ce/ZnS\cdots ZnS/SrS:Ce/ZnS$, ZnS layers are considered to be the hot electron acceleration layers and SrS:Ce layers, the EL emitting layers. Luminance of blue-green emission was doubled and the luminous efficiency of 1.3 lm/W was obtained. This idea

was applied to white-emitting multilayered $(ZnS:Mn/SrS:Ce)_n$ device[70),71),73),74)], resulting in luminance of 225 cd/m$^2$ and luminous efficiency of 1.3 lm/W at 60-Hz pulse-wave driving in the nine-layered device. Another example is the multilayered $(Y_2O_2S:Tb/ZnS)_n$ EL device[295)] In the double-insulating-layer structure, single-layered $Y_2O_2S:Tb$ did not yield any EL emission, but in the multilayered device structure with ZnS, green emission was realized with the luminance of 130 cd/m$^2$ at 1-kHz driving. Here it is considered that hot electrons accelerated in the ZnS layer are injected into $Y_2O_2S:Tb$ layer and impact excite Tb luminescent centers, resulting in green emission. On the other hand, in the green-emitting ALE-ZnS:TbS$_x$ device[196)], high luminance was obtained by concentrating terbium to layers separated by pure ZnS, i.e., by depositing alternately Tb-rich layers and Tb-free ZnS layers. Furthermore, quantum well EL structures[293)] and superlattice EL structures[296),297)] have been proposed by extending these multilayered device ideas. For the realization of these new EL devices, ALE, MOCVD, HT-CVD and MSD will be suitable deposition methods. These new EL device structures will lead to finding new materials, and both new device structures and new materials will lead to the development of new deposition methods. It is expected that this development interplay of materials, deposition methods and device structures will create not only new EL devices with high luminance and high luminous efficiency but also new physics.

Finally, we discuss drive methods. In contract to the present-day refreshed EL devices driven by multiplexing drive methods, such as the field-refresh drive method[31)] or p-n or p-p symmetric drive method[251),252)], it is possible to obtain memory EL devices by incorporating thin-film transistors (TFTs) at each pixel, which has already been done in color LCD panels. This method was first applied to EL devices, but no practical display panels were fabricated because of difficulties in obtaining large-area, high-voltage TFTs without defects. However, recent success in large-area TFTs for LCDs together with substantial improvements in thin-film fabrication technologies should give a strong impetus to the EL community in trying to fabricate TFT-driven EL display devices. One of the advantages of three-terminal TFTs over the present two-terminal devices is that the circuit system with TFTs is easier to handle. Once high-voltage TFT arrays attain a practical level of production, TFT-driven EL display devices should become the mainstream of memory devices. Recently three trials along this line were reported: Vanfleteren et al.[258)] used CdSe TFTs, Suzuki et al.[261)] used amorphous-Si TFTs to drive a thin-film ZnS:Mn EL display and Khormaei et al.[262)] used single-crystal Si MOS TFTs on SOI to drive a high-resolution thin-film ZnS:Tb EL display.

# REFERENCES

1. G. Destriau, *J. Chim. Physique (France)* **33** (1936) 587.
2. M. Takeda, Y. Kanatani, H. Kishishita and H. Uede, *Proc. SPIE* **386**, *Advances in Display Technology III* (1983) 34.
3. D. Cramer, J. Haaranen, R. Törnqvist and T. Pitkänen, *Application Digest of 1993 SID International Symposium* (1993) 57.
4. W.A. Barrow, R.E. Coovert, E. Dickey, C.N. King, C. Laakso, S.S. Sun, R.T. Tuenge, R.C. Wentross and J. Kane, *Digest of 1993 SID International Symposium* (1993) 761.
5. R.H. Mauch and K.O. Velthaus, *Displays* **13** (1992) 107.
6. K.O. Velthaus, R.H. Mauch, H.W. Schock, S. Tanaka, K. Yamada, K. Ohmi and H. Kobayashi, in *Electroluminescence-Proceedings of the Sixth International Workshop on Electroluminescence*, eds. V.P. Singh and J. C. McClure (Cinto Puntos Press, El Paso, 1992), p.187.
7. R.H. Mauch, K.O. Velthaus, H.W. Schock, S. Tanaka and H. Kobayashi, *Digest of 1992 SID International Symposium* (1992) 178.
8. W. Barrow, R. Coovert, E. Dickey, T. Flegal, M. Fullman, C. King and C. Laakso, *Conference Record of the 1994 International Display Research Conference* (1994) 448.
9. W.E. Howard, *Proc. SID* **22** (1981) 47.
10. R. Mach and G.O. Müller, *Phys. Stat. Sol.* **(a) 69** (1982) 11.
11. H. Kobayashi, in *Optoelectronic Materials and Devices*, M.A. Herman (ed.) (PWN-Polish Scientific Publishers, Warszawa, 1983), Chap. 13.
12. P.M. Alt, *Proc. SID* **25** (1984) 123.
13. Y.A. Ono, in *Encyclopedia of Applied Physics*, Vol. 5, ed. G.L. Trigg (VCH Publishers, Inc., American Institute of Physics, Weinheim and New York, 1993) p.295; in *1993 SID Seminar Lecture Notes*, Vol. II, F-1 (1993) F-1/1; in *Progress in Information Display Technology,* Vol. 1, H.L. Ong and S. Kobayashi (eds.) (World Scientific Publishing Co., Singapore, 1995), Chap. 2.
14. S. Shionoya and H. Kobayashi (eds.), *Electroluminescence-Proceedings of the Fourth International Workshop on Electroluminescence* (Springer Proceedings in Physics, Vol. 38) (Springer-Verlag, Berlin, 1989).
15. M. Leskelä and E. Nykänen (eds.), *Acta Polytechnica Scandinavica* **Ph 170** (Applied Physics Series No. 170), *Fifth International Workshop on Electroluminescence* (Finnish Academy of Technology, Helsinki, 1990).
16. V.P. Singh and J.C. McClure (eds.), *Electroluminescence-Proceedings of the Sixth International Workshop on Electroluminescence* (Cinco Puntos Press, El Paso, Texas, 1992).
17. W. Lehmann, *J. Electrochem. Soc.* **113** (1966) 40.
18. N.A. Vlasenko and Iu.A. Poplov, *Optics & Spectroscopy* **8** (1960) 39.
19. M.J. Russ and D.I. Kennedy, *J. Electrochem. Soc.* **114** (1967) 1066.
20. D. Kahng, *Appl. Phys. Lett.* **13** (1968) 210.
21. E.J. Soxman and R.D. Ketchpel, *JANAIR Report* 720903 (1972).
22. T. Inoguchi, M. Takeda, Y. Kakihara, Y. Nakata and M. Yoshida, *Digest of 1974 SID International Symposium* (1974) 84.

23. S. Mito, C. Suzuki, Y. Kanatani and M. Ise, *Digest of 1974 SID International Symposium* (1974) 86.
24. Y. Yamauchi, M. Takeda, Y. Kakihara, M. Yoshida, M. Kawaguchi, H. Kishishita, Y. Nakata, T. Inoguchi and S. Mito, *Digest of the 1974 International Electron Device Meeting* (1974) 348.
25. M. Takeda, Y. Kakihara, M. Yoshida, M. Kawaguchi, H. Kishishita, Y. Yamauchi, T. Inoguchi and S. Mito, *Digest of 1975 SID International Symposium* (1975) 7.
26. M. Takeda, Y. Kakihara, M. Yoshida, Y. Nakata, M. Kawaguchi, H. Kishishita, Y. Yamauchi, T. Inoguchi and S. Mito, *Jpn. J. Appl. Phys.* **44** (1975), *Suppl.* **44-1** (Proc. 6th Conf. Solid State Devices, Tokyo, 1974), p.103.
27. W.E. Howard, *J. Lumin.* **23** (1981) 155.
28. W.E. Howard, O. Sahni and P.M. Alt, *J. Appl. Phys.* **53** (1982) 639.
29. W.E. Howard, *IEEE Trans. Electron Devices* **ED-24** (1977) 903 and *Proc. SID* **18** (1977) 119.
30. T. Suntola, J. Antson, A. Pakkala and S. Lindfors, *Digest of 1980 SID International Symposium* (1980) 108.
31. M. Takeda, Y. Kanatani, H. Kishishita, T. Inoguchi and K. Okano, *Digest of 1980 SID International Symposium* (1980) 66 and *Proc. SID* **22** (1981) 57.
32. H. Uede, Y. Kanatani, H. Kishishita, A. Fujimori and K. Okano, *Digest of 1981 SID International Symposium* (1981) 28.
33. E.W. Chase, R.T. Heppelwhite, D.C. Krupka and D. Kahng, *J. Appl. Phys.* **40** (1969) 2512.
34. K. Okamoto, *Ph.D. thesis* (February, 1981, Osaka University).
35. H. Ohnishi, K. Yamamoto and Y. Katayama, *Conference Record of the 1985 International Display Research Conference* (1985) 159.
36. H. Ohnishi, Y. Yamasaki and R. Iwase, *Digest of 1987 SID International Symposium* (1987) 238 and *Proc. SID* **28** (1987) 345.
37. T. Ogura, A. Mikami, K. Tanaka, K. Taniguchi, M. Yoshida and S. Nakajima, *Appl. Phys. Lett.* **48** (1986) 1570.
38. H. Kobayashi, S. Tanaka, V. Shanker, M. Shiiki, T. Kunou, J. Mita and H. Sasakura, *Phys. Stat. Sol.* (a) **88** (1985) 713.
39. K. Hirabayashi, H. Kozawaguchi and B. Tsujiyama, *Japan Display '86* (1986) 254 and *Jpn. J. Appl. Phys.* **26** (1987) 1472.
40. R.T. Tuenge and J. Kane, *Digest of 1991 SID International Symposium* (1991) 279.
41. W.A. Barrow, R.T. Tuenge and M.J. Ziuchkovski, *Digest of 1986 SID International Symposium* (1986) 25.
42. N. Yamauchi, H. Kozawaguchi, O. Kogure and B. Tsujiyama, *Digest of 1987 SID International Symposium* (1987) 230.
43. M. Yamamoto, M. Inoue, T. Tohda, T. Matsuoka and A. Abe, *Japan Display '89* (1989) 228.
44. T. Konishi, Y. Fujita, M. Minamoto, S. Yamamoto and Y. Tanaka, *Digest of 1991 SID International Symposium* (1991) 271.
45. C. Laakso, R. Khormaei, C.N. King, G. Härkönen, A. Pakkala, T. Pitkänen, M. Surma-aho and R. Törnqvist, *Conference Record of the 1991 International Display Research Conference* (1991) 43.

46. N. Tsurumaki, T. Watanabe and T. Nire, *Eurodisplay '90* (1990) 212 and *Proc. SID* **32** (1991) 325.
47. K. Okibayashi, T. Ogura, K. Terada, T. Taniguchi, T. Yamashita, M. Yoshida and S. Nakajima, *Digest of 1991 SID International Symposium* (1991) 275.
48. J. Haaranen, R. Törnqvist, J. Koponen, T. Pitkänen, M. Surma-aho, W. Barrow and C. Laakso, *Digest of 1992 SID International Symposium* (1992) 348.
49. R. Törnqvist, *Displays* **13** (1992) 81.
50. W.A. Barrow, R.E. Coovert and C.N. King, *Digest of 1984 SID International Symposium* (1984) 249.
51. H. Kobayashi, S. Tanaka, V. Shanker, M. Shiiki and H. Deguchi, *J. Crystal Growth* **72** (1985) 559.
52. S. Tanaka, V. Shanker, M. Shiiki, H. Deguchi and H. Kobayashi, *Digest of 1985 SID International Symposium* (1985) 218 and *Proc. SID* **26** (1985) 255.
53. S. Tanaka, H. Deguchi, Y. Mikami, M. Shiiki and H. Kobayashi, *Digest of 1986 SID International Symposium* (1986) 29 and *Proc. SID* **28** (1987) 21.
54. K. Tanaka, A. Mikami, T. Ogura, M. Taniguchi, M. Yoshida and S. Nakajima, *Appl. Phys. Lett.* **48** (1986) 1730.
55. M. Yoshida, A. Mikami, T. Ogura, K. Tanaka, K. Taniguchi and S. Nakajima, *Digest of 1986 SID International Symposium* (1986) 41.
56. S. Tanaka, *J. Crystal Growth* **101** (1990) 958.
57. Y.A. Ono, M. Fuyama, K. Onisawa, K. Tamura and M. Ando, *J. Appl. Phys.* **66** (1989) 5564.
58. C.N. King, R.E. Coovert and W.A. Barrow, *Eurodisplay '87* (1987) 14.
59. C.N. King, *1988 SID Seminar Lecture Notes*, Vol. I (1988) 2A/1.
60. W.A. Barrow, R.E. Coovert, C.N. King and M.J. Ziuchkovski, *Digest of 1988 SID International Symposium* (1988) 284.
61. S. Tanaka, Y. Mikami, J. Nishiura, S. Ohshio, H. Yoshiyama and H. Kobayashi, *Digest of 1987 SID International Symposium* (1987) 234 and *Proc. SID* **28** (1987) 357.
62. S. Tanaka, H. Yoshiyama, J. Nishiura, S. Ohshio, H. Kawakami and H. Kobayashi, *Appl. Phys. Lett.* **51** (1987) 1661.
63. S. Tanaka, H. Yoshiyama, J. Nishiura, S. Ohshio, H. Kawakami and H. Kobayashi, *Digest of 1988 SID International Symposium* (1988) 293 and *Proc. SID* **29** (1988) 305.
64. S. Tanaka, H. Kawakami, K. Nakamura and H. Kobayashi, *Digest of 1989 SID International Symposium* (1989) 321 and *Proc. SID* **31** (1990) 25.
65. J. Mita, Q.Z. Gao, M. Kobayashi and K. Kawamura, *Digest of 1991 SID International Symposium* (1991) 290.
66. Y. Tanaka, S. Yamada, M. Minamoto, Y. Fujita and T. Konishi, *Japan Display '92* (1992) 721.
67. S. Tanaka, Y. Mikami, H. Deguchi and H. Kobayashi, *Jpn. J. Appl. Phys.* **25** (1986) L225.
68. T. Nire, A. Matsuno, F. Wada, K. Fuchiwaki and A. Miyakoshi, *Digest of 1992 SID International Symposium* (1992) 352.
69. A. Matsuno, T. Nire, F. Wada, K. Fuchiwaki and A. Miyakoshi, *Japan Display '92* (1992) 717.

70. K. Ohmi, S. Tanaka, Y. Yamano, K. Fujimoto, H. Kobayashi, R.H. Mauch, K.O. Velthaus and H.W. Schock, *Japan Display '92* (1992) 725.
71. R.H. Mauch, K.O. Velthaus, B. Hüttl and H.W. Schock, *Digest of 1993 SID International Symposium* (1993) 769.
72. M. Leppänen, G. Härkönen, A. Pakkala, E. Soininen and R. Törnqvist, *Eurodisplay '93* (1993) 229.
73. S. Tanaka, K. Ohmi, K. Fujimoto, H. Kobayashi, T. Nire, A. Matsuno and A. Miyakoshi, *Eurodisplay '93* (1993) 237.
74. B. Hüttl, K.O. Velthaus, U. Troppenz and R.H. Mauch, *Eurodisplay '93* (1993 515.
75. Y. Hamakawa, R. Fukao and H. Fujikawa, *Optoelectronics-Devices and Technologies* 3 (1988) 31.
76. D.H. Smith, *J. Luminescence* 23 (1981) 209.
77. K. Okamoto and S. Miura, *Appl. Phys. Lett.* 49 (1986) 1596.
78. A. Mikami, T. Ogura, K. Taniguchi, M. Yoshida and S. Nakajima, *J. Appl. Phys.* 64 (1988) 3650.
79. R.S. Crandall, *Appl. Phys. Lett.* 50 (1987) 551.
80. R.S. Crandall, M. Ling, J. Kane and P.N. Yokom, *Digest of 1987 SID International Symposium* (1987) 245.
81. S. Tanaka, H. Yoshiyama, Y. Mikami, J. Nishiura, S. Ohshio and H. Kobayashi, *Japan Display '86* (1986) 242 and *Proc. SID* 29 (1988) 77.
82. H. Yoshiyama, S.H. Sohn, S. Tanaka and H. Kobayashi, in *Electroluminescence-Proceedings of the Fourth International Workshop on Electroluminescence*, eds. S. Shionoya and H. Kobayashi (Springer Proceedings in Physic: Vol. 38) (Springer-Verlag, Berlin, 1989) p.48.
83. A.G. Fischer, *J. Electrochem. Soc.* 109 (1962) 1043.
84. A.G. Fischer, *J. Electrochem. Soc.* 110 (1963) 733.
85. A.G. Fischer, *J. Electrochem. Soc.* 118 (1971) 139C.
86. S. Kobayashi, Y. Aoki, K. Enjoji, I.P. Johnson, M.H. Higton and P.J. Huntley *Japan Display '89* (1989) 242.
87. S. Kobayashi, Y. Aoki, T. Yoshii, T. Anzaki and K. Enjoji, *Digest of 1991 SIL International Symposium* (1991) 84.
88. Y. Aoki, S. Kobayashi, S. Wada, K. Enjoji, S. Tanaka, N. Uchino, K. Yamada and H. Kobayashi, *Digest of 1992 SID International Symposium* (1992) 341.
89. A. Vecht, N.J. Werring and P.J.F. Smith, *Brit. J. Appl. Phys. (J. Phys. D)* Ser. 1 (1968) 134.
90. A. Vecht, N.J. Werring, R. Ellis and P.J.F. Smith, *Brit. J. Appl. Phys. (J. Phy: D)* Ser. 2, 2 (1969) 953.
91. A. Vecht and N.J. Werring, *J. Phys. D: Appl. Phys.* 3 (1970) 105.
92. A. Vecht, N.J. Werring, R. Ellis and P.J.F. Smith, *Proc. IEEE* 61 (1973) 902.
93. A. Vecht, *J. Vac. Sci. Technol.* 10 (1973) 789.
94. A. Vecht and S.S. Chadha, *Acta Polytechnica Scandinavica* Ph 170 (Applied Physics Series No. 170), *Fifth International Workshop on Electroluminescenc* eds. M. Leskelä and E. Nykänen (Finnish Academy of Technology, Helsinki, 1990) p.49.
95. C.W. Tang and S.A. VanSlyke, *Appl. Phys. Lett.* 51 (1987) 913.
96. C.W. Tang, S.A. VanSlyke and C.H. Chen, *J. Appl. Phys.* 65 (1989) 3610.

97. C. Adachi, S. Tokito, T. Tsutsui and S. Saito, *Jpn. J. Appl. Phys.* **27** (1988) L269.
98. C. Adachi, S. Tokito, T. Tsutsui and S. Saito, *Jpn. J. Appl. Phys.* **27** (1988) L713.
99. C. Adachi, T. Tsutsui and S. Saito, *Japan Display '89* (1989) 708.
100. C. Adachi, T. Tsutsui and S. Saito, *Appl. Phys. Lett.* **56** (1990) 799.
101. C. Adachi, T. Tsutsui and S. Saito, *Optoelectronics-Devices and Technologies* **6** (1991) 25.
102. M. Ishiko, K. Utsugi, K. Nunomura, S. Takano and C. Tani, *Japan Display '89* (1989) 704.
103. T. Inoguchi and S. Mito, in *Electroluminescence*, ed. J.I. Pankov (Topics in Applied Physics, Vol. 17) (Springer-Verlag, Berlin, 1977) Chapter 6, p.196.
104. C.N. King, *1985 SID Seminar Lecture Notes* Vol. 1, S-4.1 (1985) 4.1/1.
105. Y.A. Ono, H. Kawakami, M. Fuyama and K. Onisawa, *Jpn. J. Appl. Phys.* **26** (1987) 1482.
106. S. Shionoya and S. Ibuki, *Ouyou-Butsuri (Applied Physics)* **57** (1988) 935 (in Japanese).
107. K. Brennan, *J. Appl. Phys.* **64** (1988) 4024.
108. K. Bhattacharyya, S.M. Goodnick and J.F. Wager, in *Electroluminescence-Proceedings of the Sixth International Workshop on Electroluminescence*, eds. V.P. Singh and J.C. McClure (Cinco Puntos Press, El Paso, Texas, 1992) p.54.
109. K. Bhattacharyya, S.M. Goodnick and J.F. Wager, *J. Appl. Phys.* **73** (1993) 3390.
110. K. Brennan, *J. Appl. Phys.* **75** (1994) 678.
111. J. Fogarty, W. Kong and R. Solanki, *Digest of 1994 SID International Symposium* (1994) 569.
112. S.S. Pennathur, K. Bhattacharyya, S.M. Goodnick and J.F. Wager, *J. Appl. Phys.*(submitted).
113. E. Bringuier, *J. Appl. Phys.* **70** (1991) 4505.
114. E. Bringuier, in *Electroluminescence-Proceedings of the Sixth International Workshop on Electroluminescence*, eds. V.P. Singh and J.C. McClure (Cinco Puntos Press, El Paso, Texas, 1992) p.379.
115. E. Bringuier, *Digest of 1993 SID International Symposium* (1993) 847.
116. E. Bringuier, *J. Appl. Phys.* **75** (1994) 4291.
117. E. Bringuier, *Phys. Rev.* **B49** (1994) 7974.
118. Y.S. Chen and D.C. Krupka, *J. Appl. Phys.* **43** (1972) 4089.
119. W. Rühle, W. Marrello and A. Onton, *J. Electronic Materials* **8** (1979) 839.
120. H. Venghaus, D. Theis, H. Oppolzer and S. Schild, *J. Appl. Phys.* **53** (1982) 4146.
121. R. Törnqvist, *J. Crystal Growth* **59** (1982) 399.
122. R.O. Törnqvist, J. Antson, J. Skarp and V.P. Tanninen, *IEEE Trans. Electron Devices* **ED-30** (1983) 468 and Proc. SID **24** (1983) 128.
123. H. Sasakura, H. Kobayashi, S. Tanaka, J. Mita, T. Tanaka and H. Nakayama, *J. Appl. Phys.* **52** (1981) 6901.
124. H. Sasakura, H. Kobayashi, S. Tanaka, J. Mita and T. Tanaka, *J. Luminescence* **24/25** (1981) 897.

125. Z.K. Kun, D. Leksell, P.R. Malmberg, J. Asars and G.B. Brandt, *Digest of 1986 SID International Symposium* (1986) 270 and *Proc. SID* **28** (1987) 81.
126. J.D. Davidson, J.F. Wager and I. Khormaei, *Digest of 1991 SID International Symposium* (1991) 77.
127. J.D. Davidson, J.F. Wager, I. Khormaei, C.N. King and R. Williams, *IEEE Trans. Electron Devices* **ED-39** (1992) 1122.
128. A.A. Douglas and J.F. Wager, *Digest of 1992 SID International Symposium* (1992) 356.
129. A.A. Douglas and J.F. Wager, in *Electroluminescence- Proceedings of the Sixth International Workshop on Electroluminescence*, eds. V.P. Singh and J.C. McClure (Cinco Puntos Press, El Paso, Texas, 1992) p.387.
130. J.F. Wager, A.A. Douglas and D.C. Morton, in *Electroluminescence- Proceedings of the Sixth International Workshop on Electroluminescence*, eds. V.P. Singh and J.C. McClure (Cinco Puntos Press, El Paso, Texas, 1992) p.92.
131. A.A. Douglas, *M.S. thesis* (April, 1993, Oregon State University).
132. S.K. Tiku and G.C. Smith, *IEEE Trans. Electron Devices* **ED-31** (1984) 105.
133. C.S. Wang and B.M. Klein, *Phys. Rev.* **B24** (1981) 3393.
134. Y.R. Yang and C.B. Duke, *Phys. Rev.* **B36** (1987) 2763.
135. J.E. Bernard and A. Zunger, *Phys, Rev.* **B36** (1987) 3199.
136. Y. Kaneko and T. Koda, *J. Crystal Growth* **86** (1988) 72.
137. K.C. Mishra, K.H. Johnson and P.C. Schmidt, *Materials Science and Technology* **B18** (1993) 214.
138. A. Hasegawa and A. Yanase, *J. Phys. C: Solid State Physics* **13** (1980) 1995.
139. T.E. Peters and J.A. Baglio, *J. Electrochem. Soc.* **119** (1972) 230.
140. S.S. Sun, R.T. Tuenge, J. Kane and M. Ling, *J. Electrochem. Soc.* **141** (1994) 2877.
141. C. Jacoboni and P. Lugli, *The Monte Carlo Method for Semiconductor Device Simulation*, ed. S. Selberherr (Springer, Berlin, 1989).
142. C. Moglestue, *Monte Carlo Simulations of Semiconductor Devices* (Chapman & Hall, New York, 1993).
143. F. Capasso, *Semiconductors and Semimetals* **22D** (1986) 1.
144. B.K. Ridley, *J. Phys. C: Solid State Phys.* **16** (1983) 3373.
145. B.K. Ridley, *J. Phys. C: Solid State Phys.* **16** (1983) 4733.
146. B.K. Ridley, *Semicond. Sci. Technol.* **2** (1987) 116.
147. B.K. Ridley and F.A. El-Ela, *J. Phys.: Condens. Matter* **1** (1989) 7021.
148. B.K. Ridley and F.A. El-Ela, *Solid State Electronics* **32** (1989) 1393.
149. M.G. Burt, *J. Phys. C: Solid State Phys.* **18** (1985) L477.
150. S. McKenzie and M.G. Burt, *J. Phys. C: Solid State Phys.* **19** (1986) 1959.
151. S. McKenzie and M.G. Burt, *Semicond. Sci. Technol.* **2** (1987) 275.
152. G.A. Baraff, *Phys. Rev.* **128** (1962) 2507.
153. R. Mach and G.O. Müller, *J. Crystal Growth* **101** (1990) 967.
154. Shen Mengyan and Xu Xurong, *Solid State Communications* **72** (1989) 803.
155. E. Bringuier, private communication.
156. H.J. Fitting and A. von Czarnowski, *Phys. Status Solidi* **(a)93** (1986) 385.
157. A.A. Douglas, J.F. Wager, K. Bhattacharyya, S.M. Goodnick, D.C. Morton, J.B. Koh and C.P. Hogh, *Digest of 1993 SID International Symposium* (1993) 851.

158. A.A. Douglas, J.F. Wager, D.C. Morton, J.B. Koh and C.P. Hogh, *Appl. Phys. Lett.* **63** (1993) 231.
159. H.J. Fitting, A. von Czarnowski and G.O. Müller, *J. Crystal Growth* **101** (1990) 876.
160. E.K. Faulkner, R.K. Whitney and J.E. Zeman, *IEEE Trans. Electron Devices* **ED-30** (1983) 545 and *Proc. SID* **24** (1983) 205.
161. J. Antson, *Digest of 1982 SID International Symposium* (1982) 124.
162. T. Sutela, *Displays* **5** (1984) 73.
163. T. Suntola and J. Hyvärinen, *Ann. Rev. Mater. Sci.* **15** (1985) 177.
164. Y. Fujita, J. Kuwata, M. Nishikawa, T. Tohda, T. Matsuoka, A. Abe and T. Nitta, *Japan Display '83* (1983) 76 and *Proc. SID* **25** (1984) 177.
165. D.J. McClure and J.R. Crowe, *J. Vac. Sci. Technol.* **16** (1979) 311.
166. P.M. Alt, D.B. Dove and W.E. Howard, *J. Appl. Phys.* **53** (1982) 5186.
167. S.K. Tiku, G.C. Smith and M.R. Johnson, *Digest of 1983 SID International Symposium* (1983) 140.
168. A. Vecht, *Digest of 1989 SID International Symposium* (1989) 304.
169. Y.A. Ono, *Acta Polytechnica Scandinavica* **Ph 170** (Applied Physics Series No. 170), *Fifth International Workshop on Electroluminescence*, eds. M. Leskeä and E. Nykänen (Finnish Academy of Technology, Helsinki, 1990) p.41.
170. J.M. Hurd and C.N. King, *J. Electronic Materials* **8** (1979) 879.
171. S. Miura, K. Okamoto, S. Sato, S. Andoh, H. Ohnishi and Y. Hamakawa, *Japan Display '83* (1983) 84.
172. E.C. Freeman, D.H. Baird and J.R. Weaver, *Japan Display '83* (1983) 92.
173. L.L. Hope, J.L. Plumb, C.E. Mellor and E.A. Davey, *Proc. SPIE* **386**, *Advances in Display Technology III* (1983) 58.
174. M.I. Abdalla, J.L. Plumb and L.L. Hope, *Digest of 1984 SID International Symposium* (1984) 245.
175. T. Emma and M. McDonough, *J. Vac. Sci. Technol.* **A2** (1984) 362.
176. T. Matsuoka, J. Kuwata, M. Nishikawa, Y. Fujita, T. Tohda and A. Abe, *Jpn. J. Appl. Phys.* **27** (1988) 592.
177. C. Frey, D. Serafin and R. Boudreau, *Digest of 1988 SID International Symposium* (1988) 16.
178. H. Ohnishi, *Digest of 1994 SID International Symposium* (1994) 129.
179. T. Nire, T. Watanabe, S. Tanda and S. Sano, *Digest of 1987 SID International Symposium* (1987) 242.
180. T. Nire, T. Watanabe, N. Tsurumaki, A. Miyakoshi and S. Tanda, *Electro-luminescence-Proceedings of the Fourth International Workshop*, eds. S. Shionoya and H. Kobayashi (Springer Proceedings in Physics, Vol. 38) (Springer-Verlag, Berlin, 1989) p.218.
181. S. Tanda, A. Miyakoshi and T. Nire, *Conference Record of the 1988 International Display Research Conference* (1988) 122.
182. S. Tanda, A. Miyakoshi and T. Nire, *Electroluminescence-Proceedings of the Fourth International Workshop*, eds. S. Shionoya and H. Kobayashi (Springer Proceedings in Physics, Vol. 38) (Springer-Verlag, Berlin, 1989) p.180.
183. T. Nire, A. Matsuno, A. Miyakoshi and K. Ohmi, *Jpn. J. Appl. Phys.* **33** (1994), 2605.
184. T. Suntola, *Digest of 1981 SID International Symposium* (1981) 20.

185. J. Hyvärinen, M. Sonninen and R. Törnqvist, *J. Crystal Growth* **86** (1988) 695.
186. T. Suntola, *Materials Science Reports* **4** (1989) 261.
187. T. Suntola, *Thin Solid Films* **216** (1992) 84.
188. M. Leskelä, in *Electroluminescence-Proceedings of the Fourth International Workshop*, eds. S. Shionoya and H. Kobayashi (Vol. 38 of Springer Proceedings in Physics) (Springer-Verlag, Berlin, 1989) p.204.
189. M. Leskelä, M. Mäkelä, L. Niinistö, E. Nykänen and M. Tammenmaa, *Chemtronics* **3** (1988) 113.
190. M. Leskelä and L. Niinistö, *Electroluminescence Proceedings of the Sixth International Workshop on Electroluminescence*, eds. V.P. Singh and J.C. McClure (Cinco Puntos Press, El Paso, Texas, 1992) p.249.
191. V.-P. Tanninen, M. Oikkonen and T.O. Tuomi, *Phys. Stat. Sol.* (a)**67** (1981) 573; *Thin Solid Films* **109** (1983) 283.
192. D. Theis, H. Oppolzer, G. Ebbinghaus and S. Schild, *J. Crystal Growth* **63** (1983) 47.
193. R. Törnqvist and S. Koppela, *J. Crystal Growth* **59** (1982) 395.
194. H. Antson, M. Grasserbauer, M. Hamilo, L. Hiltunen, T. Koskinen, M. Leskelä, L. Niinistö, G. Stingeder and M. Tammenmaa, *Fresenius Z. Anal. Chem.* **322** (1985) 175.
195. J.A. Lahtinen, A. Lu, T. Tuomi and M. Tammenmaa, *J. Appl. Phys.* **58** (1985) 851.
196. G. Härkönen, K. Härkönen and R. Törnqvist, *Digest of 1990 SID International Symposium* (1990) 232.
197. M. Leppänen, M. Leskelä, L. Niinistö, E. Nykkänen, P. Soininen and M. Tiita, *Digest of 1991 SID International Symposium* (1991) 282.
198. E. Soininen, M. Leppänen and A. Pakkala, *Eurodisplay '93* (1993) 233.
199. A.F. Cattel, B. Cockayne, K. Dexter, J. Kirton and P.J. Wright, *IEEE Trans. Electron Devices* **ED-30** (1983) 471 and *Proc. SID* **24** (1983) 131.
200. K. Hirabayashi and O. Kogure, *Jpn. J. Appl. Phys.* **24** (1985) 1484.
201. K. Hirabayashi and H. Kozawaguchi, *Jpn. J. Appl. Phys.* **25** (1986) 711.
202. T. Shibata, K. Hirabayashi, H. Kozawaguchi and B. Tsujiyama, *Jpn. J. Appl. Phys.* **26** (1987) L1664.
203. K. Hirabayashi and H. Kozawaguchi, *Jpn. J. Appl. Phys.* **28** (1989) 814.
204. M. Migita, O. Kanehisa, M. Shiiki and H. Yamamoto, *J. Crystal Growth* **93** (1988) 686.
205. M. Shiiki, M. Migita, O. Kanehisa and H. Yamamoto, in *Electroluminescence-Proceedings of the Fourth International Workshop*, eds. S. Shionoya and H. Kobayashi (Springer Proceedings in Physics, Vol. 38), (Springer-Verlag, Berlin, 1989) p.224.
206. A. Saunders and A. Vecht, in *Electroluminescence-Proceedings of the Fourth International Workshop*, eds. S. Shionoya and H. Kobayashi (Springer Proceedings in Physics, Vol. 38) (Springer-Verlag, Berlin, 1989) p.210.
207. T. Takahara, M. Endo, K. Chiba and A. Kondo, *Digest of 1991 SID International Symposium* (1991) 66.
208. S.S. Chadha, D.W. Smith, A. Vecht and J.L. Williams, *Digest of 1991 SID International Symposium* (1991) 80.
209. A. Mikami, K. Terada, K. Tanaka, K. Taniguchi, M. Yoshida and S. Nakajima, *Digest of 1989 SID International Symposium* (1989) 309.

210. A. Mikami, K. Terada, K. Okibayashi, K. Tanaka, M. Yoshida and S. Nakajima, *J. Crystal Growth* **110** (1991) 381.
211. A. Mikami, K. Terada, M. Yoshida and S. Nakajima, *J. Crystal Growth* **117** (1992) 991.
212. A. Mikami, K. Terada, K. Okibayashi, K. Tanaka, M. Yoshida and S. Nakajima, *J. Appl. Phys.* **72** (1992) 773
213. A. Mikami and M. Yoshida, *Electroluminescence-Proceedings of the Sixth International Workshop on Electroluminescence*, eds. V.P. Singh and J.C. McClure (Cinco Puntos Press, El Paso, Texas, 1992) p.257.
214. K. Nakaji, T. Ogura, T. Yamashita, M. Yoshida and S. Nakajima, *Sharp Technical Journal* **43** (1989) 15 (in Japanese).
215. K. Katoh, Y. Tamura and O. Kogure, *Conference Record of the 1985 International Display Research Conference* (1985) 98.
216. R. Tueta and M. Braguier, *Thin Solid Films* **80** (1981) 143.
217. Y. Shimizu and T. Matsudaira, *Conference Record of the 1985 International Display Research Conference* (1985) 101.
218. M. Yoshida, K. Tanaka, K. Taniguchi, T. Yamashita, Y. Kakihara and T. Inoguchi, *Digest of 1980 SID International Symposium* (1980) 106.
219. C.N. King, *Acta Polytechnica Scandinavica* **Ph 170**, *Fifth International Workshop on Electroluminescence*, eds. M. Leskelä and E. Nykänen (Finnish Academy of Technology, Helsinki, 1990) p.59.
220. R. Törnqvist, in *Electroluminescence, Proceedings of the Sixth International Workshop on Electroluminescence*, eds. V.P. Singh and J.C. McClure (Cinco Puntos Press, El Paso, Texas, 1992) p.329.
221. J. Mita, M. Koizumi, T. Hayashi, Y. Sekido, M. Kazama and K. Nihei, *Japan Display '86* (1986) 250.
222. H. Kobayashi, S. Tanaka, T. Kunou, M. Shiiki and H. Sasakura, *Japan Display '83* (1983) 592 and *Proc. SID* **25** (1984) 187.
223. K. Okamoto and K. Watanabe, *Appl. Phys. Lett.* **49** (1986) 578.
224. A. Mikami, T. Ogura, K. Tanaka, K. Taniguchi, M. Yoshida and S. Nakajima, *J. Appl. Phys.* **61** (1987) 3028.
225. K. Hirabayashi, H. Kozawaguchi and B. Tsujiyama, *Jpn. J. Appl. Phys.* **27** (1988) 587.
226. K. Okamoto, T. Yoshimi and S. Miura, *Appl. Phys. Lett.* **53** (1988) 678 and in *Electroluminescence-Proceedings of the Fourth International Workshop on Electroluminescence*, eds. S. Shionoya and H. Kobayashi (Springer Proceedings in Physics, Vol. 38) (Springer-Verlag, Berlin, 1989) p.139.
227. H. Ohnishi and K. Okamoto, *Conference Record of the 1988 International Display Research Conference* (1988) 32.
228. K. Okamoto, T. Yoshimi, K. Nakamura, T. Kobayashi, S. Sato and S. Miura, *Jpn. J. Appl. Phys.* **28** (1989) 1378.
229. H. Ohnishi and K. Okamoto, *Jpn. J. Appl. Phys.* **28** (1989) L2239.
230. H. Ohnishi and F. Mohri, *Digest of 1992 SID International Symposium* (1992) 363.
231. H. Yoshino, M. Ohura, S. Kurokawa and H. Ohnishi, *Japan Display '92* (1992) 737.

232. R.T. Tuenge, in *Electroluminescence-Proceedings of the Fourth International Workshop on Electroluminescence*, eds. S. Shionoya and H. Kobayashi (Springer Proceedings in Physics, Vol. 38) (Springer-Verlag, Berlin, 1989) p.132.

233. T. Tohda, Y, Fujita, T. Matsuoka and A. Abe, *Appl. Phys. Lett.* **48** (1986) 95.

234. R.E. Schrader, S. Larach and P.N. Yokom, *J. Appl. Phys.* **42** (1971) 4529.

235. M. Higton, A. Vecht and J. Mayo, *Digest of 1978 SID International Symposium* (1978) 136.

236. A. Vecht, *Digest of 1980 SID International Symposium* (1980) 110.

237. H. Yoshiyama, S. Tanaka, Y. Mikami, S. Ohshio, J. Nishiura, H. Kawakami and H. Kobayashi, *J. Crystal Growth* **86** (1988) 56.

238. R.S. Crandall, *Appl. Phys. Lett.* **50** (1987) 641.

239. M. Ando and Y.A. Ono, *J. Appl. Phys.* **65** (1989) 3290.

240. C. Gonzalez, *Eurodisplay '87* (1987) 21.

241. C. Gonzales, *J. Luminescence* **40&41** (1988) 771.

242. S. Tanaka, H. Morita, K. Yamada and H. Kobayashi, *Conference Record of the 1991 International Display Research Conference* (1991) 137.

243. K. Onisawa, M. Fuyama, K. Taguchi, K. Tamura and Y.A. Ono, *J. Electrochem. Soc.* **135** (1988) 2631.

244. K. Okamoto and K. Hanaoka, *Jpn. J. Appl. Phys.* **27** (1988) L1923.

245. C.N. King, *1994 SID Seminar Lecture Notes* Vol. 1, M-9 (1994) M-9/1.

246. C.N. King, *Conference Record of the 1994 International Display Research Conference* (1994) 69.

247. Y. Inoue, K. Tanaka, S. Okamoto and K. Kobayashi, *Conference Record of the 1994 International Display Research Conference* (1994) 169.

248. P. Benalloul, C. Barthou, J. Benoit, L. Eichenauer and A. Zeinert, *Appl. Phys. Lett.* **63** (1993) 1954.

249. P. Benalloul, C. Barthou, J. Benoit, L. Eichenauer and A. Zeinert, *Eurodisplay '93* (1993) 609.

250. K. Kurahashi, K. Takahara and S. Andoh, *Eurodisplay '81* (1981) 216.

251. S. Harada, T. Ohba, Y. Kanatani and H. Uede, *Japan Display '86* (1986) 238.

252. K. Shoji, T. Ohba, H. Kishishita and H. Uede, in *Electroluminescence-Proceedings of the Fourth International Workshop on Electroluminescence* (Springer Proceedings in Physics, Vol. 38), eds. S. Shionoya and H. Kobayashi (Springer-Verlag, Berlin, 1989) p.324.

253. T.P. Brody, F.C. Luo, Z.P. Szepesi and D.H. Davies, *IEEE Trans. Electron Devices,* **ED-22** (1975) 739.

254. Z.K. Kun, F.C. Luo and J. Murphy, *Proc. SID* **21** (1980) 85.

255. K. Nomura, H. Ogawa, A. Abe and T. Nitta, *Japan Display '83* (1983) 574.

256. J. Vanfleteren, P. De Visschere, J. De Baets, I. DeRycke, J. Doutreloigne, A. Van Calster and M. Mäenpää, *Conference Record of the 1988 International Display Research Conference* (1988) 74.

257. J. Vanfleteren, J. De Baets, I. De Rycke, H. De Smet, J. Doutreloigne, A. Van Calster, P. De Visschere, K. Sallmén and R. Graeffe, Eurodisplay '90 (1990) 216.

258. J. Vanfleteren, J. Capon, J. De Baets, I. De Rycke, H. De Smet, J. Doutreloigne, A. Van Calster, P. De Visschere, K. Sallmén and R. Graeffe, *Conference Record of the 1991 International Display Research Conference* (1991) 134.

259. T. Unagami and B. Tsujiyama, *Digest of 1983 SID International Symposium* (1983) 154 and *Proc. SID* **25** (1984) 117.
260. T. Unagami and O. Kogure, *IEEE Trans. Electron Devices* **ED-35** (1988) 314.
261. T. Suzuki, Y. Uno, J. Sakurai, Y. Saito, S. Kyozuka, N. Hiji and T. Ozawa, *Digest of 1992 SID International Symposium* (1992) 344.
262. R. Khormaei, S. Thayer, K. Ping, C. King, G. Dolney, A. Ipri, F.-L. Hsueh, R. Stewart, T. Keyser, G. Becker, D. Kagey and M. Spitzer, *Digest of 1994 SID International Symposium* (1994) 137.
263. L.L Hope, J.L. Plume and D.H. Baird, *Japan Display '83* (1983) 582.
264. J. Watanabe, M. Wakitani, S. Sato and S. Miura, *Digest of 1987 SID International Symposium* (1987) 288.
265. R.T. Flegal and C.N. King, *Digest of 1986 SID International Symposium* (1986) 177.
266. G.O. Müller, R. Mach, R. Reetz and G.U. Reinsperger, *Digest of 1988 SID International Symposium* (1988) 23.
267. M.L. Higgins, *Digest of 1985 SID International Symposium* (1985) 226.
268. G. Dolny, A. Ipri, F.-L. Hsueh, R. Stewart, R. Khormaei, S. Thayer, T. Keyser, G. Becker, M. Spitzer and M. Batty, *Technical Digest of 1993 International Electron Device Meeting* (1993) 930.
269. Jim Duncker, *Digest of 1983 SID International Symposium* (1983) 42.
270. C.N. King, in *Electroluminescence-Proceedings of the Sixth International Workshop on Electroluminescence,* eds. V.P. Singh and J.C. McClure (Cinco Puntos Press, El Paso, Texas, 1992) p.337.
271. R.O. Törnqvist, T.T. Harju, J.T. Honkala, J.H. Viljanen, M.H. Åberg and H.P. Kattelus, *Digest of 1991 SID International Symposium* (1991) 63.
272. R. Schmachtenberg, T. Jenness, M. Ziuchkovski and T. Flegal, *Digest of 1989 SID International Symposium* (1989) 58.
273. C.N. King, *Japan Display '89* (1989) 224.
274. C.N. King, *Digest of 1991 SID International Symposium* (1991) 292.
275. R.E. Coovert, C.N. King and R.T. Tuenge, *Digest of 1982 SID International Symposium* (1982) 128.
276. R.E. Coovert and C.N. King, *Proc. SPIE* **386**, *Advances in Display Technology III* (1983) 63.
277. Y. Oishi, T. Kato and Y. Hamakawa, *Japan Display '83* (1983) 570.
278. C. Brunel, N. Bouadma and P. LeBerre, *Eurodisplay '87* (1987) 238.
279. D. Leksell, Z.K. Kun and G.J. Machiko, *Proc. SID* **29** (1988) 147.
280. Z.K. Kun, D. Leksel and G.B. Brandt, *J. Crystal Growth* **117** (1992) 987.
281. S. Okamoto, E. Nakazawa and T. Suzuki, *Jpn. J. Appl. Phys.* **30** (1991) L1321.
282. S. Okamoto, E. Nakazawa and T. Suzuki, *J. Crystal Growth* **117** (1992) 943.
283. A. Kitai, N. Dalacu and H. Zhizheng, *Digest of 1991 SID International Symposium* (1991) 440.
284. G.O. Müller, R. Mach, G.U. Reinsperger, E. Halden and G. Schulz, *J. Crystal Growth* **117** (1992) 948.
285. T. Moriguchi, I. Suzuki, Y. Hisazumi, T. Nakagawa and S. Kasai, *Technical Report of the Institute of Electronics, Information and Communication Engineers* EID **88-76** (1988) 11 (in Japanese).
286. A. Mikami and K. Ando, *Transactions of Institute of Electronics Communication*

*Engineers* **J68-C** (1985) 285 (in Japanese).

287. J. Mita, M. Koizumi, H. Kanno, T. Hayashi, Y. Sekido, I. Abiko and K. Nihei, *Jpn. J. Appl. Phys.* **26** (1987) L541.

288. M. Nishikawa, T. Matsuoka, T. Tohda, Y. Fujita, J. Kuwata and A. Abe, *Digest of 1988 SID International Symposium* (1988) 19 and *Proc. SID* **29** (1988) 301.

289. R. Khormaei, J.F. Wager and C.N. King, *Digest of 1989 SID International Symposium* (1989) 65.

290. K. Okamoto, M. Wakitani, S. Sato, S. Miura, S. Andoh and S. Umeda, *Digest of 1983 SID International Symposium* (1983) 16.

291. R. Khormaei, C.N. King, R.E. Coovert and J.F. Wager, *Digest of 1991 SID International Symposium* (1991) 74.

292. R.T. Flegal, R.E. Coovert and C.N. King, *Digest of 1985 SID International Symposium* (1985) 213.

293. H. Kobayashi, in *Electroluminescence-Proceedings of the Sixth International Workshop on Electroluminescence*, eds. V.P. Singh and J. C. McClure (Cinto Puntos Press, El Paso, 1992) p.179.

294. S. Tanaka, K. Ohmi, K. Yamada, Y. Yamano and H. Kobayashi, in *Electroluminescence-Proceedings of the Sixth International Workshop on Electroluminescence*, eds. V.P. Singh and J. C. McClure (Cinto Puntos Press, El Paso, 1992) p.193.

295. K. Ohmi, S. Tanaka, H. Kobayashi and T. Nire, in *Electroluminescence-Proceedings of the Sixth International Workshop on Electroluminescence*, eds. V.P. Singh and J. C. McClure (Cinto Puntos Press, El Paso, 1992) p.309.

296. H. Fujiyasu, N. Katayama, H. Yang, K. Ishino, A. Ishida, M. Kaneko and T. Ohiwa, in *Electroluminescence-Proceedings of the Fourth International Workshop on Electroluminescence* (Springer Proceedings in Physics, Vol. 38), eds. S. Shionoya and H. Kobayashi (Springer-Verlag, Berlin, 1989) p.116

297. H. Fujiyasu, Y. Takeuchi, K. Hidaka, K. Ishino and A. Ishida, J. Crystal Growth **117** (1992) 1026.

# INDEX